

# Glaciation Scenario: Groundwater and Radionuclide Transport Studies

NWMO TR-2010-09

July 2010

**Robert Walsh and John Avis**

Intera Engineering

**nwmo**

NUCLEAR WASTE  
MANAGEMENT  
ORGANIZATION

SOCIÉTÉ DE GESTION  
DES DÉCHETS  
NUCLÉAIRES



**Nuclear Waste Management Organization**  
22 St. Clair Avenue East, 6<sup>th</sup> Floor  
Toronto, Ontario  
M4T 2S3  
Canada

Tel: 416-934-9814  
Web: [www.nwmo.ca](http://www.nwmo.ca)

**Glaciation Scenario: Groundwater and Radionuclide Transport Studies**

**NWMO TR-2010-09**

July 2010

**Robert Walsh and John Avis**  
Intera Engineering

---

Disclaimer:

This report does not necessarily reflect the views or position of the Nuclear Waste Management Organization, its directors, officers, employees and agents (the "NWMO") and unless otherwise specifically stated, is made available to the public by the NWMO for information only. The contents of this report reflect the views of the author(s) who are solely responsible for the text and its conclusions as well as the accuracy of any data used in its creation. The NWMO does not make any warranty, express or implied, or assume any legal liability or responsibility for the accuracy, completeness, or usefulness of any information disclosed, or represent that the use of any information would not infringe privately owned rights. Any reference to a specific commercial product, process or service by trade name, trademark, manufacturer, or otherwise, does not constitute or imply its endorsement, recommendation, or preference by NWMO.

---

## ABSTRACT

**Title:** Glaciation Scenario: Groundwater and Radionuclide Transport Studies  
**Report No.:** NWMO TR-2010-09  
**Author(s):** Robert Walsh and John Avis  
**Company:** Intera Engineering  
**Date:** July 2010

### Abstract

Previous Canadian safety assessments have focussed on radionuclide transport from a deep geologic repository under steady climate and groundwater conditions. The purpose of the current study was to address potential impacts associated with glacial cycles.

The effects of glaciation were addressed using a three-dimensional (3-D) numerical model of a hypothetical repository in the Canadian Shield. This study investigates: (1) the impact on the hydrogeological system of a representative glacial cycle, consisting of temperate (present day climate), permafrost, ice cover and proglacial lake periods, and, (2) the impact of multiple glacial cycles on the long-term transport of radionuclides from a hypothetical defective container. Additional numeric studies were performed to assess the depth of glacial meltwater intrusion. The model included a representative set of fractures across the 13 km x 20 km model domain. Salinity effects were not included.

The current study shows that the location of the shortest groundwater pathway from the repository to surface may be different for the transient glaciation flow model. Factors such as the proximity of fracture zones are common to both steady state and transient models, but other important factors determining travel time, such as proximity to taliks, will be unique to the transient model.

Transient groundwater flow results show that hydrogeological conditions are profoundly changed during climate cycles, with median groundwater velocities within the repository footprint varying over two orders of magnitude. Glaciation induced pressure gradients are rapidly propagated horizontally and vertically through the highly connected high permeability fracture system and through hydromechanical coupling using a simplified one-dimensional strain hydromechanical model.

Although the glacial cycles do modify the flow field extensively, the cumulative impact on radionuclide transport of repeated cycles of advance and retreat tend to effectively "cancel out", leading to a general plume structure that is not substantially different from the steady-state flow and transport model. It was also seen that glacially induced overpressures can persist for thousands of years after the glacier itself has retreated, and this effect impacts transport to the surface. The study also showed that taliks (zones where permafrost is absent underneath surface water features) can have a very significant role in transmitting glacial recharge into the deep geosphere, and in acting as discrete hydraulic windows through which overpressurized water from preceding glaciation events is drained.

The Reference Case model predicted higher  $^{129}\text{I}$  concentrations in well water (albeit for limited time periods immediately after ice retreat), higher peak  $^{129}\text{I}$  mass flows to the biosphere, and higher average  $^{129}\text{I}$  mass flows to the biosphere (as indicated by higher cumulative mass flow) compared to the Steady State Temperate climate model. Peak well concentrations and mass flows in the glaciation model also occurred earlier than in the steady state model. The steady state model was run with and without a well. Mass flow comparisons were done against the model without a well, as the well intercepted the bulk of the  $^{129}\text{I}$  that would otherwise reach the small lake/talik above the repository.

Several uncertainties were considered such as the appropriate boundary conditions, higher storage coefficients, and the presence or absence of taliks under ice sheets. The broad conclusions were not very sensitive to these changes. The modelling project did not incorporate other potential sources of variation, such as alternative permeability values. However, the guiding philosophy was to choose values and assumptions that, while remaining within the bounds of hydrogeological realism, would overpredict radionuclide transport when a more detailed sensitivity analysis was not possible.



**TABLE OF CONTENTS**

	<b><u>Page</u></b>
<b>ABSTRACT</b> .....	<b>v</b>
<b>1. INTRODUCTION</b> .....	<b>1</b>
<b>2. GLACIATION SCENARIO</b> .....	<b>3</b>
<b>2.1 General Glacial Cycle</b> .....	<b>3</b>
<b>2.2 Ice Profile</b> .....	<b>4</b>
<b>3. MODEL CHARACTERISTICS</b> .....	<b>7</b>
<b>3.1 General Approach</b> .....	<b>7</b>
<b>3.2 Model Domain</b> .....	<b>9</b>
<b>3.3 Fracture Network</b> .....	<b>12</b>
<b>3.4 Material Properties</b> .....	<b>13</b>
3.4.1 Layered Properties.....	13
3.4.2 Fracture Properties .....	14
3.4.3 Permafrost Implementation .....	15
<b>3.5 Boundary Conditions</b> .....	<b>16</b>
<b>3.6 Radionuclide Source Term</b> .....	<b>20</b>
<b>3.7 Water Supply Well</b> .....	<b>22</b>
<b>4. MODELLING CASES</b> .....	<b>23</b>
<b>5. GLACIAL SEQUENCE MODELLING RESULTS</b> .....	<b>25</b>
<b>5.1 Comparison to HBC Reference Case</b> .....	<b>25</b>
<b>5.2 Single Glacial Cycle Flow Results</b> .....	<b>26</b>
5.2.1 Head and Velocity Distribution .....	26
5.2.1.1 Reference Case.....	27
5.2.1.2 High Storage Coefficient Case .....	34
5.2.1.3 No-Flow North-South Boundaries Case .....	36
5.2.1.4 Talik under Glacier Case.....	39
5.2.2 Effect of Hydromechanical Coupling .....	40
5.2.3 Repository Velocity Calculations .....	43
5.2.4 Particle Tracking Results .....	47
<b>5.3 Multiple Glacial Cycle Transport Results</b> .....	<b>55</b>
5.3.1 Concentration Distributions - Defective Container 1 (DC1).....	56
5.3.2 Concentration Distributions - Defective Container 3 (DC3).....	72
5.3.3 Mass Flow Plots.....	85
5.3.3.1 Temperate Steady State Model.....	86
5.3.3.2 Transient Modelling Cases – Defective Containers in DC1 Location .....	88
5.3.3.3 Transient Modelling Cases – Defective Containers in DC3 Location .....	93
5.3.3.4 Well Concentration.....	98
<b>5.4 Is Mass Transport Diffusion or Advection Dominated?</b> .....	<b>99</b>
<b>5.5 Numeric Performance</b> .....	<b>102</b>

<b>6.</b>	<b>ADDITIONAL NUMERIC STUDIES.....</b>	<b>103</b>
<b>6.1</b>	<b>Glacial Meltwater Intrusion.....</b>	<b>103</b>
<b>6.2</b>	<b>Rapid Drainage of Proglacial Lake .....</b>	<b>111</b>
<b>7.</b>	<b>CONCLUSIONS .....</b>	<b>113</b>
	<b>REFERENCES .....</b>	<b>117</b>
	<b>APPENDIX: REFERENCE CASE CONCENTRATION PLOTS .....</b>	<b>119</b>

## LIST OF TABLES

	<u>Page</u>
Table 2.1: Time history for reference glacial cycle (Garisto et al. 2010) .....	3
Table 2.2: Advance and retreat rates in simplified glacial cycle. Values for subsequent cycles are identical.....	6
Table 3.1: Material properties that vary between flow model layers.....	13
Table 4.1: Modelling sensitivity cases. ....	24

## LIST OF FIGURES

	<u>Page</u>
Figure 2.1: Data from the reference simulation nn2778 and the simplified reference glacial cycle used in this work.....	4
Figure 2.2: Ice surface profile.....	5
Figure 3.1: Flow and transport model domain. ....	10
Figure 3.2: Flow and transport model horizontal discretization. ....	11
Figure 3.3: Fracture network realization for the GSC model. ....	12
Figure 3.4: Vertical hydraulic conductivity profiles. ....	14
Figure 3.5: Geosphere hydraulic conductivity distribution during temperate periods. Fences are partially transparent. Darker zones at the intersections of fences should not be misinterpreted as zones of lower hydraulic conductivity. ....	15
Figure 3.6: Geosphere hydraulic conductivity distribution during permafrost periods, with 250 m deep permafrost and two open taliks. Fences are partially transparent. Darker zones at the intersections of fences should not be misinterpreted as zones of lower hydraulic conductivity. ....	16
Figure 3.7: Cross sectional schematic through a continental ice sheet, isostatic depression and forebulge phenomena are not shown (adapted from Lemieux et al., 2008).....	17
Figure 3.8: Ice surface boundary condition heads during the first glacial advance. ....	18
Figure 3.9: Hydraulic head boundary condition head 200 years into glacial advance. Above roughly 1500 mN the hydraulic head is a function of ice surface elevation, while below 1500 mN the hydraulic head boundary condition is still based on the ground surface elevation.....	19
Figure 3.10: Release rate of <sup>129</sup> Iodine from repository near-field. ....	20
Figure 3.11: Defective container source locations. Only locations DC1 and DC3 were assessed in this report. ....	21
Figure 5.1: Comparison of mass flux to the Lake for the no-well case for the HBC and GSC-CC models. ....	25
Figure 5.2: Location of cross-section for figures in Section 5.2.1.....	26
Figure 5.3: GSC-RC flow model results during initial temperate phase (stage 1 – temperate). The hydraulic head distribution is shown in (a), while the advective velocity distribution is shown in (b). Velocity vectors are only plotted where the velocity exceeds 1 mm/a.....	27
Figure 5.4: GSC-RC flow model results at 58,400 years (beginning of stage 3 – ice advance, cold based glacier). The hydraulic head distribution is shown in (a), while the advective velocity distribution is shown in (b). Velocity vectors are only plotted where the velocity exceeds 1 mm/a.....	28
Figure 5.5: GSC-RC flow model results at 65,800 years (midpoint of stage 4 – ice retreat, cold based glacier). The hydraulic head distribution is shown in (a), while the advective velocity distribution is shown in (b). Velocity vectors are only plotted where the velocity exceeds 1 mm/a. ....	29

Figure 5.6: GSC-RC flow model results at 68,550 years (start of stage 5 – permafrost). The hydraulic head distribution is shown in (a), while the advective velocity distribution is shown in (b). Velocity vectors are only plotted where the velocity exceeds 1 mm/a. ....30

Figure 5.7: GSC-RC flow model results at 100,500 years (end of stage 5 – permafrost). The hydraulic head distribution is shown in (a), while the advective velocity distribution is shown in (b). Velocity vectors are only plotted where the velocity exceeds 1 mm/a. ....31

Figure 5.8: GSC-RC flow model results at 143,200 years (midpoint of stage 10 – ice advance, warm based glacier). The hydraulic head distribution is shown in (a), while the advective velocity distribution is shown in (b). Velocity vectors are only plotted where the velocity exceeds 1 mm/a. ....32

Figure 5.9: GSC-RC flow model results at 159,000 years (end of stage 11 – ice retreat, warm based glacier). The hydraulic head distribution is shown in (a), while the advective velocity distribution is shown in (b). Velocity vectors are only plotted where the velocity exceeds 1 mm/a. ....33

Figure 5.10: GSC-RC flow model results at 160,000 years (midpoint of stage 12 – pro-glacial lake). The hydraulic head distribution is shown in (a), while the advective velocity distribution is shown in (b). Velocity vectors are only plotted where the velocity exceeds 1 mm/a. ....34

Figure 5.11: GSC-HS flow model results at 58,400 years (beginning of stage 3 – ice advance, cold based glacier). The hydraulic head distribution is shown in (a), while the advective velocity distribution is shown in (b). Velocity vectors are only plotted where the velocity exceeds 1 mm/a. ....35

Figure 5.12: GSC-HS flow model results at 68,550 years (start of stage 5 – permafrost). The hydraulic head distribution is shown in (a), while the advective velocity distribution is shown in (b). Velocity vectors are only plotted where the velocity exceeds 1 mm/a. ....36

Figure 5.13: GSC-NF flow model results at 58,400 years (beginning of stage 3 – ice advance, cold based glacier). The hydraulic head distribution is shown in (a), while the advective velocity distribution is shown in (b). Velocity vectors are only plotted where the velocity exceeds 1 mm/a. ....37

Figure 5.14: GSC-NF flow model results at 65,800 years (midpoint of stage 4 – ice retreat, cold based glacier). The hydraulic head distribution is shown in (a), while the advective velocity distribution is shown in (b). Velocity vectors are only plotted where the velocity exceeds 1 mm/a. ....38

Figure 5.15: GSC-NF flow model results at 68,550 years (start of stage 5 – permafrost). The hydraulic head distribution is shown in (a), while the advective velocity distribution is shown in (b). Velocity vectors are only plotted where the velocity exceeds 1 mm/a. ....39

Figure 5.16: GSC-TK flow model results at 58,400 years (beginning of stage 3 – ice advance, cold based glacier). The hydraulic head distribution is shown in (a), while the advective velocity distribution is shown in (b). Velocity vectors are only plotted where the velocity exceeds 1 mm/a. ....40

Figure 5.17: GSC-NF with no hydromechanical coupling. Results at 58,400 years (beginning of stage 3 – ice advance, cold based glacier). The hydraulic head distribution is shown in (a), while the advective velocity distribution is shown in (b). Velocity vectors are only plotted where the velocity exceeds 1 mm/a. ....41

Figure 5.18: Ratio of the advective flow velocity magnitude for GSC-NF with and without hydromechanical coupling. Results are shown at (a) 58,400 years (300 years into cold based glacial advance), (b) 59,300 years (1200 into glacial advance), and (c) 61,100 years (3000 years into glacial advance) .....42

Figure 5.19: Differences between the hydraulic heads for GSC-NF with and without hydromechanical coupling. Results are shown at (a) 58,400 years (300 years into cold

based glacial advance), (b) 59,300 years (1200 into glacial advance), and (c) 61,100 years (3000 years into glacial advance) .....	43
Figure 5.20: GSC-RC flow model, average vertical component of advective velocity within the repository footprint. Positive velocities are upward, negative velocities are downward. ....	44
Figure 5.21: GSC-RC flow model, cumulative average vertical advective flow distance within the repository footprint. Calculated by integrating Figure 5.20 over time.....	45
Figure 5.22: GSC-HS flow model, average vertical component of advective velocity within the repository footprint. Positive velocities are upward, negative velocities are downward. ....	46
Figure 5.23: GSC-RC flow model, cumulative average vertical advective flow distance within the repository footprint. Calculated by integrating Figure 5.20 over time.....	47
Figure 5.24: 100 year particle travel CDFs for selected flow times, GSC-RC model.....	48
Figure 5.25: Particle travel time to discharge for steady-state temperate flow system. ....	49
Figure 5.26: Particle elevation with time of fastest travelling particle. ....	50
Figure 5.27: 3D visualisation of particle tracks for steady-state temperate flow system.....	50
Figure 5.28: 3D visualisation of particle tracks at 61,400 years, flow system midway through the first glacial advance (cold based). ....	51
Figure 5.29: 3D visualisation of particle tracks at 66,800 years, flow system at the start of the second permafrost period.....	52
Figure 5.30: 3D visualisation of particle tracks at 100,500 years, flow system near the end of the second permafrost period. ....	53
Figure 5.31: 3D visualisation of particle tracks at 65,800 years, flow system midway through the first glacial retreat (cold based).....	54
Figure 5.32: 3D visualisation of particle tracks at 160,200 years, flow system midway through the proglacial lake period.....	54
Figure 5.33: Location of cross-sections for figures in Sections 5.3.1 and 5.3.2.....	55
Figure 5.34: GSC-RC DC1, Y-Z cross section showing <sup>129</sup> I plume after 103,500 years, the end of the second permafrost period. Arrows illustrate direction and magnitude of the advective velocity. ....	56
Figure 5.35: GSC-RC DC1, Y-Z cross section showing <sup>129</sup> I plume after 114,300 years, the end of the second glacial advance (cold-based). Arrows illustrate direction and magnitude of the advective velocity. ....	57
Figure 5.36: GSC-RC DC1, Y-Z cross section showing <sup>129</sup> I plume after 120,000 years, the end of the second glacial retreat (warm-based). Arrows illustrate direction and magnitude of the advective velocity. ....	58
Figure 5.37: GSC-RC DC1, Y-Z cross section showing <sup>129</sup> I plume after 124,300 years, 4000 years into the third permafrost period. Arrows illustrate direction and magnitude of the advective velocity. ....	59
Figure 5.38: GSC-RC (Reference Case) DC1 X-Y planar section of transport model results during the assessment period. Section elevation of 0.0 mASL (approx. 350 mBGS). ....	60
Figure 5.39: GSC-RC (Reference Case) DC1 Y-Z cross-section of transport model results at 6 times during the assessment period. Section easting of 8325 mE. ....	61
Figure 5.40: GSC-CC (constant climate) DC1 X-Y planar section of transport model results at 6 times during the assessment period. Section elevation of 0.0 mASL (approx. 350 mBGS) .	63
Figure 5.41: GSC-CC (constant climate) DC1 Y-Z cross-section of transport model results at 6 times during the assessment period. Section easting of 8325 mE. ....	64
Figure 5.42: GSC-HS (High Storage coefficient) DC1 X-Y planar section of transport model results at 6 times during the assessment period. Section elevation of 0.0 mASL (approximately 350 mBGS). ....	65
Figure 5.43: GSC-HS (High Storage coefficient) DC1 X Y-Z cross-section of transport model results at 6 times during the assessment period. Section easting of 8325 mE.....	66

Figure 5.44: GSC-NF (No-Flow North-South boundaries) DC1 X-Y planar section of transport model results at 6 times during the assessment period. Section elevation of 0.0 mASL (approximately 350 mBGS). .....67

Figure 5.45: GSC-NF (No-Flow North-South boundaries) DC1 Y-Z cross-section of transport model results at 6 times during the assessment period. Section easting of 8325 mE. ....68

Figure 5.46: GSC-TK (Talík under glacier) DC1 X-Y planar section of transport model results at 6 times during the assessment period. Section elevation of 0.0 mASL (approximately 350 mBGS). .....69

Figure 5.47: GSC-TK (Talík under glacier) DC1 Y-Z cross-section of transport model results at 6 times during the assessment period. Section easting of 8325 mE. ....70

Figure 5.48: All cases comparison of DC1 X-Y planar section through <sup>129</sup>I plume. Section elevation of 0.0 mASL (approximately 350 mBGS). .....71

Figure 5.49: GSC-RC (Reference Case) DC3 X-Y planar section of transport model results at 6 times during the assessment period. Section elevation of 0.0 mASL (approx. 350 mBGS). .74

Figure 5.50: GSC-RC (Reference Case) DC3 X-Z cross-section of transport model results at 6 times during the assessment period. Section northing of 4825 mN. ....75

Figure 5.51: GSC-CC (constant climate) DC3 X-Y planar section of transport model results at 6 times during the assessment period. Section elevation of 0.0 mASL (approx. 350 mBGS). .76

Figure 5.52: GSC-CC (constant climate) DC3 X-Z cross-section of transport model results at 6 times during the assessment period. Section northing of 4825 mE. ....77

Figure 5.53: GSC-HS (High Storage Coefficient) DC3 X-Y planar section of transport model results at 6 times during the assessment period. Section elevation of 0.0 mASL (approximately 350 mBGS). .....78

Figure 5.54: GSC-HS (High Storage Coefficient) DC3 X-Z cross-section of transport model results at 6 times during the assessment period. Section northing of 4825 mN. ....79

Figure 5.55: GSC-NF (No-Flow N-S boundaries) DC3 X-Y planar section of transport model results at 6 times during the assessment period. Section elevation of 0.0 mASL (approximately 350 mBGS). .....80

Figure 5.56: GSC-NF (No-Flow N-S boundaries) DC3 X-Z cross-section of transport model results at 6 times during the assessment period. Section northing of 4825 mN. ....81

Figure 5.57: GSC-TK (Talík under glacier) DC3 X-Y planar section of transport model results at 6 times during the assessment period. Section elevation of 0.0 mASL (approx. 350 mBGS). .....82

Figure 5.58: GSC-TK DC3 (Talík under glacier) X-Z cross-section of transport model results at 6 times during the assessment period. Section northing of 4825 mN. ....83

Figure 5.59: All cases comparison of DC3 X-Y planar section through <sup>129</sup>I plume. Section elevation of 0.0 mASL (approximately 350 mBGS). .....84

Figure 5.60: GSC transport mass flow calculation zones. ....86

Figure 5.61: GSC-CC results with no well. Displayed are mass flow rate and cumulative mass from DC1 and DC3. Lines in the legend that do not appear on the plot are below the minimum value on the Y-axis. ....87

Figure 5.62: GSC-RC <sup>129</sup>I mass flow rate and cumulative mass from DC1, compared to GSC-CC (without well). Mass flow only plotted for North Lake to improve legibility of plot. Mass flow data processed to remove small negative flows. Shaded regions show the second permafrost state in each glacial cycle. ....88

Figure 5.63: The <sup>129</sup>I concentration in water crossing the North Lake control plane, for the GSC-RC and GSC-CC modelling cases. ....89

Figure 5.64: GSC-RC DC1 <sup>129</sup>I mass flow rates for second glacial cycle. ....90

Figure 5.65: GSC-HS <sup>129</sup>I mass flow rate and cumulative mass from DC1, compared to GSC-CC (without well). Mass flow only plotted for North Lake to improve legibility of plot. Mass

flow data processed to remove small negative flows. Shaded regions show the second permafrost state in each glacial cycle. ....	91
Figure 5.66: GSC-NF mass flow rate and cumulative mass from DC1, compared to GSC-CC (without well). Mass flow only plotted for North Lake to improve legibility of plot. Mass flow data processed to remove small negative flows. Shaded regions show the second permafrost state in each glacial cycle. ....	92
Figure 5.67: GSC-TK mass flow rate and cumulative mass from DC1, compared to GSC-CC (no well). Mass flow only plotted for North Lake to improve legibility of plot. Mass flow data processed to remove small negative flows. Shaded regions show the second permafrost state in each glacial cycle. ....	93
Figure 5.68: GSC-RC mass flow rate and cumulative mass from DC3, compared to GSC-CC (no well). Mass flow only plotted for Western region to improve legibility of plot. Mass flow data processed to remove small negative flows. Shaded regions show the second permafrost state in each glacial cycle. ....	94
Figure 5.69: GSC-RC DC3 <sup>129</sup> I mass flow rates for second glacial cycle. ....	95
Figure 5.70: GSC-HS <sup>129</sup> I mass flow rate and cumulative mass from DC3, compared to GSC-CC (no well). Mass flow only plotted for Western region to improve legibility of plot. Mass flow data processed to remove small negative flows. Shaded regions show the second permafrost state in each glacial cycle. ....	96
Figure 5.71: GSC-NF <sup>129</sup> I mass flow rate and cumulative mass from DC3, compared to GSC-CC (no well). Mass flow only plotted for Western region to improve legibility of plot. Mass flow data processed to remove small negative flows. Shaded regions show the second permafrost state in each glacial cycle. ....	97
Figure 5.72: GSC-TK <sup>129</sup> I mass flow rate and cumulative mass from DC3, compared to GSC-CC (no well). Mass flow only plotted for Western region to improve legibility of plot. Mass flow data processed to remove small negative flows. ....	98
Figure 5.73: <sup>129</sup> I concentrations in water-supply well for all DC1 calculation cases. ....	99
Figure 5.74: Figure of Merit during at (a) temperate climate, (b) the start of the second permafrost period (following glaciation), and (c) the end of the same period, when glacially induced overpressures have dissipated. Section easting is 8325 mE. ....	100
Figure 5.75: Figure of Merit during at (a) temperate climate, (b) the start of the second permafrost period (following glaciation), and (c) the end of the same period, when glacially induced overpressures have dissipated. Section easting is 5425 mE. ....	101
Figure 6.1: Normalized meltwater concentrations at 153,000 years, the end of the third glacial advance. ....	104
Figure 6.2: Reference case normalized meltwater concentration in the vicinity of the repository at 153,000 years, the end of the third glacial cycle. The location of the two cross-sections is shown in the plan section. ....	105
Figure 6.3: GSC-TK normalized meltwater concentration in the vicinity of the repository at 136,900 years, the end of the cold based advance during the third glacial cycle. The location of the two cross-sections is shown in the plan section. ....	107
Figure 6.4: GSC-TK normalized meltwater concentration in the vicinity of the repository at 153,000 years, the end of the warm based advance during the third glacial cycle. The location of the two cross-sections is shown in the plan section. ....	108
Figure 6.5: Normalized meltwater concentrations at 136,900 years, the end of the cold-based ice advance during the third glacial cycle. ....	109
Figure 6.6: GSC-HS normalized meltwater concentration in the vicinity of the repository at 153,000 years, the end of the warm based advance during the third glacial cycle. The location of the two cross-sections is shown in the plan section. ....	110
Figure 6.7: Mass flow rate across North Lake control surface for the Rapid Drainage DC1 cases, compared to GCS-RC DC1 result. ....	111

Figure 6.8: Mass flow rate across Western control surface for the Rapid Drainage DC3 cases, compared to GCS-RC DC3 result..... 112

Figure 7.1: Total cumulative mass for all sensitivity cases. <sup>129</sup>I mass is summed over all transport mass flow calculation zones. .... 115

## 1. INTRODUCTION

Previous Canadian safety assessments have focussed on radionuclide transport from a deep geologic repository under steady climate and groundwater conditions (Gierszewski et al. 2004a; Garisto et al. 2005). Over the 0.8 Ma assessment period used in this study, it is expected that the repository will be subjected to the influences of multiple glacial cycles. The effect of glacial cycles on groundwater flow and transport may be important in assessing overall facility performance. The primary purpose of the current study is to address an illustrative glaciation scenario using a three-dimensional (3-D) numerical model based on a hypothetical repository in the Canadian Shield. The results of this study are part of a larger assessment of the effects of glacial cycles on contaminant transport described in Garisto et al. (2010).

This study investigates the evolution of the groundwater flow domain over a single glacial cycle, the impact of a talik feature on groundwater flow, and the effect of multiple glacial cycles on the transport of radionuclides from a hypothetical defective container.

Additionally, numeric studies were undertaken to assess the depth of glacial meltwater penetration, using the conservative assumption of constant density fluid.

The methodology focuses on detailed 3-D groundwater flow modelling and 3-D transport modelling for a single radionuclide ( $^{129}\text{I}$ ). The study is limited to one hypothetical repository site, but looks at transport from failed canisters at two separate locations within the repository footprint. The possible impacts of ice sheet loading were included in the model through use of a 1D hydromechanical coupling algorithm.

The assumed site is the hypothetical site considered in the Third Case Study (TCS) (Gierszewski et al. 2004a,b), and the repository design is based on the horizontal borehole emplacement concept (HBC) (Garisto et al. 2005). In this report, these previous studies are referred to as the TCS and HBC studies. The current study is denoted as the Glaciation SCenario study model (GSC)

The report is organized as follows:

- **Glaciation Scenario**– This section describes the simplified reference glaciation scenario selected for modelling and the approach used to generate the glacial profile that was used for generating model boundary conditions.
- **Model Characteristics** – This section includes a description of the general approach, the modelling domain, the boundary conditions and the geosphere properties used for each component of the sequence. There is also a description of the defective container source term.
- **Modelling Cases** – A description of the modelling sensitivity cases used to assess the effect of changes to parameter and boundary conditions is included in this section.
- **Glacial Sequence Modelling Results** – This section includes a comparison of steady-state results to previous HBC transport models, a discussion of flow model results for a single glacial cycle, and a discussion of transport model results over the multiple glacial cycles in the 0.8 Ma simulation period.

- **Additional Numeric Studies** – This section describes analyses undertaken to assess the depth of glacial meltwater penetration and the effect of rapid drainage of the proglacial lake on radionuclide mass flow to the surface.

## 2. GLACIATION SCENARIO

Peltier (2003, 2006) has modelled the effects of North American continent wide long-term climate change on ice-sheet advance and retreat. From the many simulations documented in Peltier (2006), a single reference simulation, denoted nn2778, has been selected as a representative glacial cycle (Garisto et al. 2010). Time-varying results from the nn2778 simulation were extracted at the hypothetical TCS site location to provide the basis for the simplified glacial cycle used in this report. This simulation includes various features of interest, including multiple ice sheet advances and retreats within a single cycle, as well as periods of both warm-based and cold-based ice sheets at the study location, and extensive periods of permafrost.

### 2.1 General Glacial Cycle

Simulation nn2778 describes a glacial cycle of 121 ka duration characterized by temperate (present day climate), permafrost, ice-sheet cover, and proglacial lake periods. The reference scenario includes an initial temperate period of 50,300 years, to account for the smaller expected amplitude of solar insolation variations, and the probability that anthropogenic climate warming might delay the onset of glaciation (Garisto et al. 2010). The glacial cycles are subsequently repeated indefinitely for the duration of the calculations. (Subsequent temperate interglacial periods are 10,800 years.) The simplified reference glacial cycle described in Garisto et al. (2010) is detailed in the table below.

**Table 2.1: Time history for reference glacial cycle (Garisto et al. 2010)**

Stage <sup>#</sup>	Relative Time Period (years) <sup>1</sup>	Actual Times During First Cycle (years)	Duration of State (years)	Description of Glaciation State
1	-----	0 – 50,300		Temperate (current Interglacial)
2	0 – 7,800	50,300 – 58,100	7,800	Permafrost
3	7,800 – 14,500	58,100 – 64,800	6,700	Ice Sheet Advance, permafrost underneath
4	14,500 – 16,400	64,800 – 66,700	1,900	Ice Sheet Retreat, permafrost underneath
5	16,400 – 53,200	66,700 – 103,500	36,800	Permafrost
6	53,200 – 64,000	103,500 – 114,300	10,800	Ice Sheet Advance, permafrost underneath
7	64,000 – 70,000	114,300 – 120,300	6000	Ice Sheet Retreat, no permafrost underneath
8	70,000 – 79,200	120,300 – 129,500	9,200	Permafrost
9	79,200 – 86,600	129,500 – 136,900	7,400	Ice Sheet Advance, permafrost underneath
10	86,600 – 102,700	136,900 – 153,000	16,100	Ice Sheet Advance, no permafrost underneath
11	102,700 – 109,200	153,000 - 159,500	6,500	Ice Sheet Retreat, no permafrost underneath
12	109,200 – 110,400	159,500 – 160,700	1,200	Proglacial Lake
13	110,400 – 121,200	160,700 – 171,500	10,800	Temperate

<sup>1</sup>In the Glaciation Scenario the current interglacial period is assumed to extend 50,000 years into the future and immediately precedes the start of the first glacial cycle at 50,300 years. The glacial cycle repeats itself starting at: 171,500; 292,700; 413,900; etc. years.

<sup>#</sup>Stage number used to identify particular state in following sections.

For the purposes of this model, a simplified version of the nn2778 simulation from Peltier (2006) was required. Figure 2.1 shows the ice height and permafrost depth at the study site location for the reference glacial cycle nn2778 and the simplified glacial cycle used for the current flow and transport model. The simplified model neglects the short periods of ice cover that occur before the second and third major glaciation events. The model also neglects the short term variation of permafrost depth. This was done to simplify the model development process. The permafrost has very low hydraulic conductivity compared to the remainder of the shallower rock formations, so the practical significance of having a permafrost depth of 100 m instead of 150 m is small for vertical flow, as any amount of permafrost still provides a very effective hydraulic barrier. Finally, during the Proglacial Lake phase, which lasts for 1200 years, the head at the surface is maintained constant at 540 m of water for the first 800 years (equivalent to an average lake depth of 168 m), and then reduced gradually over the remaining 400 years until it equals the topographic elevation.

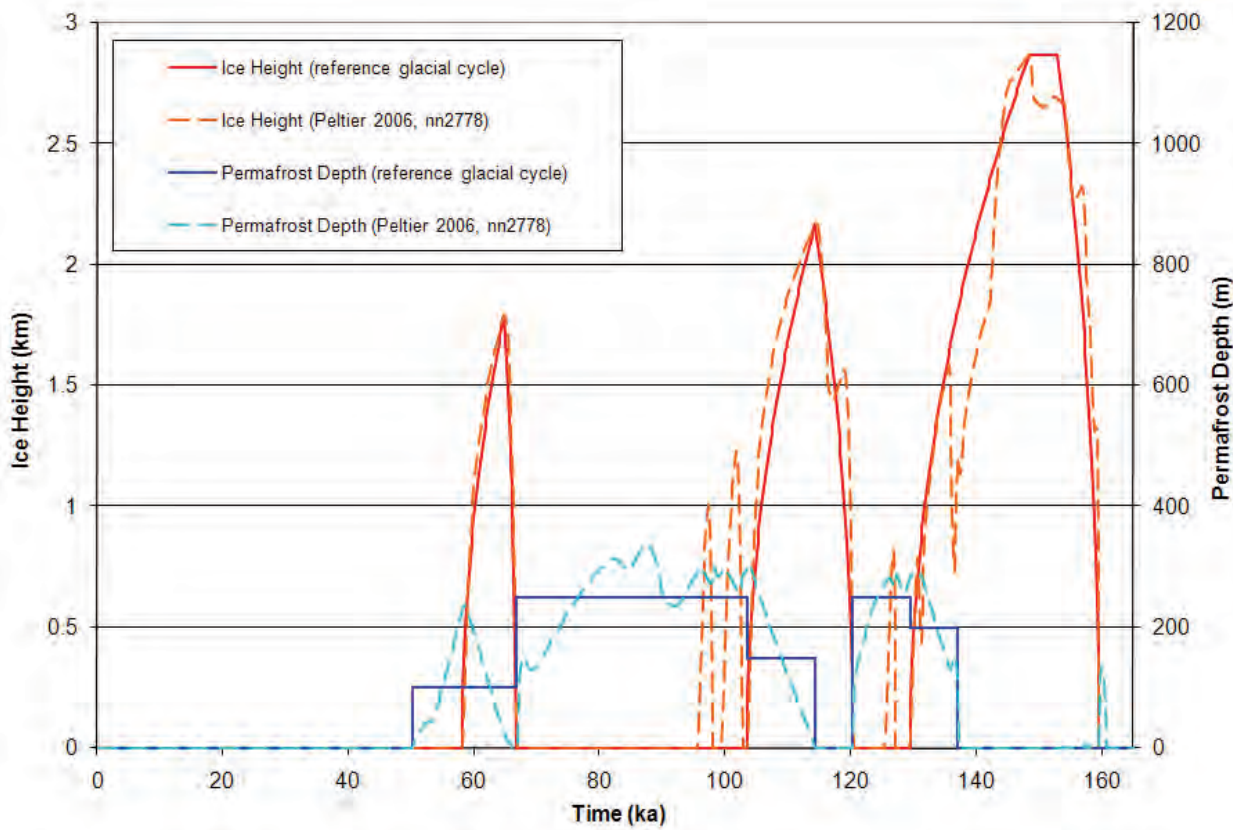


**Figure 2.1: Data from the reference simulation nn2778 and the simplified reference glacial cycle used in this work.**

## 2.2 Ice Profile

A major interest in this modelling project is the transient behaviour of the flow system occurring as a result of ice-sheet movement across the model domain during ice-sheet advance and retreat periods. Ice sheet thickness data can be extracted from the stress data presented in the nn2778 simulation but this would require constantly changing surface boundary conditions over the entire duration of ice-sheet periods. Furthermore, the nn2778 simulation had insufficient spatial resolution to determine

variation over the model domain. A simplified model has been selected where the transient ice-sheet profile was specified by an analytical model.

The equation for the glacial surface profile as a function of the strength and density of the ice was developed by Oerlemans (2005):

$$h(x) = \sqrt{\frac{2\tau_0}{\rho g(1 + \delta)}} x \quad (2.1)$$

where:

- $h(x)$  glacial ice thickness profile, as a function of distance from terminus (m)
- $x$  distance from glacial terminus (m)
- $\tau_0$  yield stress (Pa)
- $\rho$  ice density ( $\text{kg m}^{-3}$ )
- $\delta$  isostatic depression parameter

Oerlemans (2005) suggests values of 50 kPa to 300 kPa for yield stress and 0.33 for the isostatic depression parameter. A value of 50 kPa was specified for yield stress and ice density was assumed to be  $900 \text{ kg m}^{-3}$ . Application of these values to Equation 2.1 results in the profile shown in Figure 2.2.

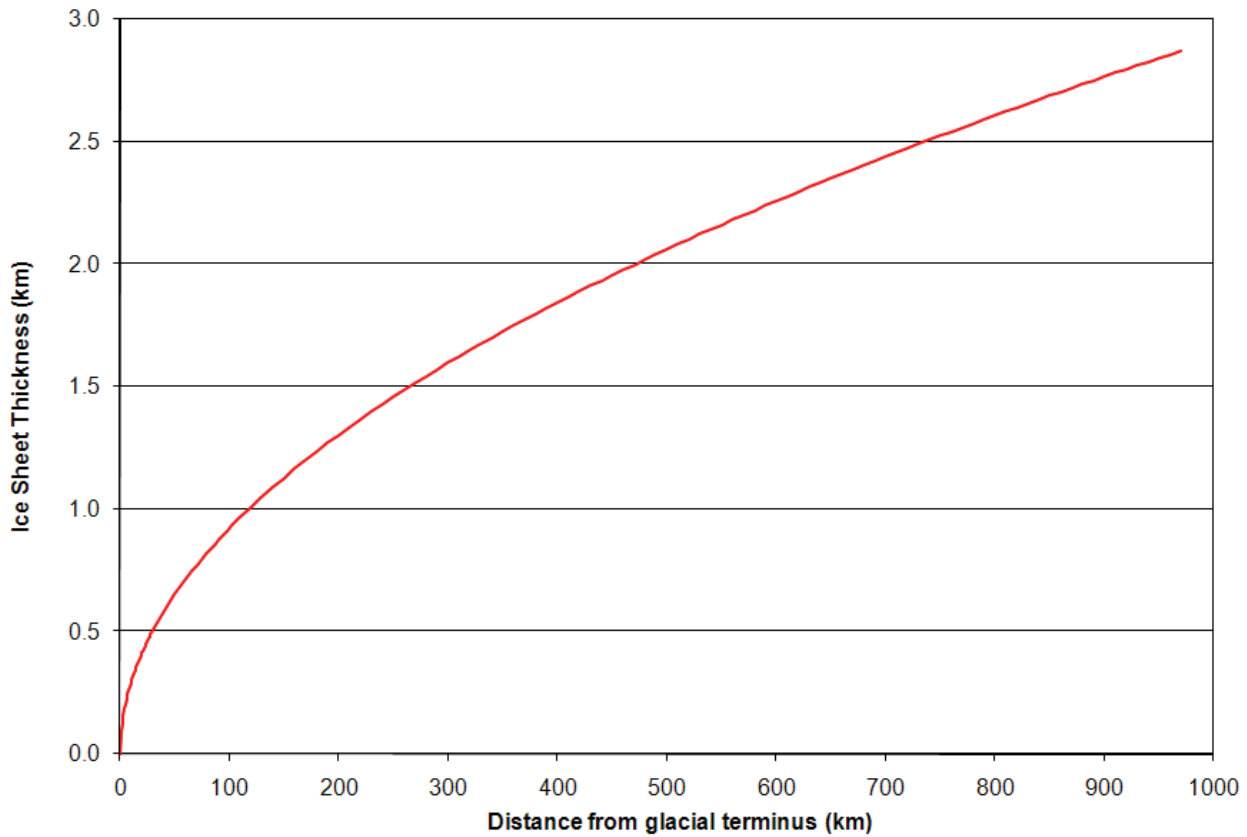


Figure 2.2: Ice surface profile.

In order to fit the ice thickness values from Peltier (2006) as closely as possible (see Figure 2.1), the ice advance/retreat rates were used as fitting parameters. The calculated advance and retreat rates are shown in Table 2.2. It should be noted that the advance/retreat rates do not necessarily represent the velocity of the ice sheet but rather the rate of movement of the ice front which could, for example, be due to snow accumulation, ice melting, and ice sheet movement.

Once the time-dependent ice-sheet profile had been generated, the ice-sheet thickness was converted to an assumed equivalent freshwater hydraulic head by multiplying ice-sheet thickness by ice-sheet density (assumed to be  $900 \text{ kg/m}^3$ ), and ignoring deformation of the crust beneath the ice load. Thus for this study, the water pressure below the glacier is assumed to be close to the pressure required to float the glacier. This is undoubtedly a simplified representation of subglacial hydrology, but it is not unreasonable. Numerous references from the field of glaciology confirm that subglacial hydraulic head can reach a significant fraction of the ice pressure. According to Clark (2005), water pressure beneath fast flowing glaciers in the western Antarctic can be very close to the flotation pressure. Piterowski and Kraus (1997) used the stress characteristics of compacted fine grained sediments as a proxy measure to estimate that the subglacial water pressure was approximately 72% of the ice thickness during the last glaciation in northwestern Germany. Hooke et al. (1990) demonstrated water pressure between 50 and 75% of the ice overburden pressure. Seasonal variation in subglacial heads has also been measured. In an Icelandic glacier, Boulton et al. (2007a) measured water pressures very close to the ice overburden stress in summer, followed by a much lower potential surface in winter.

Modellers have also found indirect evidence for high subglacial water pressures. To represent subglacial water flows, Moeller et al. (2007) used a recharge boundary condition based on meltwater production rates due to friction and surface melting. The model predicted very high porewater pressures, often exceeding the flotation pressure of the glacier. Boulton et al. (1995) used the ice overburden pressure as the limiting subglacial pressure in his model, and again found that this limiting pressure was often achieved when calculated surface and basal meltwater rates were applied.

**Table 2.2: Advance and retreat rates in simplified glacial cycle. Values for subsequent cycles are identical.**

<b>Time Period (years)</b>	<b>Glaciation Period or Stage</b>	<b>Advance/Retreat rate (m/a)</b>
58,100 – 64,800	Ice sheet advance	56.2
64,800 – 66,700	Ice sheet retreat	-198.2
103,500 – 114,300	Ice sheet advance	51.1
114,300 – 120,300	Ice sheet retreat	-91.9
129,500 – 148,400	Ice sheet advance	51.1
148,400 – 153,000	Ice sheet stationary	0.0
153,000 – 159,500	Ice sheet retreat	-148.5

### 3. MODEL CHARACTERISTICS

#### 3.1 General Approach

The Glaciation Scenario (GSC) groundwater flow model is a continuation of the Horizontal Borehole Concept (HBC) model presented in Garisto et al. (2005). The objective of the current modelling exercise was the assessment of sub-regional scale glacial cycle impacts. This requires the use of a transient flow model over the entire model domain to capture the changes induced by glacial cycling.

In steady-state systems, fixed heads at vertical boundary nodes of the embedded transport model can be easily specified, however, for transient flow models the variable boundary conditions must be specified at each vertical boundary node of the model over the duration of the simulation. The model uses a horizontal grid resolution of 50 m in the vicinity of the repository, which increases to 100 m at the model boundary. This relatively coarse resolution precluded direct incorporation of repository features and required use of relatively large dispersivity values (longitudinal dispersivity of 80 m, transverse dispersivity of 8 m). However, as the primary purpose of the current modelling is to examine flow system wide transport, these are acceptable compromises. The greater dispersivity is an assumption that it is likely to enhance the rate of solute transport, although peak mass flux rates may be reduced.

The GSC model includes the following features:

- A model domain of 13 km East to West, and 20 km North to South (see Figure 3.1). The repository is located in the general center of this domain. Trial studies indicated that these dimensions reduced the effect of boundary conditions on flow and transport near the repository.
- The activation of two open taliks within the model domain during permafrost periods (see Figure 3.1). These two lakes are sufficiently large and deep to support open taliks during permafrost periods. The southern talik was included to explore whether head differences between two taliks in an otherwise closed system could promote flow and transport of radionuclides into either of the taliks.
- Depth-dependent rock mass and fracture zone permeability.
- Incorporation of simplified 1D hydromechanical coupling in the model.

FRAC3DVS-OPG Version 1.1 (64 bit) (Therrien et al. 2007) was used for the groundwater flow and transport calculations. This model includes the ability to represent discrete fractures, as well as variable-density fluids. However, it was not practical to include these features of the model for the scale in space and time of the transient transport model. Rather, fractures were represented as equivalent-porous-medium, and a constant freshwater head was used. The latter is likely a conservative approximation, in that incorporating salinity would tend to dampen deep groundwater flow (Normani 2009).

The FRAC3DVS hydromechanical (HM) coupling module, is based on the work of Neuzil (2003), and assumes purely vertical strain. This allows a great simplification of the hydromechanical analysis, allowing transient flow due to hydromechanical coupling to be fully represented by the fluid flow equation alone. The effect on the flow field of a pressure increase caused by mechanical loading is incorporated in an additional storage term in the hydraulic mass balance equation, as follows:

$$\frac{\partial}{\partial x_i} \left( K_{ij} \frac{\partial h}{\partial x_j} \right) = S_{s1} \frac{\partial h}{\partial t} - \zeta S_{s1} \frac{1}{\rho g} \frac{\partial \sigma_{zz}}{\partial t} \pm Q \quad i, j = 1,2,3 \quad (3.1)$$

where

- h = hydraulic head (m),
- $K_{ij}$  = hydraulic conductivity tensor (m/s),
- $S_{s1}$  = one-dimensional specific storage coefficient (1/m),
- $\zeta$  = one-dimensional loading efficiency (-),
- $\rho$  = fluid density ( $\text{kg/m}^3$ ),
- g = gravitational acceleration ( $\text{m/s}^2$ ),
- $\sigma_{zz}$  = vertical total stress (Pa), and
- Q = water sources or sinks (1/s).

For the transient flow model, the storage coefficient defines the speed of the time dependent response of the flow system. The one-dimensional specific storage coefficient was calculated using the following expression (Neuzil 2003):

$$S_{s1} = \rho g \left[ \left( \frac{1}{K} - \frac{1}{K_s} \right) \left( 1 - 2\alpha \frac{1-2\nu}{3(1-\nu)} \right) + n \left( \frac{1}{K_f} - \frac{1}{K_s} \right) \right] \quad (3.2)$$

where

- K = porous medium bulk modulus (Pa),
- $K_s$  = solid minerals bulk modulus (Pa),
- $\alpha$  = Biot-Willis coefficient (-),
- $\nu$  = Poisson's ratio (-),
- n = porosity (-), and
- $K_f$  = fluid bulk modulus (Pa).

The bulk modulus (K) was calculated using the expression:

$$K = \frac{E}{3(1-2\nu)} \quad (3.3)$$

where E is Young's modulus (Pa).

The one-dimensional loading efficiency,  $\zeta$ , is analogous to Skempton's coefficient (B), but is valid for the assumption of uni-axial strain (Neuzil 2003). The one dimensional loading efficiency is given by Neuzil (2003) as:

$$\zeta = \frac{B(1+\nu)}{3(1-\nu) - 2\alpha B(1-2\nu)} \quad (3.4)$$

The term in Equation 3.1 containing  $\zeta$  and  $\sigma_{zz}$  defines the hydromechanical coupling component of the equation, releasing water from storage as the load increases (pore compression), and abstracting water into storage as the load is decreased.

Using this simplified expression requires the assumption that horizontal gradients in fluid pressure and stress are small compared to vertical gradients. This assumption is reasonable for a relatively homogeneous and extensive vertical load, such as would occur underneath a glacier (Neuzil 2003). This assumption is not valid where vertical loads vary significantly within the model domain, as would occur during the early stages of a glacial advance when the ice margin is within the model domain. The short interval during which the ice margin crosses the domain (350-400 years during glacial advances, shorter during retreats) means that the one dimensional HM model is reasonably accurate for the majority of the simulation time. Therefore the one dimensional hydromechanical model

provides an acceptable estimate of how transient glacial loading might impact the flow field and the resulting transport solution.

Changes in geosphere permeability caused by the increased load are similarly unaccounted for in the model. Leaving the permeability unchanged under increased ice load is a conservative assumption, as the increased load beneath a continental glacier would reduce the permeability through compression of pores and closure of fractures.

If it is assumed that current temperate climate remains unchanged for the next million years, boundary conditions and geosphere properties would remain constant for the duration of the simulation and it would be possible to model transport for the entire assessment period with a single model execution. However, the glaciation scenario model requires that geosphere properties consistent with permafrost be applied during seven of the 12 climate stages described in Table 2.1. FRAC3DVS-OPG does not support time varying material properties in a subsection of a model layer (i.e., a talik in permafrost). Furthermore, time varying surface boundary conditions can be more accurately modelled for shorter time periods. Consequently, the model simulated each sequence separately, with sequences coupled by restart files. Nodal heads and concentrations at the end of one time period served as initial conditions for the start of the subsequent time period. A total of 72 separate simulations (12 time periods for 6 glacial cycles) were combined to form the composite response for the 0.8 Ma assessment period. Initial head conditions at the start of the first cycle were extracted from a steady-state flow model based on temperate period surface boundary conditions and geosphere properties.

### **3.2 Model Domain**

Figure 3.1 illustrates the model extent, surface topography, surface water features, fracture zones at the repository depth (-300 mASL (metres above sea level), or approximately 670 mBGS (metres below ground surface)), and the location of the hypothetical repository emplacement drifts. The model used a horizontal grid resolution of 50 m in the vicinity of the repository, which increased to 100 m at the model boundary (see Figure 3.2). For vertical discretization, the maximum element thickness was 50 m, but near the surface thinner elements were used. At the elevation of the repository the elements had dimensions of 50 x 50 x 50 m.

The lake above the eastern edge of the repository was identified in previous studies as a discharge zone and was the terminus of the shortest flow pathline from the repository under constant climate conditions. For the current study, the lake has been designated a talik, which means that the ground underneath it remains unfrozen during permafrost conditions. This is a deliberately conservative choice since, as will be seen later, the talik serves as an important outlet for groundwater flows and therefore potential contaminant flows during the glacial cycle.

Another larger lake, roughly five kilometres south of the repository, has also been designated a talik, to examine whether multiple zones of discontinuous permafrost with different hydraulic potential could cause significant flows during permafrost periods. For the majority of modelling scenarios the taliks are assumed to exist only during permafrost periods, and to freeze over when covered by ice. One calculation case examines the effect of open taliks in sub-ice-sheet permafrost.

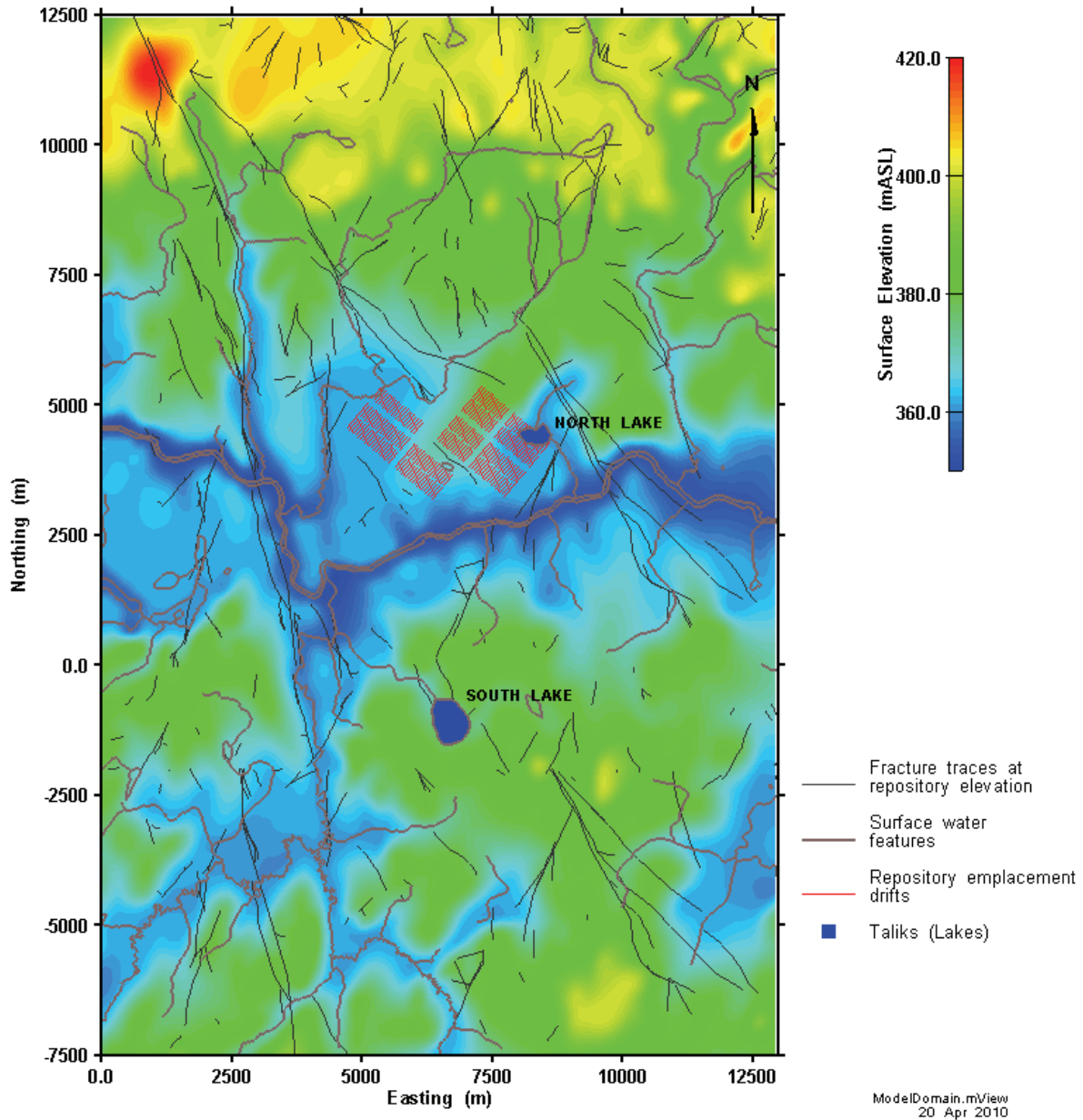


Figure 3.1: Flow and transport model domain.

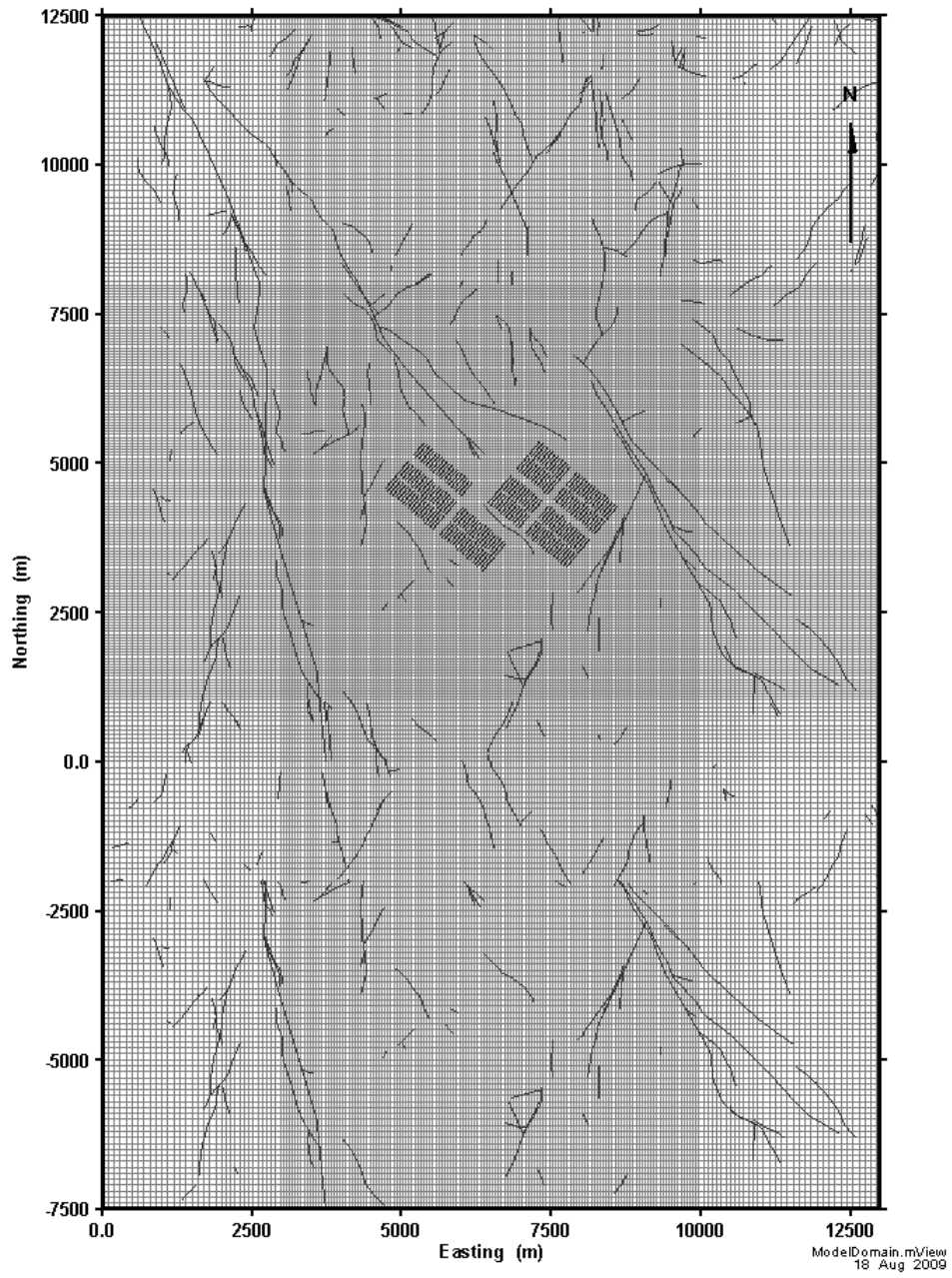
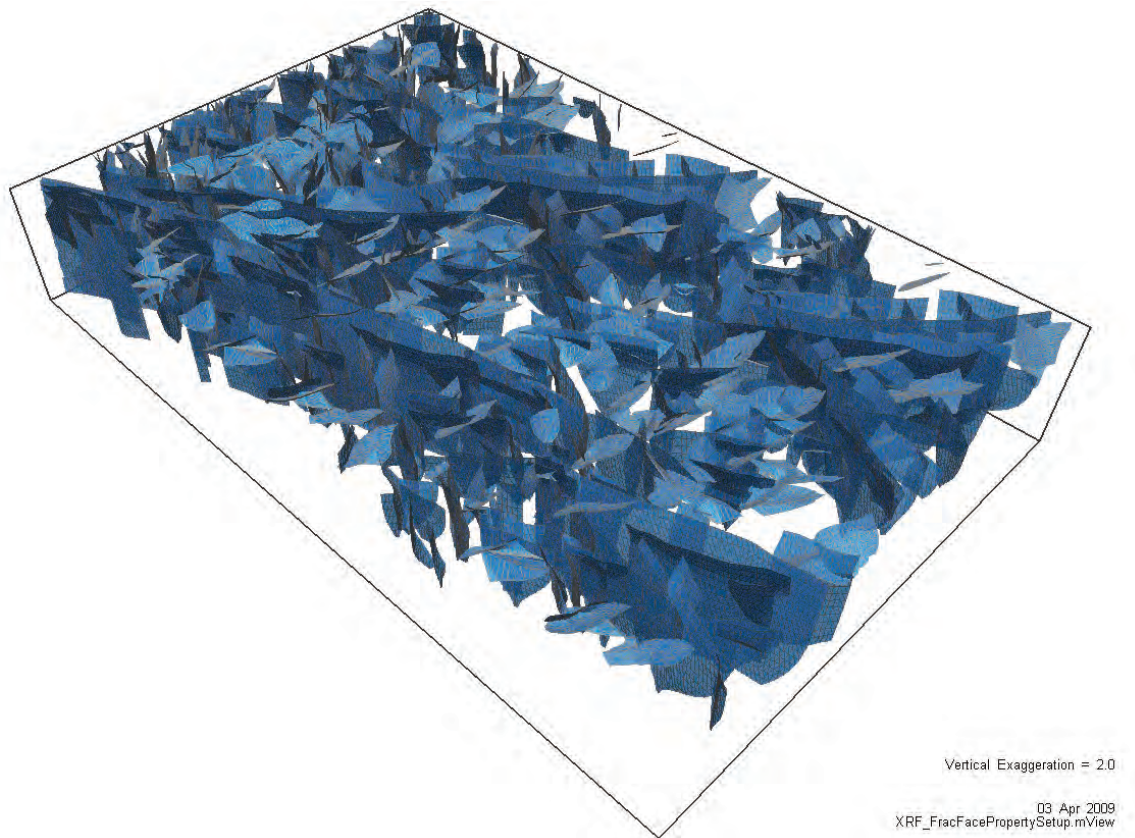


Figure 3.2: Flow and transport model horizontal discretization.

### 3.3 Fracture Network

As in earlier modelling work on the Third Case Study site, the discrete fracture set from Srivastava (2002) was used. This data set did not extend to the area south of approximately Northing 2000 m. To incorporate fractures in the southernmost 5000 m of the domain, the fracture distribution was partially duplicated, extending the fracture system all the way to the model boundary. This provided a representative fracture system for this portion of the model domain that is statistically consistent with the rest of the fracture system. The three dimensional fracture network used as a basis for the GSC model is shown in Figure 3.3.



**Figure 3.3: Fracture network realization for the GSC model.**

### 3.4 Material Properties

#### 3.4.1 Layered Properties

As in the Third Case Study model, rock matrix properties are assumed to vary only vertically. The variation in material properties is represented as a series of horizontal layers with homogeneous and isotropic material properties within the layer. These layers span the entire model domain. The rock mass hydraulic conductivity values are the same as used in the TCS and HBC studies (the Case 2 permeability values described in Gierszewski et al. 2004b), with the conversion from permeability to hydraulic conductivity calculated by assuming that the fluid is fresh water.

Porosity of rock mass was set to 0.003 throughout the model domain, to be consistent with Gierszewski et al. (2004b).

Values for Young's modulus were chosen to be consistent with Chan and Stanchell (2008): E = 20 GPa between 0.0 and 150.0 mBGS (property groups K10, K70, K150); E = 30 GPa between 150 mBGS and 75 mASL (property group K300); and E = 60 GPa between 75 and -1225 mASL (property groups K500, K700, K1500). The solid minerals bulk modulus ( $K_s$ ) was set to 45 GPa for all layers, a typical value for granite (Wang 2000). The Biot-Willis coefficient ( $\alpha$ ) was set to 0.73 and Poisson's ratio was set to 0.25, for all layers. These are the same values used by Chan and Stanchell (2008). The fluid bulk modulus was set to 2.3 GPa (Wang 2000).

Hydraulic conductivities, storage coefficients, and Young's modulus for the model layers are shown in Table 3.1. These are the only parameters that vary between layers. Young's modulus is not a model input, but is used to calculate bulk modulus and specific storage, as described in Section 3.1.

**Table 3.1: Material properties that vary between flow model layers.**

Property Identifier	Depth Range <sup>1</sup>	Hydraulic Conductivity (m/s)	Storage Coefficient (m <sup>-1</sup> )	Young's Modulus (GPa)
K10	Ground Surface to 10 mBGS	7.00E-07	3.63E-07	20.0
K70	10 to 70 mBGS	7.00E-08	3.63E-07	20.0
K150	70 to 150 mBGS	8.00E-10	3.63E-07	20.0
K300	150 mBGS to 75 mASL	7.00E-11	1.97E-07	30.0
K500	75 to -125 mASL	3.00E-11	3.18E-08	60.0
K700	-125 to -325 mASL	7.00E-12	3.18E-08	60.0
K1500	-325 to -1225 mASL	1.00E-12	3.18E-08	60.0

<sup>1</sup>mBGS = meters below ground surface; mASL = metres above sea level. Near surface layers follow topography. Ground surface is at approximately 350 mASL.

Finally, to maintain consistency with the work of Chan and Stanchell (2008), the one-dimensional loading efficiency,  $\zeta$ , was set equal to a value of one third. Using a value of 0.5 for Skempton's B coefficient gave a loading efficiency of 0.33 for the entire model domain. Skempton's coefficient is the ratio of the induced pore pressure to the change in applied stress under undrained conditions. A value of 0.5 is a reasonable estimate for intact granite (Wang 2000).

### 3.4.2 Fracture Properties

The layered permeability has been modified to account for the existence of fracture zones in the model domain. Earlier work used a constant value for fracture permeability, but the current model uses a depth dependent fracture zone permeability. The fracture zone permeability function was defined according to the work done by Normani et al. (2007). Permeability values were based on the 50<sup>th</sup> percentile best fit cubic spline for fracture permeability with depth (Normani et al. 2007).

Fracture information was incorporated into the model through the equivalent porous medium (EPM) approach. Three-dimensional model elements intersected by fractures were assigned a permeability based on the log-average of the fracture and intact rock permeability, weighted by the respective thicknesses of the fracture zone and intact rock in the element. An arithmetic mean was used in the direction parallel to the fracture face, and a harmonic mean was used in the direction perpendicular to the fracture face. As a result, the equivalent porous medium hydraulic conductivity of elements containing fractures is variable and anisotropic. The choice of an EPM model, rather than a discrete fracture network (DFN) model, allowed the use of particle tracking as a tool for visualisation of the flow field. Earlier work confirmed that the EPM and DFN models produced comparable flow and transport results (Garisto et al. 2005).

Figure 3.4 shows the depth dependent hydraulic conductivity profiles of the intact rock, the discrete fractures (from Normani et al. 2007), and the average EPM vertical hydraulic conductivity of elements intersected by fracture zones, within the model layers. As indicated by the figure, the presence of a fracture zone intersecting a model element leads on average to an approximately one order of magnitude increase in vertical hydraulic conductivity. Figure 3.5 shows the spatial distribution of hydraulic conductivity within the model domain. Elements representing fracture zones are clearly visible and distinct from the surrounding intact rock.

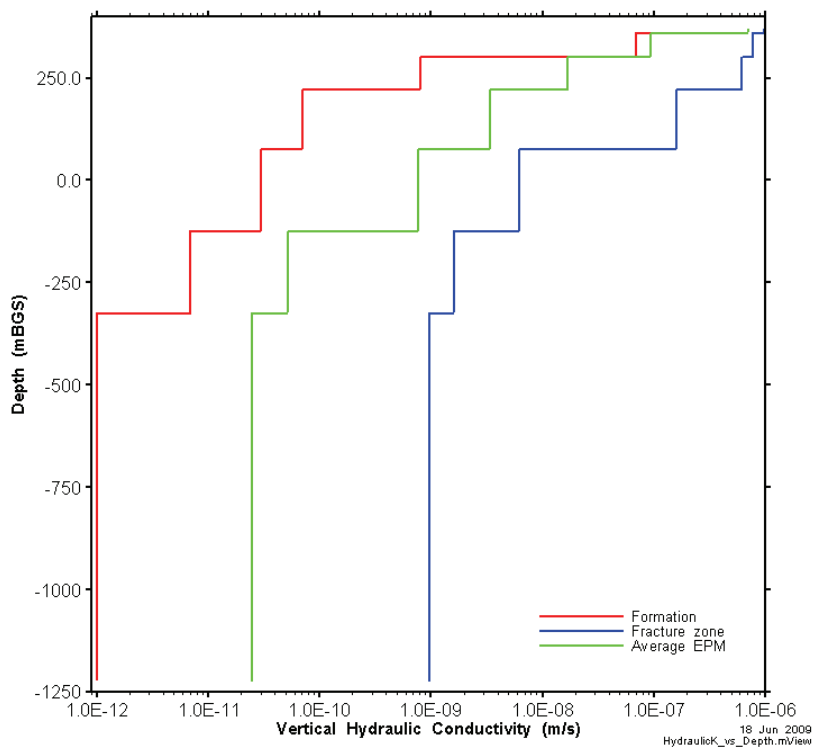
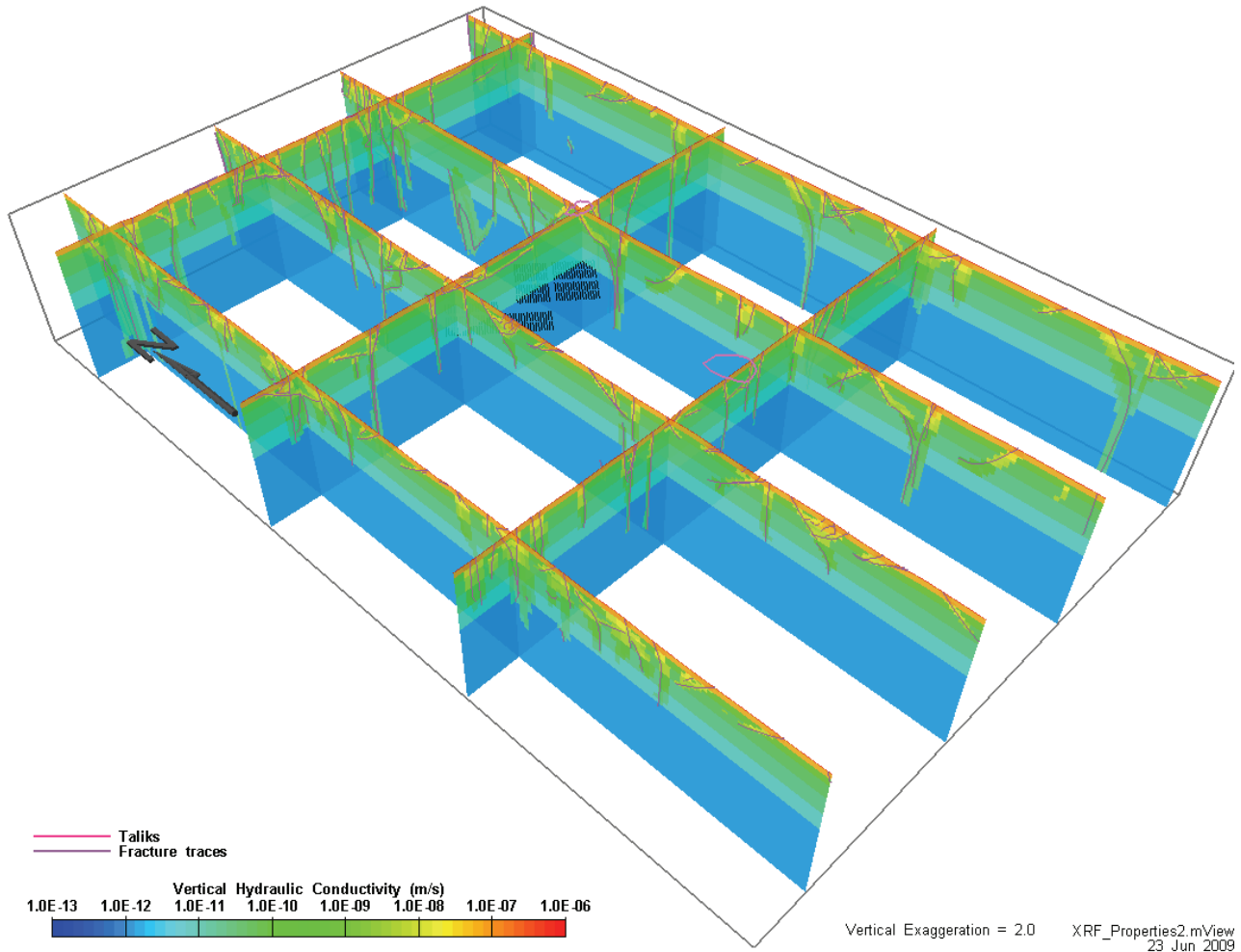


Figure 3.4: Vertical hydraulic conductivity profiles.



**Figure 3.5: Geosphere hydraulic conductivity distribution during temperate periods. Fences are partially transparent. Darker zones at the intersections of fences should not be misinterpreted as zones of lower hydraulic conductivity.**

### 3.4.3 Permafrost Implementation

Permafrost is modelled by modifying the hydraulic conductivity of all materials (except taliks) above a given elevation to  $10^{-13}$  m/s. All other important flow and transport parameters, including porosity and molecular diffusion coefficient, were conservatively assumed to remain unchanged in the permafrost zone. The depth of the permafrost was varied between 100 and 250 m, depending on the permafrost period (see Figure 2.1). Model cells underlying the talik retained their original permeability. During glacial advance and retreat, when permafrost was present, it was assumed that the taliks freeze over. In one calculation case the talik remained open beneath the glacial ice (see Section 4). Figure 3.6 shows the assigned hydraulic conductivities during a permafrost period with 250 m deep permafrost, and two open taliks.

The implementation approach, described in preceding sections, couples flow regimes by nodal head at each sequence transition. As a consequence, the transition between permafrost and non-permafrost states is instantaneous. This is not realistic, as permafrost will develop from surface down over a period of time, and will initially be discontinuous. However, the instant application of permafrost

is a simplifying assumption that will not substantially alter the resulting flow domain over longer time periods. In general, the transition from unfrozen to frozen conditions occurs over a relatively short time period in the nn2778 simulation.

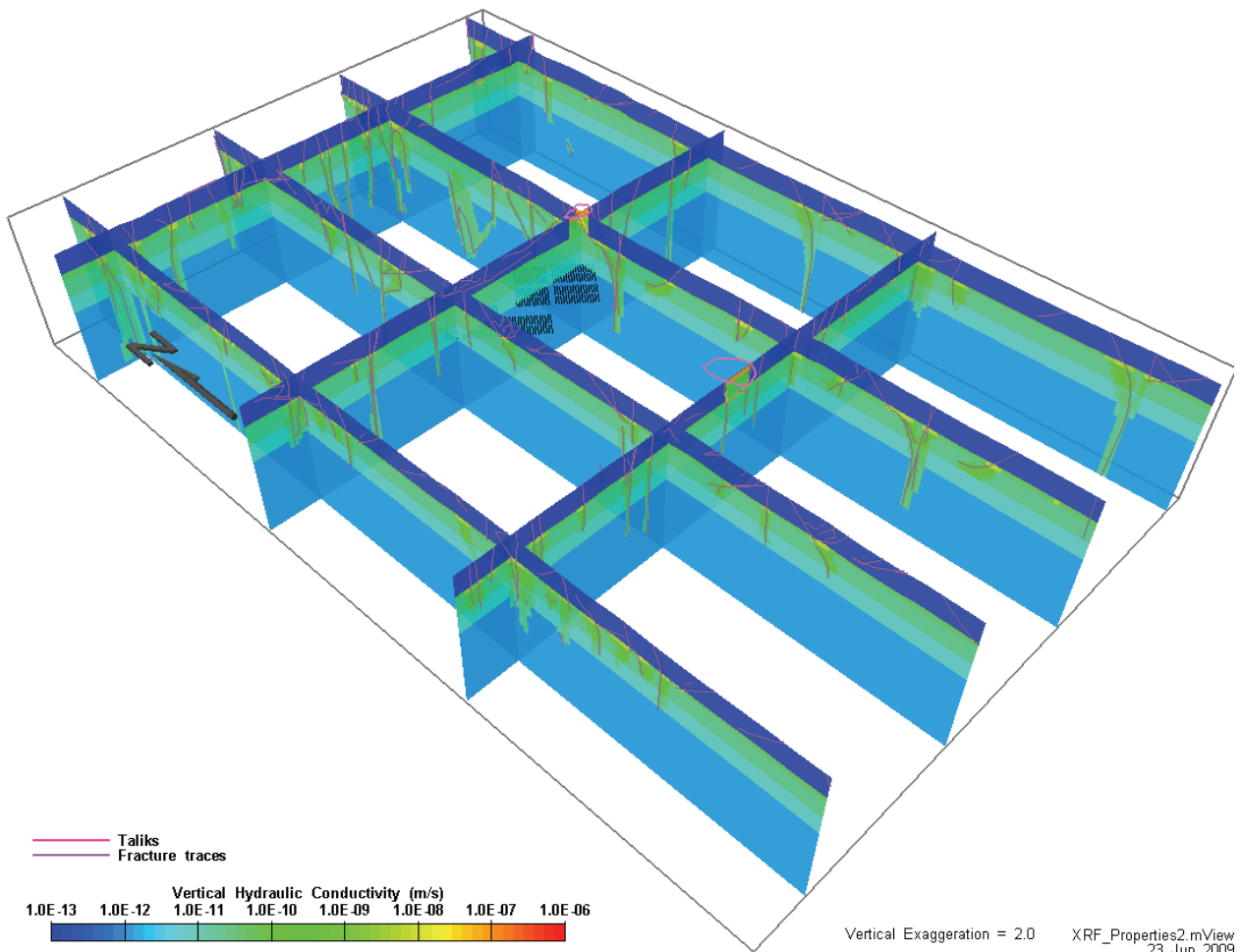


**Figure 3.6: Geosphere hydraulic conductivity distribution during permafrost periods, with 250 m deep permafrost and two open taliks. Fences are partially transparent. Darker zones at the intersections of fences should not be misinterpreted as zones of lower hydraulic conductivity.**

### 3.5 Boundary Conditions

Boundary conditions at ground surface are fixed hydraulic head at ground surface elevation for all temperate and permafrost periods. During the proglacial lake periods, hydraulic head at the surface is uniform across the model domain and is set equal to the elevation of the lake surface.

During periods of ice cover, the surface boundary heads are transient with variable pressure head calculated to reflect the ice load over the site as glaciers advance and retreat (see Section 2.2). Below the ice sheet it is assumed that free water exists over the ground surface and recharges to or accepts discharges from the hydrogeological system. The pressure head at ground surface was determined from the ice-load, calculated as the ice thickness multiplied by density (assumed 900

$\text{kg m}^{-3}$ ). This is close to the pressure required to float the glacier, a reasonable assumption based on the available literature on sub-glacial hydraulic pressures (see Section 2.2).

The continental glacier was assumed to traverse the model domain from North to South, with relatively little variation in thickness (and therefore hydraulic pressure) in the East-West direction. Therefore the East and West boundaries were set as zero flow, as was the bottom boundary.

The choice of boundary conditions at the North and South boundaries during glacial advances and retreats is specified as follows. The northern and southern boundaries were modelled as constant head boundaries, with the head set equal to the head at the surface (i.e., ice thickness, multiplied by density). This allows horizontal flow into and out of the model domain, and implicitly assumes that the vertical hydraulic gradient is zero at these boundaries. The advantage of having such a boundary condition is that it allows the pressure gradients caused by the glacier to push water ahead of it as it advances. This process could enhance radionuclide transport, and is therefore of interest. To ensure that these boundary conditions were not having an undue effect on the model results, a calculation case with no-flow Neumann boundary condition on all boundaries (except the surface) was also undertaken (see Section 4).

It can be argued that the constant head hydraulic boundary under a cold-based glacier is not valid, as the water production rate of a cold-based glacier should be greatly reduced, and the subsurface should be isolated from heads at surface. However, it is important to remember that the model domain represents a very small portion of a much larger continental glacier system. Permafrost is expected to persist around the edges of the continental glacier (see Figure 3.7), while toward the interior the permafrost will melt due to friction, geothermal heat, and insulation provided by ice cover. During the cold-based advances (see Figure 2.1) the model domain remains near the outer edge of the larger continental ice sheet. Due to meltwater production in the interior parts of the glacier, it is not unreasonable to expect elevated heads in the interior of the ice sheet. The difference between these heads, and the lower heads in the periglacial zone should drive horizontal flow below the permafrost, and perhaps also above the permafrost. Furthermore, despite the specified head boundary at the top surface during cold-based glaciation stages, the hydraulic connection between the surface and the underlying geosphere is severely impeded by the presence of continuous permafrost (see Section 3.4.3).

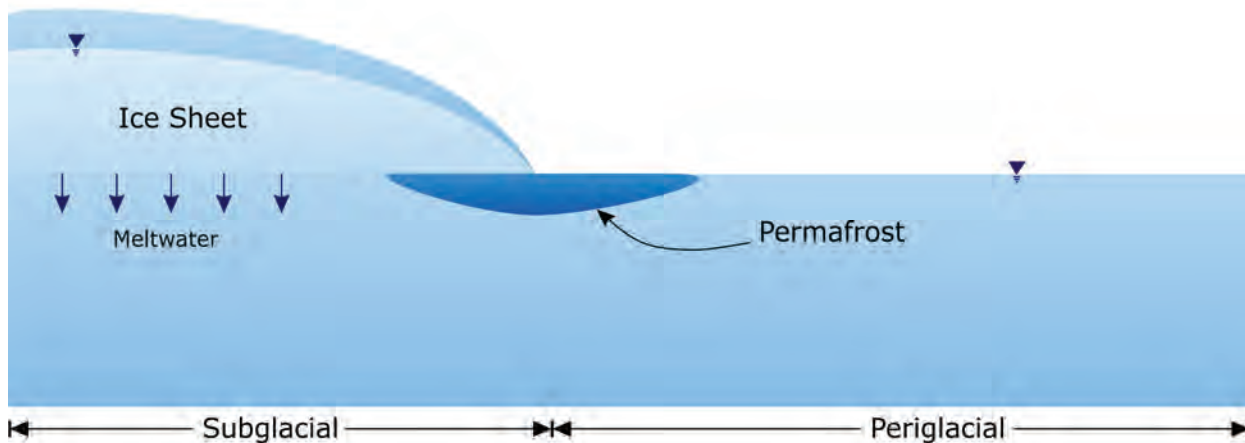


**Figure 3.7: Cross sectional schematic through a continental ice sheet, isostatic depression and forebulge phenomena are not shown (adapted from Lemieux et al., 2008).**

Rather than using a perfectly smooth glacial profile as depicted in Section 2.2, a smoothed surface which reflected a 50% moderation of the topographic variation was created. In nature, the ice surface elevation and subsurface hydraulic head may not closely track the subsurface topography (Boulton et al. 2007b). However, with a perfectly smooth ice surface, the resulting hydraulic pressure distribution would have caused relatively stagnant flow underneath the glacial ice, with very few local flow systems. The presence of drainage channels beneath glaciers requires some variation in subsurface hydraulic heads and the presence of local flow fields. Thus, although using a moderation of the surface topography is not strictly correct, it is a simple way to allow local circulation systems to exist under the glacial ice. This will tend to enhance spreading and transport beneath the glacier, particularly during later stages of the ice advance, or early stages of the ice retreat, when the glacial slope is low.

Figure 3.8 shows the boundary condition heads at various times during a glacial advance along a North-South transect through the site. Times shown on the figure represent time since the start of the ice-sheet advance sequence. Profiles for later ice sheet advances have the same overall shape, although the advance rates are slightly different and the maximum ice depths are greater (see Figure 2.1). For the ice-sheet retreats the profile is the same, but reversed in time. The retreat rates are much faster than the advance rates (see Table 2.2). The spatial distribution of hydraulic heads at the top model boundary near the start of the first glacial advance cycle is shown in Figure 3.9.

For transport, model boundaries are set as Neumann type boundaries with a concentration gradient of zero on all sides of the model. This allows solute to leave the model domain with the advective flow, but assumes that dispersive and diffusive flux are equal to zero.

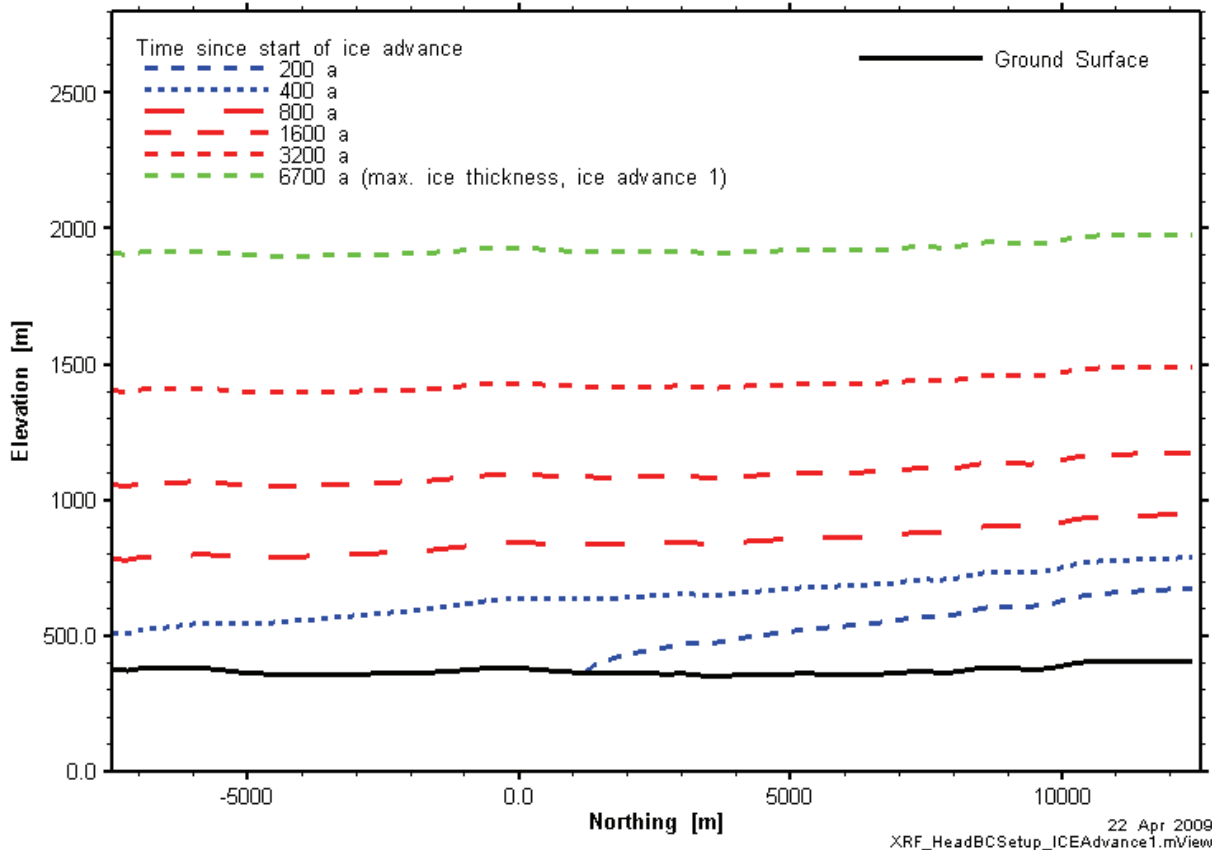
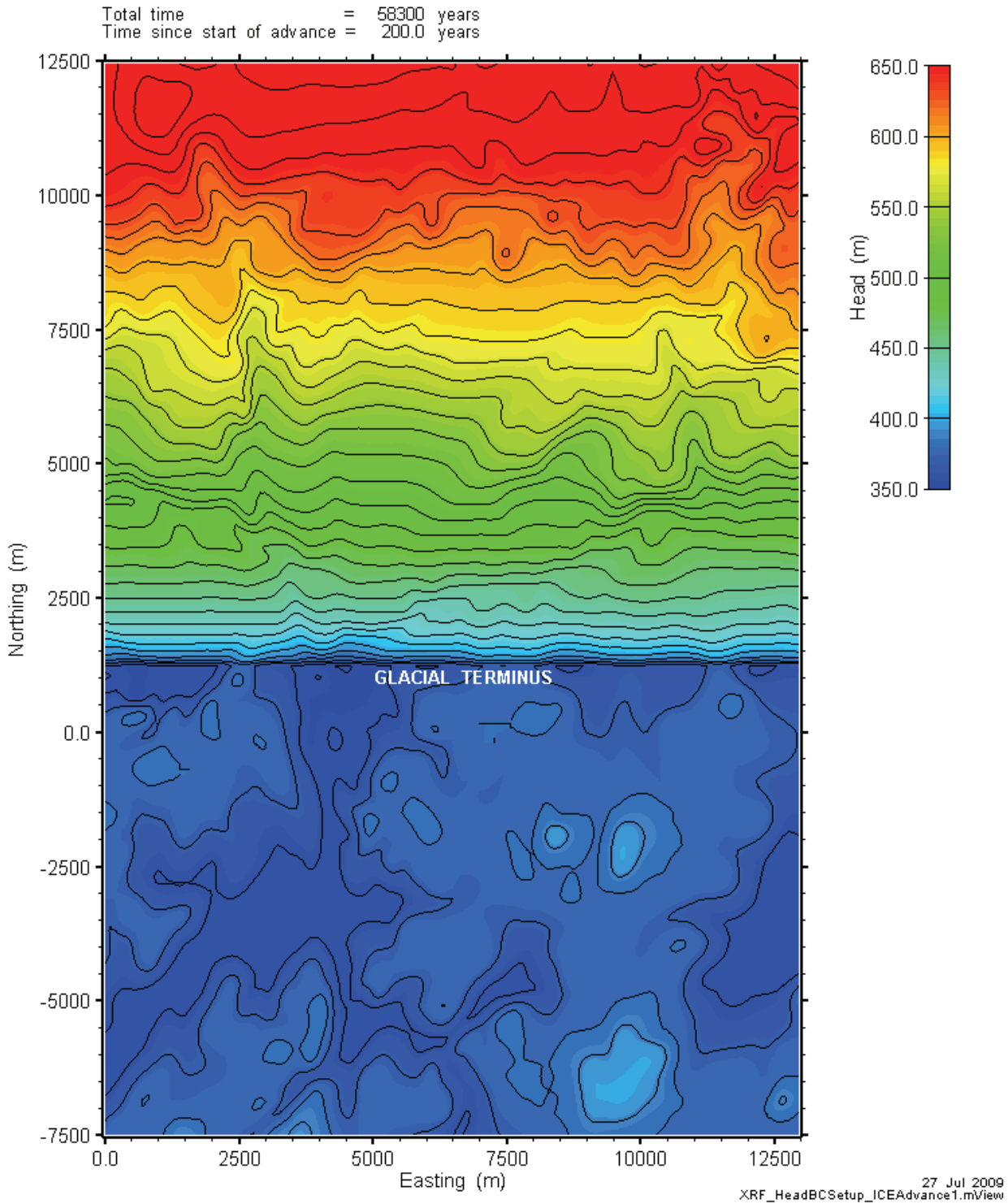


Figure 3.8: Ice surface boundary condition heads during the first glacial advance.



**Figure 3.9: Hydraulic head boundary condition head 200 years into glacial advance. Above roughly 1500 mN the hydraulic head is a function of ice surface elevation, while below 1500 mN the hydraulic head boundary condition is still based on the ground surface elevation.**

### 3.6 Radionuclide Source Term

The reference radionuclide is  $^{129}\text{I}$ . This is a long-lived and mobile radionuclide that was found to be of most importance in previous modelling of a Canadian deep geologic repository. For this radionuclide, a half-life of  $1.57 \times 10^7$  years (or a decay constant of  $1.4 \times 10^{-15} \text{ s}^{-1}$ ) and a free solution diffusion coefficient of  $1 \times 10^{-9} \text{ m}^2 \text{ s}^{-1}$  were used. Tortuosity was set to 1.0. This is a very conservative value for tortuosity in intact rock. Sorption of  $^{129}\text{I}$  is negligible in the geosphere and was not modelled.

The transport modelling used the radionuclide source term previously developed for the HBC modelling (Garisto et al. 2005). The HBC source term assumed the failure of two containers in the repository sector having the shortest groundwater travel time to surface. Mass flux from the container, through the engineered barrier system and out into the surrounding geosphere was calculated using a detailed model with a geometrically accurate representation of all system components.

The total mass flux calculated by the HBC vault model is shown in Figure 3.10. This mass flux was divided by four and applied to four adjacent nodes at the repository elevation (-300 mASL), which enclosed the selected source location.

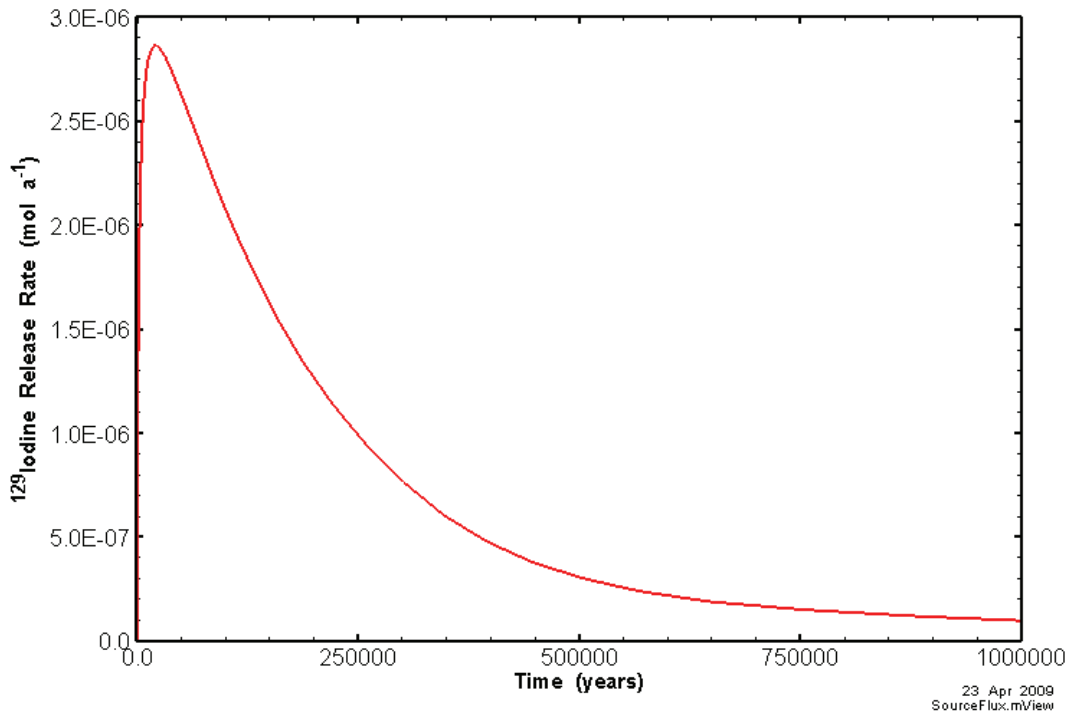


**Figure 3.10: Release rate of  $^{129}\text{I}$ iodine from repository near-field.**

To examine the effect of alternate source locations, the source term was applied at two locations within the repository footprint, as shown in Figure 3.11. These particular locations were selected as the groundwater travel times to the surface were relatively short for these locations during different stages of the glacial cycle (i.e., temperate, permafrost, etc.). The location designated Defective Container 1 (DC1) has the shortest groundwater travel time to the surface for the HBC model under steady temperate climate conditions. The second location, Defective Container 3 (DC3), also has a relatively short groundwater travel time to surface, particularly during postglacial lake periods.

Two approximations were involved in applying these source terms in the current model. Firstly, the HBC vault model used steady-state flow boundary conditions, based on a temperate climate. This is not consistent with the current model, where the transient flow field varies throughout the simulation period. In the case of source location DC3 the approximation is greater, as the flow field in this location is less similar to that in the HBC model. Nevertheless, this is an acceptable approximation as the contaminant release rate from the repository into the geosphere is probably not highly dependent on the local flow field (see Garisto et al. 2005).

Secondly, the source term is applied in the current model at nodes which are a greater distance (maximum 50 m) from the source location than the HBC model (maximum 27.5m). This approximation is conservative since, in effect, approximately 10 metres of intact rock is bypassed, causing more rapid transport of the contaminants away from the actual source.

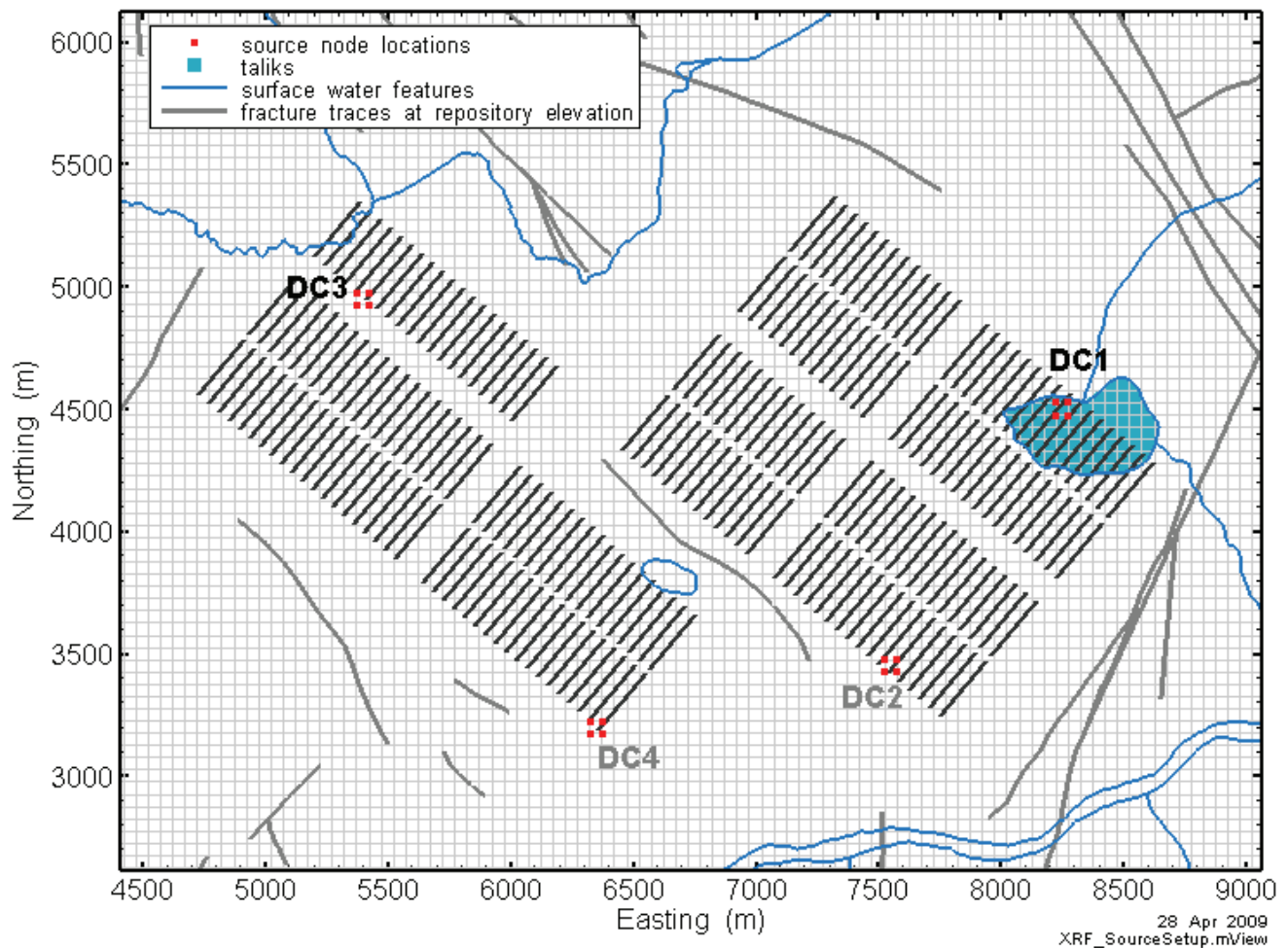


**Figure 3.11: Defective container source locations. Only locations DC1 and DC3 were assessed in this report.**

### 3.7 Water Supply Well

The HBC reference case model assumed a water supply well was in constant use throughout the simulation period. The well was located at approximately 100 m depth next to the small lake above the eastern edge of the repository, and was conservatively located so as to intercept the radionuclide plume from the defective containers at location DC1. The well used a constant pumping rate of  $738 \text{ m}^3 \text{ a}^{-1}$ , based on the water demand for a small family farm.

The GSC model includes an identical well; however, it is only active during the temperate period in each glacial cycle. The planar model coordinates of the well are 8275 mE and 4225 mN. The well is represented by sinks on two nodes, at elevations of 261.0 and 288.0 mASL.

#### 4. MODELLING CASES

Detailed modelling was performed for a reference case (RC) model and for a number of parameter and conceptual model sensitivity cases. The development and general characteristics of the Reference Case model were described in Section 3, and are summarized as follows:

- Transient model, with sequential variations in climate and boundary conditions simulating periods of temperate conditions, permafrost conditions, glaciated conditions (warm and cold based), and proglacial lake conditions;
- During permafrost periods, two taliks are left open (since permafrost is represented by areas where the permeability is reduced to simulate frozen ground, the taliks are represented by areas where the permeability is not reduced);
- During periods where glacial ice is advancing over permafrost, taliks are frozen over;
- Stratigraphic, hydrogeologic, and transport properties as outlined in Section 3, generally a layered system with layered properties interrupted by fracture zones;
- Constant density water flow;
- $^{129}\text{I}$  source term based on results of the HBC vault model;
- Radioactive decay of  $^{129}\text{I}$ , no sorption in any formation;
- $^{129}\text{I}$  transport from two different locations in the repository (DC1 and DC3); and
- Generally, a 0.8M year simulation period.

Modelling cases have been defined to assess the sensitivity of model predictions to alternate boundary conditions, geosphere properties, and long term climate conditions. In general, the sensitivity cases were developed as described in Section 3, and differed from the reference case in very specific ways. Table 4.1 describes the defined sensitivity cases.

For the GSC-CC case, there were two versions - with and without a well. The presence or absence of a well significantly affects the radionuclide flux to some of the control surfaces.

For the GSC-HS case the storage coefficient was increased by an order of magnitude throughout the model domain while all other parameters were held constant. This is slightly unrealistic, as the storage coefficient is not really an independent parameter, but rather a function of bulk modulus, porosity, Biot's  $\alpha$ , and Poisson's ratio. Using Equation 3.2, a factor 10 increase in storage coefficient can be achieved by reducing the porous medium bulk modulus while holding all other parameters constant. However, it may be unrealistic to expect deeply buried and confined granite to deform so easily, and it may also be unrealistic to treat such parameters as porous medium bulk modulus, porosity, and Biot's  $\alpha$  as independent parameters. Generally, a reduction in the bulk modulus should correlate positively with an increased porosity, and perhaps an increase in Biot's  $\alpha$ .

**Table 4.1: Modelling sensitivity cases.**

<b>Model Name</b>	<b>Abbreviated Name</b>	<b>Description</b>
Reference Case	GSC-RC	As described in Section 3 and preceding paragraphs.
Constant Climate Scenario	GSC-CC	Temperate state conditions persist for the entire assessment period. This is a steady-state flow model. Useful for understanding the influence of glaciation on radionuclide fluxes to the biosphere.
High Storage Coefficient	GSC-HS	Geosphere storage coefficients increased by one order of magnitude throughout model domain. Used to study the importance of system response time on the results.
No-Flow N-S Boundaries	GSC-NF	Boundary conditions at the North and South vertical boundaries changed from specified head boundaries to no-flow boundaries. All other boundary conditions remain unchanged. Studies the influence of boundary conditions on the results.
Talik under Glacier	GSC-TK	Taliks remain open when ice is advancing over permafrost (sequences 3,4,6, and 9, see Table 2.1). Used to assess the impact of unfrozen areas in sub-glacial permafrost on flow and transport.

## 5. GLACIAL SEQUENCE MODELLING RESULTS

Modelling results presented in this section include a comparison to previous results, a detailed discussion of flow system behaviour during a single glacial cycle, and discussion of radionuclide transport over the full 0.8 Ma assessment period.

### 5.1 Comparison to HBC Reference Case

The GSC model approach differs numerically from that used for the HBC transport modelling (Garisto et al. 2005). As described above, the grid discretization is coarser (50 - 100 m for GSC versus 27.5 m or less for HBC) and the dispersivity is larger (80 m longitudinal for the GSC versus 50 m for HBC). The larger dispersivity is required to meet numeric criteria for the larger discretization. A single verification simulation (GSC-CC) was performed to ensure that the GSC model results are broadly comparable with the HBC results. The verification case assumed no water-supply well, steady-state boundary conditions and no permafrost in the geosphere. The metric for the comparison is  $^{129}\text{I}$  mass flux to the talik lake region and results are presented in Figure 5.1.

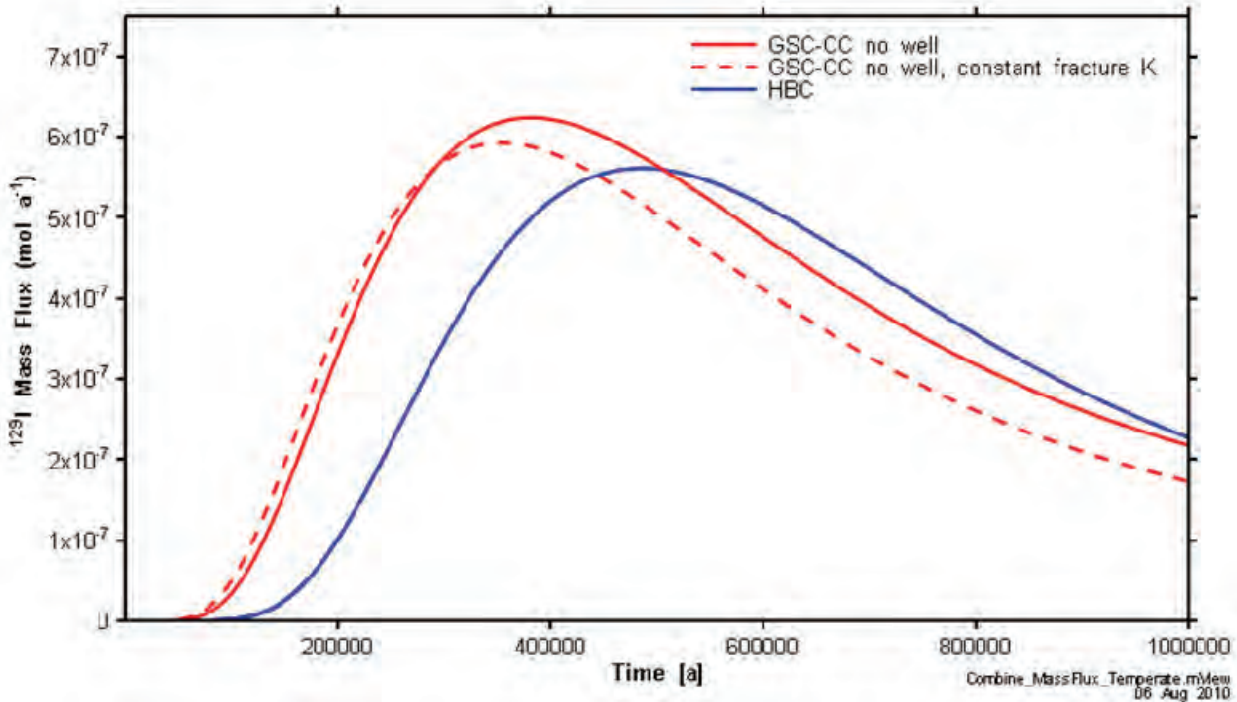


**Figure 5.1: Comparison of mass flux to the Lake for the no-well case for the HBC and GSC-CC models.**

The GSC-CC model results in a maximum mass flux rate to the lake similar to the HBC model. The overall mass flux is comparable, although the peak has an earlier arrival time (385 ka for GSC-CC, 485 ka for HBC). The early arrival may be due to the higher dispersivity or the somewhat altered flow field.

To assess the impact of the depth dependent fracture permeability in the GSC model a further simulation with constant hydraulic conductivity fractures (with  $K_{\text{fracture}} = 10^{-6}$  m/s) was performed. (Note that fracture permeability used in the HBC study was depth independent). The results are shown in Figure 5.1. The dotted red line represents a model with constant hydraulic conductivity fractures. The

higher fracture conductivities result in a slightly earlier first arrival time, and slightly lower and earlier peak mass flux to the small lake. Overall, the predictions of the GSC-CC model are quite similar to the earlier HBC model, and the effects of lower conductivity fractures are not very significant. The limited impact of the fracture conductivity reduction is likely due to the very low hydraulic conductivity of the intact rock formation and the relatively large distance between the radionuclide source and the nearest fracture zone.

## 5.2 Single Glacial Cycle Flow Results

### 5.2.1 Head and Velocity Distribution

Chronologically ordered visualizations of flow model results presented in this section show the transient nature of the flow system response over a single glacial cycle. The figures portray results on a vertical cross-section on a North-South transect (the direction of glacial advance) cutting through the northern talik that is above the repository. The location of this cross-section is shown in Figure 5.2. The figures on the following pages present head contours at several different scales over different head magnitudes, as well as velocity vectors and advective velocity magnitude as a color field. The large variation in hydraulic head at different times requires that the hydraulic head range varies between figures. The advective velocity scale is maintained constant between all figures.

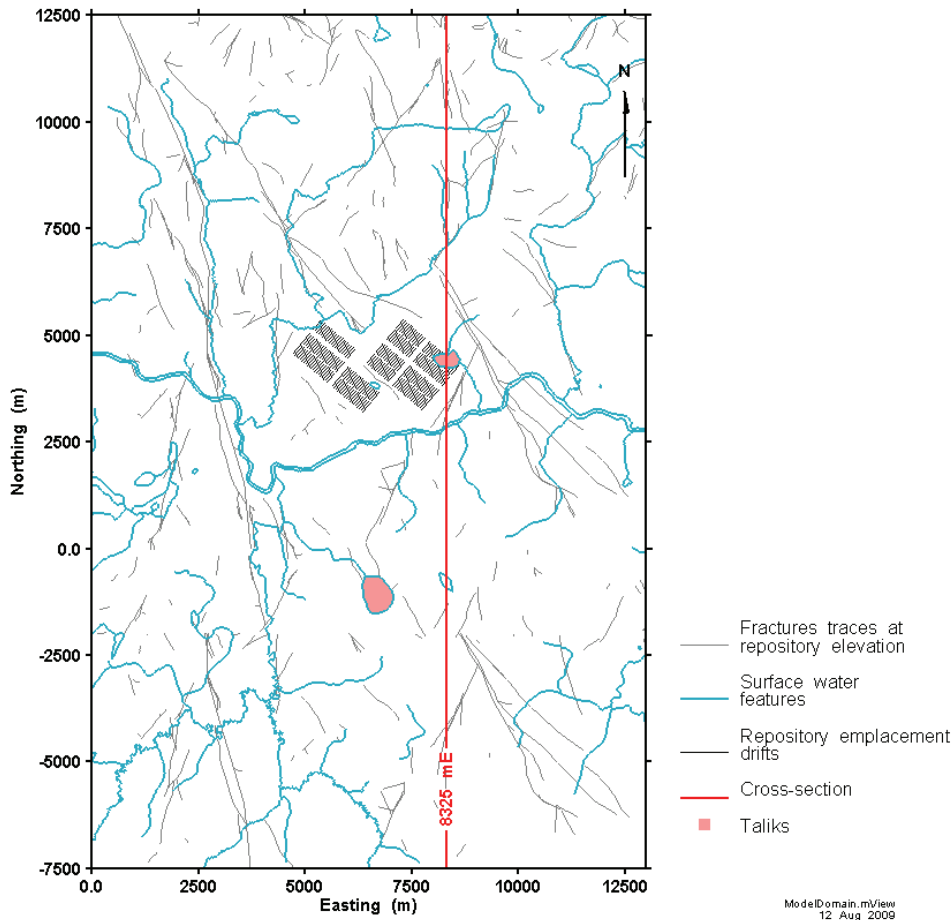
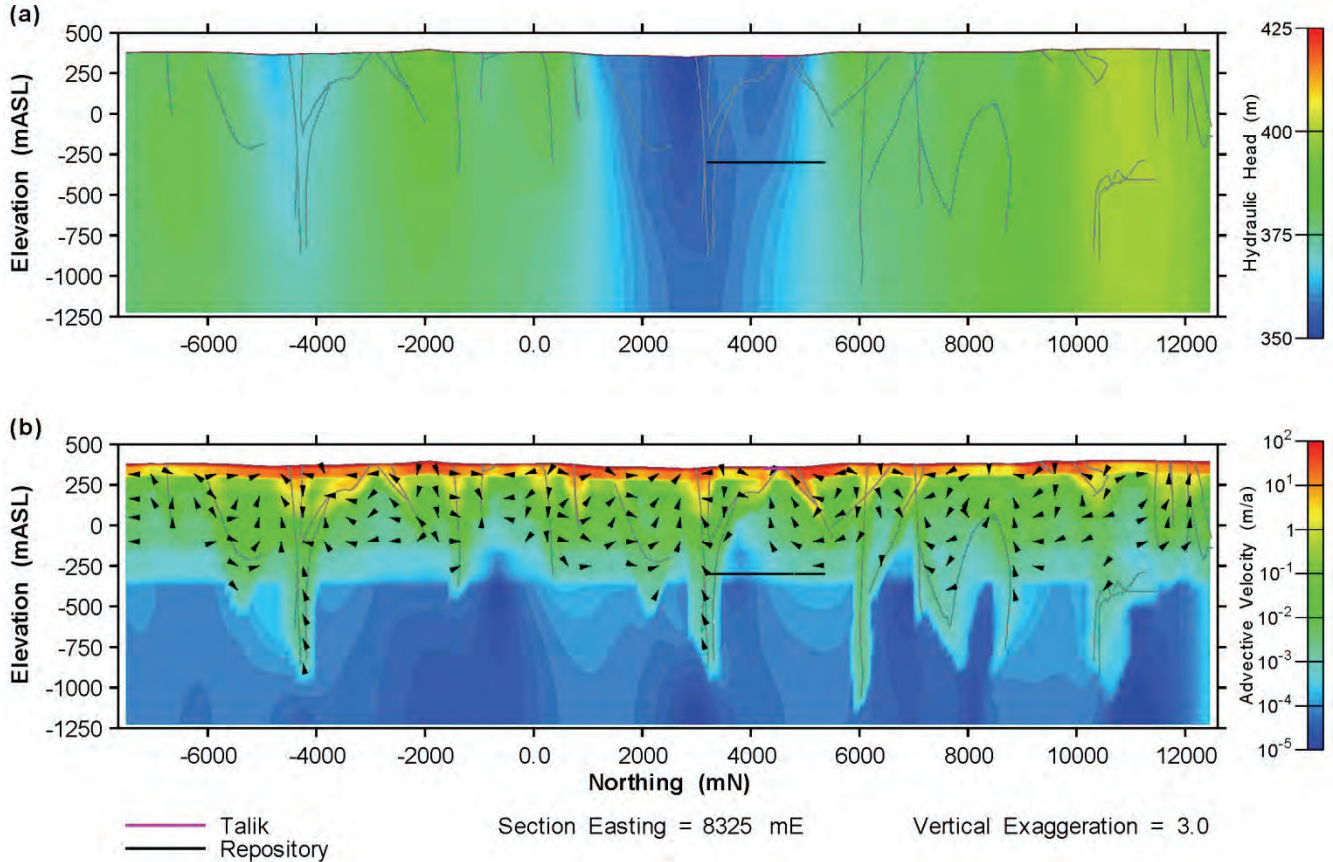


Figure 5.2: Location of cross-section for figures in Section 5.2.1.

### 5.2.1.1 Reference Case

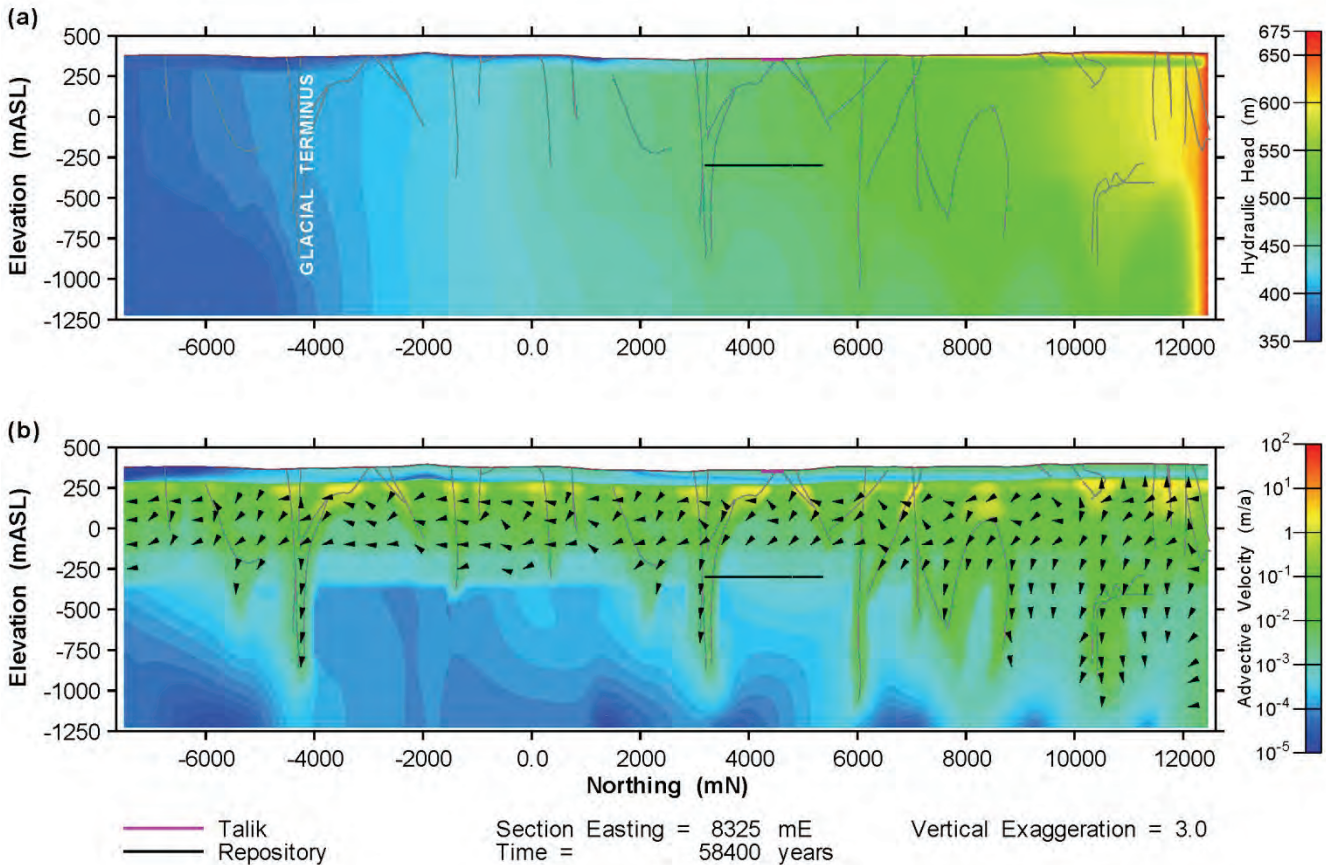
Figure 5.3 illustrates the steady-state flow domain that exists during the initial temperate period. The head boundary condition is equal to the surface elevation, so flow is topographically driven. This results in small-scale flow circulation systems, with the vast majority of flow occurring in the more permeable shallow system. There is some minor flow at depths, particularly within the fracture system.



17 Aug 2009  
NoTalik\_Head\_2D\_SECTION\_Temp.mView

**Figure 5.3: GSC-RC flow model results during initial temperate phase (stage 1 – temperate). The hydraulic head distribution is shown in (a), while the advective velocity distribution is shown in (b). Velocity vectors are only plotted where the velocity exceeds 1 mm/a.**

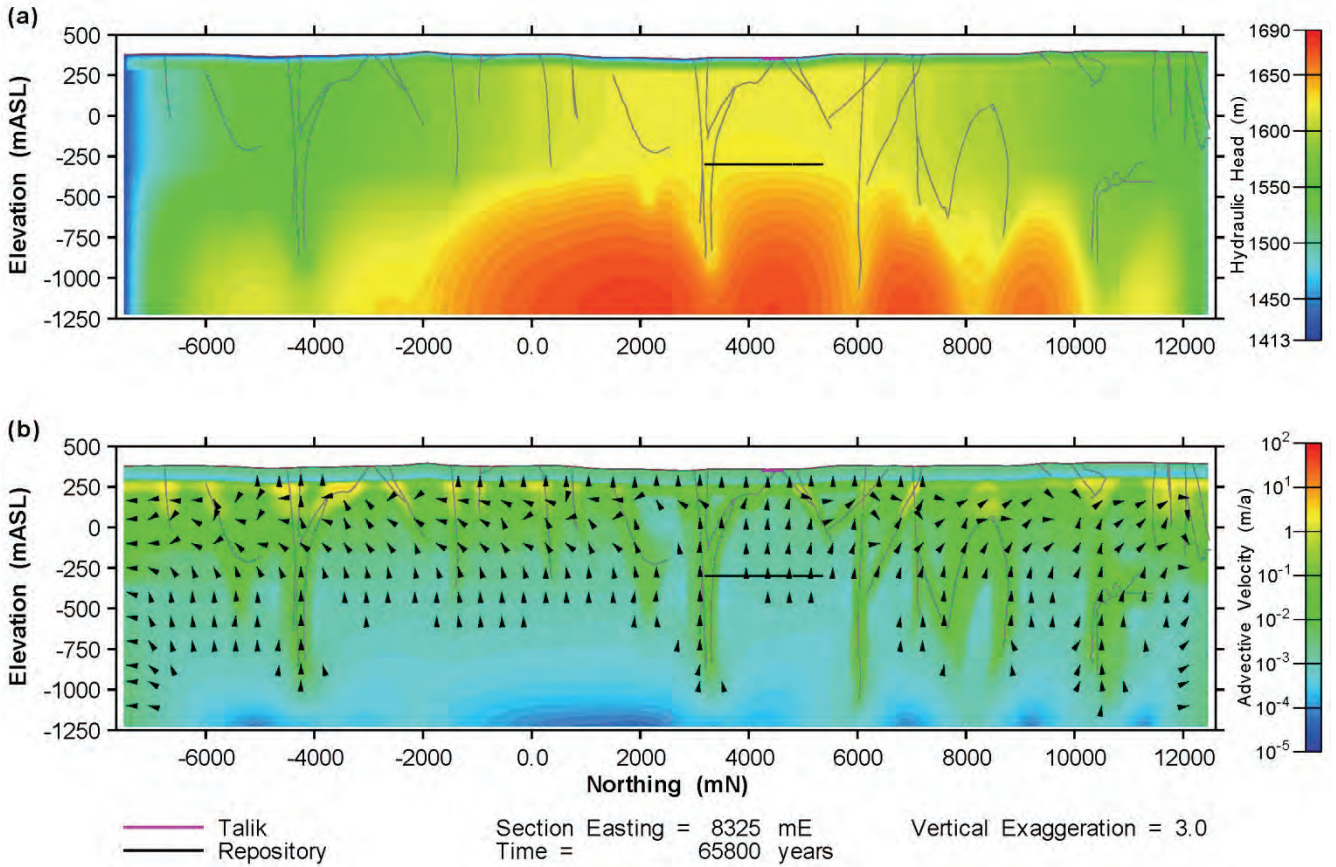
Figure 5.4 shows the flow field 300 years into the first glacial advance. At this time, ice largely covers the model, except for the southernmost 2000 m. The subsurface below the glacier is significantly pressurized. This pressurization comes from two sources, namely the hydromechanically induced pressures in the subsurface and the fixed head hydraulic boundary condition on the northern boundary. The boundary condition causes an instant pressurization on the right hand boundary of Figure 5.4 (a). Throughout the remainder of the model domain, the transmission of heads from surface to depth is dampened by storage effects. The overall impact of the advancing glacial front is to cause relatively high lateral flows below the permafrost and above approximately -125 mASL.



18 Aug 2009  
NoTalík\_Head\_2D\_SECTION\_Ice1.mView

**Figure 5.4: GSC-RC flow model results at 58,400 years (beginning of stage 3 – ice advance, cold based glacier). The hydraulic head distribution is shown in (a), while the advective velocity distribution is shown in (b). Velocity vectors are only plotted where the velocity exceeds 1 mm/a.**

Figure 5.5 shows the head and velocity contours during the first glacial retreat. In this cold-based retreat, the only hydraulic outlets for stored, glacially-induced heads are the northern and southern boundaries. This leads to a rather unusual flow regime, with divergent flow from the center of the model towards the northern and southern boundaries. In the vicinity of the repository, the flow direction is vertically upward toward the more permeable layers. For this particular period, no-flow boundaries around the entire model domain might provide more realistic results. However, the major flow-system discrepancies are limited to the near-boundary area. Flow within the centre zone of the model where transport occurs is likely representative.



17 Aug 2009  
NoTalik\_Head\_2D\_SECTION\_Ice1-R.mView

**Figure 5.5: GSC-RC flow model results at 65,800 years (midpoint of stage 4 – ice retreat, cold based glacier). The hydraulic head distribution is shown in (a), while the advective velocity distribution is shown in (b). Velocity vectors are only plotted where the velocity exceeds 1 mm/a.**

Figure 5.6 shows an intermediate transition period approximately 2000 years after the start of the second permafrost sequence. After 2000 years, elevated heads caused by the relatively rapid glacial retreat remain at greater depths, especially where fracture zones do not provide a drainage pathway. Impermeable permafrost covers most of the ground surface, locking in the pressurization and directing flow towards the only hydraulic outlets of the system, the North-South boundaries and the two taliks. The northern talik, above the repository, is at a lower elevation than the larger southern talik, and consequently a larger proportion of the flow is focused on this talik. (Note that the southern talik is not intersected by the cross-section in Figure 5.6.)

In the transport results (see Section 5.3), this flow into the northern talik leads to a significant increase in the transport of <sup>129</sup>I through the talik. For source DC1, the highest rates of mass flux to the northern talik occur at the beginning of the second permafrost period in each glacial cycle. The second permafrost period has the highest mass flow rates to the talik because the preceding glacial retreat is cold based (i.e., a continuous permafrost layer is still present under the glacier) and the high pressures induced by the ice load are unable to dissipate out the top of the model. If the first glacial retreat were warm-based, the resulting <sup>129</sup>I flow to the northern talik would likely be much lower. Indeed, the mass flow at the beginning of the third permafrost period, which follows a warm-based glacial retreat, is much lower.

The high pressure zone seen at the top right of Figure 5.6 (a) is an artefact caused by the instantaneous application of permafrost to the post-retreat hydraulic head distribution down to a depth of 250 m. This traps some relatively high hydraulic heads in the low-permeability permafrost zone. These heads take some time to dissipate, but have a minor effect on the flow field in the underlying more permeable zones.

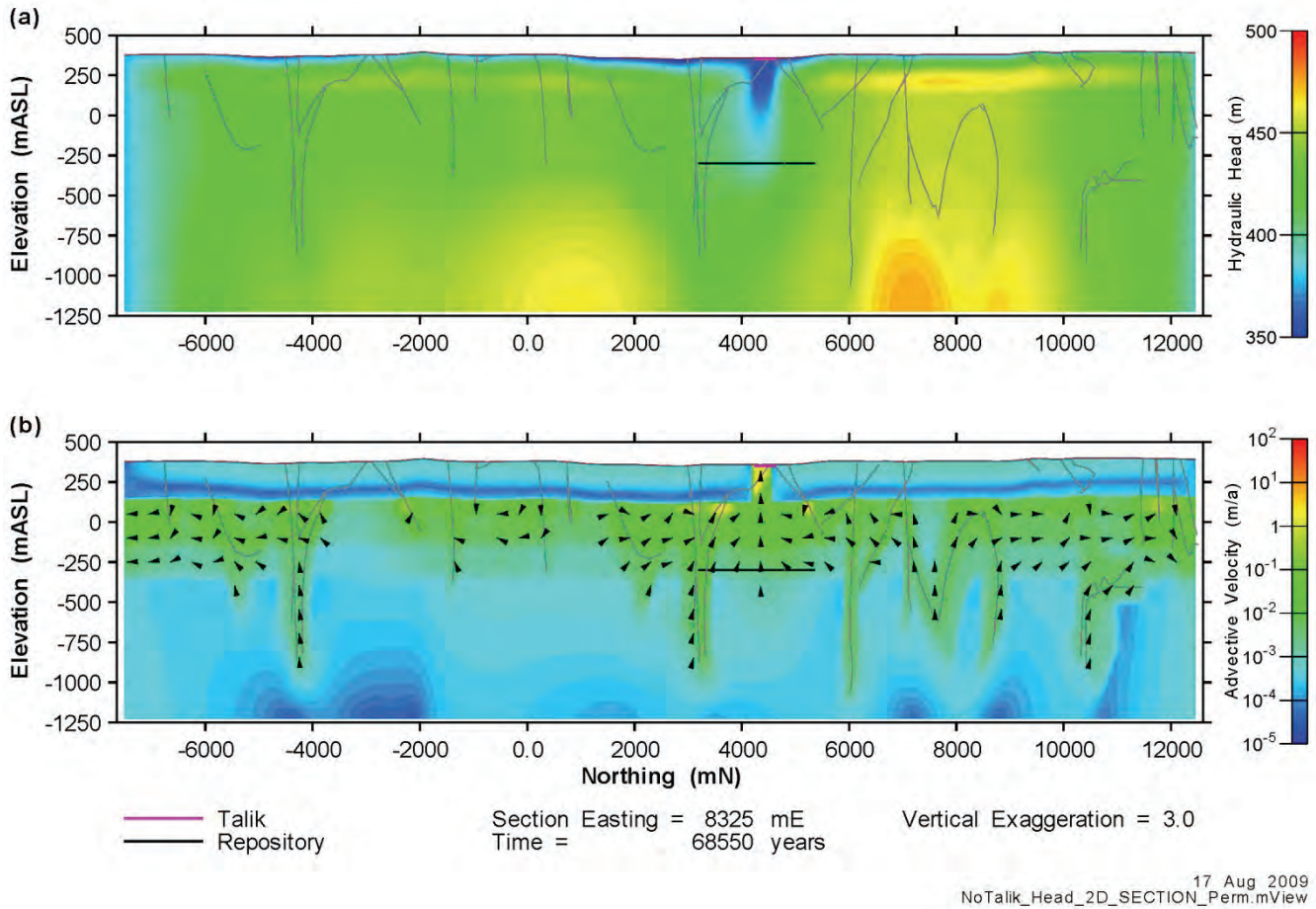
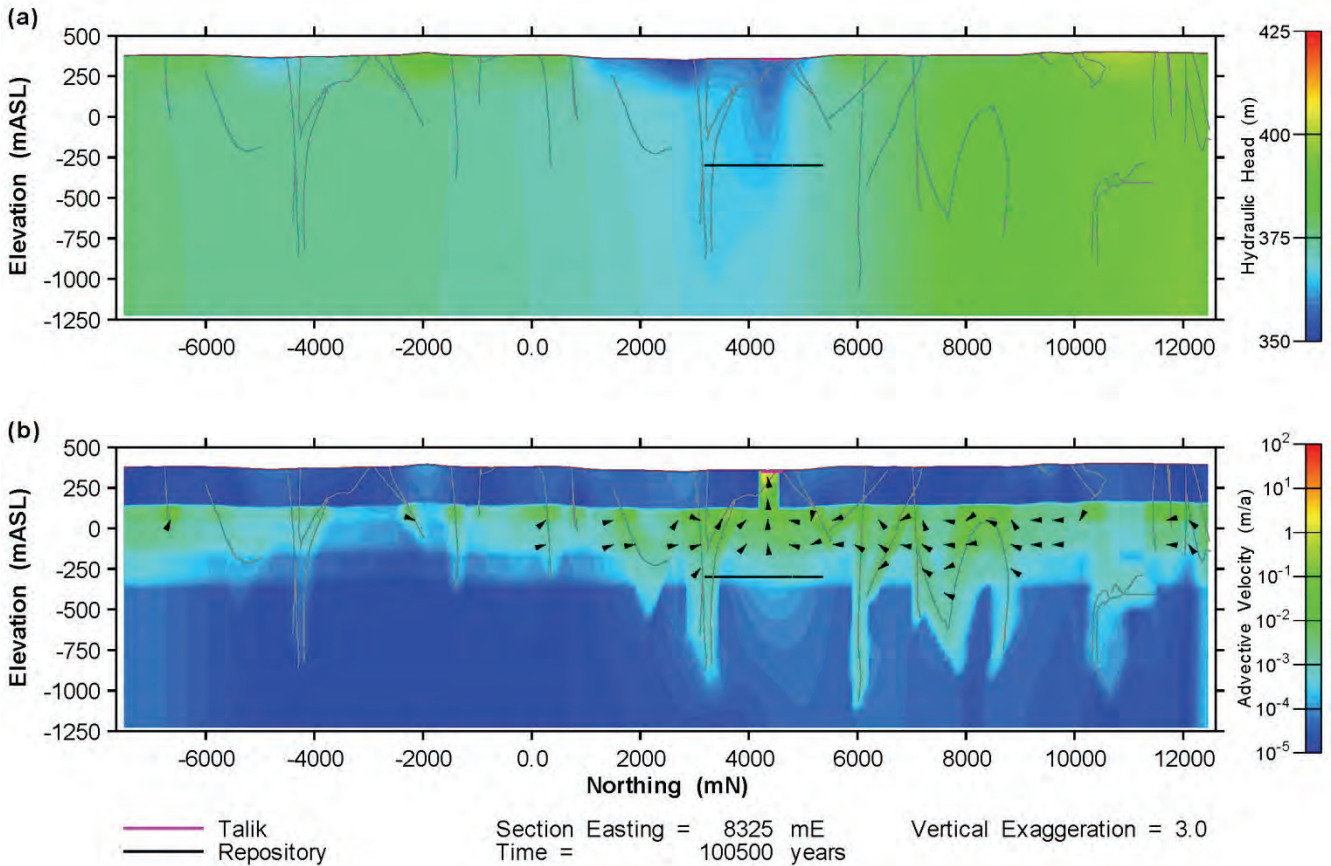


**Figure 5.6: GSC-RC flow model results at 68,550 years (start of stage 5 – permafrost). The hydraulic head distribution is shown in (a), while the advective velocity distribution is shown in (b). Velocity vectors are only plotted where the velocity exceeds 1 mm/a.**

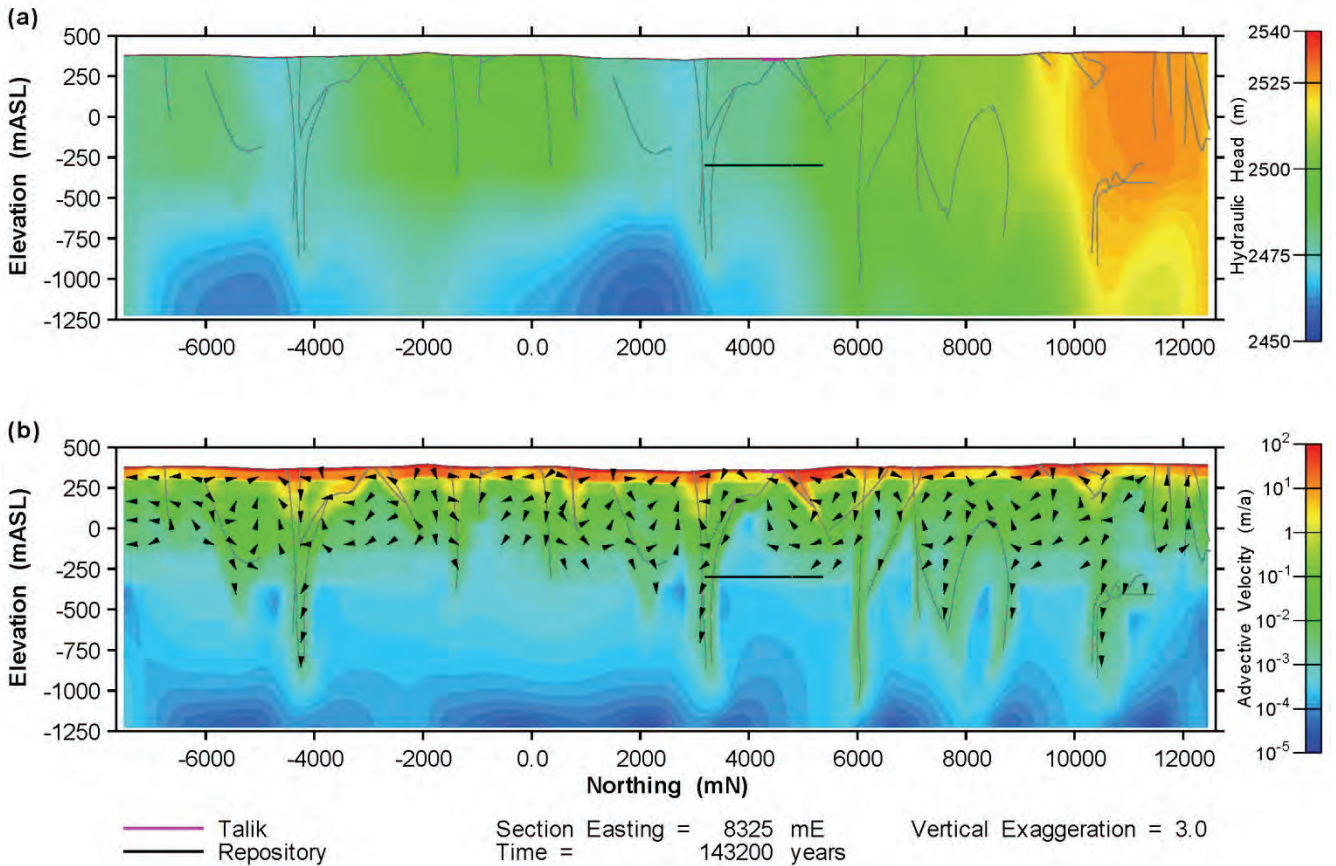
Figure 5.7 shows the flow field at a time near the end of the second permafrost period. The system has long since reached a steady state. Head gradients at depth have been reduced as water has been released from the system. Flow in the less permeable parts of the model (below -300 mASL and within the permafrost) is effectively stagnant. In the more permeable zones between the permafrost and deeper low-permeability rock some flow persists. This flow is driven by the specified hydraulic heads at the North-South boundaries and the two taliks. As the northern talik has the lowest fixed hydraulic head within the model, it serves as the primary hydraulic outlet, meaning that the flow converges on this talik. Consequently, the overall flow and mass transport rates through the talik remain high relative to other stages in the glacial cycle.



17 Aug 2009  
NoTalík\_Head\_2D\_SECTION\_Perm.mView

**Figure 5.7: GSC-RC flow model results at 100,500 years (end of stage 5 – permafrost). The hydraulic head distribution is shown in (a), while the advective velocity distribution is shown in (b). Velocity vectors are only plotted where the velocity exceeds 1 mm/a.**

Figure 5.8 shows the flow field at the midpoint of glacial stage 10, a warm-based glacial advance. Ice covers the entire model domain, with a depth of approximately 2.2 km. This flow field contrasts with that shown in previous figures largely because the glacier is now warm-based, with no permafrost barrier impeding the transmission of the very high hydraulic heads at the base of the glacier, as well as significantly more ice at this stage in the glacial cycle. In the shallow system, flow is driven by the topography of the ice-sheet thickness boundary condition. At the elevation of the repository and deeper, the low rates of flow are directed downward toward under-pressurized zones at greater depth.

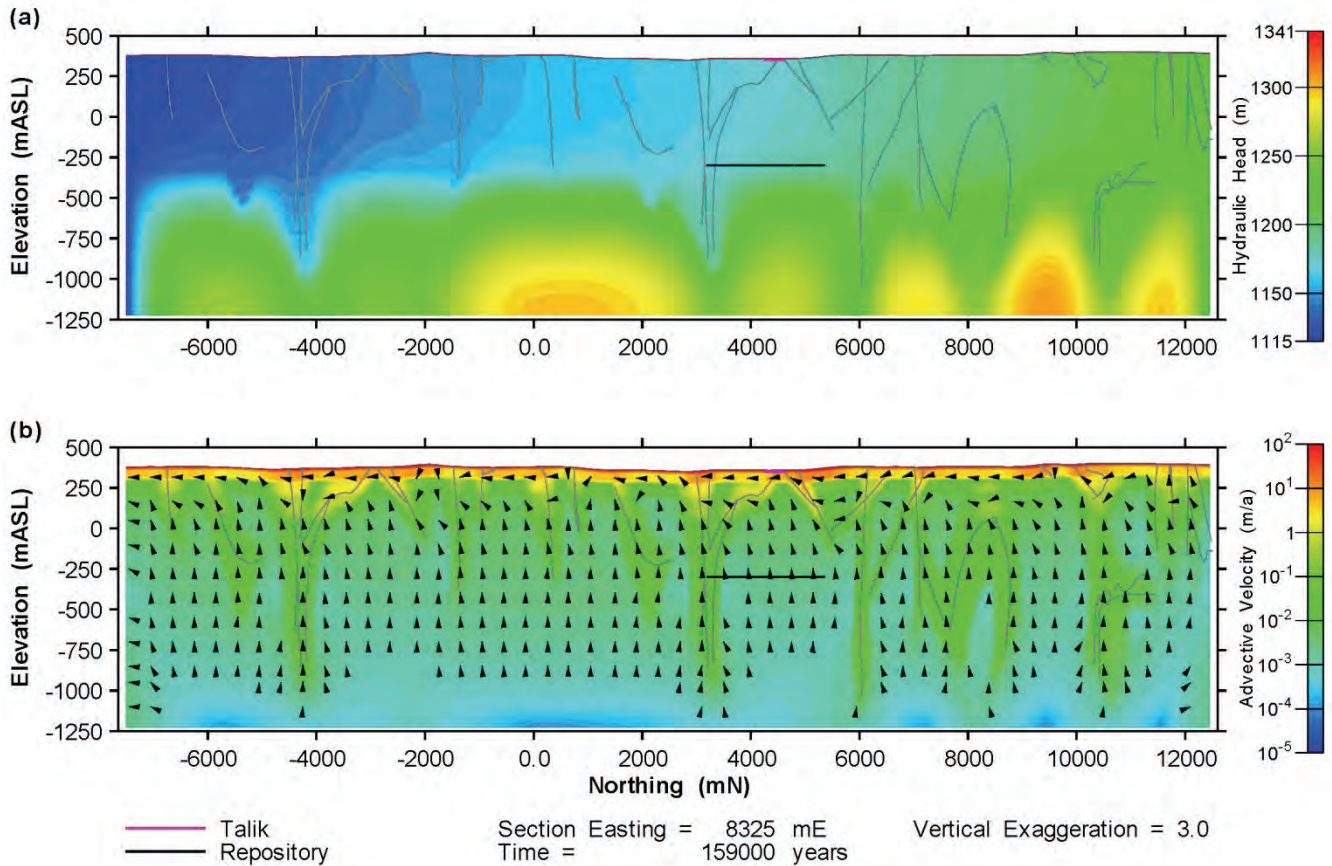


17 Aug 200  
NoTalík\_Head\_2D\_SECTION\_Ice3-A2.mVie

**Figure 5.8: GSC-RC flow model results at 143,200 years (midpoint of stage 10 – ice advance, warm based glacier). The hydraulic head distribution is shown in (a), while the advective velocity distribution is shown in (b). Velocity vectors are only plotted where the velocity exceeds 1 mm/a.**

Figure 5.9 shows the flow field near the end of stage 11, during a warm-based glacial retreat stage. Ice still covers the entire model domain, but the ice thickness and therefore the specified heads at the surface have dropped relatively rapidly from their peak values. This leads to a reversal of the prevailing downward flow direction during the preceding ice advance stage. High hydraulic heads remain stored in the deeper, less permeable system while the heads at the surface have dropped rapidly. Consequently, below roughly 200 mASL the predominant flow direction is vertically upward.

Above 200 mASL, the flow direction shifts to predominantly horizontal and southward. This is caused by the slope of the retreating ice sheet. So, although the flow from the repository is vertically upward with a velocity of millimetres to centimetres per year, very little radionuclide actually reaches the northern talík at this stage, as the plume above the repository is swept to the south and diluted.

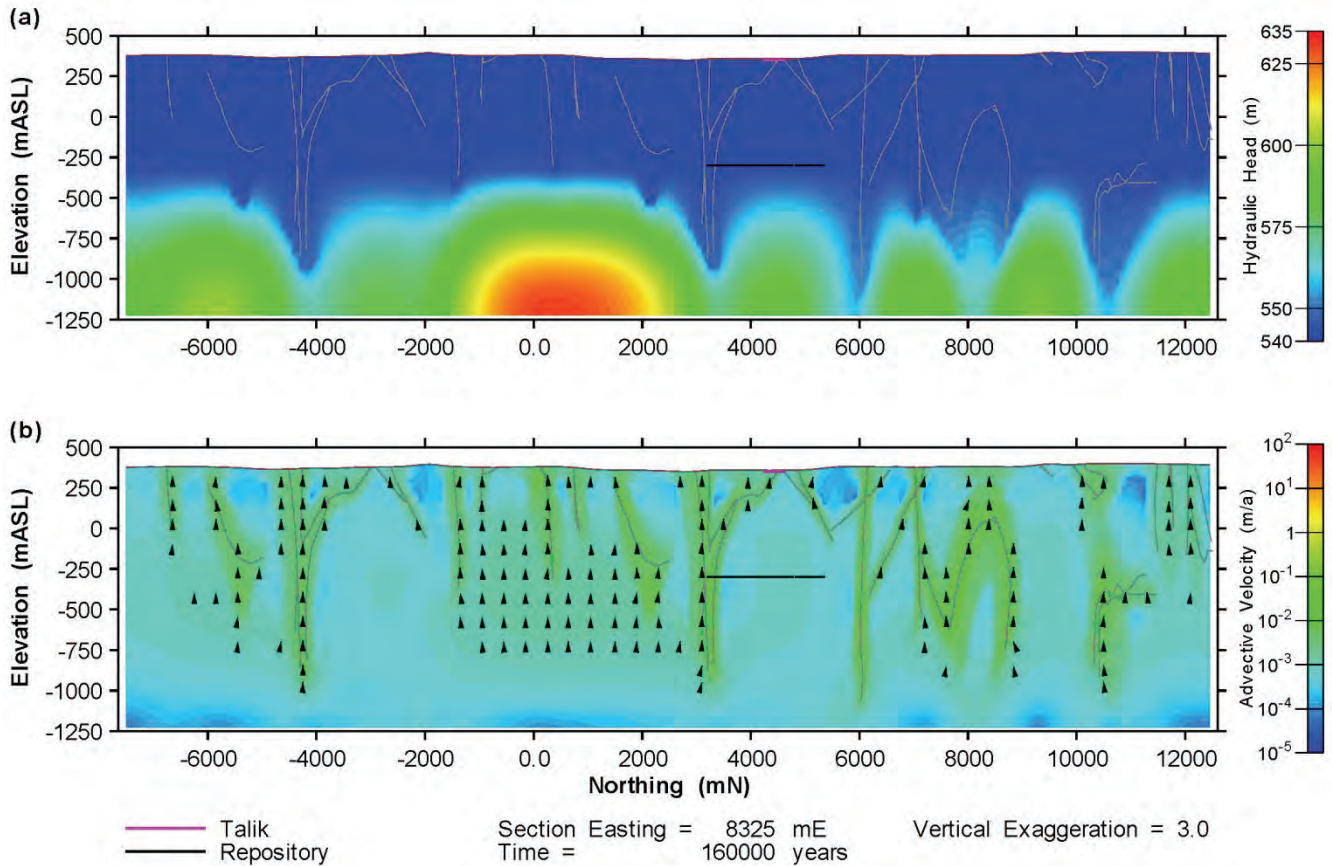


17 Aug 2009  
NoTalik\_Head\_2D\_SECTION\_lce3-R.mView

**Figure 5.9: GSC-RC flow model results at 159,000 years (end of stage 11 – ice retreat, warm based glacier). The hydraulic head distribution is shown in (a), while the advective velocity distribution is shown in (b). Velocity vectors are only plotted where the velocity exceeds 1 mm/a.**

Figure 5.10 shows the flow field midway through stage 12, at which time a constant head boundary of 540 m is applied at the entire top surface of the model domain to simulate a proglacial lake. Water is still being released from storage in the deeper formations, driving flow vertically upward throughout the model domain. The stored overpressures persist into the following temperate period, finally returning to the initial steady state flow field 3500 years after the end of stage 12 (at approximately 164,200 years).

Because the groundwater flow system attains a steady state during the temperate periods, the flow fields of the subsequent glacial cycles required to reach the end of the assessment period are identical to those presented above and in Figure 5.10.



17 Aug 2009  
NoTalik\_Head\_2D\_SECTION\_Lake.mView

**Figure 5.10: GSC-RC flow model results at 160,000 years (midpoint of stage 12 – pro-glacial lake). The hydraulic head distribution is shown in (a), while the advective velocity distribution is shown in (b). Velocity vectors are only plotted where the velocity exceeds 1 mm/a.**

### 5.2.1.2 High Storage Coefficient Case

The High Storage Coefficient Case (GSC-HS) is identical to the reference case, with the exception that storage coefficients throughout the model were increased by one order of magnitude. The higher storage coefficient causes a delay in the reaction of the system to changes in boundary conditions. Hydraulic head in the system increases more slowly than the RC case during glacial advances. Conversely, when the ice retreats the glacially induced overpressures in the subsurface persist for a longer time. During permafrost periods the onset of steady state conditions is delayed. As an example, Figure 5.11 shows the head distribution below the advancing ice sheet 300 years into the first glacial advance. In comparison to Figure 5.4, the high hydraulic heads produced by the glacier and the northern hydraulic boundary have not penetrated as far into the model domain. Overall advective velocities are somewhat lower throughout the model domain and within the repository footprint.

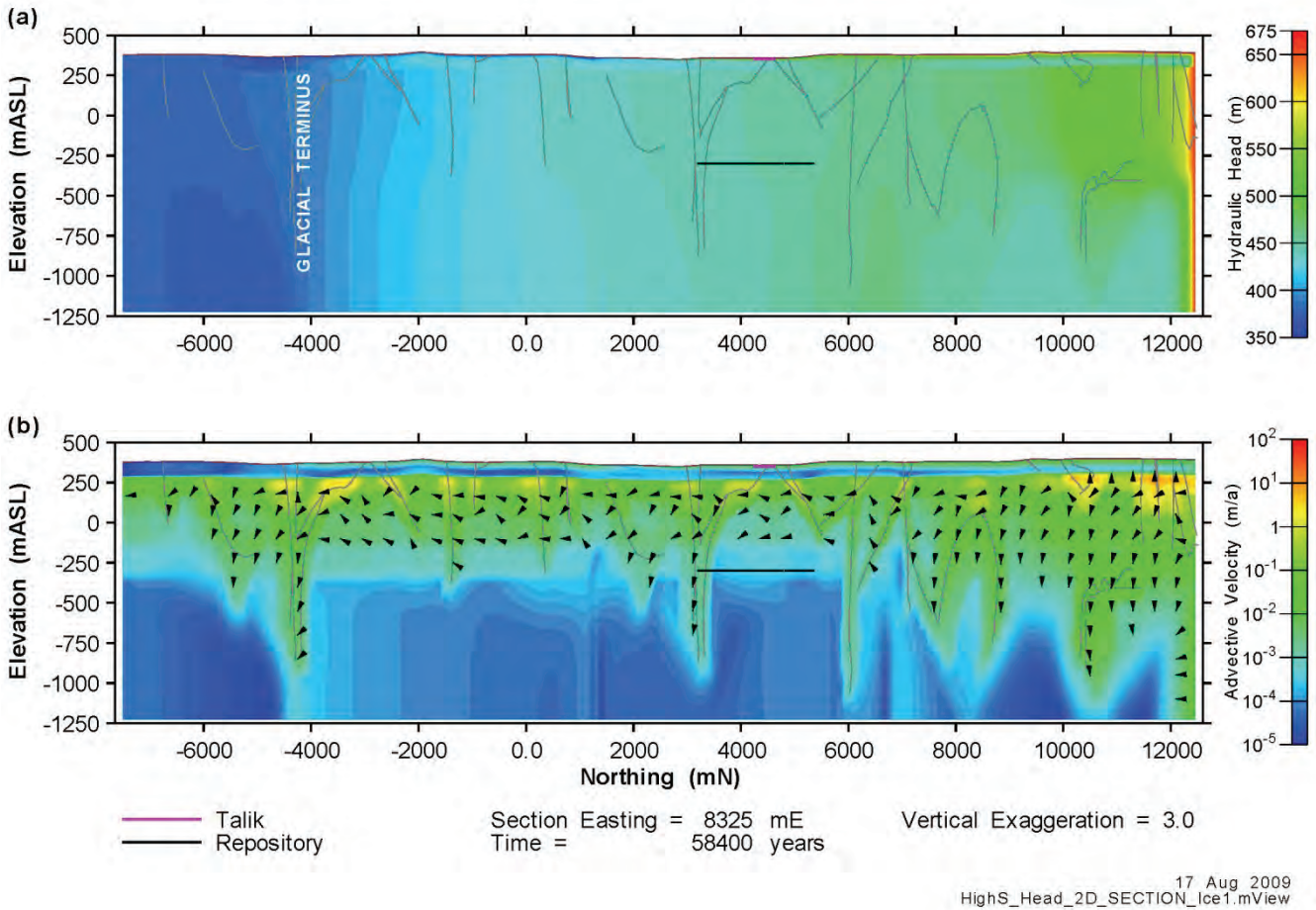


**Figure 5.11: GSC-HS flow model results at 58,400 years (beginning of stage 3 – ice advance, cold based glacier). The hydraulic head distribution is shown in (a), while the advective velocity distribution is shown in (b). Velocity vectors are only plotted where the velocity exceeds 1 mm/a.**

Comparing results at 68,550 years, the start of the second permafrost stage (GSC-HS in Figure 5.12, GSC-RC in Figure 5.6), the effect of the higher storage coefficients is reversed. In the GSC-HS model significantly higher hydraulic heads remain stored in the deep geosphere, driving much higher flow rates and flow velocities throughout the model and within the repository footprint itself. The thin layer of high hydraulic potential at the top of the model in Figure 5.12 is an artefact in the model caused by the instantaneous application of low permeability permafrost down to a depth of 250 m. This traps pressurized water in this upper zone. This is not realistic, but has a minimal effect on the flow field in the more permeable units below, as evidenced by the hydraulic head and velocity distributions. Flow from this permafrost zone is very low in comparison to the volumes of flow in the unfrozen formations below the permafrost.

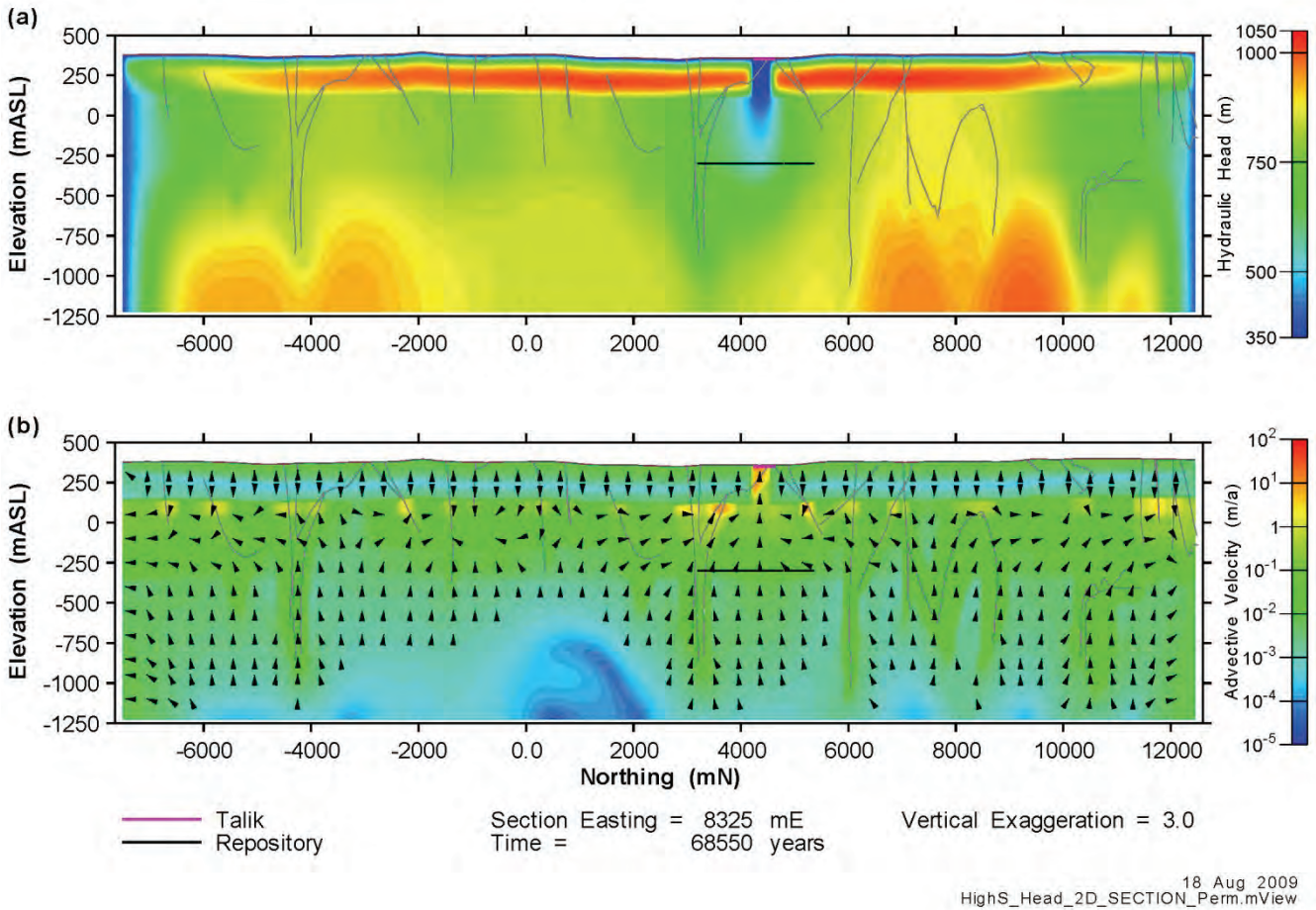
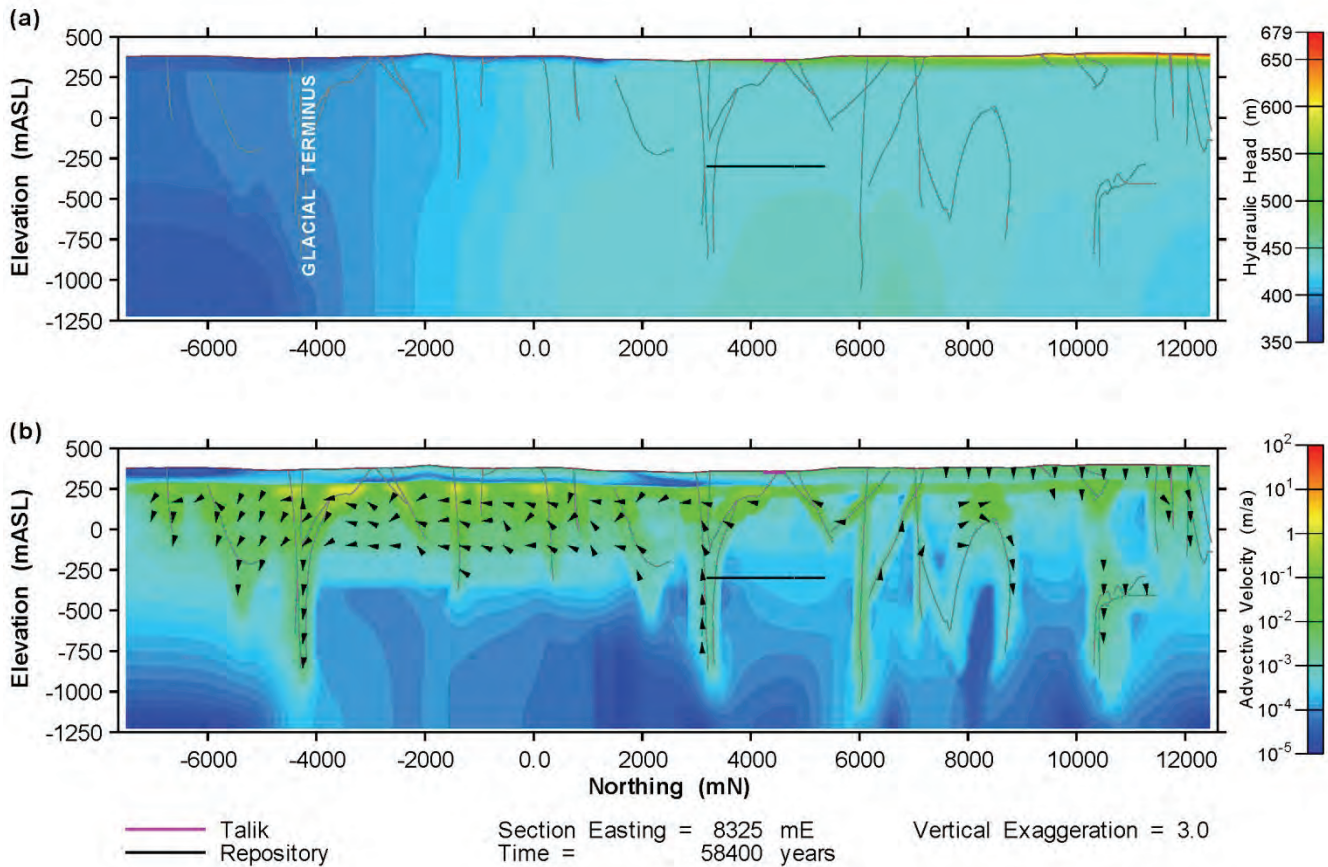


**Figure 5.12: GSC-HS flow model results at 68,550 years (start of stage 5 – permafrost). The hydraulic head distribution is shown in (a), while the advective velocity distribution is shown in (b). Velocity vectors are only plotted where the velocity exceeds 1 mm/a.**

### 5.2.1.3 No-Flow North-South Boundaries Case

The No-Flow North-South Boundaries Case (GSC-NF) differs from the reference case (GSC-RC) in that, in addition to the bottom, East, and West boundaries, the North and South boundaries are also no-flow Neumann boundaries. In the reference case these N-S boundaries are set as constant head, equal to the applied head at the surface (i.e. no vertical head gradient). Neither boundary condition perfectly describes the actual likely boundary conditions that would be present in the real physical system. Rather, they represent two extreme endpoints bounding the likely behaviour of the hydrogeological system. The choice of boundary condition has a sizeable impact on the flow behaviour of the model system. However, the effect on transport from the repository to the biosphere is rather limited (see section 5.3.3).

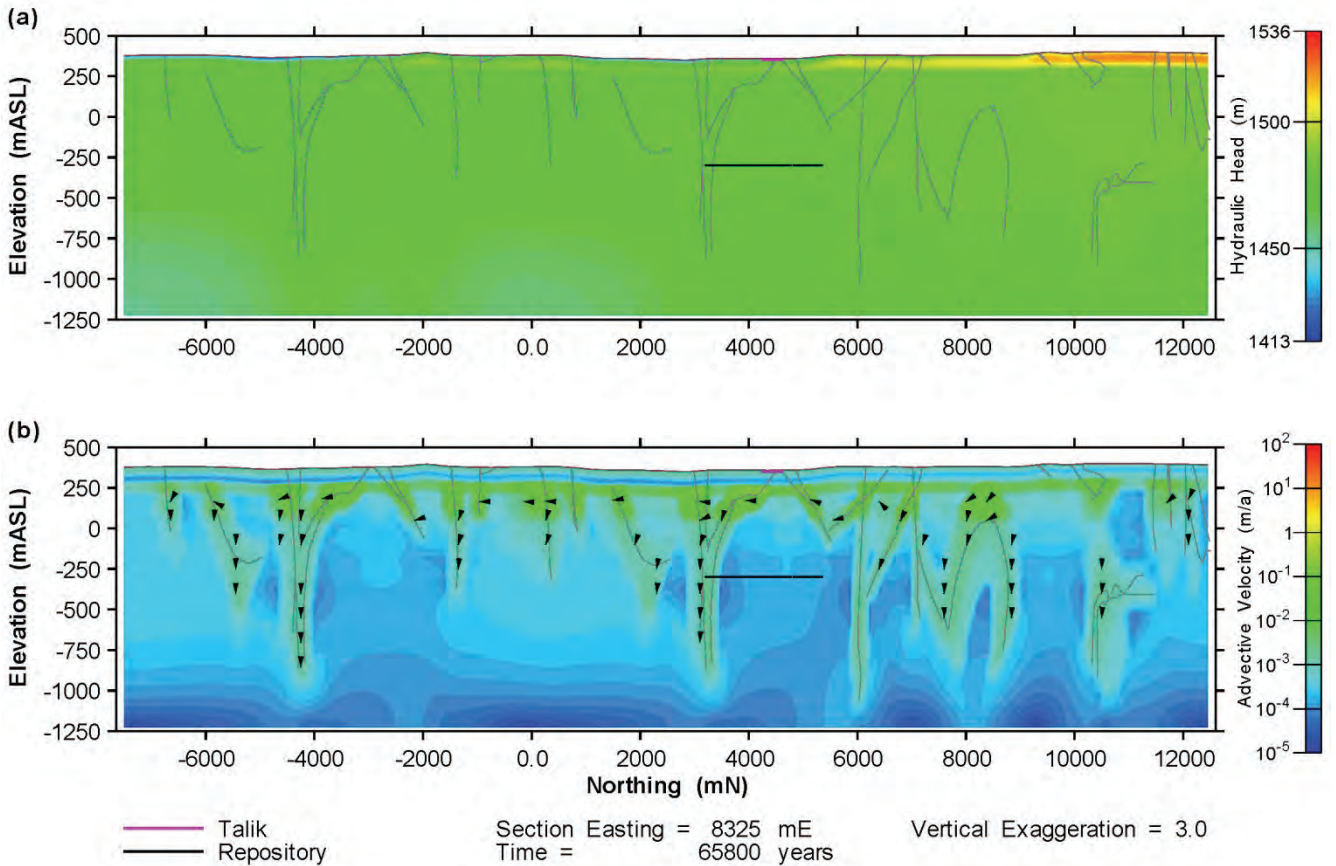
Figure 5.13 shows the GSC-NF flow field 300 years into the first glacial advance, and is directly comparable to Figure 5.4. The pressurization of the subsurface due to the hydraulic boundary condition on the northern boundary observed in Figure 5.4 is absent in Figure 5.13. There is a moderate pressurization of the subsurface due to hydromechanical coupling. This causes some higher horizontal flow velocities in the more permeable units, particularly in the general vicinity of the glacial terminus where the hydraulic gradient is the highest. Overall, the velocities are much lower than those observed for GSC-RC. The change in boundary condition causes a change in the flow system, particularly in the upper, more permeable layers.



29 Sep 2009  
NoFlow\_Head\_2D\_SECTION\_Ice1.mView

**Figure 5.13: GSC-NF flow model results at 58,400 years (beginning of stage 3 – ice advance, cold based glacier). The hydraulic head distribution is shown in (a), while the advective velocity distribution is shown in (b). Velocity vectors are only plotted where the velocity exceeds 1 mm/a.**

Figure 5.14 shows the GSC-NF model results during cold-based glacial retreat, and may be compared directly with Figure 5.5. The average head in the GSC-NF model is of a similar magnitude to the GSC-RC model, but the variation in the hydraulic head below the permafrost is much lower, and the flow field is virtually stagnant. This is not surprising, as no flow boundaries on the sides and bottom, and the frozen upper surface mean that the hydraulic system is essentially a closed box. It is not unlikely that in the interior of a continental glacier under which permafrost exists such a stagnant system could exist. However, the real flow system under a retreating glacier is likely to be somewhere between the GSC-RC and GSC-NF models, with some horizontal flow gradients in the upper system, greater than in model GSC-NF, but less than GSC-RC.



17 Aug 2009  
NoFlow\_Head\_2D\_SECTION\_Ice1-R.mView

**Figure 5.14: GSC-NF flow model results at 65,800 years (midpoint of stage 4 – ice retreat, cold based glacier). The hydraulic head distribution is shown in (a), while the advective velocity distribution is shown in (b). Velocity vectors are only plotted where the velocity exceeds 1 mm/a.**

During the ice advance over permafrost, the no-flow northern and southern boundaries had the effect of reducing the flow velocities in the repository, and thereby reducing the rate of advective transport from the repository. The exact opposite occurs during the second permafrost stage. Figure 5.15 shows a cross-section of the flow field during the same intermediate transition period approximately 2000 years after the start of the second permafrost sequence as Figure 5.6. In the GSC-RC model (Figure 5.6) there are 4 hydraulic outlets for the glacially induced heads, the two taliks and the North and South boundaries. In the GSC-NF model (Figure 5.15) the stored pressures cannot escape at the North and South boundaries, causing higher heads and hydraulic gradients to persist for a longer time. During this permafrost stage the two taliks also form a hydraulic dipole system, with the southern talik, which is at a higher elevation, forming the source, while the smaller northern talik acts as the only sink in the model.

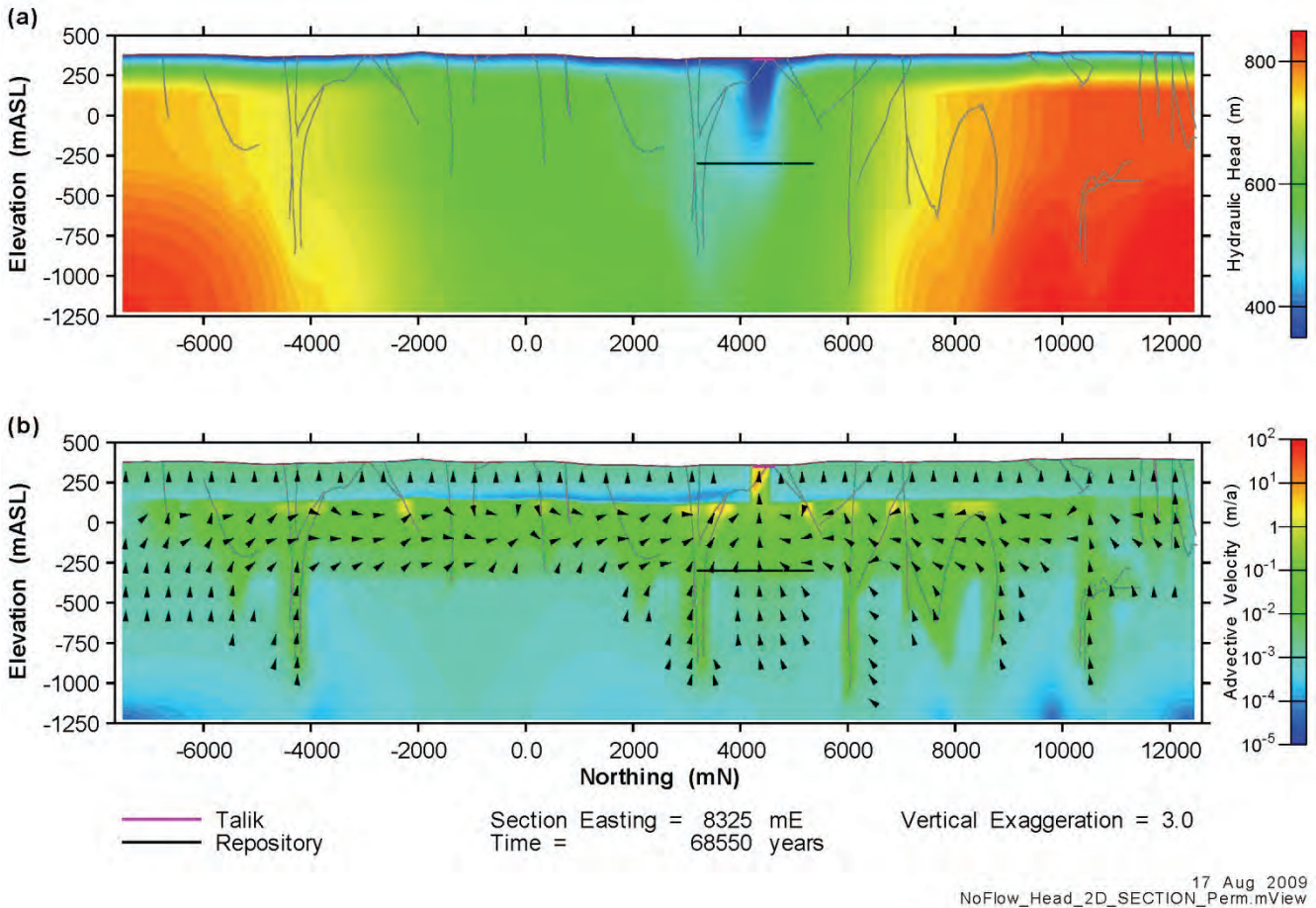


**Figure 5.15: GSC-NF flow model results at 68,550 years (start of stage 5 – permafrost). The hydraulic head distribution is shown in (a), while the advective velocity distribution is shown in (b). Velocity vectors are only plotted where the velocity exceeds 1 mm/a.**

#### 5.2.1.4 Talik under Glacier Case

The Talik under Glacier Case (GSC-TK) is identical to GSC-RC, except that taliks in the permafrost layer remain open during the cold based glacier stages (stage 3, 4, 6, and 9 in Table 2.1). These taliks are assumed to be fully pressurised by the overlying ice and water. Figure 5.16 shows a cross section of the flow field at the 58,400 years, the beginning of the first glacial advance. Comparing it to Figure 5.4, it is evident that this small opening in the talik has had a minimal impact on both the hydraulic head and velocity distributions, except very near the talik. However, as the repository was located directly below the talik, it did impact the flow field in the repository, causing increased vertical flow rates. In Figure 5.16 the flow direction is downward, and velocity is roughly an order of magnitude higher than seen in the GSC-RC model (Figure 5.4). The same occurred during the cold-based glacial retreat (stage 4), except that the flow direction at the repository during the retreat was vertically upward.

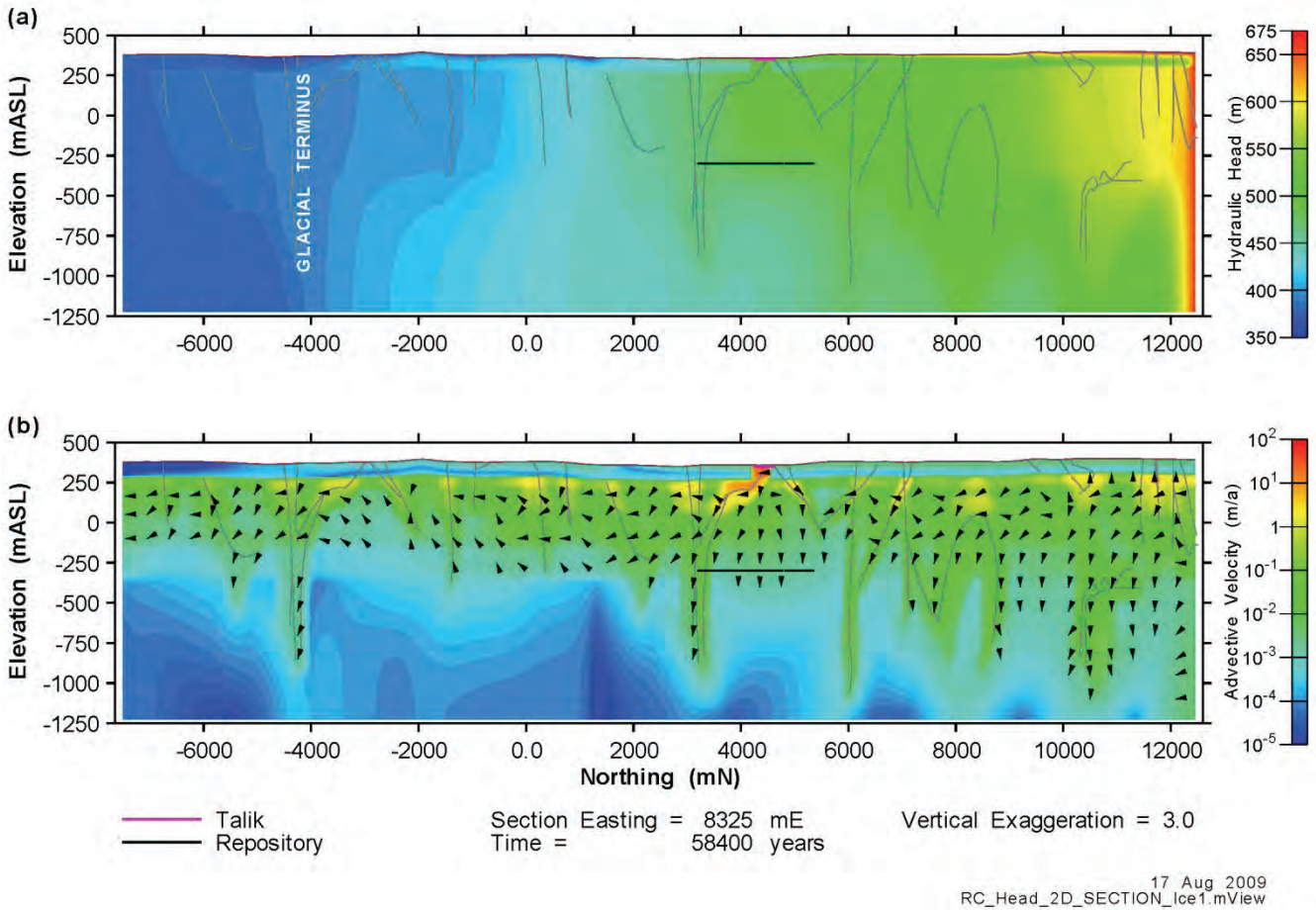
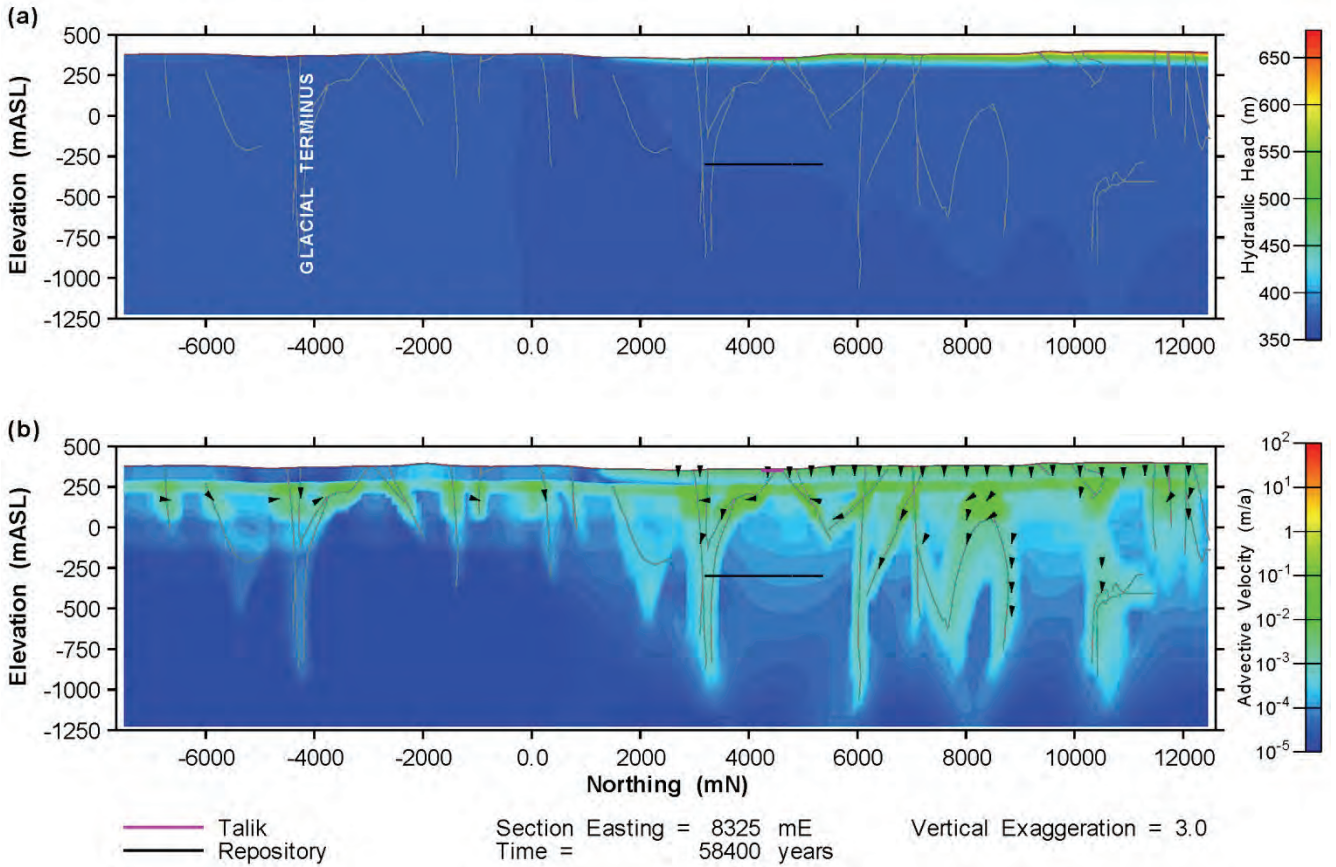


**Figure 5.16: GSC-TK flow model results at 58,400 years (beginning of stage 3 – ice advance, cold based glacier). The hydraulic head distribution is shown in (a), while the advective velocity distribution is shown in (b). Velocity vectors are only plotted where the velocity exceeds 1 mm/a.**

### 5.2.2 Effect of Hydromechanical Coupling

The inclusion of hydromechanical coupling in modelling sub-glacial hydrogeology is an important feature of this model. To understand how hydromechanical coupling affects the flow system, the first (cold-based) glacial stage of the GSC-NF model was run with the hydromechanical coupling module deactivated. This case should show the most extreme contrast between the models with and without hydromechanical coupling, as the model is closed on all sides. The base and sides of the model have no-flow boundary conditions, while the top of the model is covered with a continuous 100 m thick permafrost layer with hydraulic conductivity of  $10^{-13}$  m/s. Figure 5.17 shows the head and velocity contours at the beginning of the glacial advance, when the model domain is not yet entirely covered by ice. It is evident in the figure that a small amount of water passes through the permafrost layer, due to the extremely high hydraulic gradient. However, the head and velocity increase in the deeper geosphere is very small. Comparing these results to Figure 5.13 (GSC-NF results including hydromechanical coupling) shows that hydromechanical coupling significantly increases hydraulic head and horizontal and vertical velocity in the subsurface. During a warm based glacial advance, the effect of hydromechanical coupling on head and velocity is reduced.



17 Aug :  
NoFlow-NoHM\_Head\_2D\_SECTION\_Ice1.m

**Figure 5.17: GSC-NF with no hydromechanical coupling. Results at 58,400 years (beginning of stage 3 – ice advance, cold based glacier). The hydraulic head distribution is shown in (a), while the advective velocity distribution is shown in (b). Velocity vectors are only plotted where the velocity exceeds 1 mm/a.**

Figure 5.18 shows the advective flow velocity magnitude of model GSC-NF divided by the velocity magnitude of GSC-NF without hydromechanical coupling at three times. Early in the glacial advance the difference is striking, particularly in the vicinity of the glacial terminus where velocities are 100 to 1000 times higher in the model with hydromechanical coupling (Figure 5.18 (a)). However, this is a very transient effect. As the glacial advance proceeds the difference between the models is greatly reduced, as shown in Figure 5.18 (b) and Figure 5.18 (c). Figure 5.19 shows the differences between the hydraulic heads for the cases with and without hydromechanical coupling. In contrast to the velocity, the hydraulic head difference increases during the first few thousand years of the glacial advance, especially in the deeper parts of the rock mass increases. It is evident that the large velocity contrast at 58,400 years is caused by the large horizontal gradients that occur when the glacier partially covers the surface. These are not present when hydromechanical coupling is inactive.

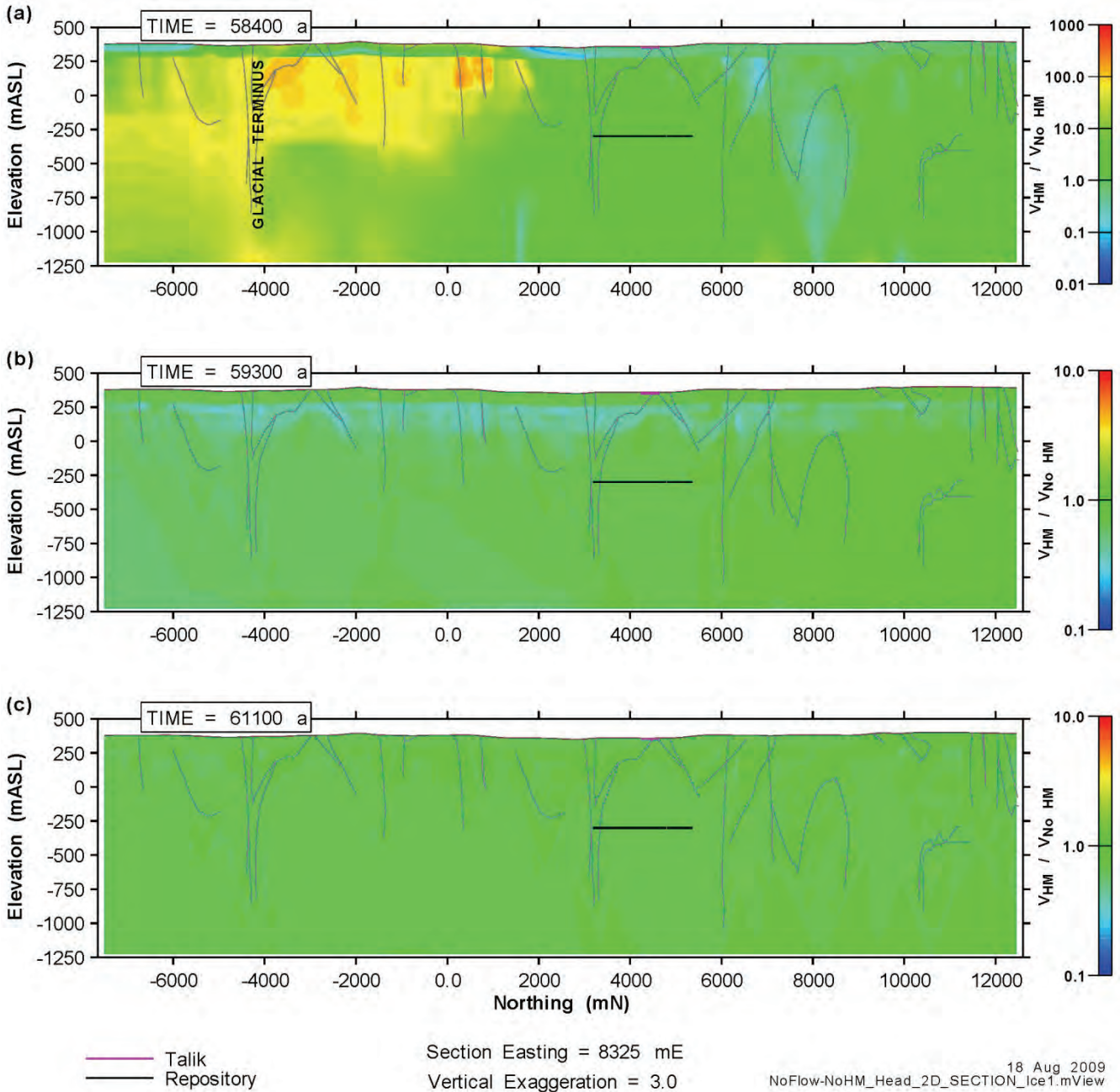


**Figure 5.18: Ratio of the advective flow velocity magnitude for GSC-NF with and without hydromechanical coupling. Results are shown at (a) 58,400 years (300 years into cold based glacial advance), (b) 59,300 years (1200 into glacial advance), and (c) 61,100 years (3000 years into glacial advance)**

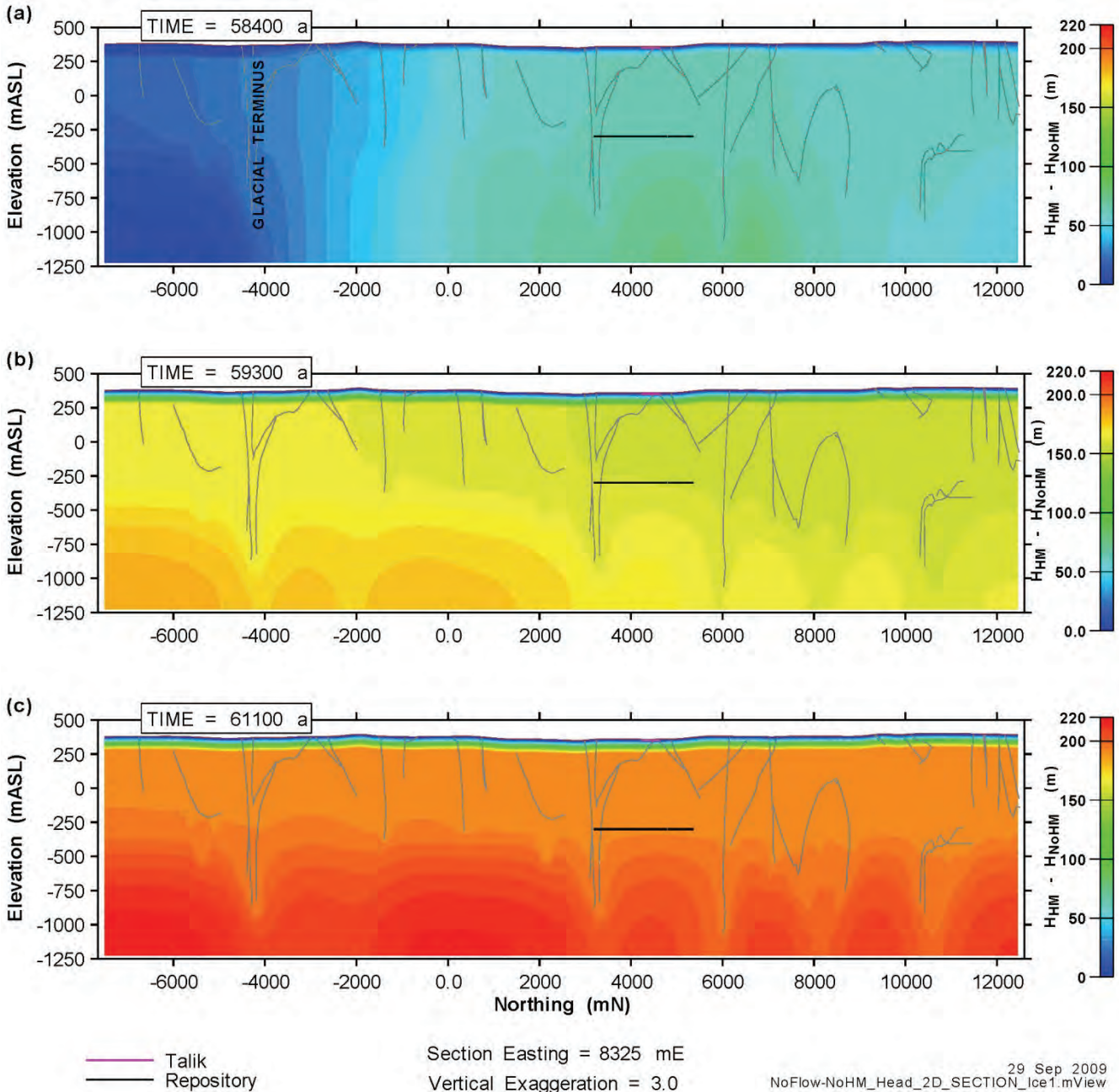


**Figure 5.19: Differences between the hydraulic heads for GSC-NF with and without hydromechanical coupling. Results are shown at (a) 58,400 years (300 years into cold based glacial advance), (b) 59,300 years (1200 into glacial advance), and (c) 61,100 years (3000 years into glacial advance)**

### 5.2.3 Repository Velocity Calculations

The figures in the preceding section provide a snapshot of the flow field in the repository, at one time and across one vertical slice through the repository. These plots do not provide a continuous description of the flow field. Figure 5.20 shows how the average vertical component of the advective velocity within the repository footprint changes with time and varying boundary conditions. The plot

clarifies the impact of different hydraulic boundary conditions on the flow field in the repository. Advancing glaciers, both cold- and warm-based, lead to relatively large negative or downward vertical velocities. Retreating glaciers have the reverse effect, and this effect persists into the following permafrost stages, as the rapid retreat does not allow all the pressure stored during the glacial advance to dissipate.

Integrating the velocities shown in Figure 5.20 gives the average vertical travel distance within the repository footprint during one glacial cycle. The total positive (upward) movement only slightly exceeds the sum of the negative (downward) movement (see Figure 5.21). As a result, the cumulative vertical distance travelled is only about one meter after a 121,000 year long glacial sequence. This means that, although the glacial cycling leads to increases in velocity and changes in flow direction, within the repository the hydraulic impacts of glacial advances and retreats effectively cancel each other out. This is also evident in the  $^{129}\text{I}$  mass flow curves presented in section 5.3.3, where the cumulative  $^{129}\text{I}$  mass flow of the reference case only moderately exceeds the cumulative flow for the Constant Climate case (GSC-CC). Given the much larger flow velocities in the transient Reference Case, larger mass flows in the Reference Case model might have been expected, but were not actually observed in the model results.

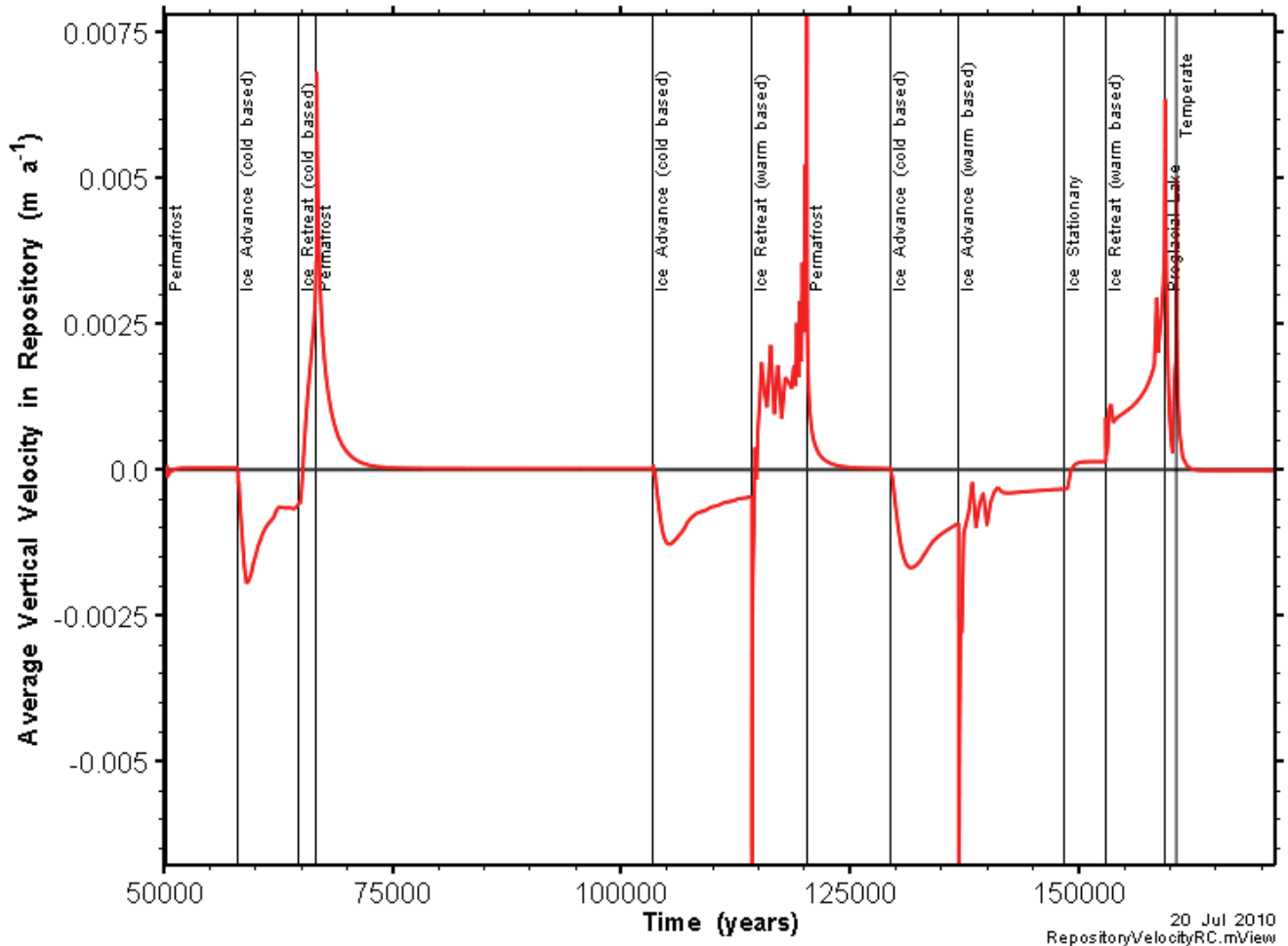


**Figure 5.20: GSC-RC flow model, average vertical component of advective velocity within the repository footprint. Positive velocities are upward, negative velocities are downward.**

A caveat needs to be added to the preceding analysis. Although Figure 5.21 seems to imply that the cumulative advective travel distance at the end of one glacial cycle will be on the order of one meter, particle tracking simulations (see section 5.2.4) and transport simulations (see section 5.2.4) show that material does escape and travel further from the repository. Although average velocities are very low within the repository itself, there is significant variation between the lowest and highest velocities within the repository, and at certain locations particles (i.e., contaminants) need only travel a short distance from the repository before they enter a fracture zone, where velocities are higher. The particle tracking and transport simulations also indicate that transport near the repository is largely diffusion dominated, especially during periods when velocities are relatively low (see Section 5.4).

Figure 5.20 also shows some evidence of numerical instability in the flow solution, particularly during the second (warm-based) ice retreat between 235,500 and 241,500 years. This numerical instability is brought about by a very sudden alteration of the flow field and boundary conditions, caused by the instantaneous removal of the permafrost layer and the shift from an advancing to a retreating glacier. This numerical instability reduces the accuracy of the model to a limited degree during this stage of the glacial cycle. However, the oscillations remain relatively small and decay as the glacial retreat proceeds and the results are still sufficiently accurate for the purposes of this report.

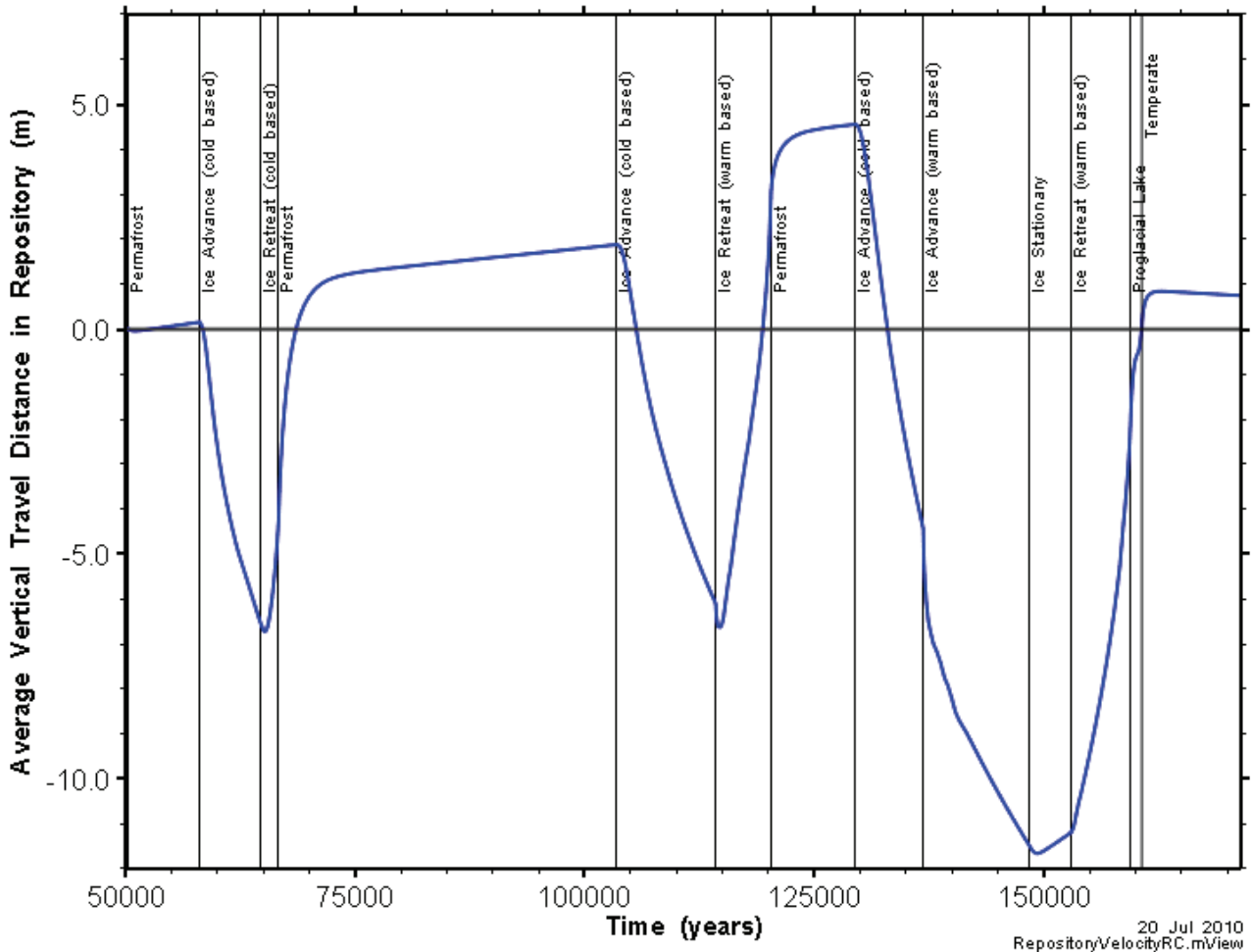
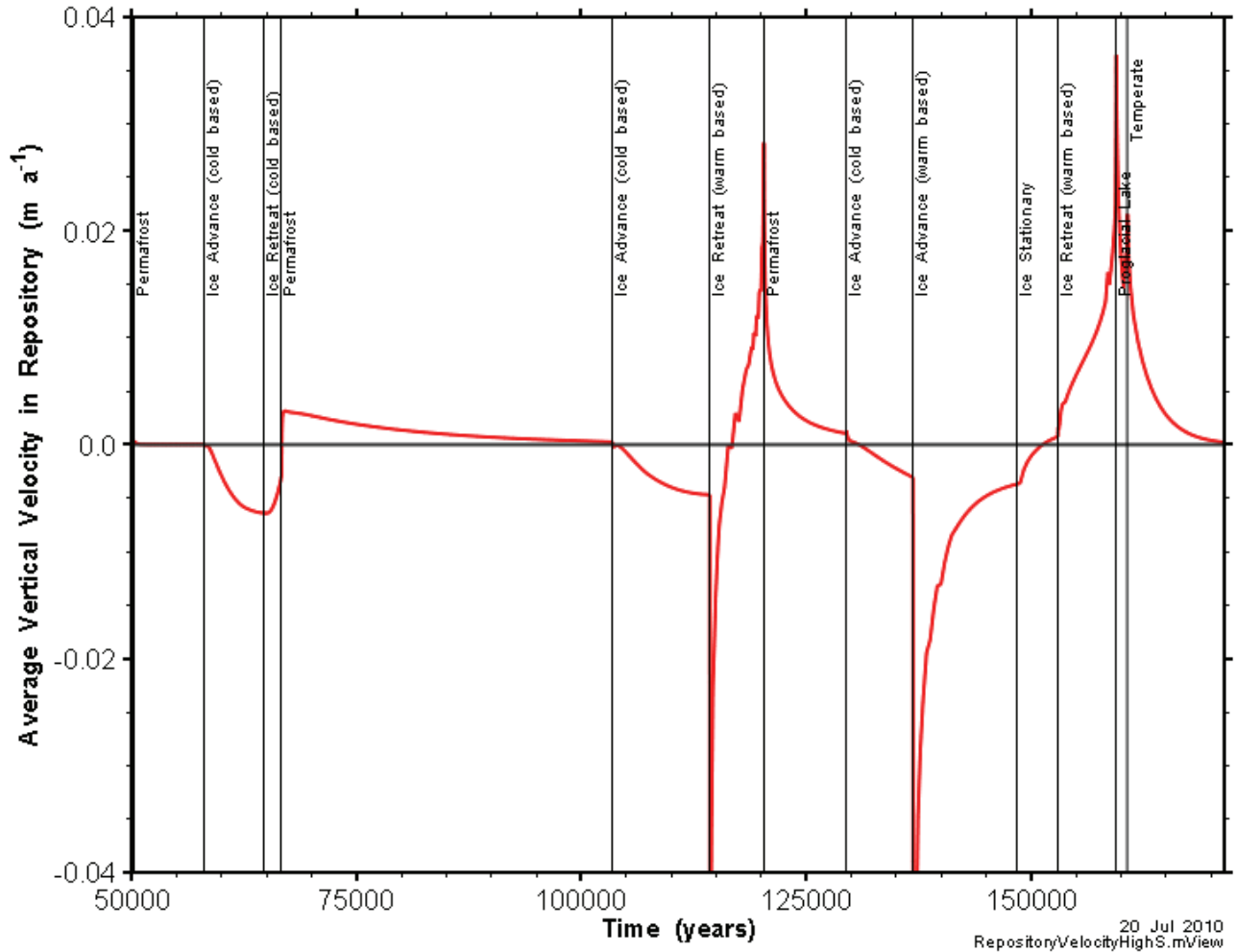


Figure 5.21: GSC-RC flow model, cumulative average vertical advective flow distance within the repository footprint. Calculated by integrating Figure 5.20 over time.

The calculation case with a flow field that differs most from the Reference Case (GSC-RC) is the high storage coefficient case (GSC-HS). The higher storage coefficients cause glacially induced heads to persist for much longer, leading to increased flow and velocity for a longer time. The effect on the repository vertical advective velocity is shown in Figure 5.22. Note that the Y-axis range is much larger than in Figure 5.20.



**Figure 5.22: GSC-HS flow model, average vertical component of advective velocity within the repository footprint. Positive velocities are upward, negative velocities are downward.**

If the curve in Figure 5.22 is integrated over time, we obtain the curve shown in Figure 5.23. As was seen in Figure 5.21, although the advective flow distance can be significant during a given stage of the glaciation scenario, the positive and negative vertical flows tend to cancel one another. For the GSC-HS case this leads to a net travel distance of only -14 m at the end of the glacial cycle.

As before, this analysis must be qualified by the observation that the transport simulations (see section 5.3.1) show that material does escape and travel further from the repository, upward as well as downward. Again, although average velocities are very low within the repository itself, there is significant variation between the lowest and highest velocities within the repository, and at certain locations particles (i.e., contaminants) must only travel a short distance from the repository before they enter a fracture zone, where velocities are higher.

However, the analysis of the vertical velocity and total travel distance within the repository footprint does clearly show how the changing boundary conditions during glacial advances and retreats affect the repository flow field. The analysis suggests that because the head added during a glacial advance and subsequently removed during a glacial retreat are equal and opposite, the periods of positive and negative vertical velocity tend to cancel one another, making the net effect of glacial advances and retreats rather small, especially when one considers the sizable imposed hydraulic heads during glacial advances. This is confirmed by comparison of the transport and mass flow results of the GSC-CC and GSC-RC models.

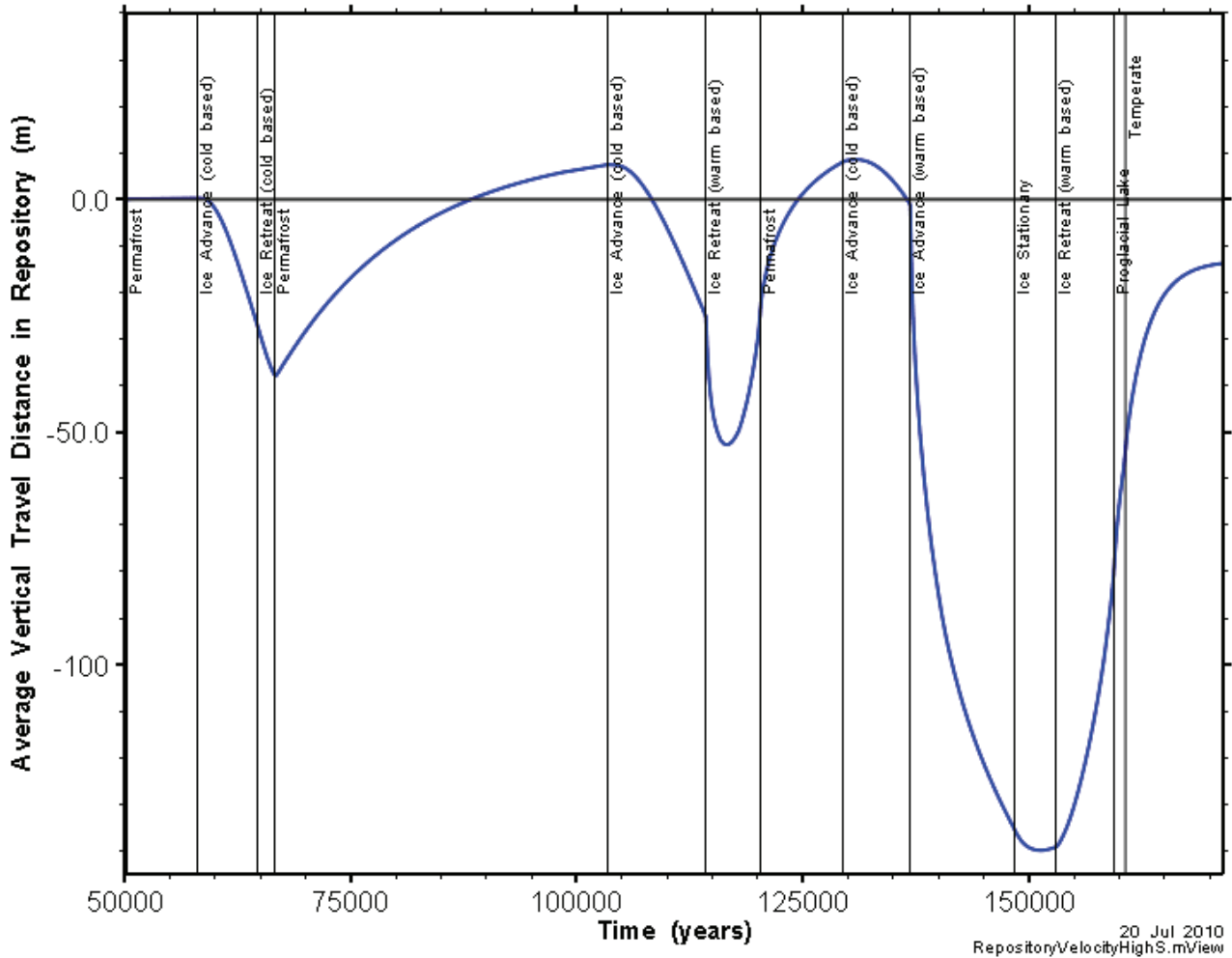


Figure 5.23: GSC-RC flow model, cumulative average vertical advective flow distance within the repository footprint. Calculated by integrating Figure 5.20 over time.

#### 5.2.4 Particle Tracking Results

In addition to the repository velocity, another metric has been developed to qualitatively assess effects on transport at the repository horizon of the various flow systems present throughout the glacial cycle. Velocities at selected times were used to generate particle tracks for particles originating at repository nodes. The particle tracks assumed that the selected velocity field represented steady-state flow. The tracks were then processed to calculate the distance traveled by each particle in a 100 year period after release. Calculated distances were further processed as cumulative distribution functions

(CDF) to present the range of particle distances over the entire repository. This metric allows for a simple comparison of the advective velocity fields, and is a useful complement to the average repository velocity presented in the preceding section. However, it is important to note that although the curves do provide the travel distance, they do not show the travel direction. Results of the simulations at selected times are presented below in Figure 5.24.

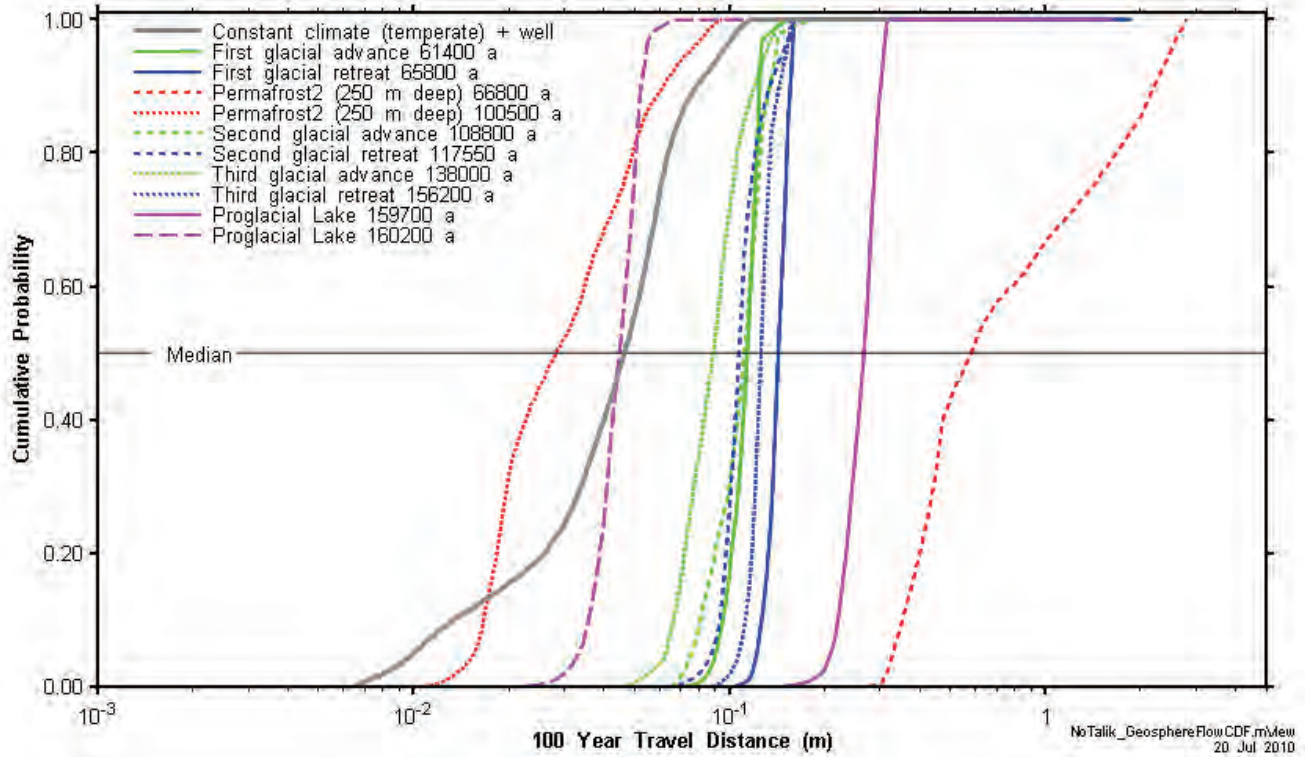


Figure 5.24: 100 year particle travel CDFs for selected flow times, GSC-RC model.

Differences in the flow systems are readily apparent with median travel distances varying over roughly 1.5 orders of magnitude. There can be a very large variation in behaviour within one stage. For instance, the two dotted red lines in Figure 5.24 show the 100 year travel distance near the start and towards the end of the second permafrost cycle. At the start of the cycle, stored heads from the preceding glaciation drive relatively high velocities in the repository footprint, but eventually the high heads dissipate and the system reaches a steady state at much lower velocities.

The particle track results are also useful in examining variations in discharge locations. The location of the defective container was selected in previous studies from the start location of the particle with the fastest travel path to a discharge location, based on the steady-state temperate flow field. Figure 5.25 is a map of travel time from the particle release location to discharge for the GSC steady-state model based on the temperate geosphere. The fastest particle, located almost directly beneath the lake, takes approximately 610,000 years to travel from the repository to discharge in the pumping well adjacent to the lake. This differs from the peak concentration time shown in Figure 5.1 (385 ka). If the transport from DC1 source location to the surface was advective, the travel time of the fastest particle and the peak of the  $^{129}\text{I}$  mass flux across the northern talik should be approximately coincident. This suggests that diffusion and/or dispersion (which are not included in the particle track calculations) are important transport mechanisms.

The difference between the fastest particle and peak arrival time is thus primarily due to very low velocities in the intact rock adjacent to the repository. Figure 5.26 shows how the elevation of the fastest particle changes with time, and whether the particle is travelling in intact rock or a fracture zone. For roughly 600,000 years the particle travels very slowly in the intact rock, after which the particle reaches a fracture zone and traverses the remaining distance to the pumping well relatively rapidly. In contrast to the particle tracking solution, in the transport model, contaminants from the source zone reach the fracture zone much more rapidly due to diffusion/dispersion processes. Thus, for the steady state temperate GSC-CC model, transport from the repository is diffusion/dispersion dominated. During some short stages of the GSC-RC model, advective transport may become important even in the vicinity of the repository due to much higher velocities (see Figure 5.20).

Finally, particle tracking simulations also provide an alternative means of visualising the local flow field near the repository. Figure 5.27 shows a three-dimensional image of the particle tracks for the steady-state temperate flow system.

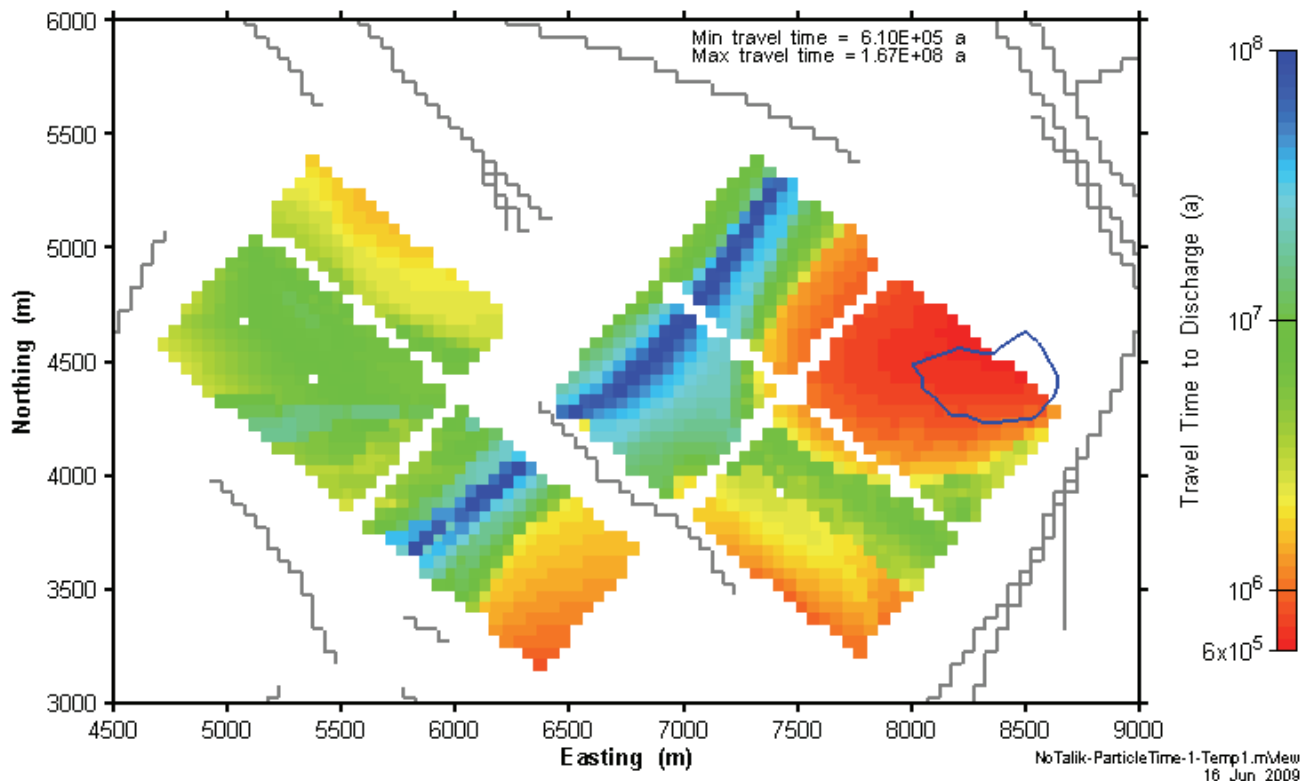


Figure 5.25: Particle travel time to discharge for steady-state temperate flow system.

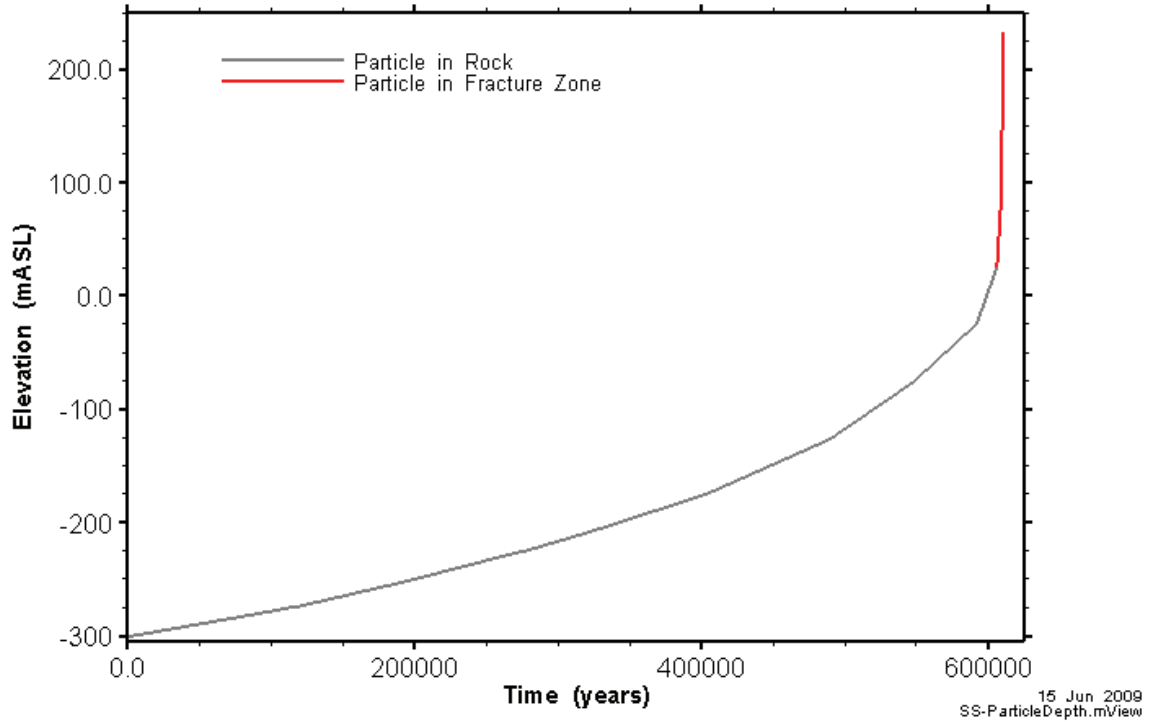


Figure 5.26: Particle elevation with time of fastest travelling particle.

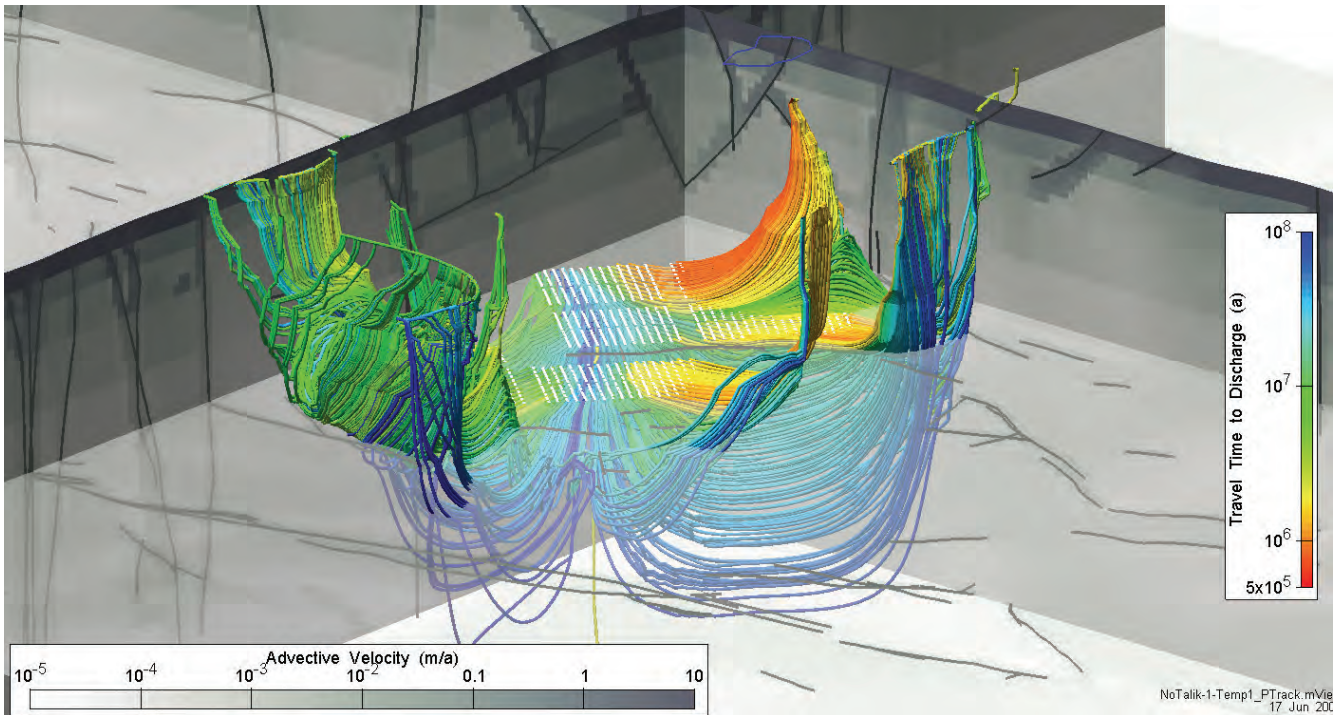
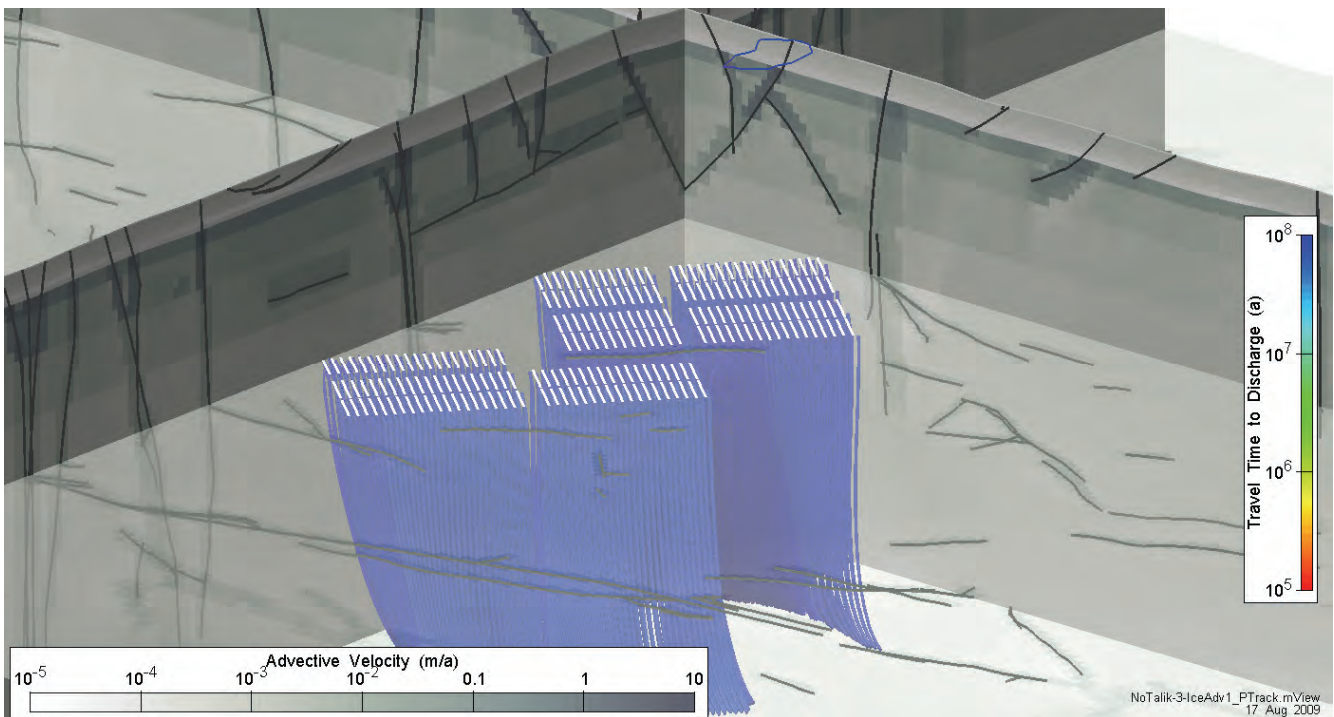


Figure 5.27: 3D visualisation of particle tracks for steady-state temperate flow system.

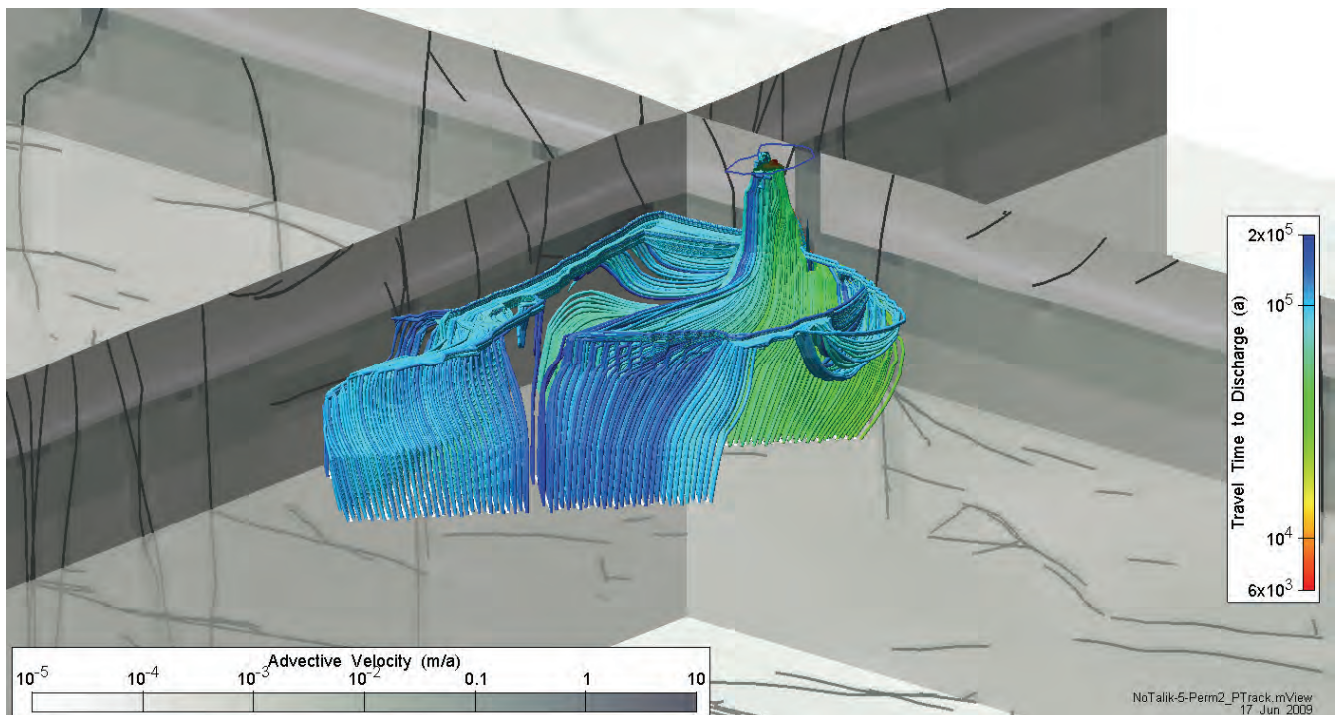
Particle tracks can also provide a reasonable three-dimensional snapshot of the local flow system during any particular stage of the glacial cycle. The pictures on the following pages show particle tracks generated by extracting the velocity field at a particular time, and running steady-state particle tracking on that flow field. As a result, the particle tracks and the travel times are not in fact true representations of how the particles would move in the transient flow field, but are only used to illuminate flow paths. Typically, the travel time to discharge of even the fastest particles far exceeds the duration of a given configuration of the flow system, meaning that no particle leaving the repository would actually follow one of the depicted flow paths. However, the particle tracks do offer an alternative method of visualizing the three-dimensional flow field, and the figures on the following pages provide an excellent illustration of the variability of the flow system during the Glaciation Scenario.

Figure 5.28 shows steady state particle tracks during the first glacial advance, which is cold-based. At and below the elevation of the repository the flow direction is vertically downward. Velocities below the repository are very low, and it requires well over one million years for particles to travel downward and reach the lower boundary, at which point they are deactivated by the MODPATH particle tracking software.



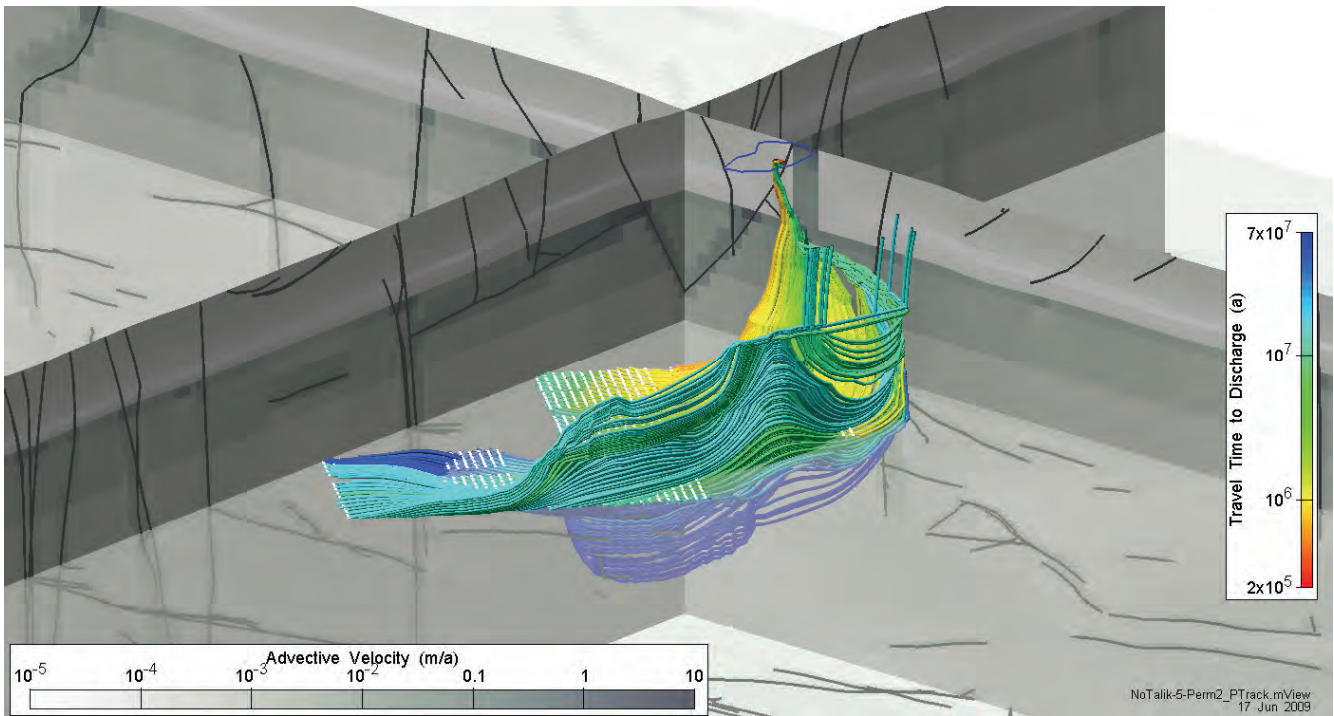
**Figure 5.28: 3D visualisation of particle tracks at 61,400 years, flow system midway through the first glacial advance (cold based).**

Figure 5.29 shows particle tracks for the flow system extent at the beginning of the second permafrost period. High heads stored in the system from the preceding glaciation, combined with the fact that the northern talik is the primary hydraulic outlet of the system, draw particles vertically upwards through the low permeability intact rock above the repository. When particles reach the more permeable, shallower fracture system, all the paths converge towards northern talik. The high head gradients in this system mean that a few of the fastest particles reach the talik in as little as 6000 years. However, this is due to the rather extreme gradients and velocities at the start of the permafrost period, and these do not persist for 6000 years. Velocities are reduced to half of the initial velocity within roughly 300 years, and to a quarter of the initial velocity within 900 years, and have reached a much lower steady-state velocity field (see next paragraph) within approximately 5000 years. In addition, it is unknown whether the sudden application of a few small openings (taliks) in the permafrost layer post-glaciation provides a good representation of reality. There are no readily available data in the scientific literature describing the evolution of taliks in a permafrost environment.



**Figure 5.29: 3D visualisation of particle tracks at 66,800 years, flow system at the start of the second permafrost period.**

Figure 5.30 shows the particle tracks near the end of the second permafrost period. The flow system has attained a steady-state, with complete dissipation of all glacially induced heads. While the northern talik remains the primary outlet for the particles, the paths travelled by the particles are significantly altered, and the fastest particle now requires just over 250,000 years to reach the surface.

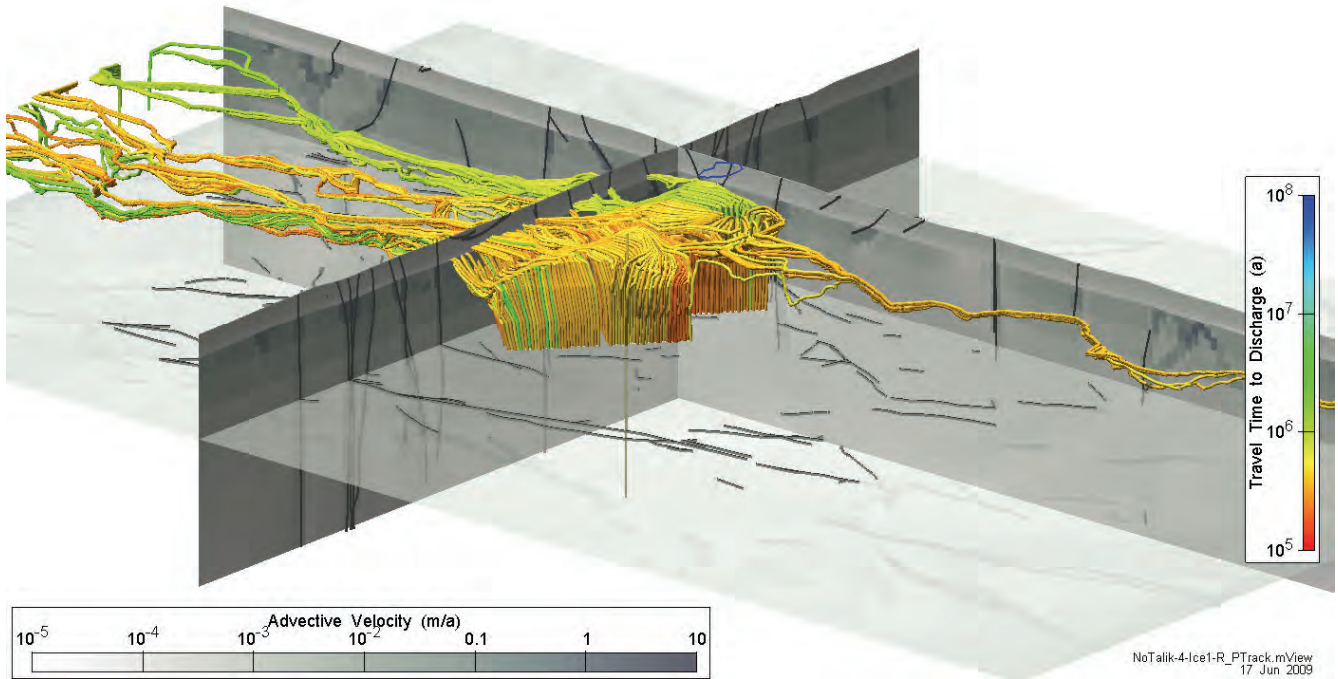


**Figure 5.30: 3D visualisation of particle tracks at 100,500 years, flow system near the end of the second permafrost period.**

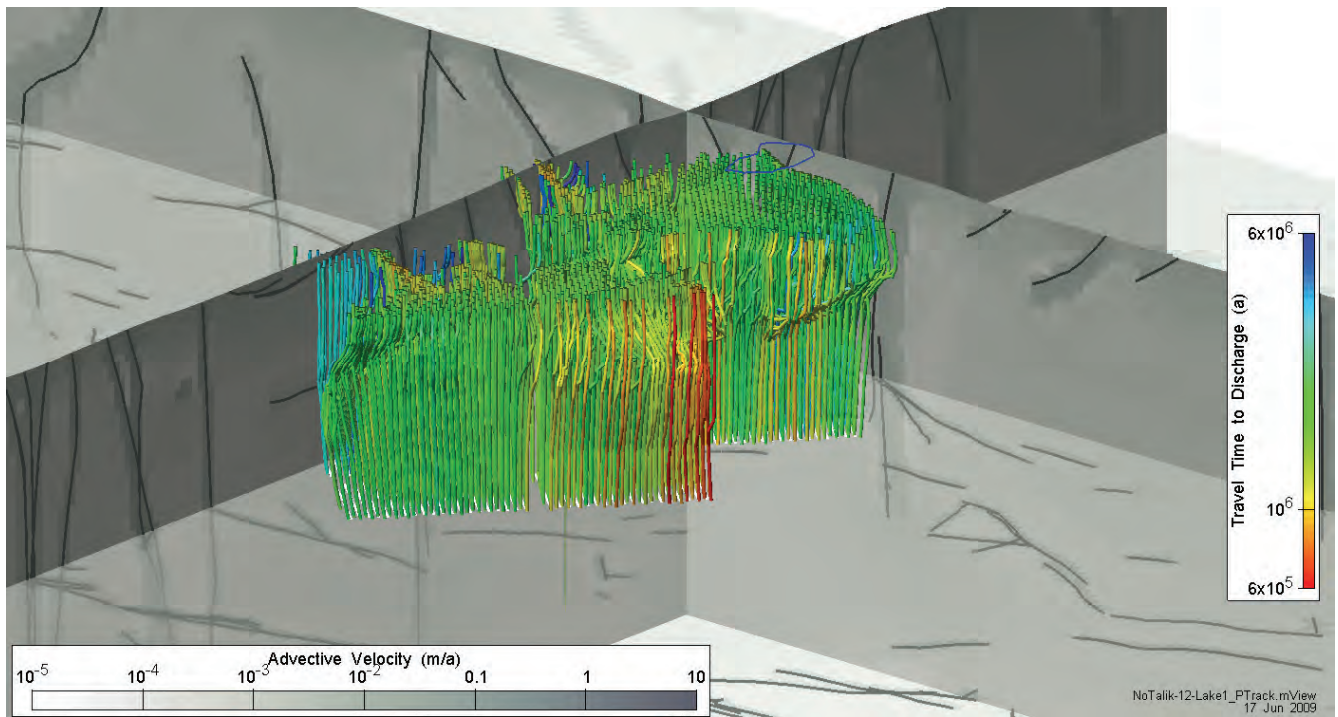
Figure 5.31 shows particle tracks during the first glacial retreat, which is cold based. The reduced hydraulic heads at the surface and at the northern and southern boundaries cause the particles to travel vertically upwards through the intact rock above the repository, after which they travel towards the two hydraulic outlets, the northern and southern boundaries. These particle tracks are the result of the flow system shown in Figure 5.5. This result may not be very realistic, and for this particular period, no-flow boundaries around the entire model domain might provide more realistic results.

Figure 5.32 shows particle tracks during the proglacial lake period. At greater depths, the tracks look similar to those in Figure 5.31, but the lack of an intervening permafrost layer means that the particles continue to flow vertically and exit the model at the surface. Travel times to the surface are rather long, with the fastest particle requiring 600,000 years to reach the surface. However, these velocities are only representative of this snapshot of the flow system. Travel times at the start and the end of the proglacial lake period are shorter.

For the Reference Case, the defective containers were located at the repository location having the shortest groundwater travel time to the surface, as identified with the steady state temperate groundwater flow field. However, the groundwater flow system is transient during a glacial cycle and conditions can change quickly as illustrated in the figures above. It is possible that particles released from alternate source locations may travel to discharge faster than indicated by the steady-state temperate flow model.



**Figure 5.31: 3D visualisation of particle tracks at 65,800 years, flow system midway through the first glacial retreat (cold based).**



**Figure 5.32: 3D visualisation of particle tracks at 160,200 years, flow system midway through the proglacial lake period.**

### 5.3 Multiple Glacial Cycle Transport Results

Transport model results show how the transient nature of the flow system response over many glacial cycles affects the fate of radionuclides from the repository. The figures in this section present plan sections and vertical cross-sections through the radionuclide plume in the vicinity of the repository and the radionuclide source locations. Plan sections are shown at elevation 0.0 mASL (approximately 350 mBGS). For source DC1, cross sections at easting 8325 mE, through the plume on a North-South transect (the direction of glacial advance), are shown. For source DC3, cross sections at northing 4825 mN, through the plume on an East-West transect, are shown. The locations of the cross-sections are shown in Figure 5.33. The figures on the following pages present concentration contours on a logarithmic scale that is consistent for all figures. During the course of a given glacial cycle the shape and location of the plume changes constantly. The six "snapshots" of the plume provide a representative picture of plume evolution during the course of the entire assessment period.

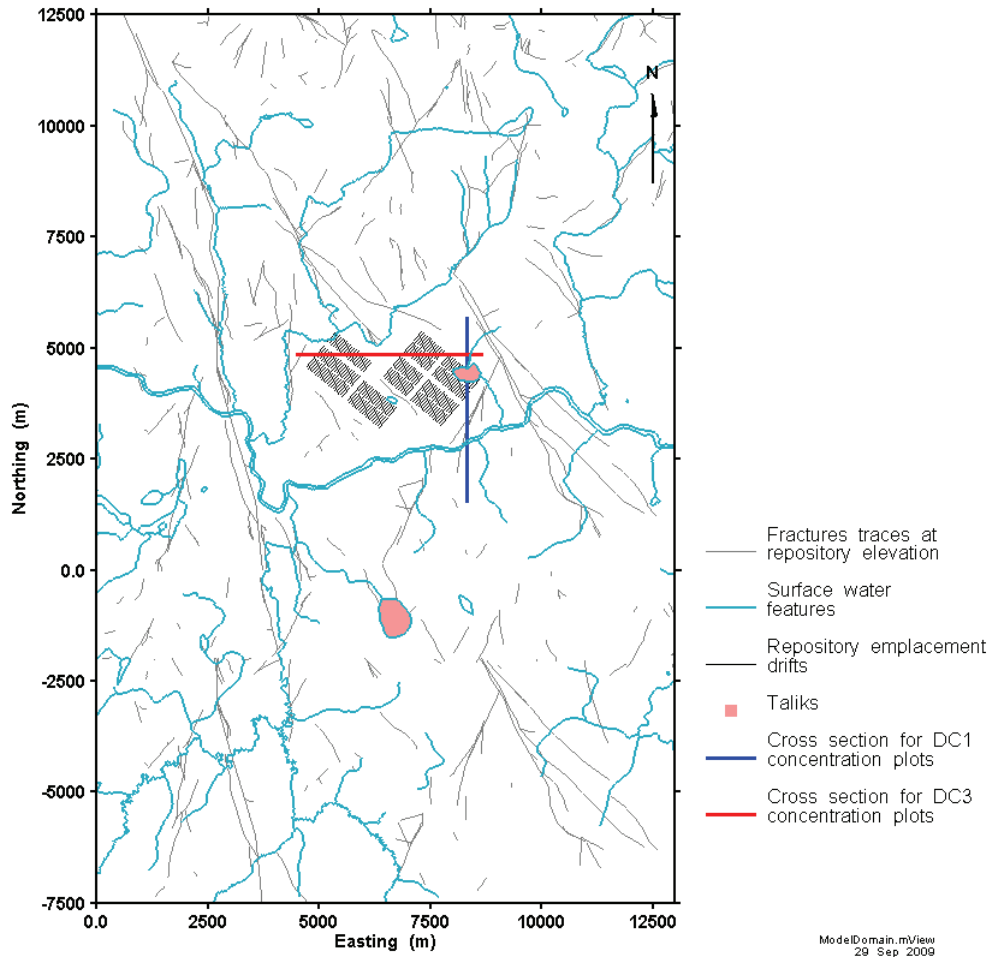
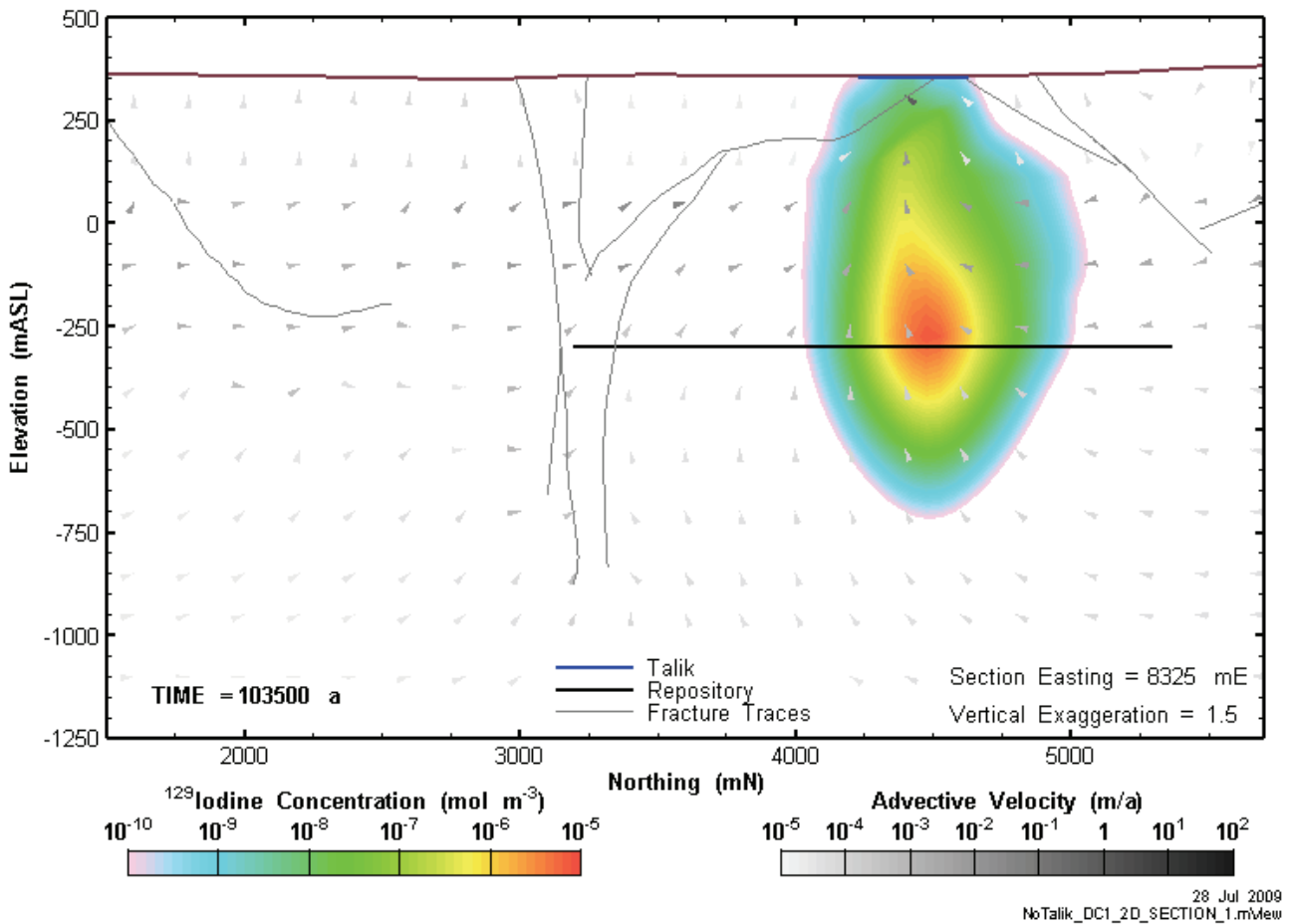


Figure 5.33: Location of cross-sections for figures in Sections 5.3.1 and 5.3.2.

### 5.3.1 Concentration Distributions - Defective Container 1 (DC1)

Transport modelling results vary continuously throughout the 0.8 Ma assessment period. The figures below present snapshots of transport along the North-South transect shown in Figure 5.33. In contrast to the flow results presented in section 5.2.1, results are focused on a smaller area, comprising the entire lateral extent of the radionuclide plume rather than the entire model domain. Results are shown as shaded colors in the figures.

Figure 5.34 to Figure 5.37 show detailed cross-sections of the GSC-RC radionuclide plume bracketing the second glacial advance and retreat during the first glacial cycle. This series of figures illustrates the general impact of a glacial advance and retreat on flow and transport. The figures start at 103,500 years as the plume has developed sufficiently by this time for the transport implications to be observable without complicating the analysis by including the superimposed effects of multiple previous advances and retreat.



**Figure 5.34: GSC-RC DC1, Y-Z cross section showing  $^{129}\text{I}$  plume after 103,500 years, the end of the second permafrost period. Arrows illustrate direction and magnitude of the advective velocity.**

Figure 5.34 shows the radionuclide plume and velocity field at the end of the second permafrost period. There has been 50,300 years of temperate conditions, followed by 7800 years of permafrost, 6700 years of cold-based glacial advance, 1900 years of cold-based glacial retreat, and 36,800 years of permafrost. The plume has spread in all directions, being drawn upward towards the northern talik

in particular during the permafrost period. As explained in section 5.2.1.1, this is due to the northern talik being the primary hydraulic outlet for the entire system during the permafrost period.

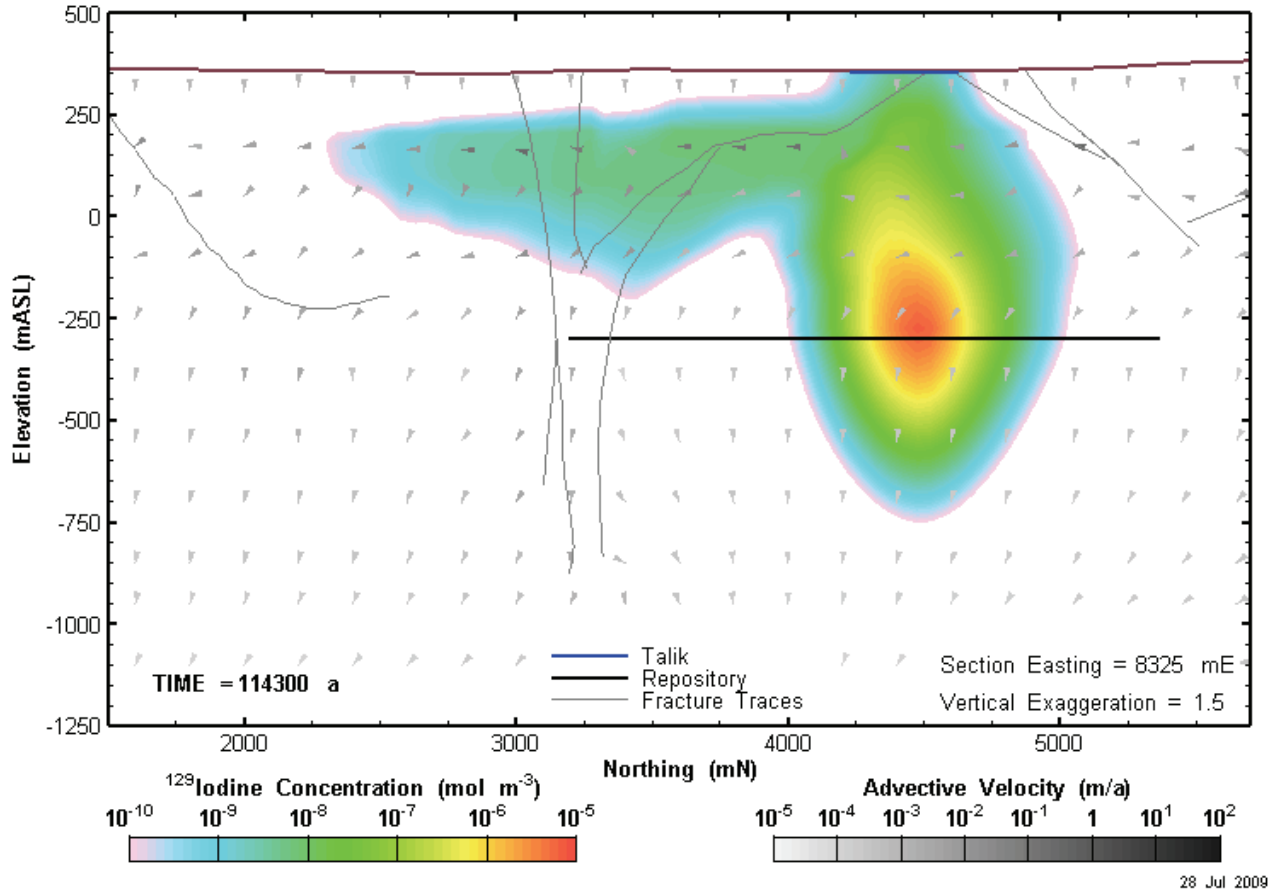


**Figure 5.35: GSC-RC DC1, Y-Z cross section showing  $^{129}\text{I}$  plume after 114,300 years, the end of the second glacial advance (cold-based). Arrows illustrate direction and magnitude of the advective velocity.**

Figure 5.35 shows the radionuclide plume at the end of the second glacial advance. This advance is cold-based, and the high hydraulic heads on the ground surface do not penetrate to great depth. Nevertheless, the hydromechanically induced heads and the specified heads at the north and south boundaries do lead to a general North-South gradient, and promote flow towards the south in the upper, more permeable units. At the elevation of the repository the flow direction is downward, as more pressurised water in the shallower units moves to equilibrate the heads. The downward flow is caused by very high specified heads at the surface (based on ice sheet thickness), and the similarly high hydraulic heads at the northern and southern flow boundaries. As expected, the flow field in the more permeable units drives the upper part of the  $^{129}\text{I}$  plume to the south. As a consequence, the glacial advance spreads the plume laterally at the top, and pushes it deeper at the bottom.

As a general observation, it should be noted that this downward directed flow is not a necessary consequence of a glacial advance, but instead reflects the HM coupling parameterization of the current model. In particular, if the deeper rock mass had a higher loading efficiency, then the hydromechanically induced head increase would be greater at depth, perhaps leading to a vertically upward hydraulic gradient, at least locally.

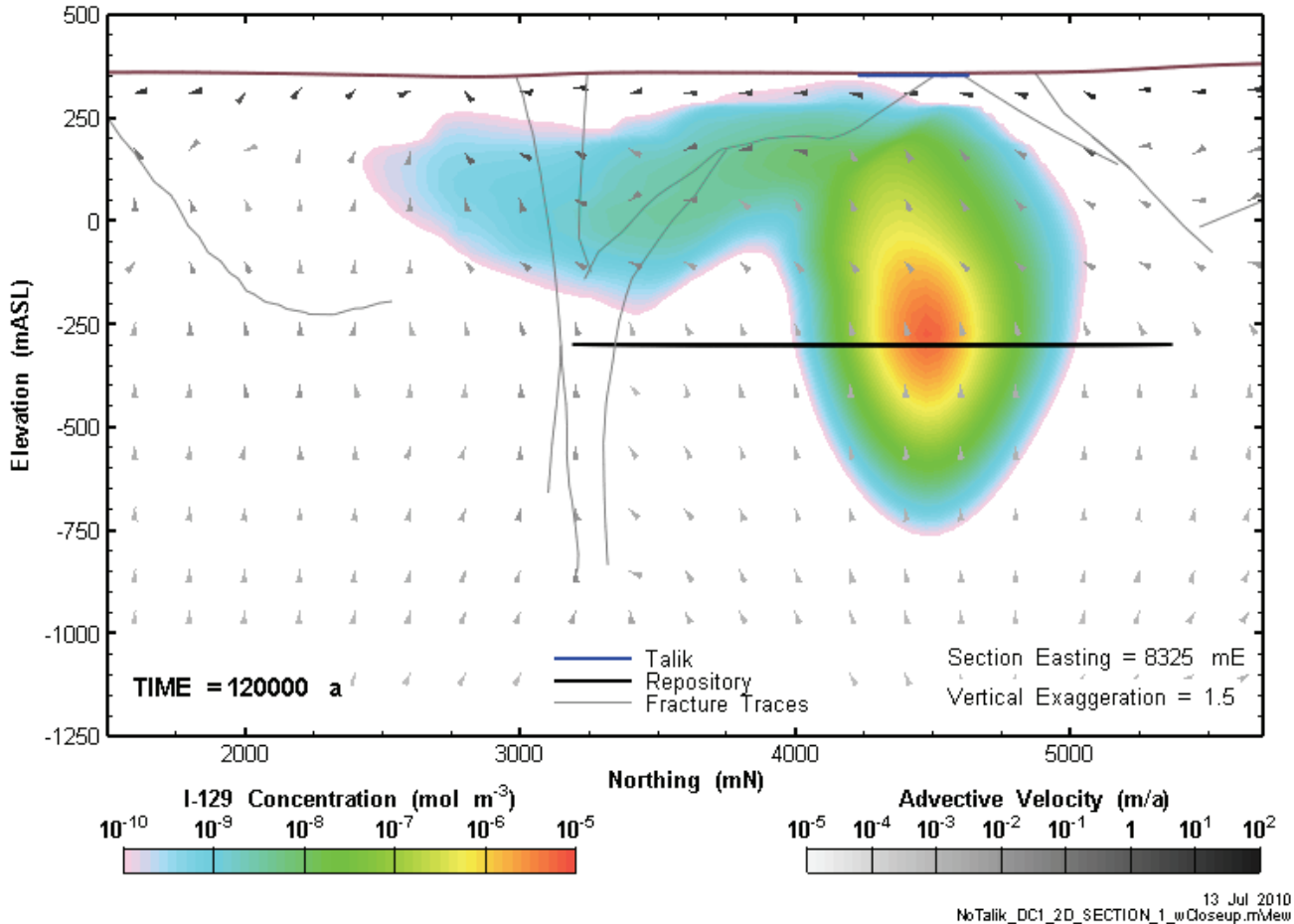


**Figure 5.36: GSC-RC DC1, Y-Z cross section showing  $^{129}\text{I}$  plume after 120,000 years, the end of the second glacial retreat (warm-based). Arrows illustrate direction and magnitude of the advective velocity.**

Figure 5.36 shows the plume at the end of the second glacial retreat, which is warm based. There is now a very strong southward flow at the top of the model, caused by the slope of the retreating glacier (which is located north of  $\approx 3000\text{mN}$ ). At the elevation of the repository the advective flow direction is upwards. This upward flow is driven by the pressurized fluid stored at depth during the preceding glacial advance. Although the prevailing flow direction in the upper units is still southward, the southernmost reaches of the plume seem to contract during this stage. This can be attributed largely to dilution, as the iodine is drawn upwards into the permeable shallow aquifer and swept away to the south more rapidly than it can be replaced from below. This effect is much weaker if the retreat is cold-based. Also, it should once again be noted that upward flow is a result of the HM coupling parameterization and is not a necessary consequence of glacial retreat. Downward flow could occur if the deeper rock had a higher loading efficiency, leading to relative underpressures in this softer rock upon removal of the ice load.

Figure 5.37 shows the plume 4000 years into the third permafrost period. At this stage, elevated heads still persist at greater depths, driving flow upward within the repository footprint. In the more permeable units, water is drawn from all sides towards the talik, which is the primary hydraulic outlet of the system. This causes lateral shrinkage of the plume, particularly in the southernmost reaches. However, the radionuclide plume is generally drawn upward and into the northern talik, leading to relatively high mass fluxes during permafrost periods, relative to other stages of the model. The actual concentrations remain low because of the associated higher groundwater flows.

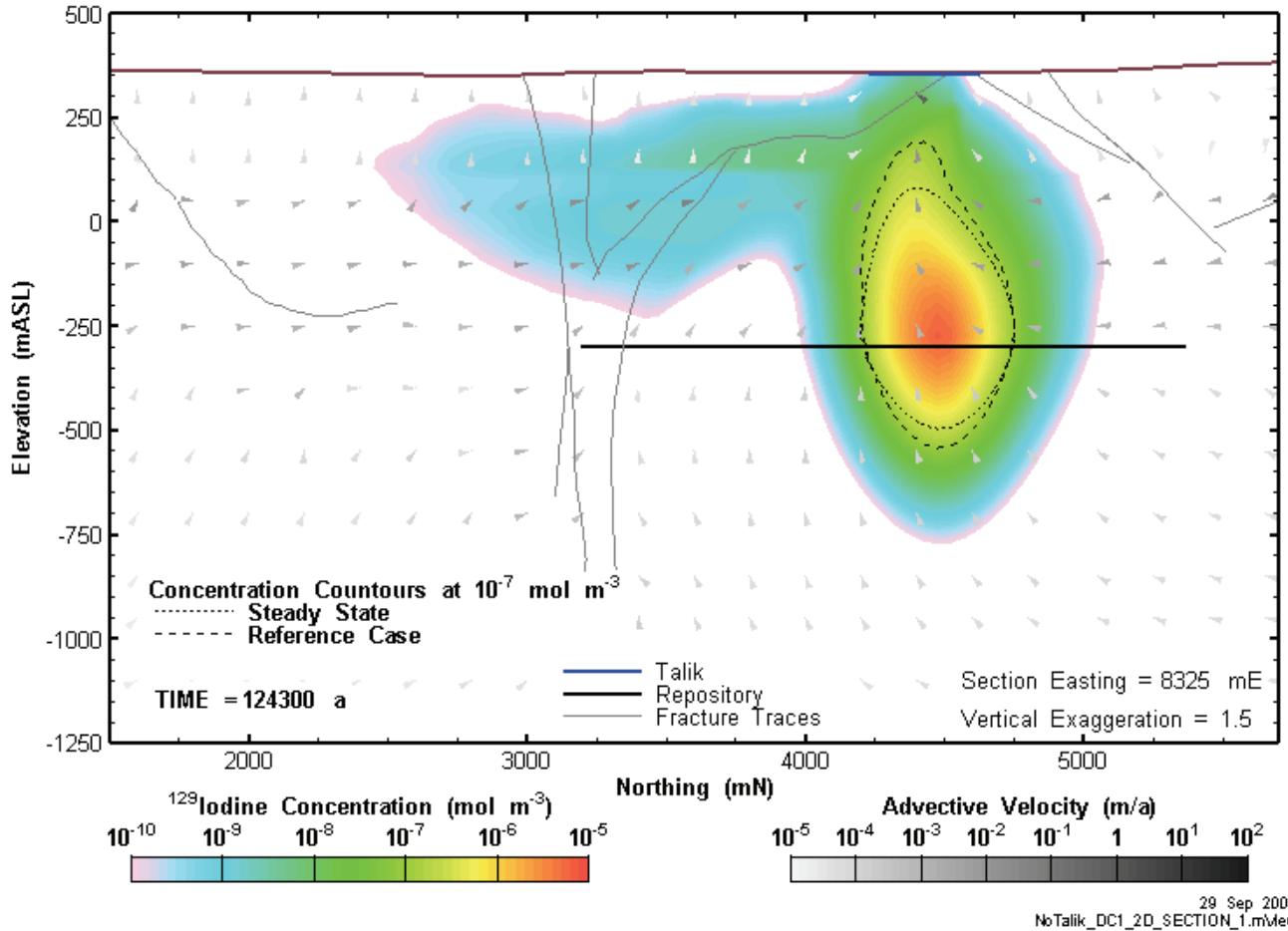


**Figure 5.37: GSC-RC DC1, Y-Z cross section showing  $^{129}\text{I}$  plume after 124,300 years, 4000 years into the third permafrost period. Arrows illustrate direction and magnitude of the advective velocity.**

The effects of a typical glacial advance-retreat cycle on the contaminant plume are largely confined to the upper part of the plume in the more permeable, shallower units. Comparing Figure 5.34 to Figure 5.37, it is evident that the core of the plume, above concentrations of  $10^{-7} \text{ mol/m}^3$ , remains relatively unaffected by the massive hydraulic perturbations induced by the advancing and retreating ice field. To emphasize this fact, the concentration contours at  $10^{-7} \text{ mol/m}^3$  for the GSC-RC and GSC-CC models have been plotted in Figure 5.37. After 125,000 years of transport, the contours are remarkably similar. This is largely due to the low permeability of the deeper geosphere, and the roughly equal and opposite effects of the glacial advance and retreat stages. Within the repository footprint, the flow direction is generally downward during ice advances, and upward during retreats. At all times, the velocities within the repository footprint remain very low, on the order of millimetres per year or less.

Figure 5.38 shows plan sections of the GSC-RC DC1  $^{129}\text{I}$  plume at 6 different times during the entire 0.8Ma assessment period. (More plan sections of the plume are shown in the Appendix.) These plan sections are at elevation 0.0 mASL, or 300 m above the repository horizon. As shown in the preceding figures, the outer reaches of the plume advance and retreat during different parts of the glacial cycle, but the core remains largely stable. It is difficult to define or determine when the radionuclide plume reaches its maximum extent, but the plume in Figure 5.38 (c) is close to the maximum. Before this point the outer reaches of the plume generally grow larger, while after this point the plume generally shrinks. Figure 5.39 shows a North-South cross section through the centre of the plume, at the same six times as Figure 5.38.

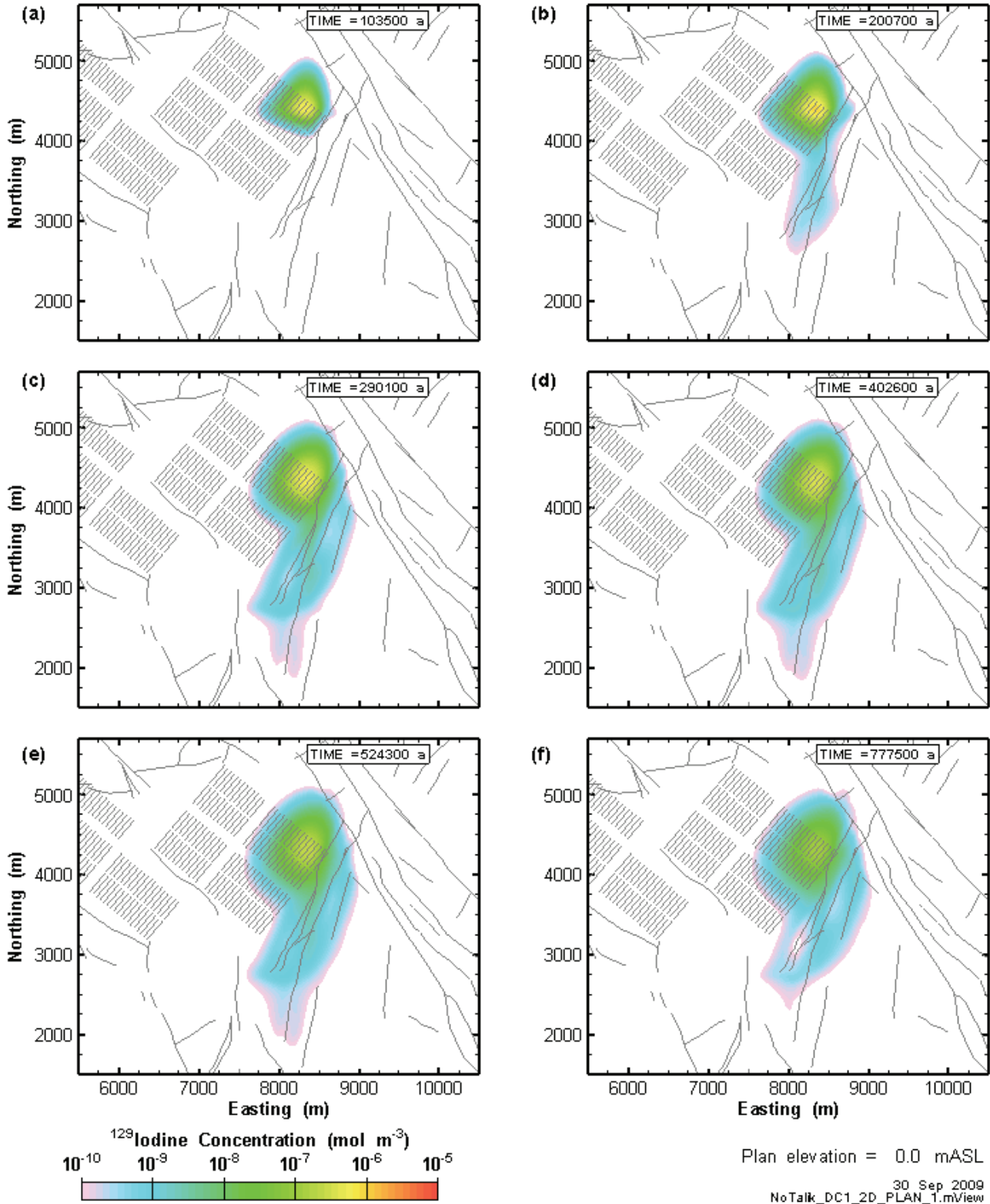


Figure 5.38: GSC-RC (Reference Case) DC1 X-Y planar section of transport model results during the assessment period. Section elevation of 0.0 mASL (approx. 350 mBGS).

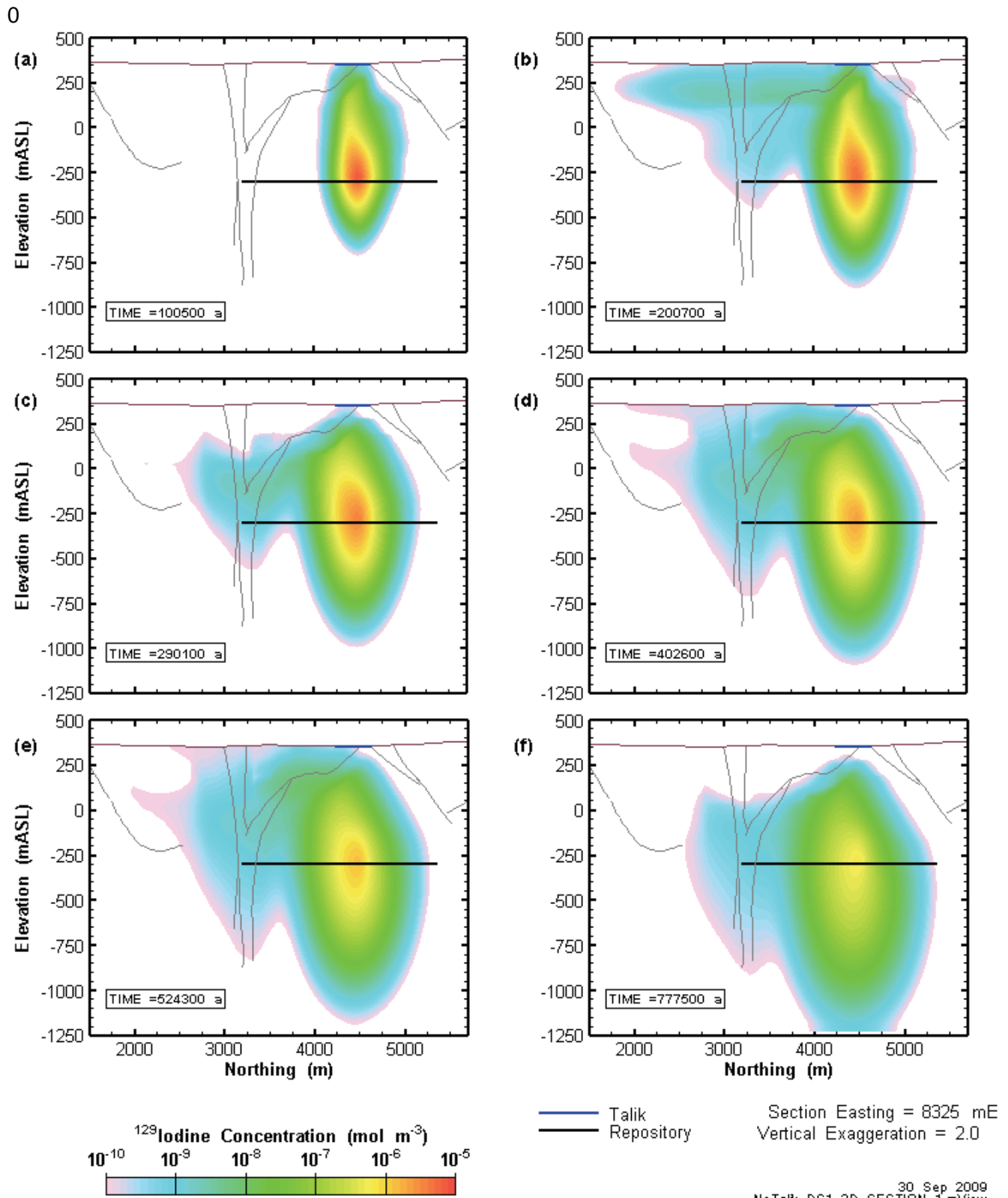


Figure 5.39: GSC-RC (Reference Case) DC1 Y-Z cross-section of transport model results at 6 times during the assessment period. Section easting of 8325 mE.

Figure 5.40 shows plan sections of modelling case **GSC-CC (constant climate)** for the plume from the DC1 source location at 6 different times during the entire one million year assessment period. As in Figure 5.38, these plan sections are at elevation 0.0 mASL, or 300 m above the repository horizon and are snapshots of the plume at approximately the same times. Comparing Figure 5.40 to Figure 5.38, there are clear differences between the two plumes. Because there are no glacial advances and retreats in the GSC-CC model, the outer part of the plume does not spread as far as in GSC-RC. However, above roughly  $10^{-8}$  mol/m<sup>3</sup> the steady state GSC-CC and the GSC-RC plumes do not differ greatly. The concentrations at the centre of the GSC-CC plume remain higher than for the Reference Case plume because of the lower average flow velocity at the source. The higher velocities in the reference case spread the plume over a larger area, with lower concentrations resulting. The differences between plumes in the GSC-CC and GSC-RC cases is much less than might be expected, given the extreme perturbations of the hydraulic system induced by glacial loading and unloading. Figure 5.41 shows six North-South cross sections through the centre of the GSC-CC plume, at the same times as Figure 5.40. Once again, the similarity to the GSC-RC plume is evident although the GSC-CC plume is slightly more compact.

Figure 5.42 and Figure 5.43 present snapshots of the transport results of the higher storage coefficient **GSC-HS (High Storage coefficient)** DC1 calculation case. The picture presented in these figures is quite distinct from the GSC-RC results in Figure 5.38 and Figure 5.39. The extent of the plume in the GSC-HS model is much smaller than that seen for the GSC-RC model. By contrast, the concentration at the centre of the plume declines much more rapidly in the GSC-HS model. The combination of these two observations suggests that, in the GSC-HS case, the radionuclide is being spread further (vertically and horizontally) throughout the model domain due to the increased groundwater flow rates in the model domain (see section 5.2.3). Consequently, the plume is more dilute in GSC-HS than in GSC-RC. Because concentrations are not plotted below  $10^{-10}$  mol/m<sup>3</sup>, the plume appears much smaller. Overall, the plume in Figure 5.43 also appears to have a downward migrating trend, as compared to the GSC-RC plume. This downward movement agrees with the repository velocity analysis from section 5.2.3, where it was shown that the average net advective travel direction over the course of a complete glacial cycle was downward within the repository footprint.

Figure 5.44 and Figure 5.45 show the **GSC-NF (No-Flow N-S boundaries)** DC1 plume at six times during the assessment period, in plan and cross section respectively, as in previous figures. The GSC-NF plume differs significantly from the GSC-RC plume. The long, low concentration extensions of the radionuclide plume in the upper, more permeable units are significantly stunted in the GSC-NF model. This is a reflection of the generally much lower velocities in the GSC-NF model during glaciation events (compare for example Figure 5.4 and Figure 5.13). The lower velocities are caused by having no-flow North and South boundaries, rather than specified head boundaries. In the GSC-RC model, the difference between the northern and southern specified heads leads to a sizable hydraulic gradient during glaciated periods. This gradient is absent in the GSC-NF model.

The effect of having a few open taliks under an otherwise permafrost-based glacier is shown very clearly in Figure 5.46 and Figure 5.47. These figures show transport results for the model **GSC-TK (Talík under glacier)**, which differs from the reference case only in that the two taliks remain open during cold-based glacial advances. As one would expect, the very high specified heads at the surface of the taliks lead to water flowing downward through the taliks. This relatively high flow, spreads and disperses the upper part of the radionuclide plume to the East, West, and North, leading to a larger but more dilute plume than for case GSC-RC. Nevertheless, the more concentrated core of the plume remains relatively unchanged. This is particularly evident in Figure 5.47.

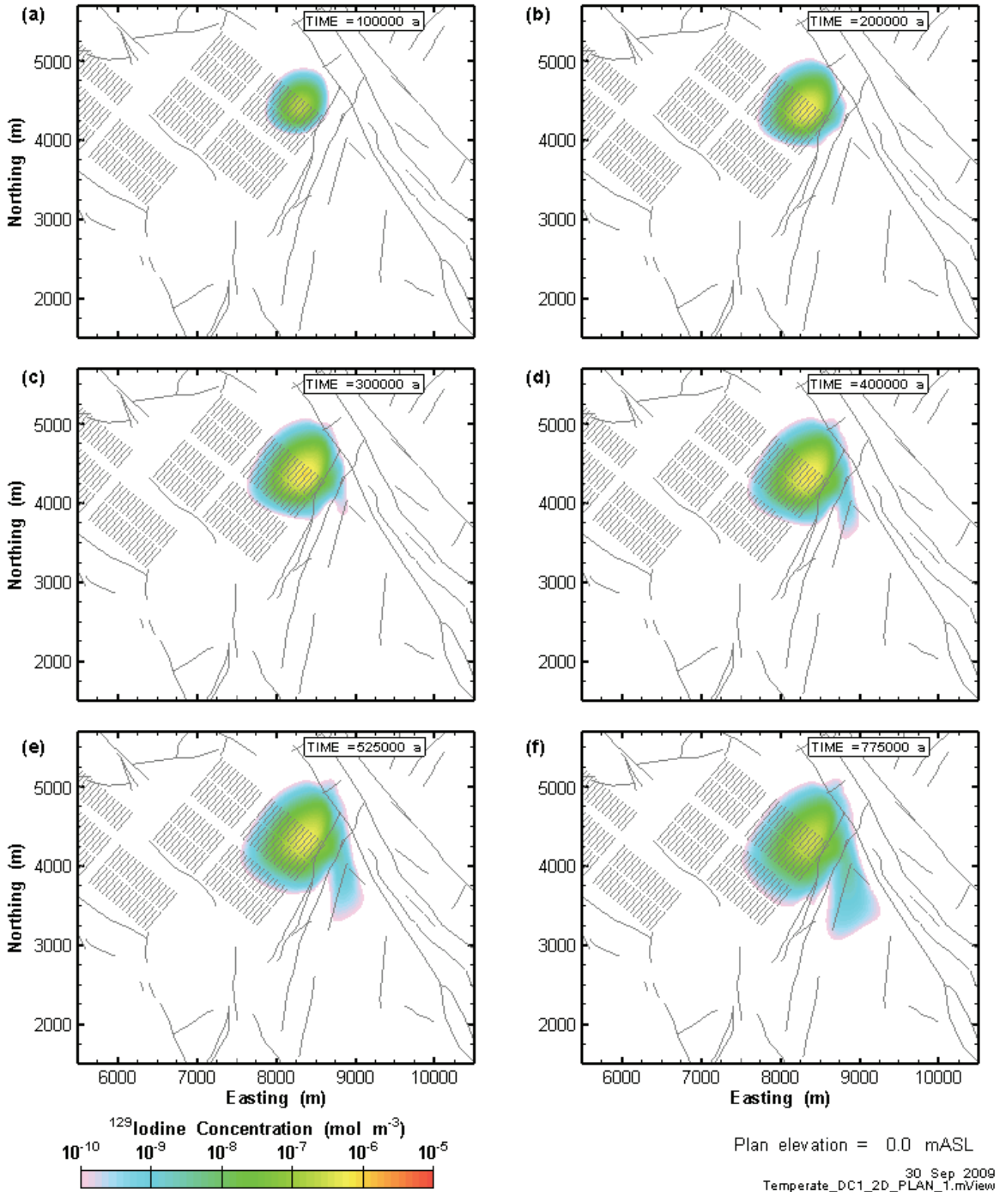


Figure 5.40: GSC-CC (constant climate) DC1 X-Y planar section of transport model results at 6 times during the assessment period. Section elevation of 0.0 mASL (approx. 350 mBGS).

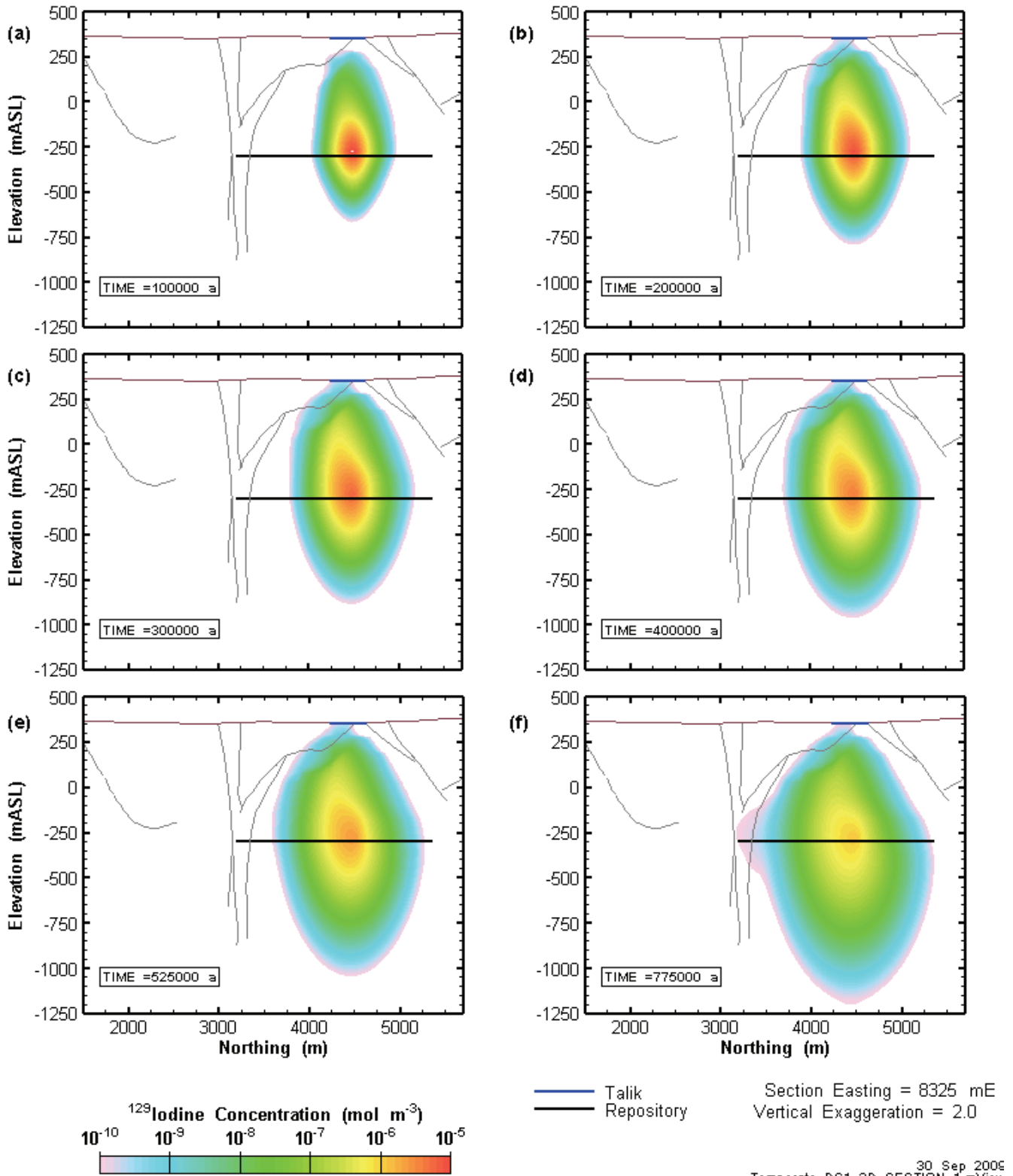


Figure 5.41: GSC-CC (constant climate) DC1 Y-Z cross-section of transport model results at 6 times during the assessment period. Section easting of 8325 mE.

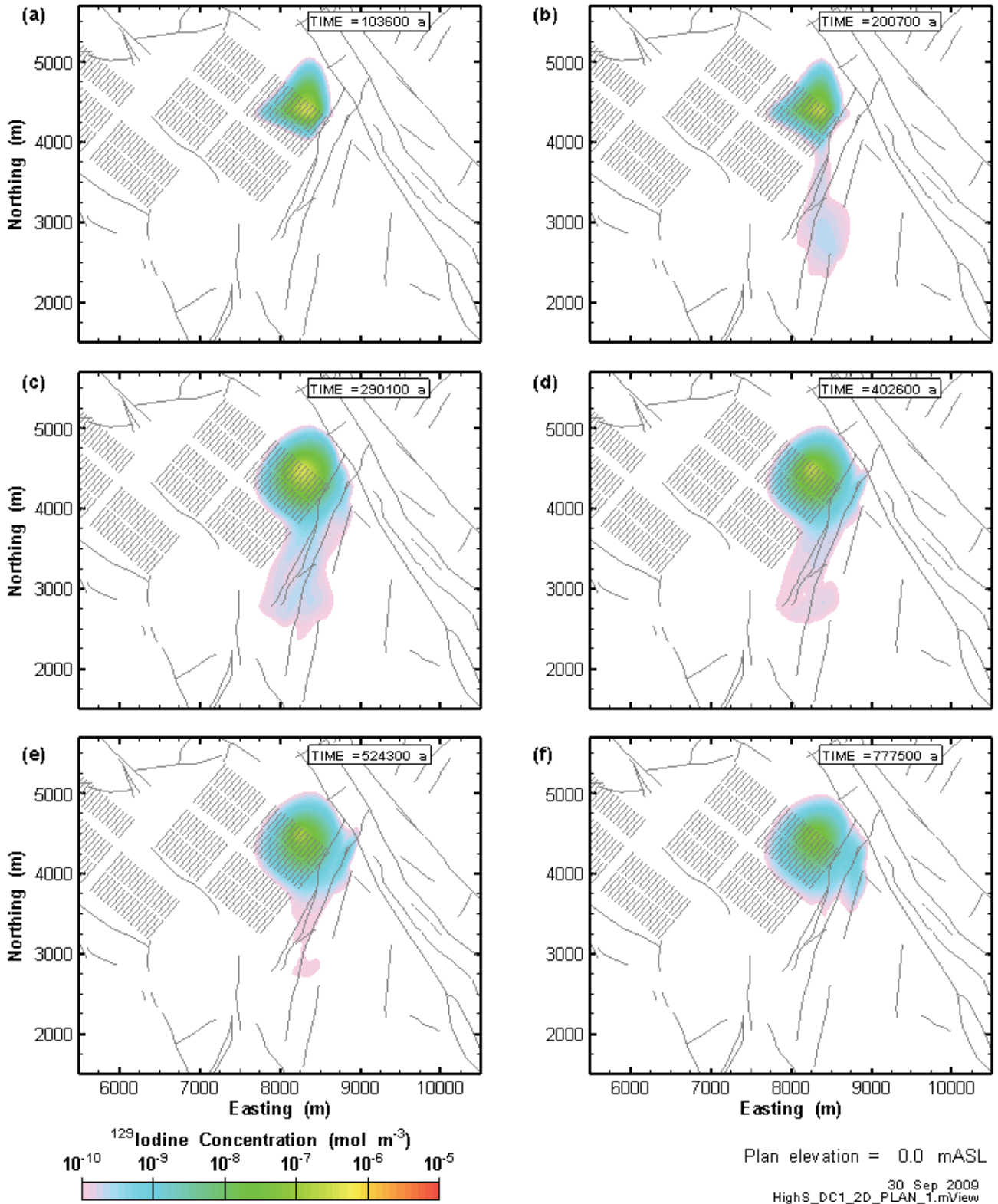


Figure 5.42: GSC-HS (High Storage coefficient) DC1 X-Y planar section of transport model results at 6 times during the assessment period. Section elevation of 0.0 mASL (approximately 350 mBGS).

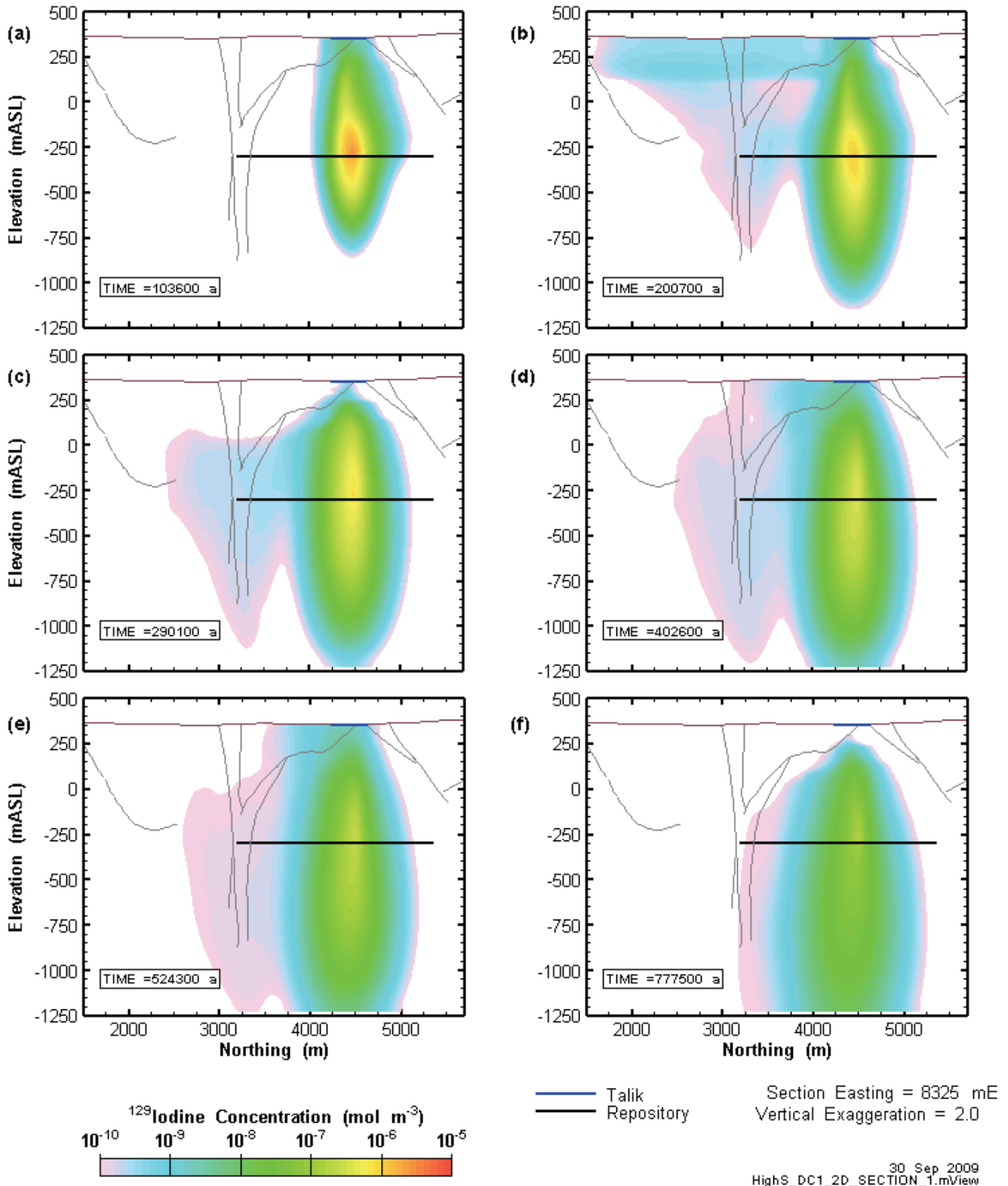


Figure 5.43: GSC-HS (High Storage coefficient) DC1 X Y-Z cross-section of transport model results at 6 times during the assessment period. Section easting of 8325 mE

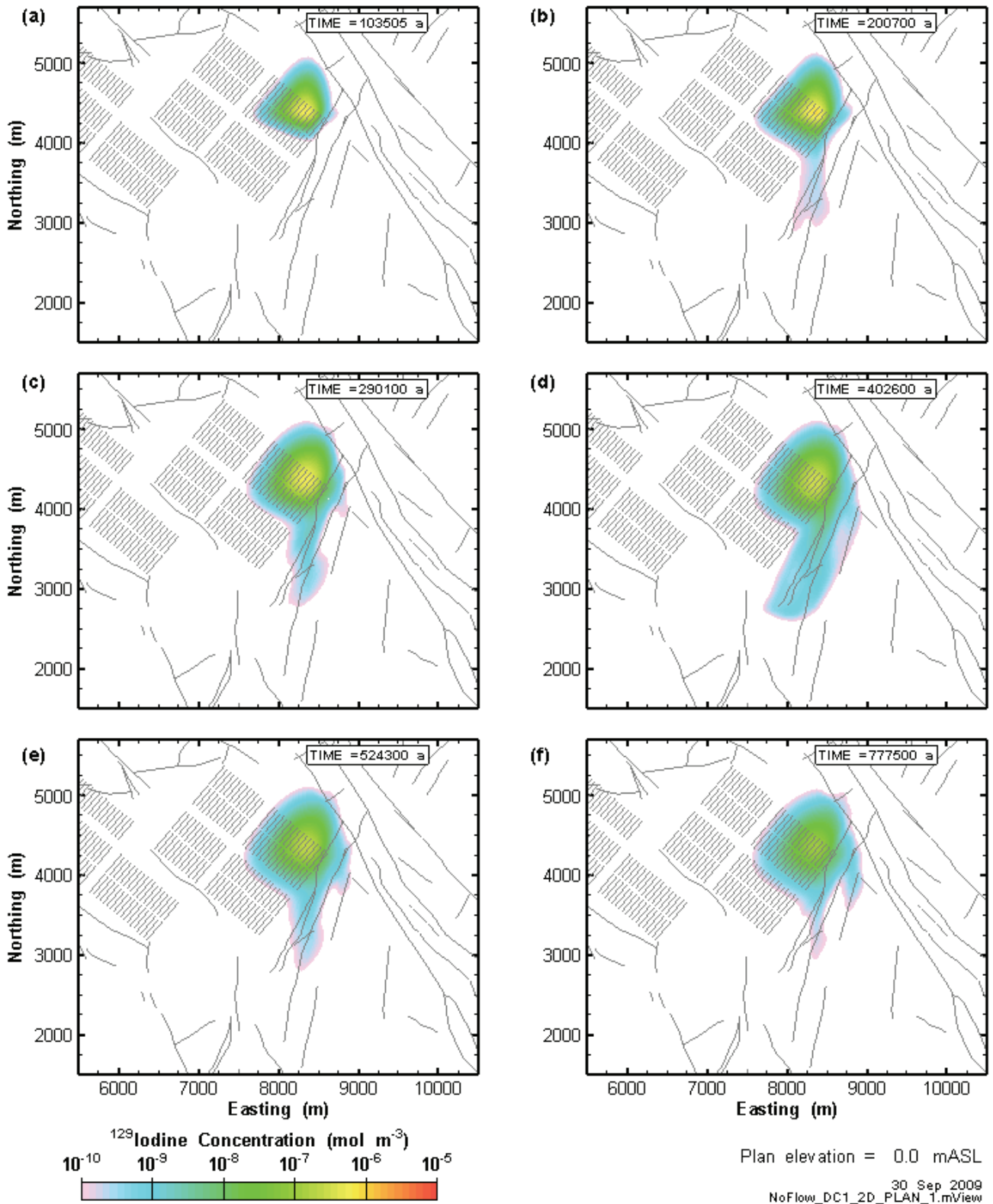


Figure 5.44: GSC-NF (No-Flow North-South boundaries) DC1 X-Y planar section of transport model results at 6 times during the assessment period. Section elevation of 0.0 mASL (approximately 350 mBGS).

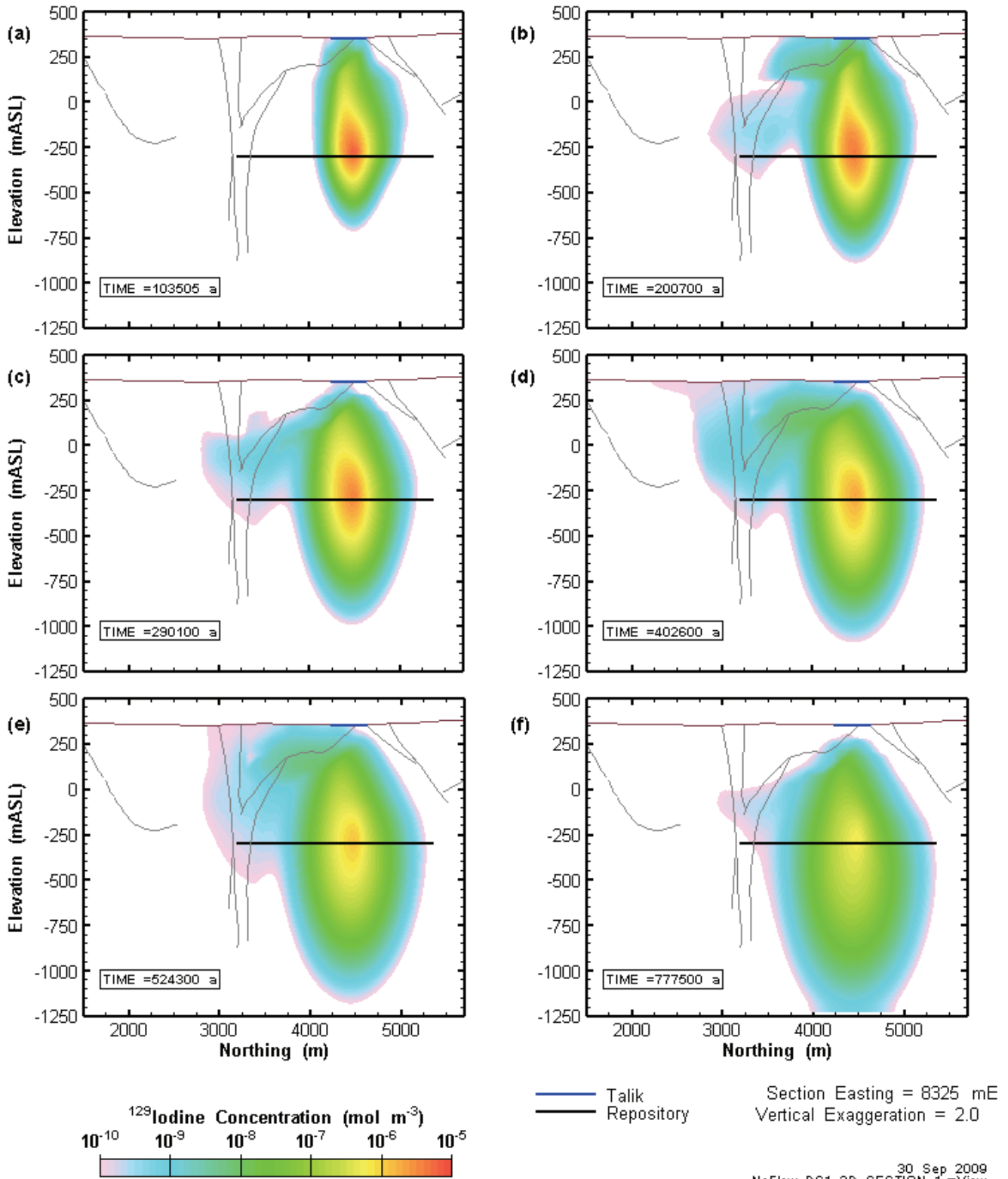


Figure 5.45: GSC-NF (No-Flow North-South boundaries) DC1 Y-Z cross-section of transport model results at 6 times during the assessment period. Section easting of 8325 mE.

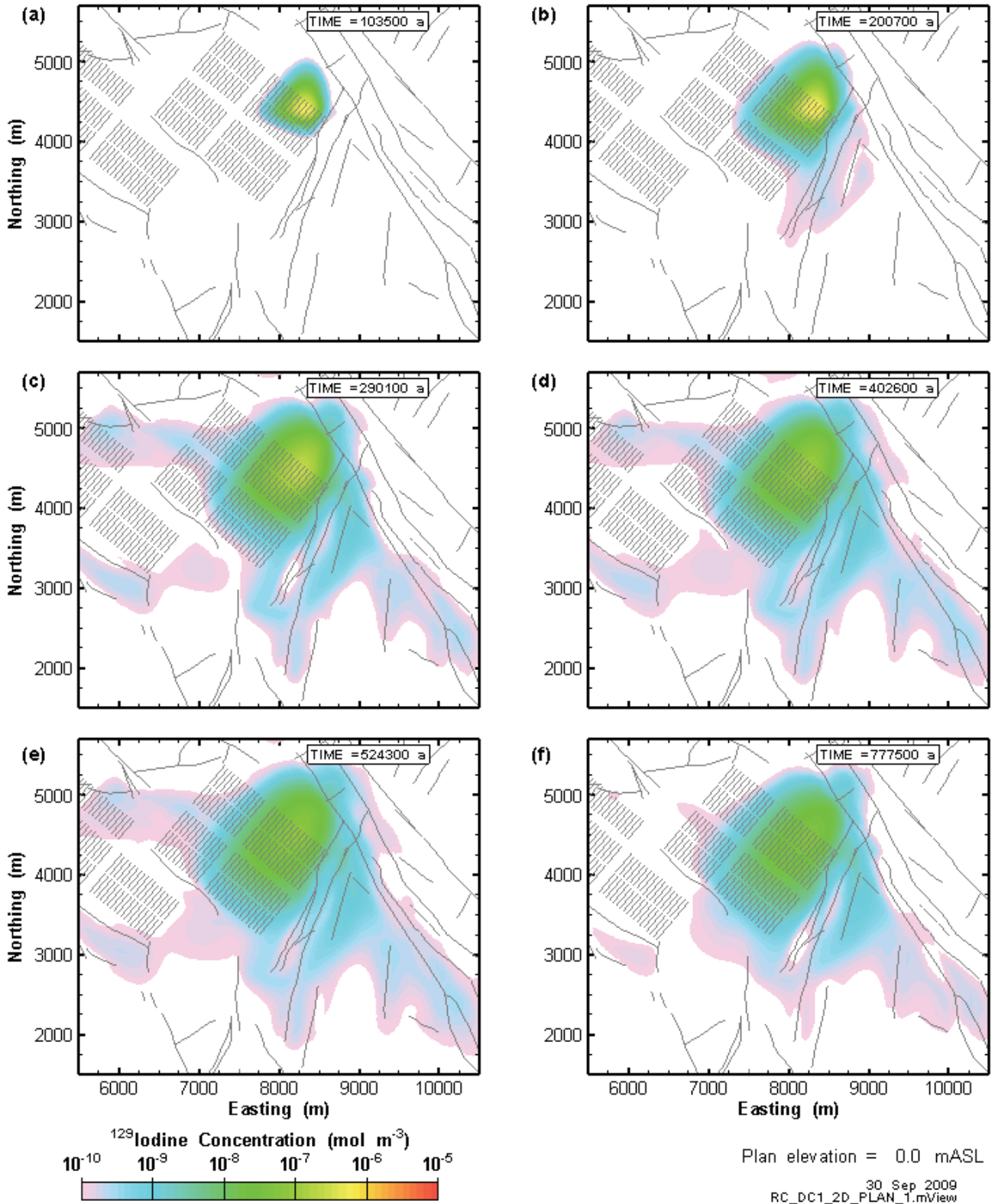
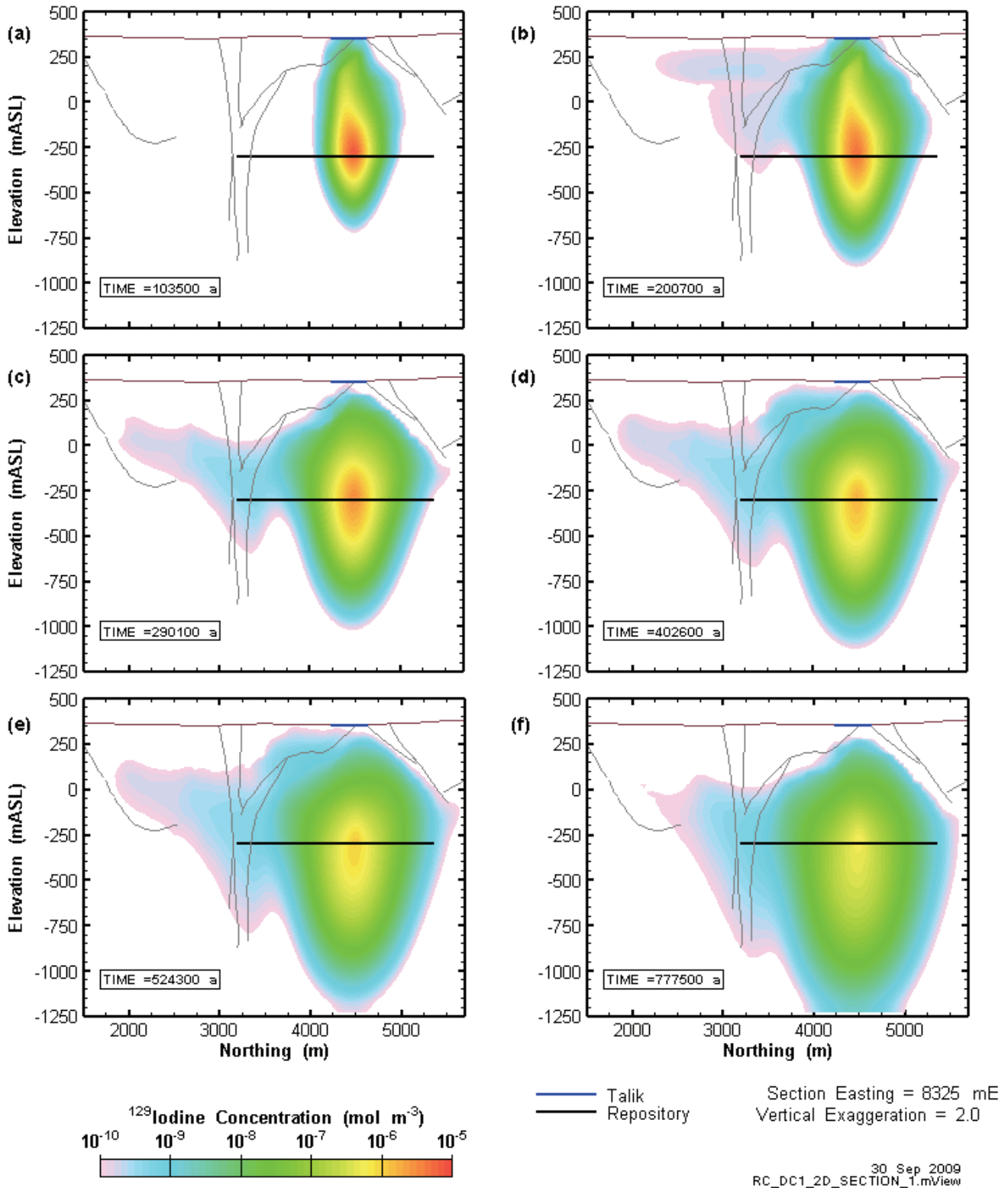


Figure 5.46: GSC-TK (Taluk under glacier) DC1 X-Y planar section of transport model results at 6 times during the assessment period. Section elevation of 0.0 mASL (approximately 350 mBGS).



**Figure 5.47: GSC-TK (Talik under glacier) DC1 Y-Z cross-section of transport model results at 6 times during the assessment period. Section easting of 8325 mE.**

Figure 5.48 shows plan sections through all the case results at approximately 400,000 years. As a general conclusion, although the glacial cycles do modify the flow field extensively, the cumulative

impact of repeated cycles of advance and retreat tend to effectively “cancel out”, leading to a general plume structure that is not substantially different from the steady-state flow and transport model. However, at shallower depths, there are significant differences between the various models, as the glacier advance and retreat and flow at the talik disperses  $^{129}\text{I}$  in the upper zones below the permafrost. The higher permeability fracture system is the primary conduit for plume dispersal.

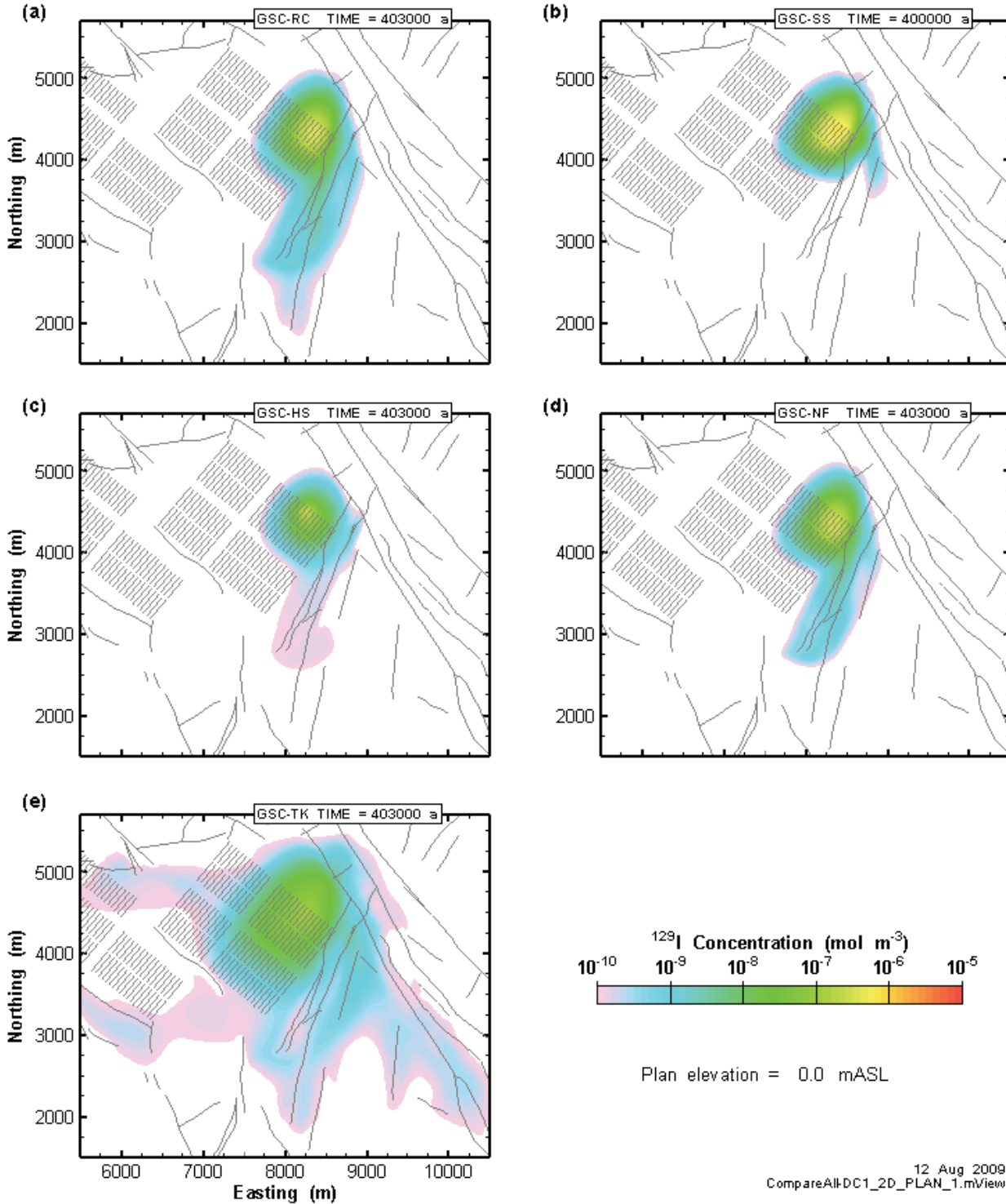


**Figure 5.48: All cases comparison of DC1 X-Y planar section through  $^{129}\text{I}$  plume. Section elevation of 0.0 mASL (approximately 350 mBGS).**

### 5.3.2 Concentration Distributions - Defective Container 3 (DC3)

This section of the report presents a number of snapshots of radionuclide plumes at various times for the various calculation cases, for contaminant source location DC3. In section 5.3.1, cross-sectional results were presented on a North-South cross section through the contaminant plume. For contaminant source DC3, the lateral spread of the plume is predominantly East-West, so the cross-sectional figures use an East-West transect at 4825 mN (see Figure 5.33). Detailed cross-sections, as presented in Figure 5.34 to Figure 5.37 are not presented, as they would provide little additional information.

Figure 5.49 shows the plan sections at elevation 0.0 mASL of the **GSC-RC (Reference Case)** plume at various times throughout the 0.8Ma assessment period. As the source term and the flow field are identical to those that produced the DC1 plume, it is evident that the location of the radionuclide source has a significant impact on the evolution and morphology of the plume. The dominant effect of the northern talik on plume migration during permafrost periods is very evident in Figure 5.49 (b), where the plume extends towards the talik. During permafrost periods, the upper plume is evidently drawn towards the northern talik. During glacial advances, however, the North-South hydraulic gradient pushes the plume to the south. Figure 5.49 (c) through (f) show how the alternation in flow direction spreads the plume across the region South and East of the defective container.

Figure 5.50 shows the same data, along an East-West cross-section through the plume. The extension of the plume to the east is very evident in the figure. As was seen for DC1, the more concentrated core of the plume remains relatively stationary; it is generally unaffected by the large, widespread perturbations of the flow field. In the figures, the red line at ground surface delineates the western discharge region, where the majority of the  $^{129}\text{I}$  mass flows to the biosphere from DC3 occur (see Figure 5.60).

Figure 5.51 shows plan sections of modelling case **GSC-CC (Constant Climate)** DC3 plume at six different times during the one million year assessment period at an elevation of 0.0 mASL, or 300 m above the repository horizon. Comparing Figure 5.51 to Figure 5.49, there are clear differences between the two plumes. Similar to the results for source DC1, the outer part of the GSC-CC plume does not spread as far as in GSC-RC. In Figure 5.52 which shows six East-West cross sections through the centre of the GSC-CC plume, the large extensions of the plume above approximately -250 m that were seen in Figure 5.50 are largely absent. However, above a concentration of approximately  $10^{-8} \text{ mol/m}^3$  the steady state GSC-CC and the GSC-RC plumes do not differ greatly, with slightly more vertical spreading in the GSC-RC DC3 plume. Again, the differences between plumes in the GSC-CC and GSC-RC cases are much less than might be expected, given the extreme perturbations of the hydraulic system induced by glacial loading and unloading.

Figure 5.53 and Figure 5.54 present the DC3 results for the **GSC-HS (Higher Storage coefficient)** model. As was seen for the DC1 plume, the much higher velocities in the GSC-HS case spread the plume over a wider area, and dilute the core of the plume. As was seen in the GSC-RC results, the alternation between prevailing eastward and southward flow directions spreads the plume laterally across the quadrant southeast of the DC3 source. Further, the alternation between upward and downward vertical flow direction spreads the plume vertically, to a much greater extent than seen in the reference case model.

Figure 5.55 and Figure 5.56 present the DC3 results for the **GSC-NF (No-Flow N-S boundaries)** model. The effect of the no-flow boundaries is clearly evident in Figure 5.55. As in GSC-RC, the plume spreads to the East due to the influence of the talik during permafrost periods, but the

southward spread of the plume is greatly attenuated because velocities are much lower during glacial advances and retreats (see Figure 5.14).

Figure 5.57 and Figure 5.58 show results for the **GSC-TK (Talík under glacier)** model with source DC3. The overall structure of the GSC-TK DC3 plume is very similar to the GSC-RC plume. There are only relatively minor differences. As the core of the DC3 plume is much further away from the northern talík, this result is perhaps to be expected.

Figure 5.59 shows results for all cases, at 403,000 years, the end of the third glacial cycle. In general, the transport results for source DC3 once again indicate that even very large changes in the flow system during the glacial cycle have a rather minor impact on transport at the core of the plume. In the more permeable upper geological units, the impact of both glaciation and the talíks are clearly evident, causing a dilute plume to spread over a much larger area than that predicted in the steady-state temperate model (GSC-CC). During permafrost periods, the impact of the talík(s) is in some ways greater than that seen in the DC1 transport simulation. Having the sink talík offset from the core of the plume caused much greater lateral spreading. On the other hand, the next section of the report will show that the actual mass of <sup>129</sup>I reaching the northern talík is much lower for source DC3 than for DC1.

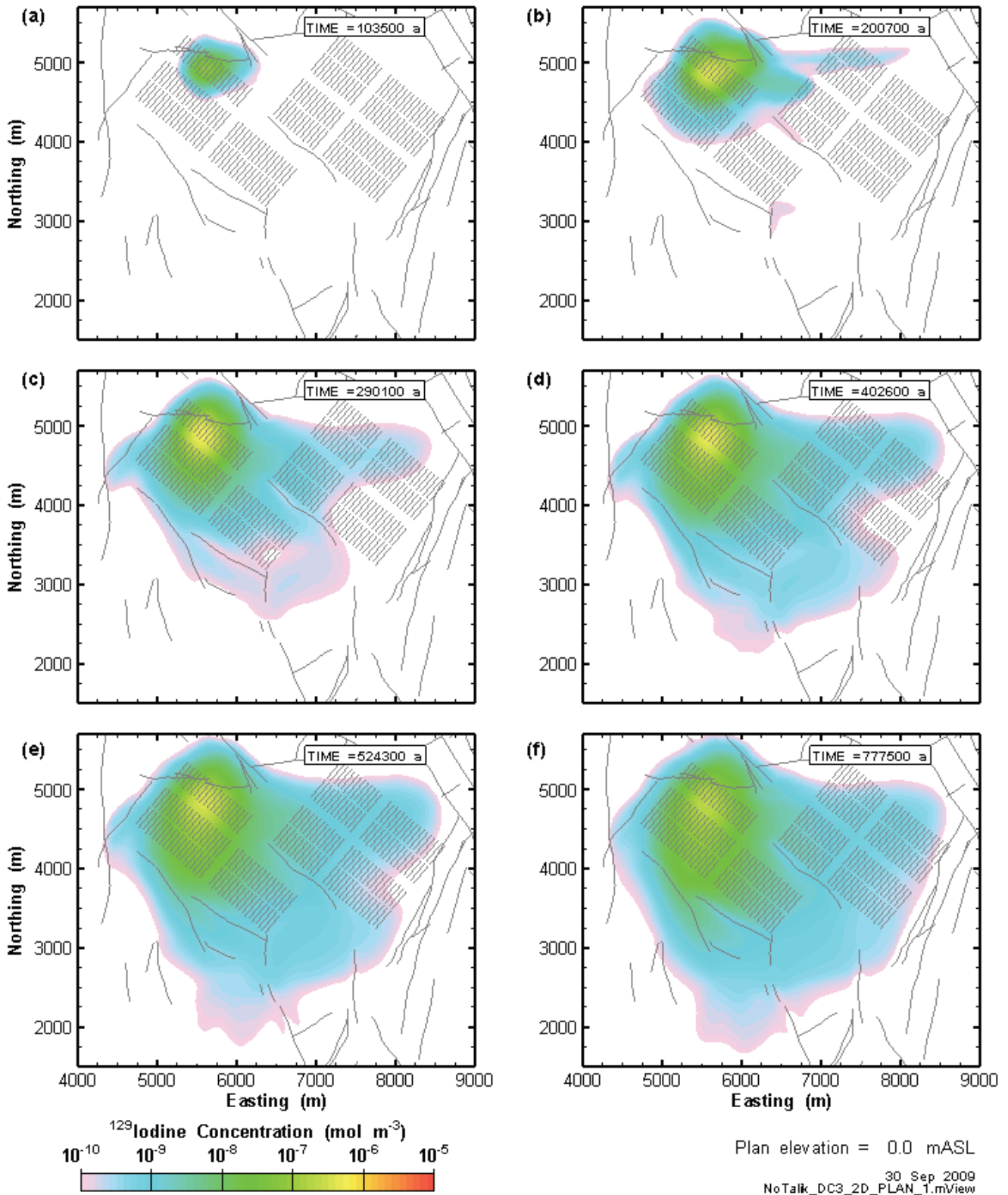


Figure 5.49: GSC-RC (Reference Case) DC3 X-Y planar section of transport model results at 6 times during the assessment period. Section elevation of 0.0 mASL (approx. 350 mBGS).

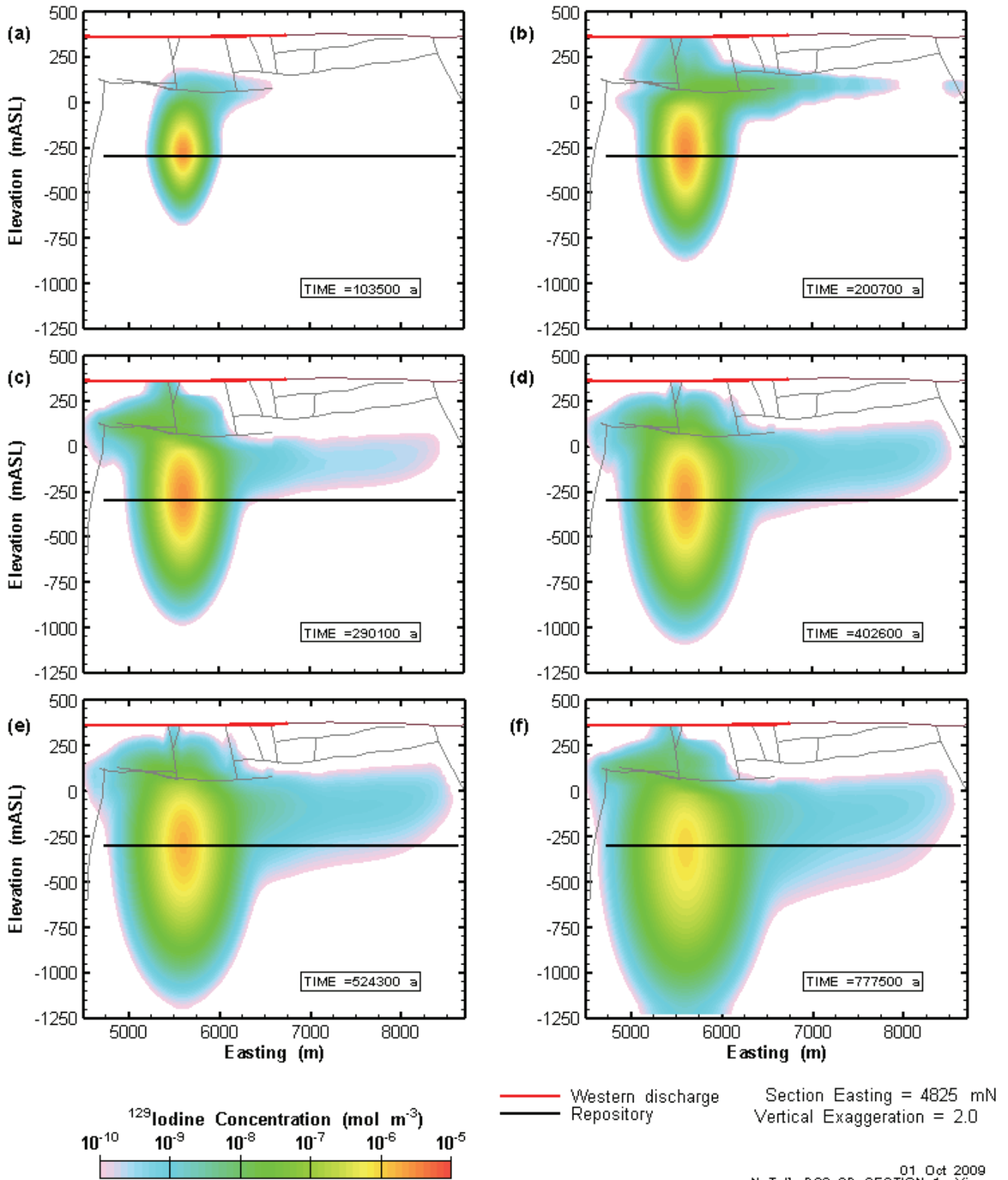


Figure 5.50: GSC-RC (Reference Case) DC3 X-Z cross-section of transport model results at 6 times during the assessment period. Section northing of 4825 mN.

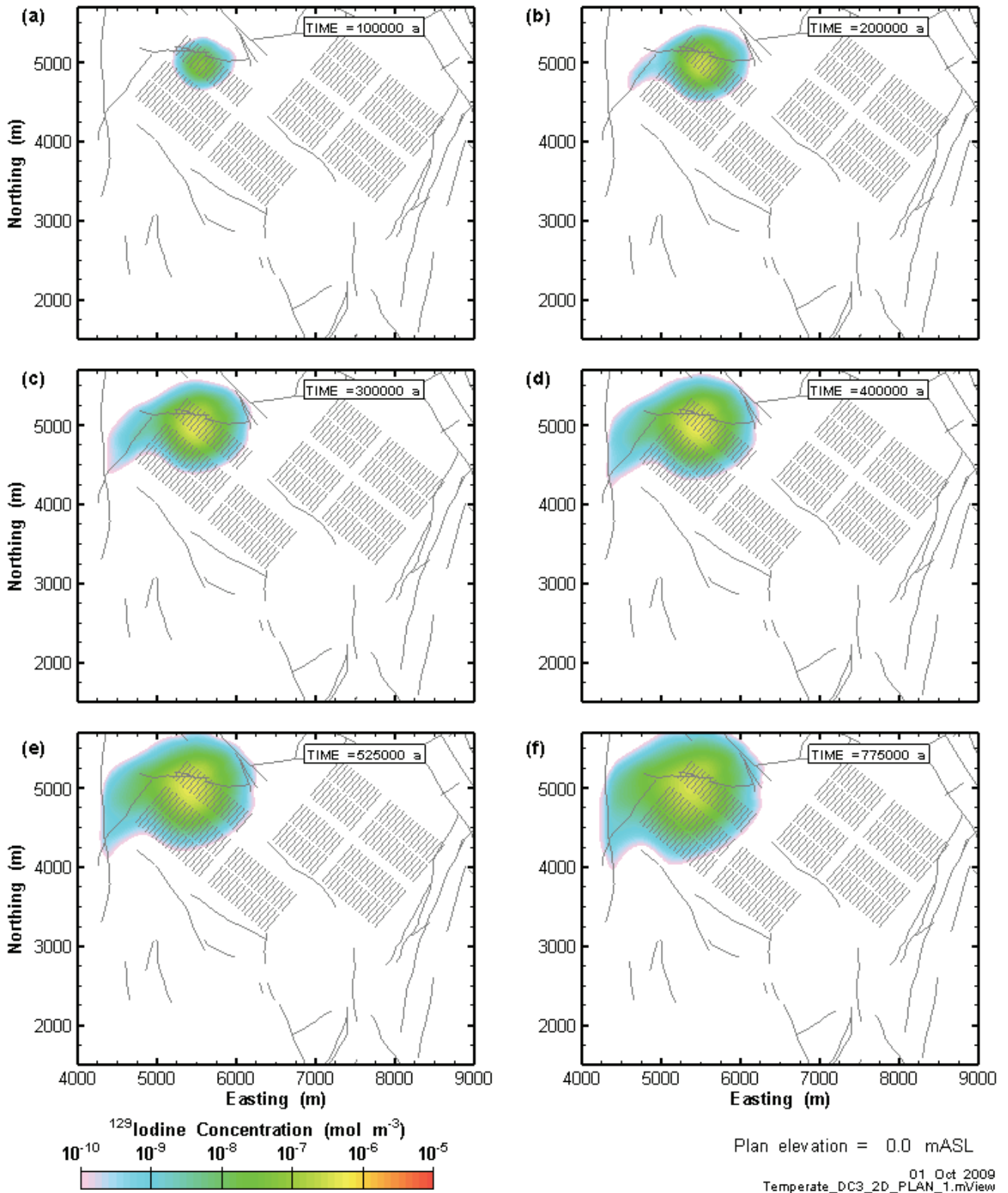


Figure 5.51: GSC-CC (constant climate) DC3 X-Y planar section of transport model results at 6 times during the assessment period. Section elevation of 0.0 mASL (approx. 350 mBGS).

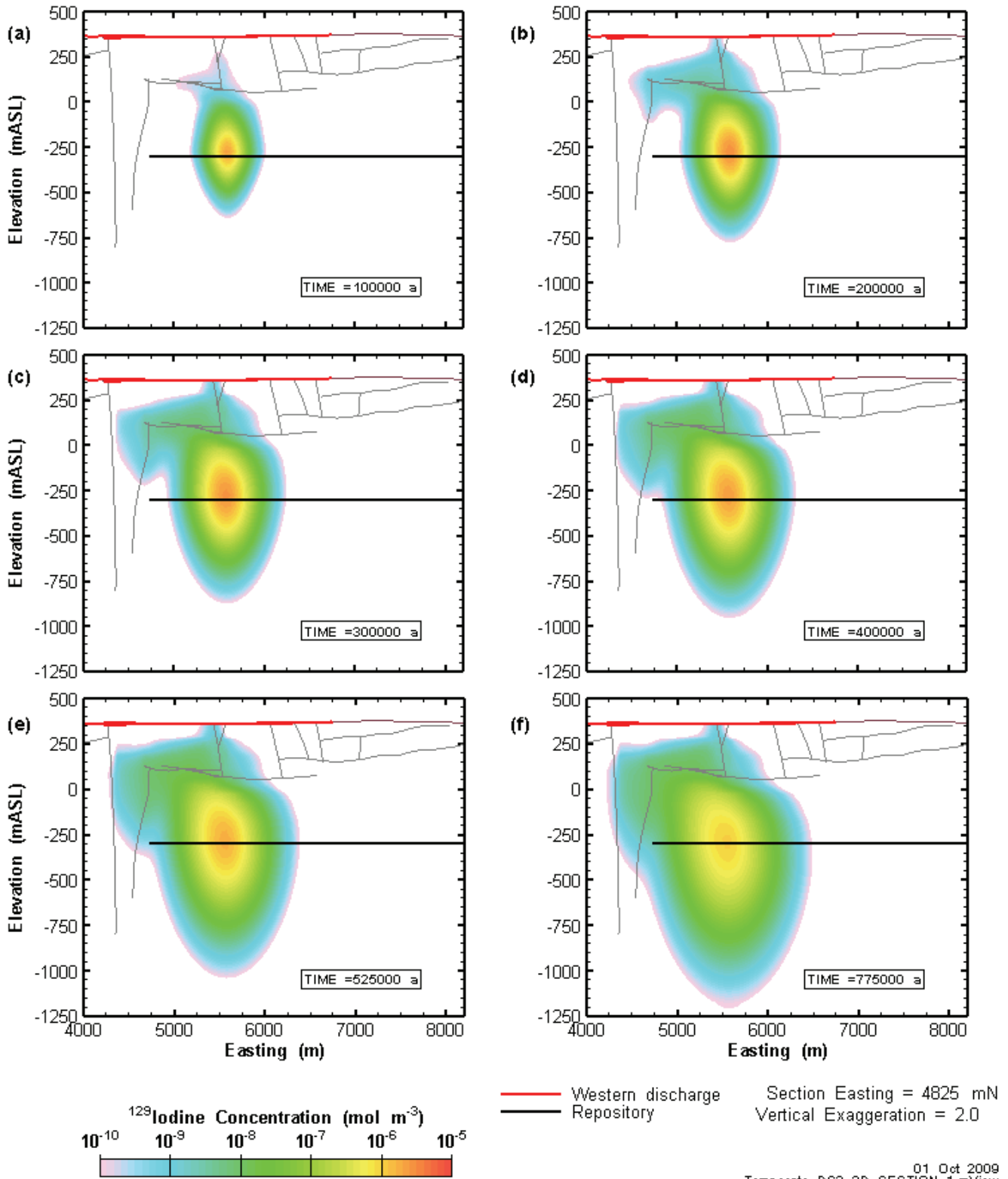


Figure 5.52: GSC-CC (constant climate) DC3 X-Z cross-section of transport model results at 6 times during the assessment period. Section northing of 4825 mE.

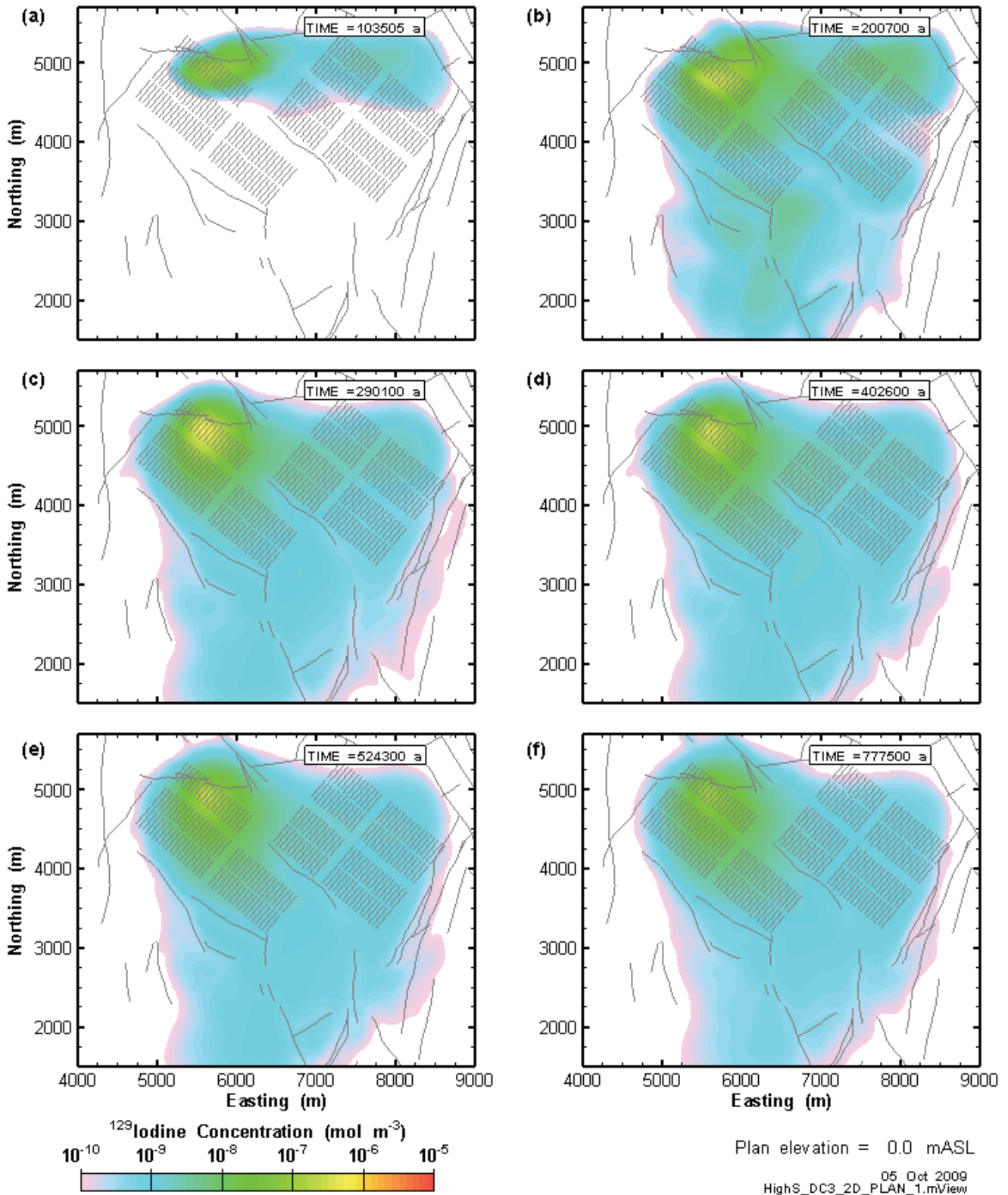


Figure 5.53: GSC-HS (High Storage Coefficient) DC3 X-Y planar section of transport model results at 6 times during the assessment period. Section elevation of 0.0 mASL (approximately 350 mBGS).

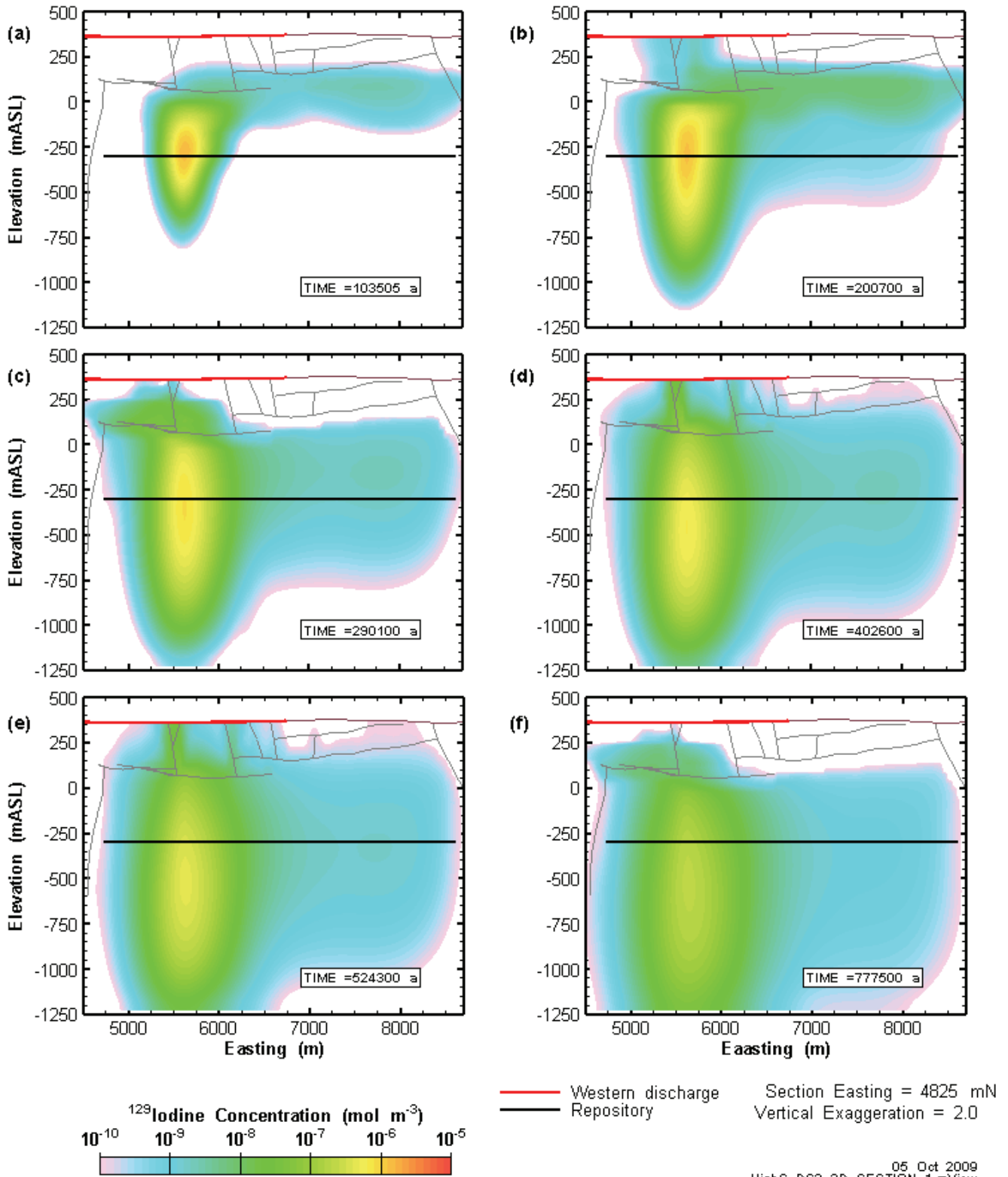


Figure 5.54: GSC-HS (High Storage Coefficient) DC3 X-Z cross-section of transport model results at 6 times during the assessment period. Section northing of 4825 mN.

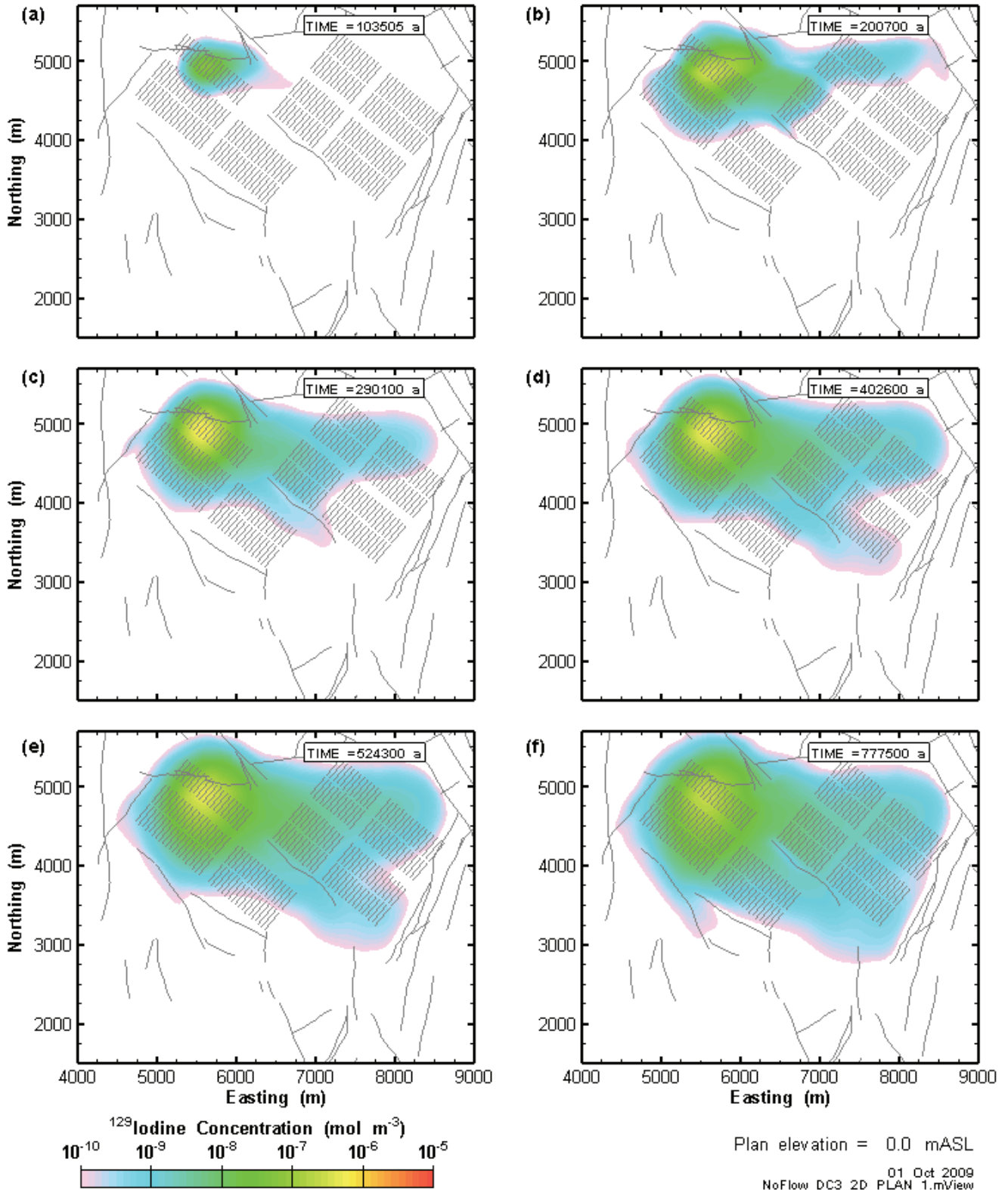


Figure 5.55: GSC-NF (No-Flow N-S boundaries) DC3 X-Y planar section of transport model results at 6 times during the assessment period. Section elevation of 0.0 mASL (approximately 350 mBGS).

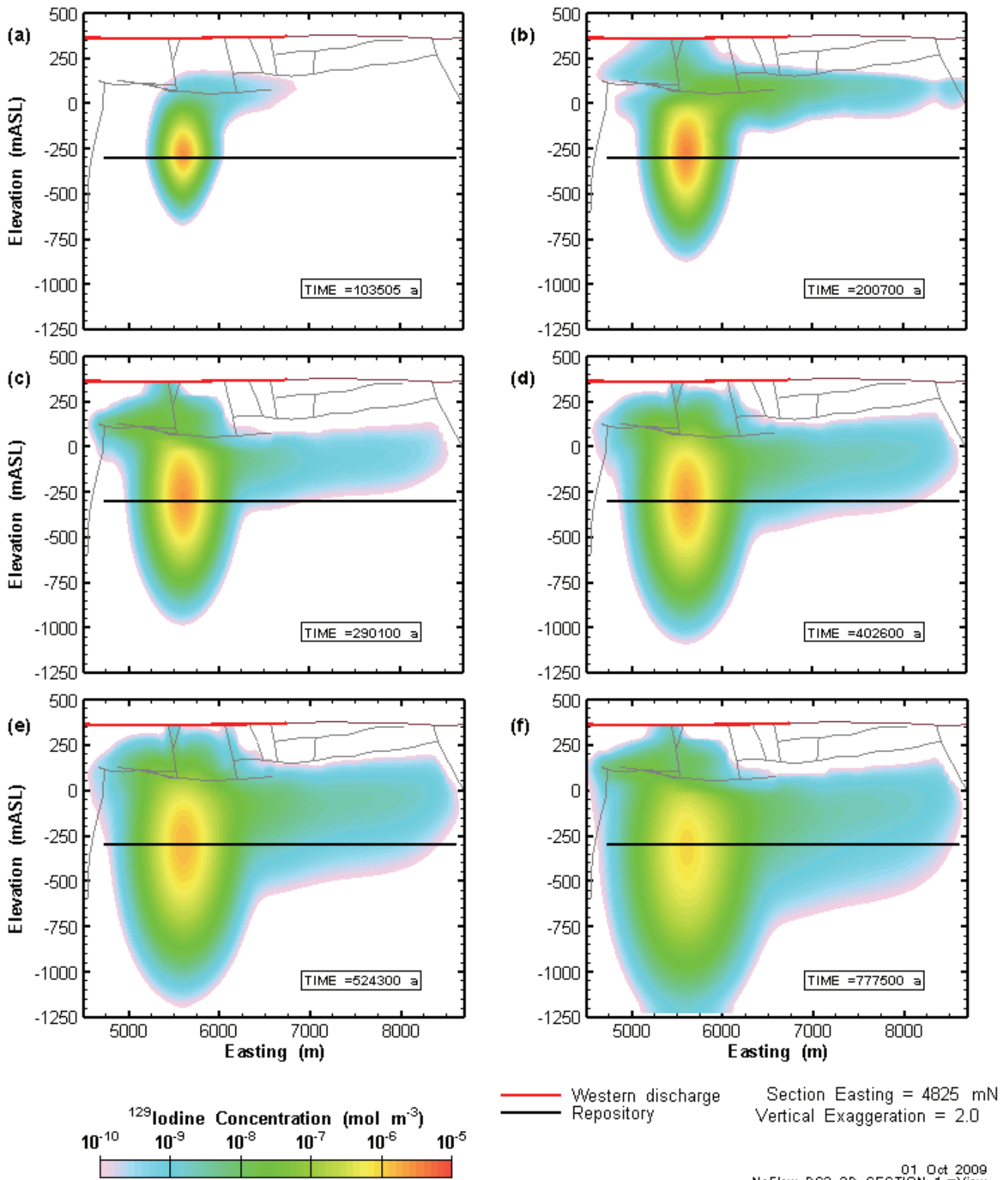


Figure 5.56: GSC-NF (No-Flow N-S boundaries) DC3 X-Z cross-section of transport model results at 6 times during the assessment period. Section northing of 4825 mN.

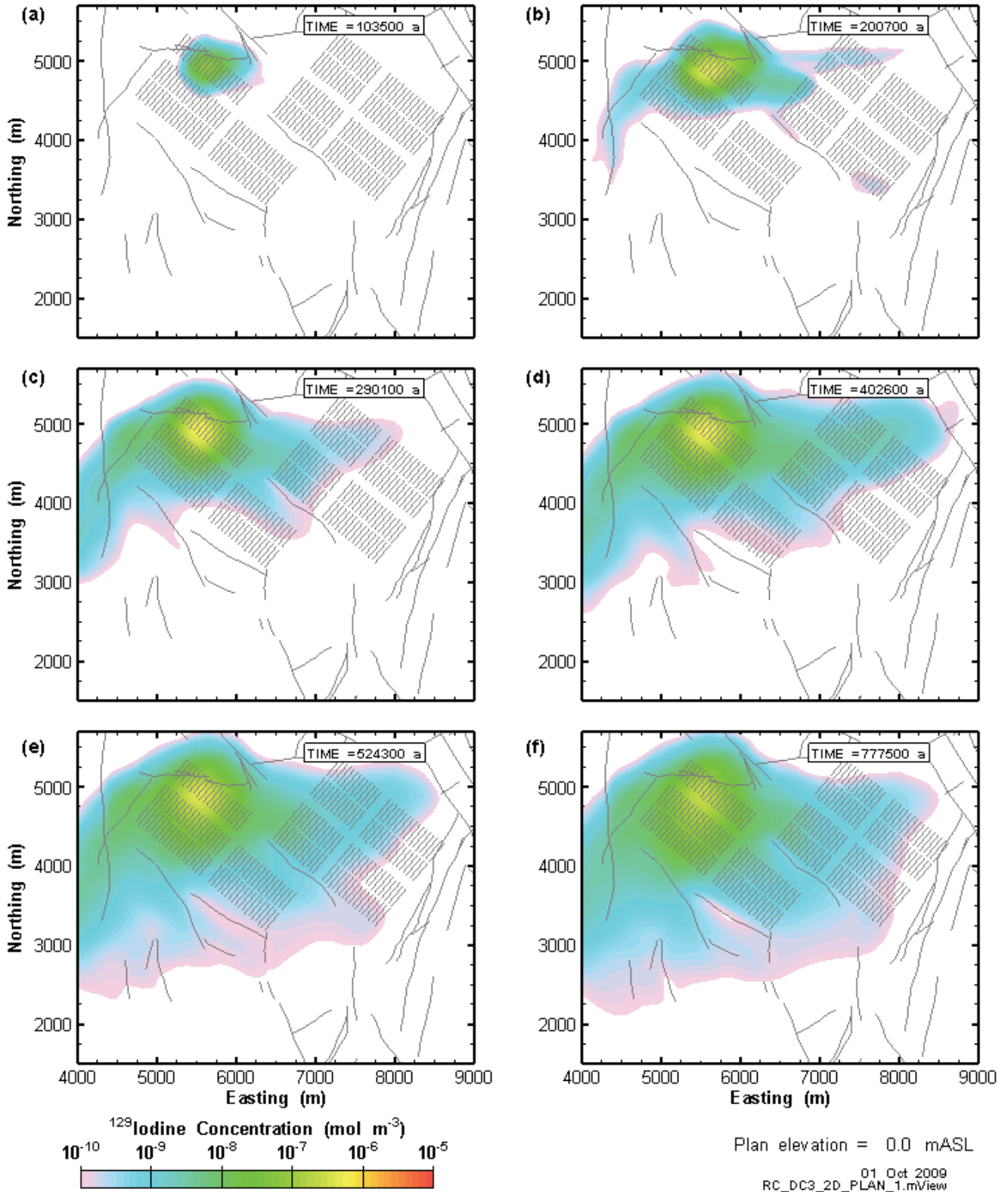


Figure 5.57: GSC-TK (Taluk under glacier) DC3 X-Y planar section of transport model results at 6 times during the assessment period. Section elevation of 0.0 mASL (approx. 350 mBGS).

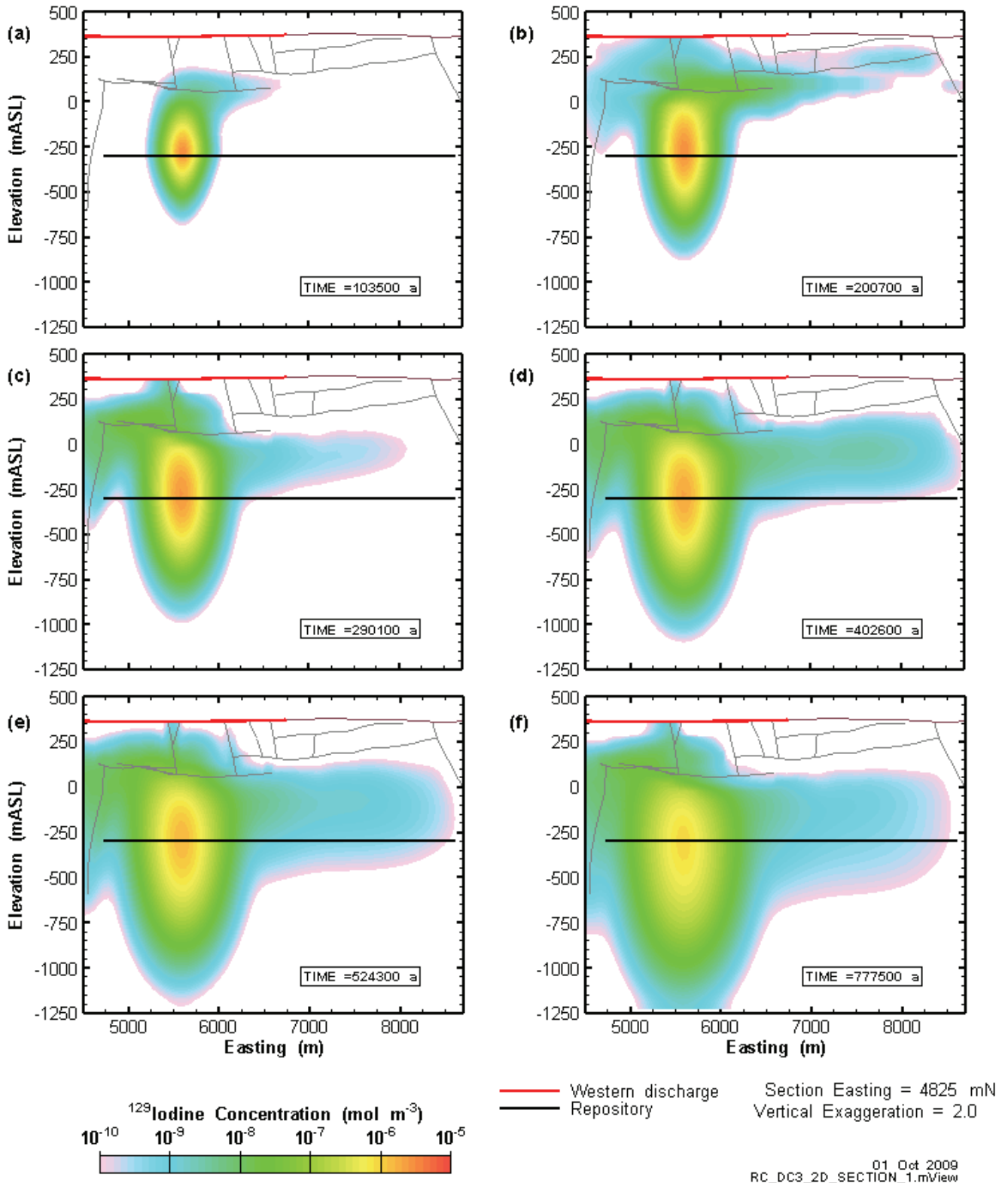


Figure 5.58: GSC-TK DC3 (Talick under glacier) X-Z cross-section of transport model results at 6 times during the assessment period. Section northing of 4825 mN.

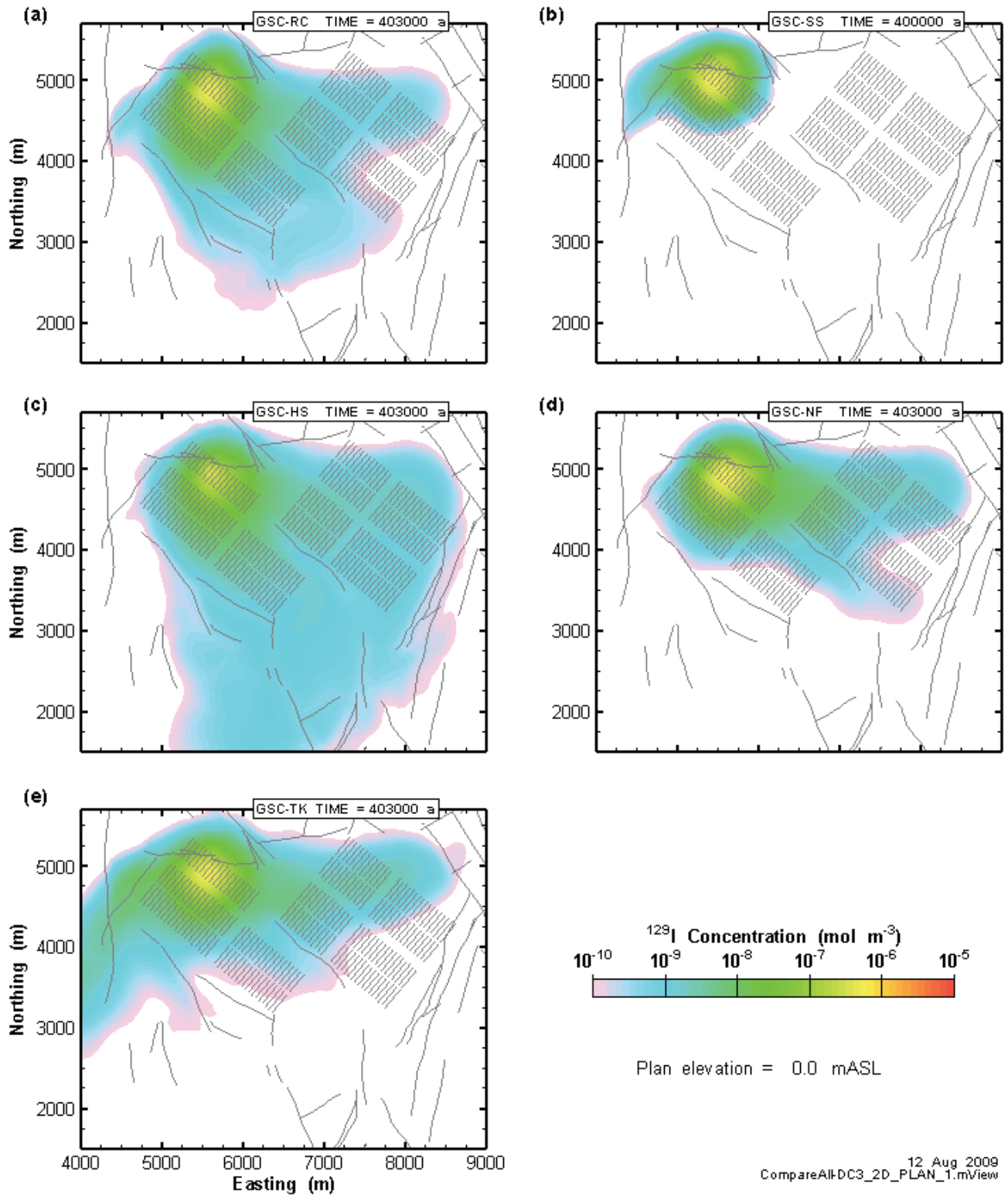


Figure 5.59: All cases comparison of DC3 X-Y planar section through <sup>129</sup>I plume. Section elevation of 0.0 mASL (approximately 350 mBGS).

### 5.3.3 Mass Flow Plots

Mass flow to the biosphere was calculated over the duration of the assessment period. Previous studies had measured  $^{129}\text{I}$  mass flow to the northern talik (referred to as North Lake in the HBC Study) and to the major river south of the repository (River). Results from the GSC simulations also showed mass flux exiting the geosphere in the area several km to the west, due primarily to the dispersal of radionuclides underneath the permafrost during glacial advances. Accordingly, an additional mass flux zone (denoted “Western”) was incorporated in the GSC modelling as shown in Figure 5.60. The southern lake included as a second talik in the current study was also included as a separate mass flow zone (South Lake). All mass flux zones are located at a depth of 30 m below ground surface, and it is assumed that all the  $^{129}\text{I}$  mass crossing this depth will reach the surface biosphere.

Mass flows of  $^{129}\text{I}$  across these zones are presented in the figures on the following pages. Some post-processing of the results has been performed to remove periods of negative (downward) mass flow caused when radionuclide concentrations transported to surface above the mass flux zones during discharge periods were re-injected into the formation when the flow direction reversed. In reality, radionuclides entering a talik, lake, or catchment zone would likely be diluted and swept downstream in a relatively short time, and not be available for reinjection. Removal of the negative mass flux periods is a conservative approach to addressing possible numeric and model errors due to this process.

The mass flow figures present the data as both rates in moles per year and cumulative mass flow in moles. To maintain legibility of the figures for the transient data, the mass flow rate only for the zone with the highest mass flow is typically presented. Typically the difference between the mass flow across the zone with the highest and second highest mass flows is at least a factor of 10. The results shown are limited by the minimum value on the Y-axis, which is  $10^{-8}$  mol/a for the mass flow and  $10^{-4}$  mol for the cumulative mass. Consequently, not all zones may be displayed on all figures. If the cumulative mass curve is not shown, this indicates that the cumulative mass never exceeds the minimum value on the Y-axis. Transient GSC simulation results are compared to corresponding results for the temperate steady-state model without a well in all figures, providing a baseline for comparison between figures. The steady state results without a well are used for comparison because there is no well during most of the transient simulation (e.g., when the area is glaciated or covered by permafrost).

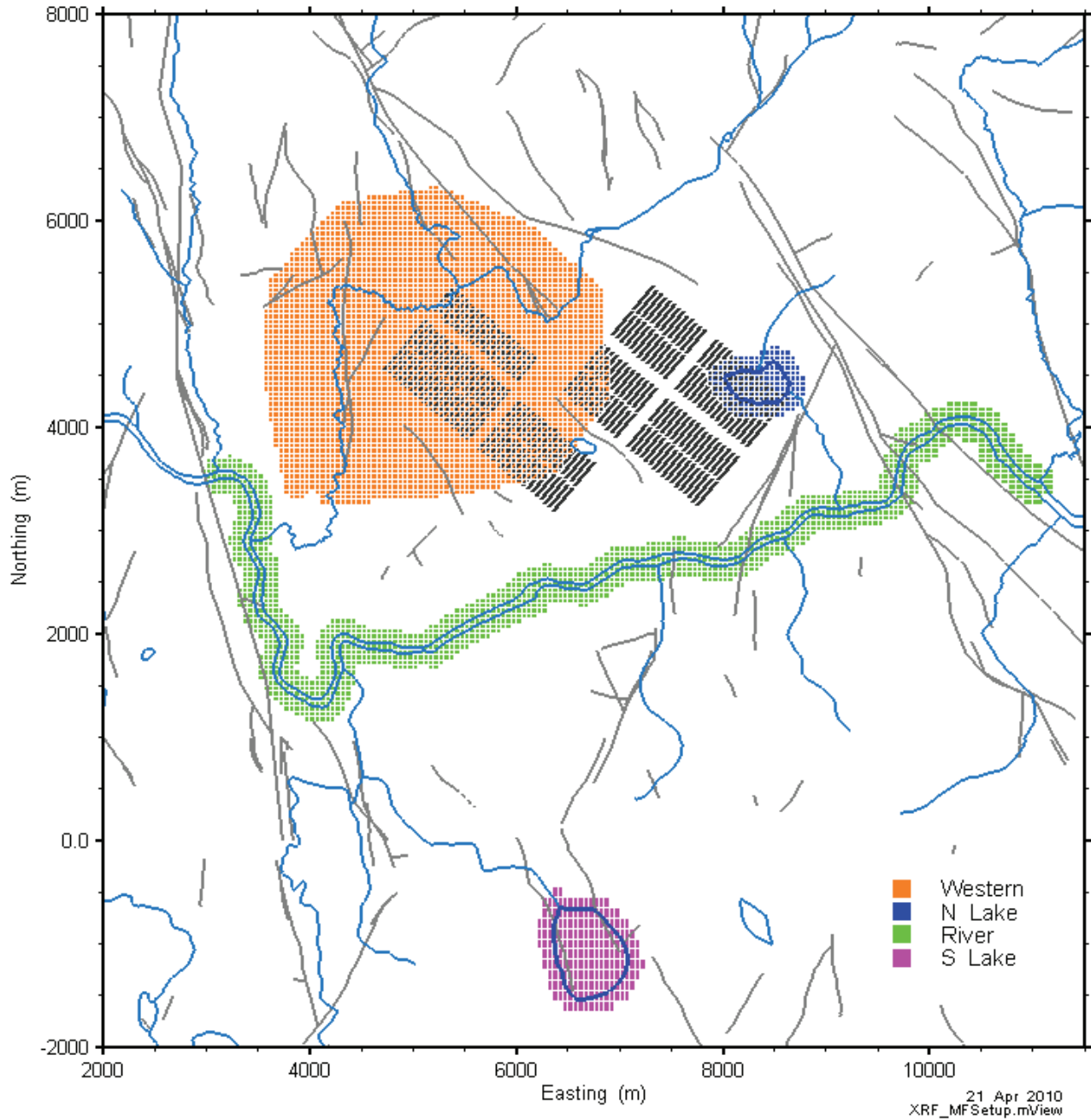


**Figure 5.60: GSC transport mass flow calculation zones.**

### 5.3.3.1 Constant Temperate Climate Model

Figure 5.61 shows the mass flow and cumulative mass results for the 1 million year temperate steady-state flow and transport simulation (GSC-CC), for both Defective Container 1 (DC1) and Defective Container 3 (DC3) locations (see Section 3.6). The mass flow curves are for the case where the well is inactive. This is more directly comparable to the transient runs, where the well is only active during temperate periods. When the well is present, it intercepts the majority of the  $^{129}\text{I}$  that would otherwise cross the North Lake control plane. DC1 is directly below the North Lake zone, so it is unsurprising

that presence of defective containers in this zone would lead to much higher  $^{129}\text{I}$  mass flows to the lake. A small proportion of the contaminant from DC1 also reaches the River zone. No significant amounts of  $^{129}\text{I}$  reach the Western and South Lake zones. In the case of DC3, the only significant mass flow is into the Western zone. DC3 is located below the Western zone.

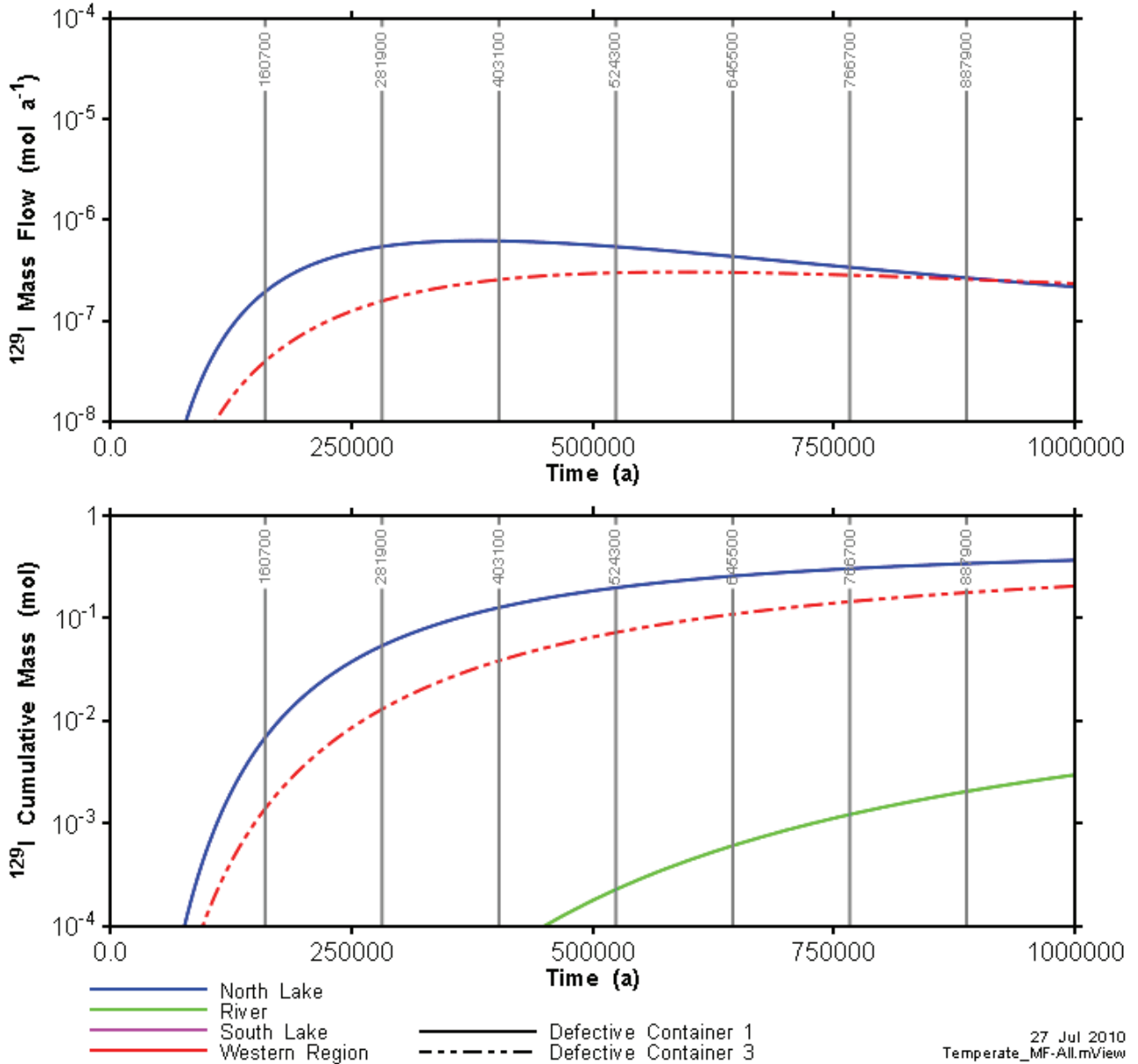
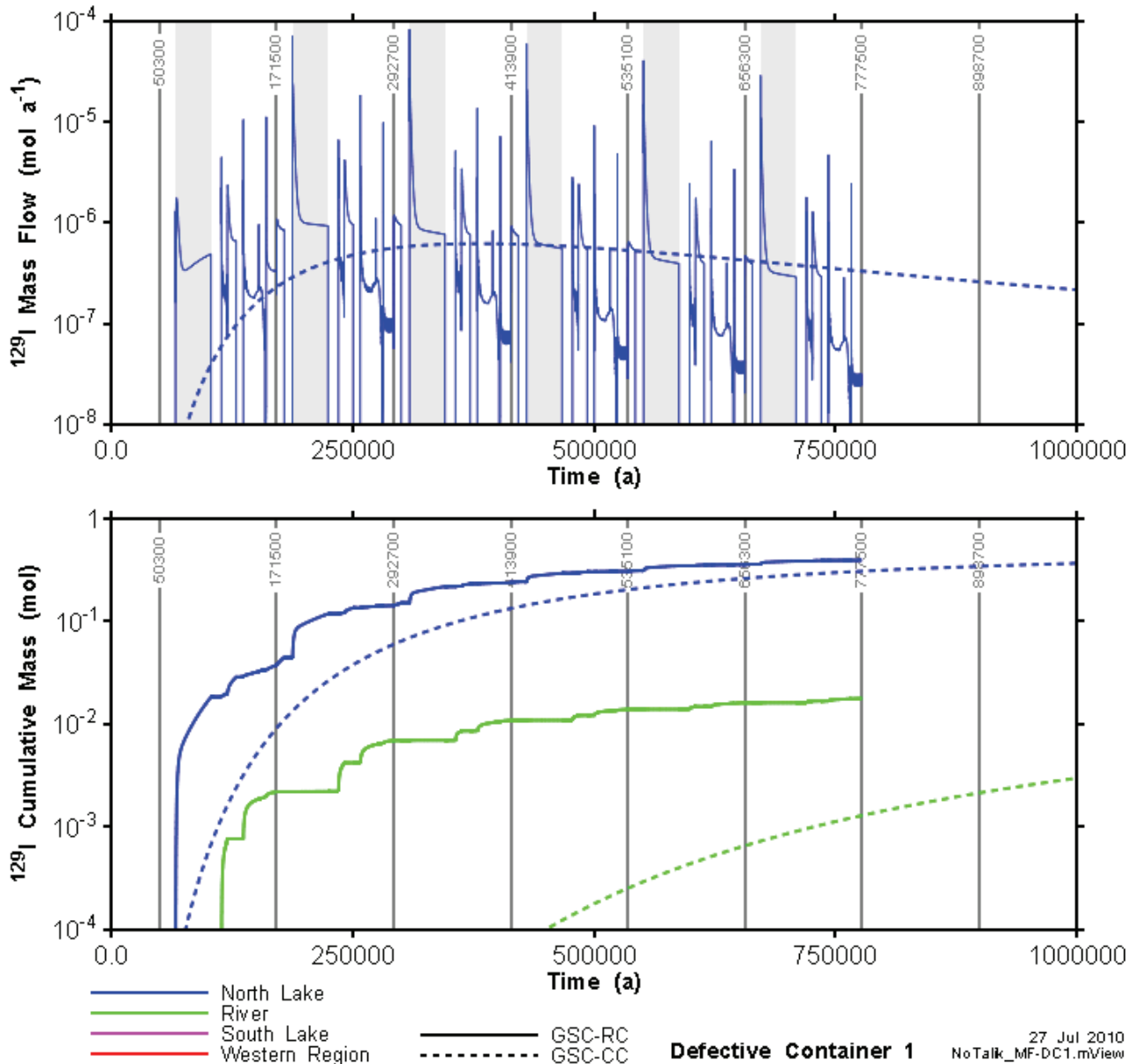


Figure 5.61: GSC-CC results with no well. Displayed are mass flow rate and cumulative mass from DC1 and DC3. Lines in the legend that do not appear on the plot are below the minimum value on the Y-axis.

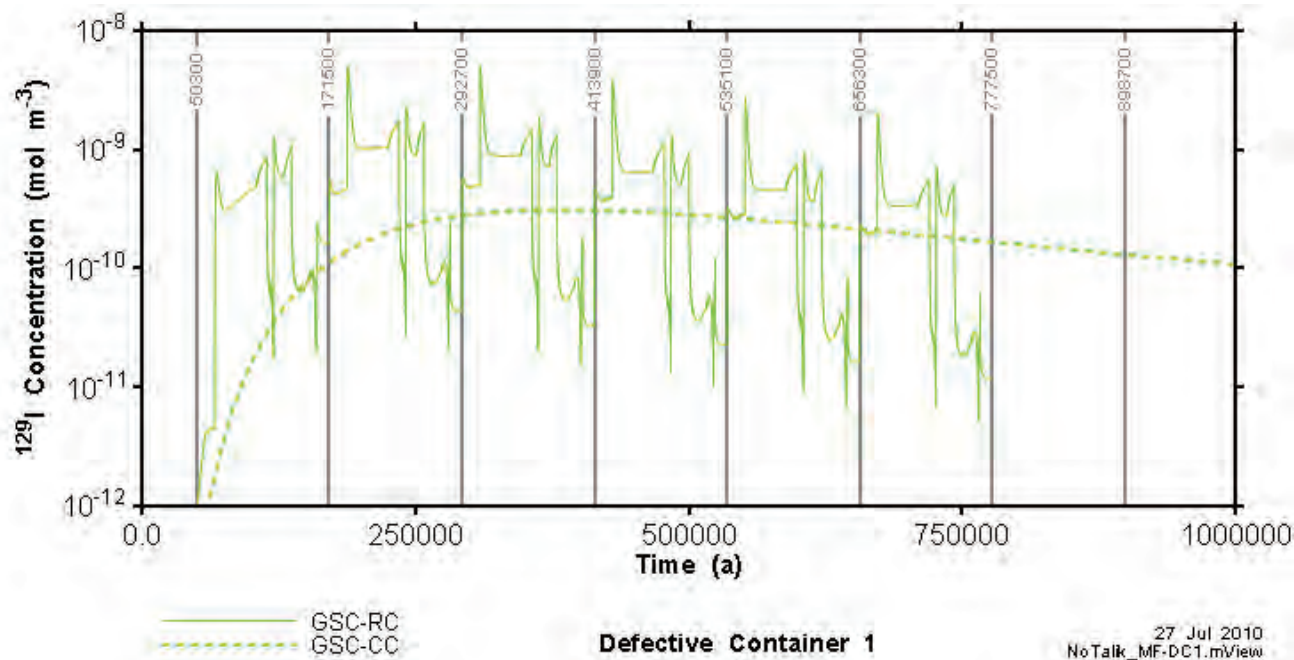
### 5.3.3.2 Transient Modelling Cases – Defective Containers in DC1 Location

Figure 5.62 shows the mass flow results for the Reference Case (GSC-RC) transient model with the DC1 source, and the corresponding GSC-CC results. The mass flow rate curve is clearly quite different for the transient model, with a large variation in the  $^{129}\text{I}$  mass flow rate. However, the overall trend is similar. The transient model predicts roughly similar cumulative mass flows through the North Lake zone by the end of the simulation at 0.8Ma. The GSC-RC model clearly causes  $^{129}\text{I}$  to be transported over a larger region, as evinced by higher flows to the River zone as compared to the GSC-CC model.



**Figure 5.62: GSC-RC  $^{129}\text{I}$  mass flow rate and cumulative mass from DC1, compared to GSC-CC (without well). Mass flow only plotted for North Lake to improve legibility of plot. Mass flow data processed to remove small negative flows. Shaded regions show the second permafrost state in each glacial cycle.**

Note that these results show  $^{129}\text{I}$  mass flows and not concentrations. The variability of the concentration is more muted because the larger  $^{129}\text{I}$  mass flows are associated with higher water discharge rates. Figure 5.63 shows the average concentration of  $^{129}\text{I}$  in water crossing the North Lake control surface. The concentration varies over two orders of magnitude, as opposed to the roughly three orders of magnitude variation in  $^{129}\text{I}$  mass flow. Although concentration alone does not explain the variation in mass flow rate, increased mass flow and concentration are correlated, as the more concentrated water flows up from greater depths.



**Figure 5.63: The  $^{129}\text{I}$  concentration in water crossing the North Lake control plane, for the GSC-RC and GSC-CC modelling cases.**

Some of the mass flow results for this transient model are rather counterintuitive. Figure 5.64 is a close-up of the second glacial cycle. It is evident that the highest mass flows occur at the beginning of permafrost stages, particularly the second permafrost stage (stage 5, Table 2.1). High mass flow rates at the start of this stage are due to high pressures stored in the subsurface from the preceding glaciation. With the surface largely covered by an impermeable permafrost layer, the northern talik (North Lake), located directly above DC1, is one of the few hydraulic outlets for the system. Thus flow is focussed in the vicinity of this talik, causing high velocities and promoting transport of  $^{129}\text{I}$  from the repository to the surface across this control plane (see Figure 5.6). However, it is clear from Figure 5.9, Figure 5.10, and Figure 5.20 that the glacial retreat (stage 11) and postglacial lake (stage 12) also have relatively high upward advective flows in the vicinity of the repository. The high vertical advective velocity is not reflected in the observed  $^{129}\text{I}$  mass flow. Above roughly 200 mASL, the predominant flow direction shifts from vertically upward to horizontally southward, due to the variable specified head at the surface that represents the slope of the ice surface. This horizontal flow sweeps the  $^{129}\text{I}$  plume towards the south, away from the area directly below the northern talik. Although upward flow is re-established in the pro-glacial lake stage, the  $^{129}\text{I}$  concentration directly below the North Lake zone is now rather low, and this stage is not long enough to bring significant amounts of radionuclide from greater depths to cross the mass flow zones at the surface. So, although the overall vertical upward gradient is high during both the glacial retreat and the proglacial lake stages, the mass flux across the defined surfaces is low.

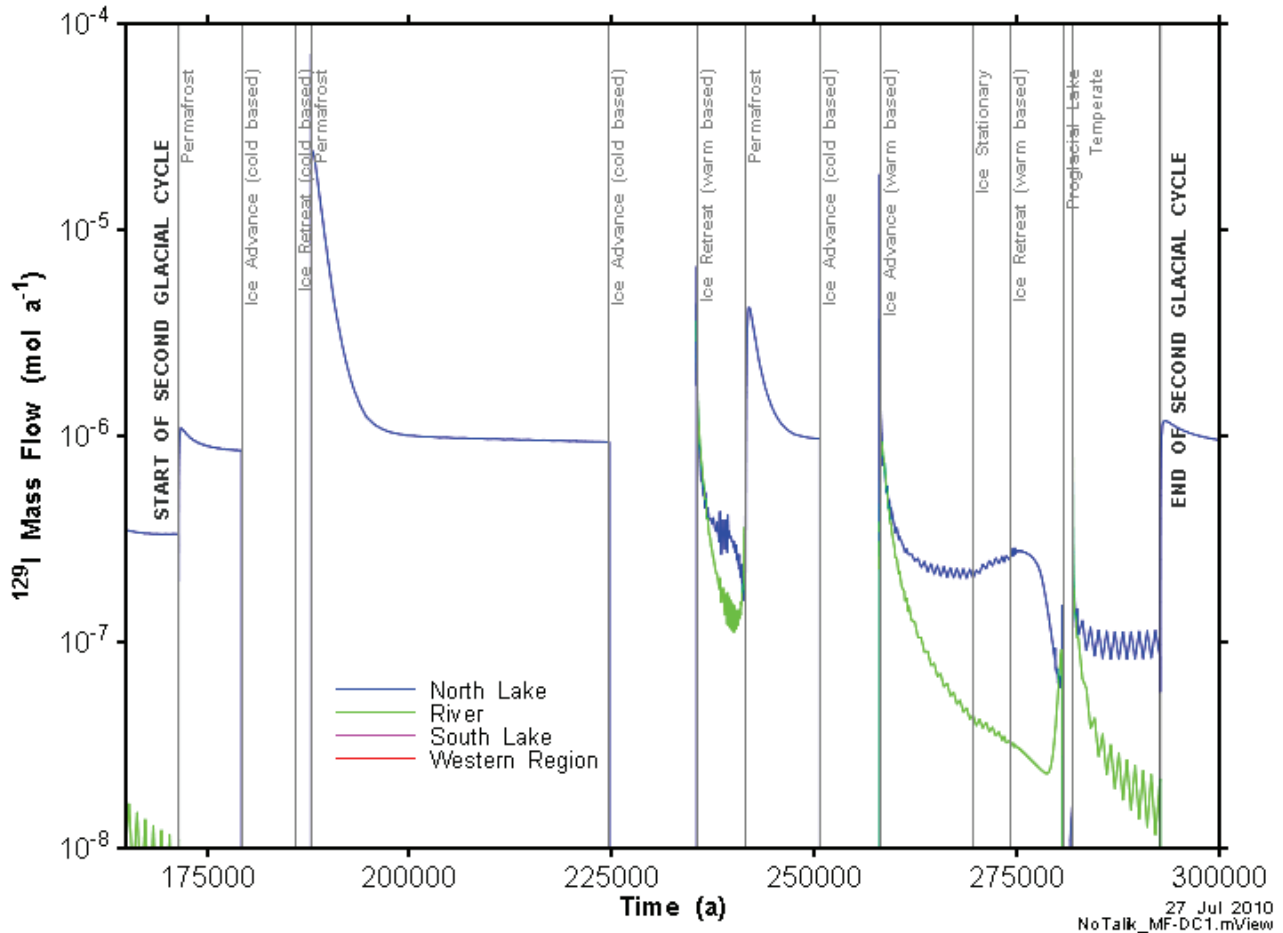
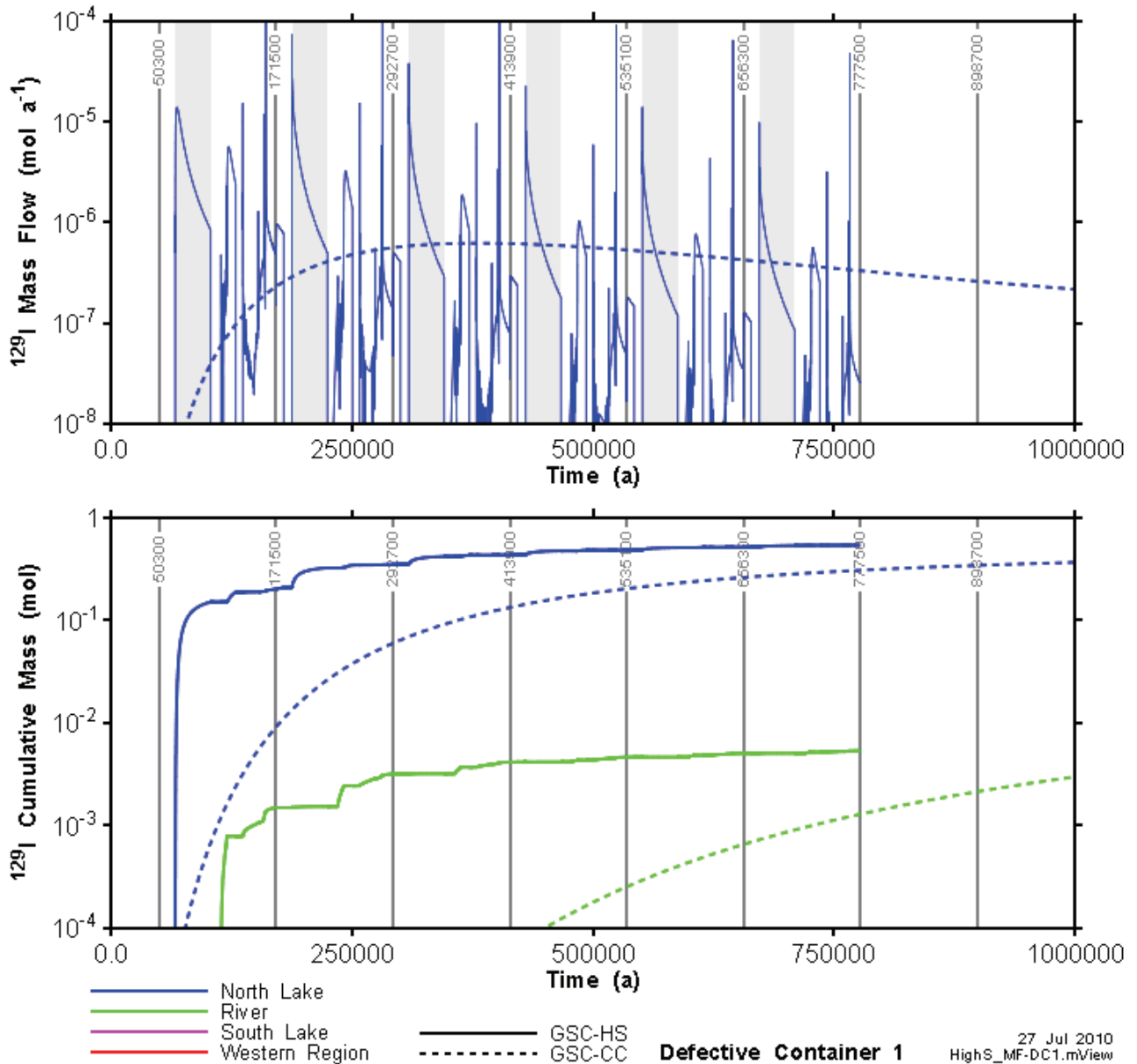


Figure 5.64: GSC-RC DC1  $^{129}\text{I}$  mass flow rates for second glacial cycle.

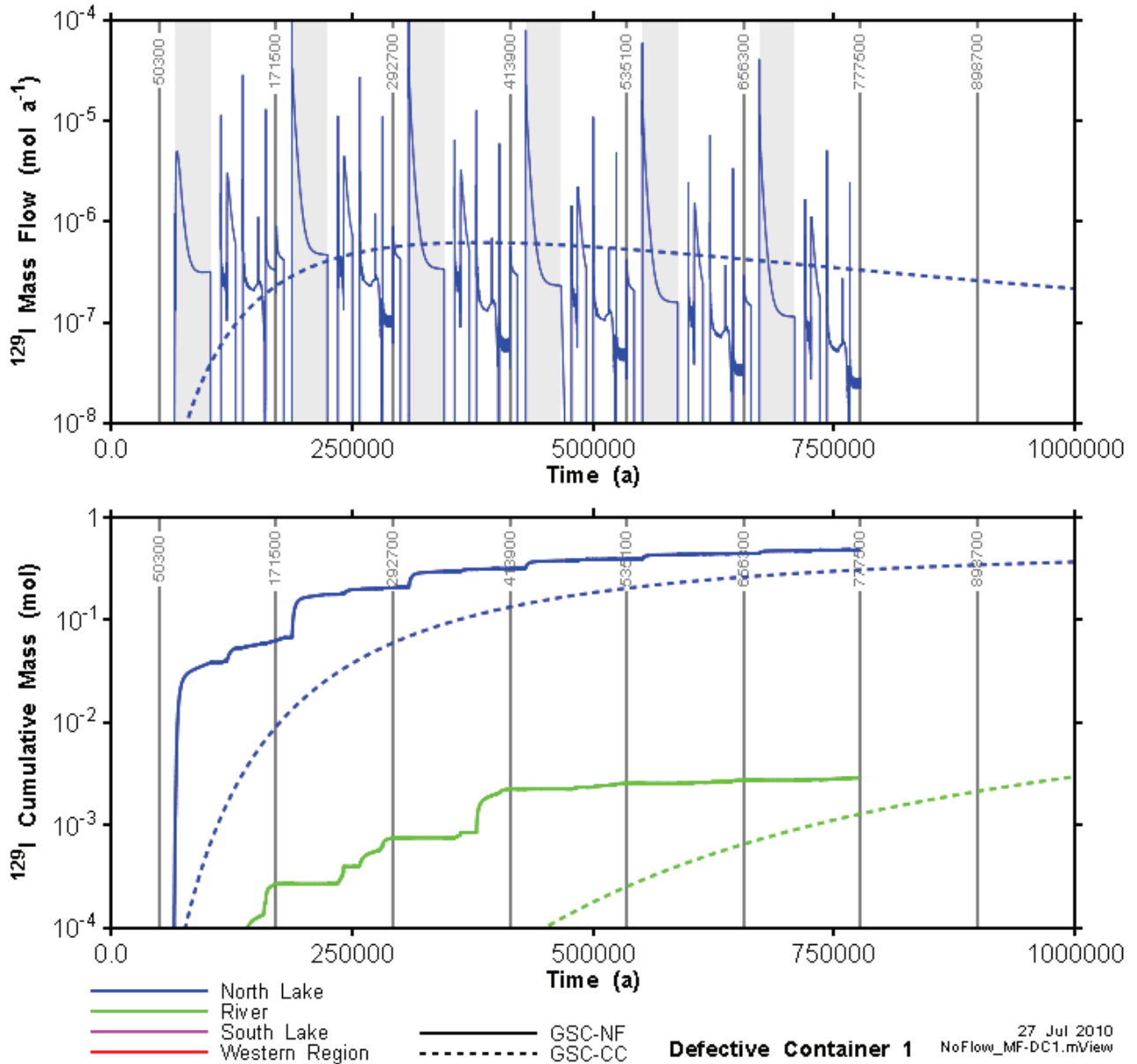
Figure 5.64 shows some evidence of numerical instability in the flow solution, particularly during the second (warm-based) ice retreat between 235,500 and 241,500 years. The oscillations are a direct consequence of the small oscillation in the flow solution (see Figure 5.20). This numerical instability reduces the accuracy of the model to a limited degree during these stages of the glacial cycle. However, the fluctuations remain relatively small and tend to oscillate around a mean correct value so the results are still sufficiently accurate for the purposes of this report.

Figure 5.65 shows the  $^{129}\text{I}$  mass flows for the GSC-HS case. As described earlier, in sections 5.2.1.2 and 5.2.3, the average advective velocity is much higher in the GSC-HS model as compared to the Reference Case. High heads stored in deeper units during glacial advance persist for much longer after the ice has retreated. The difference between the two cases is especially clear in mass flow curves during the second permafrost period in each glacial cycle. In Figure 5.62, the peak mass flux occurs at the beginning of the second permafrost period, but decays to a steady state flow rate in less than 10,000 years, as the stored pressures in the deep units dissipate. In contrast, in Figure 5.65, the mass flow rate during the second permafrost period never reaches a steady state, meaning that at the beginning of the next ice advance, after 36,800 years of permafrost cover, stored heads from the preceding glaciation are still present in the deeper parts of the geological sequence. Naturally, the presence of high vertical gradients for a much longer time promotes increased vertical transport. The cumulative  $^{129}\text{I}$  mass flow across the North Lake mass flow boundary is 26% higher than in the GSC-RC case. The slower response time of the GSC-HS system causes a slower decrease in the mass flows following peaks as compared to the reference case.



**Figure 5.65: GSC-HS <sup>129</sup>I mass flow rate and cumulative mass from DC1, compared to GSC-CC (without well). Mass flow only plotted for North Lake to improve legibility of plot. Mass flow data processed to remove small negative flows. Shaded regions show the second permafrost state in each glacial cycle.**

In some ways, the GSC-NF case, with no flow North and South boundaries, mirrors the GSC-HS case, although the mechanism is different. The peak mass flux in any given glacial cycle occurs at the beginning of the second permafrost period, when significant heads from the preceding glaciation are stored in the hydrogeological system. Because the no-flow vertical boundaries to the North and South in the GSC-NF case do not provide hydraulic outlets for the stored pressure, the only route for water to escape is through the two taliks. This forces flow from the entire model domain through these two relatively small areas, and causes the system to require a much longer time to reach steady state (roughly 25,000 years). So, despite the fact that heads in the subsurface do not reach the same level during the preceding cold-based advance and retreat, the GSC-NF model still ultimately has higher cumulative mass flows across the North Lake zone, 12% higher than the Reference Case.



**Figure 5.66: GSC-NF mass flow rate and cumulative mass from DC1, compared to GSC-CC (without well). Mass flow only plotted for North Lake to improve legibility of plot. Mass flow data processed to remove small negative flows. Shaded regions show the second permafrost state in each glacial cycle.**

The GSC-TK case is very similar to the Reference Case, except that the two taliks remain open under cold-based glacial advances and retreats, resulting in only rather small and transient alterations to the radionuclide plume, as seen in section 5.3.1. During glacial advances and retreats, when the taliks are open, there is a greater spreading and dilution of the upper part of the plume caused by the inflow across the northern talik. Comparing Figure 5.67 to Figure 5.62 indicates that this has a small overall effect on the mass flow rate. In fact, the cumulative  $^{129}\text{I}$  mass flow across the North Lake mass flow boundary is only 22% less than the GSC-RC case. However, the  $^{129}\text{I}$  mass flow to the Western region is larger for case GSC-TK than case GSC-RC because groundwater injected across the taliks during

cold based glaciation spreads the dilute outer plume more widely than in the Reference Case model (see Figure 5.48).

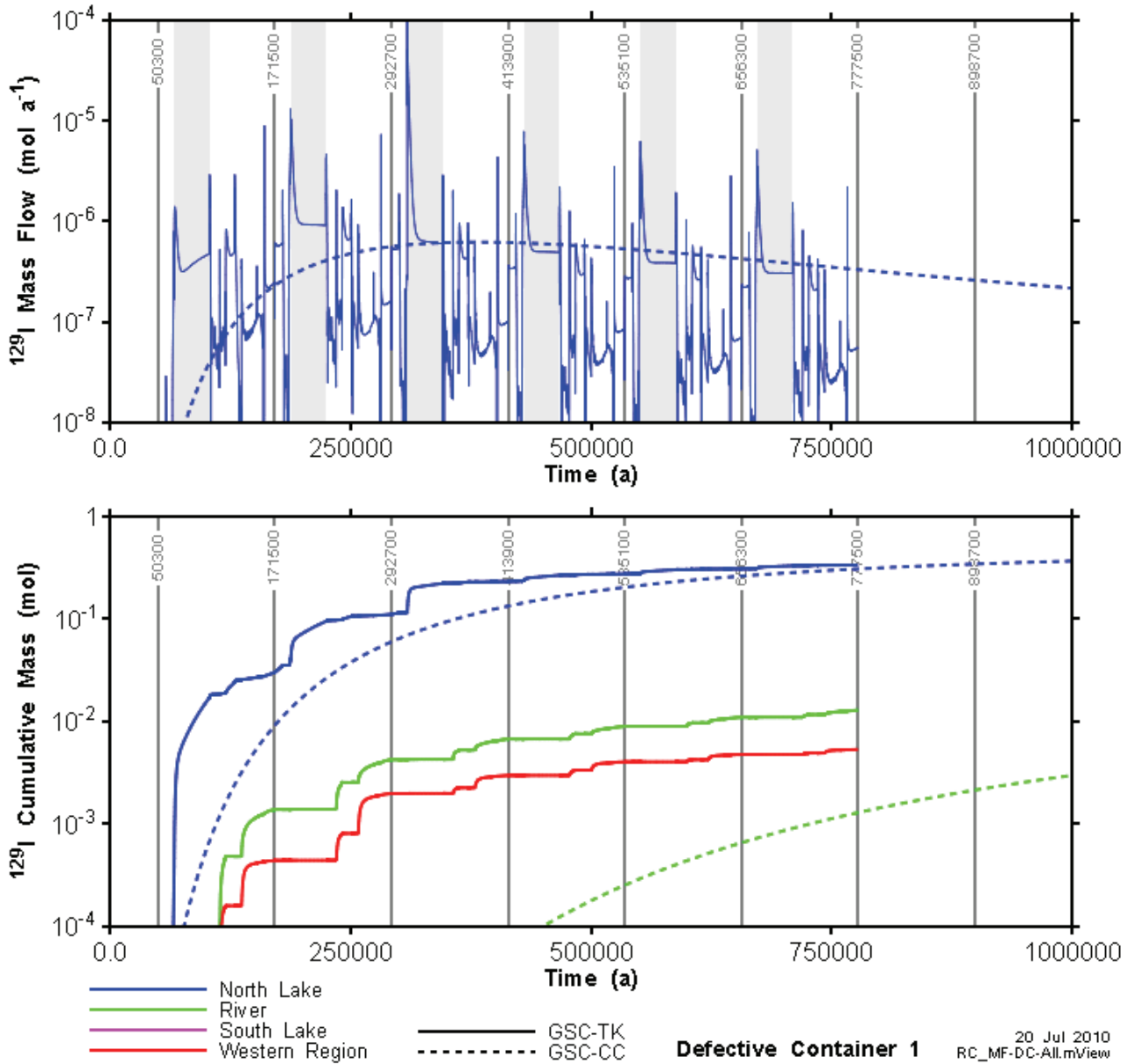


**Figure 5.67: GSC-TK mass flow rate and cumulative mass from DC1, compared to GSC-CC (no well). Mass flow only plotted for North Lake to improve legibility of plot. Mass flow data processed to remove small negative flows. Shaded regions show the second permafrost state in each glacial cycle.**

### 5.3.3.3 Transient Modelling Cases – Defective Containers in DC3 Location

Figure 5.68 shows the Reference Case mass flow curves for source DC3. The DC3 source is located beneath the Western discharge zone, and consequently the highest mass flows are across this

surface. Despite the very different flow fields there is a remarkable correspondence between the GSC-RC DC3 and GSC-CC DC3 cumulative mass curve for the Western Region.

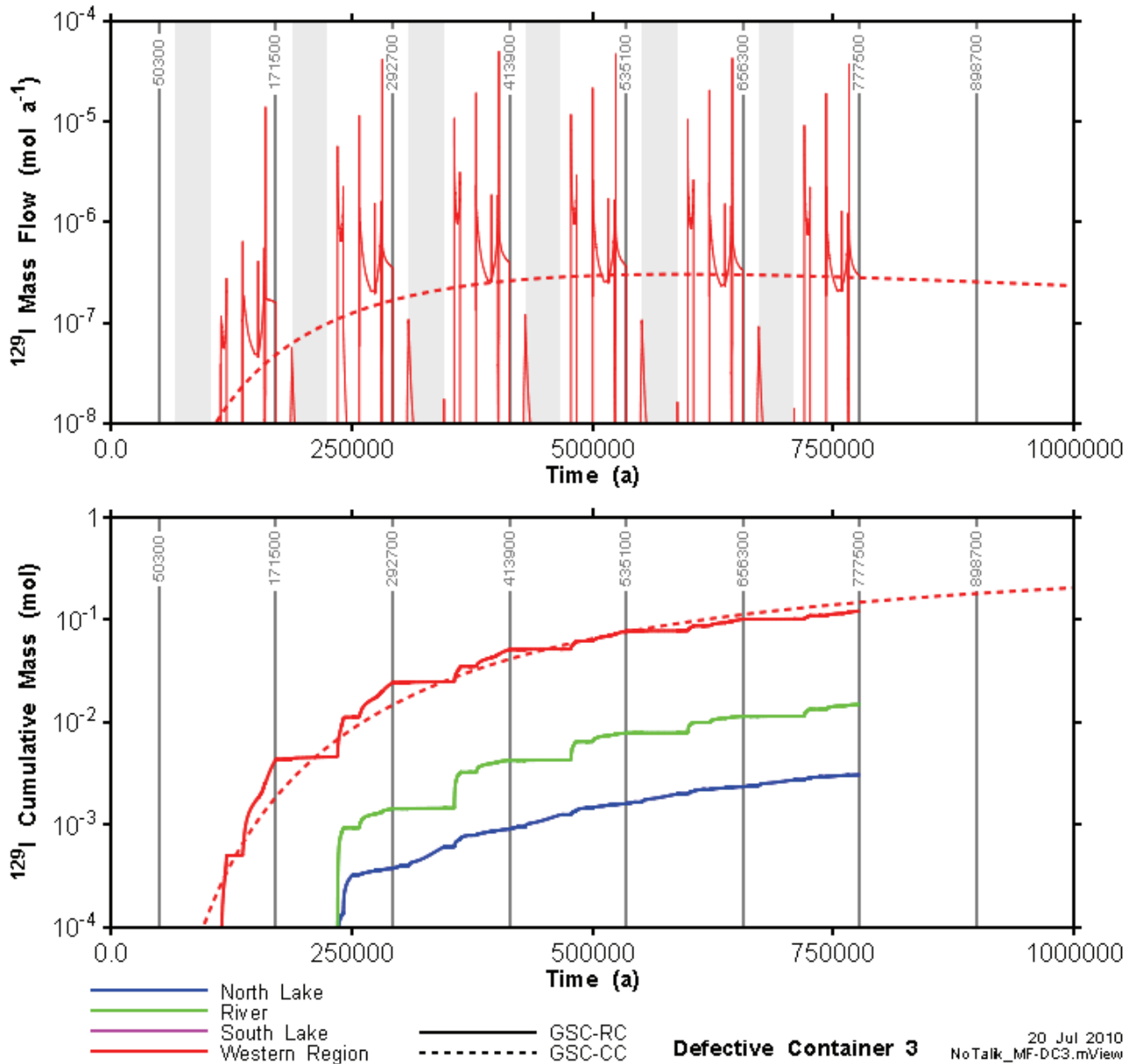


**Figure 5.68: GSC-RC mass flow rate and cumulative mass from DC3, compared to GSC-CC (no well). Mass flow only plotted for Western region to improve legibility of plot. Mass flow data processed to remove small negative flows. Shaded regions show the second permafrost state in each glacial cycle.**

Figure 5.69 shows the mass flow curve for the second glacial cycle in greater detail. Unlike the DC1 mass flux curves, the  $^{129}\text{I}$  mass flows during permafrost periods are not very high, evidently because there is no open talik directly above the DC3 source during permafrost periods. The highest mass flows occur when there is no permafrost cover, particularly during warm based glacial retreats when the upward advective flow velocity is at its highest (since the specified head at the surface drops continuously). Overall, radionuclide mass reaches the surface more slowly from DC3 than it does from DC1.

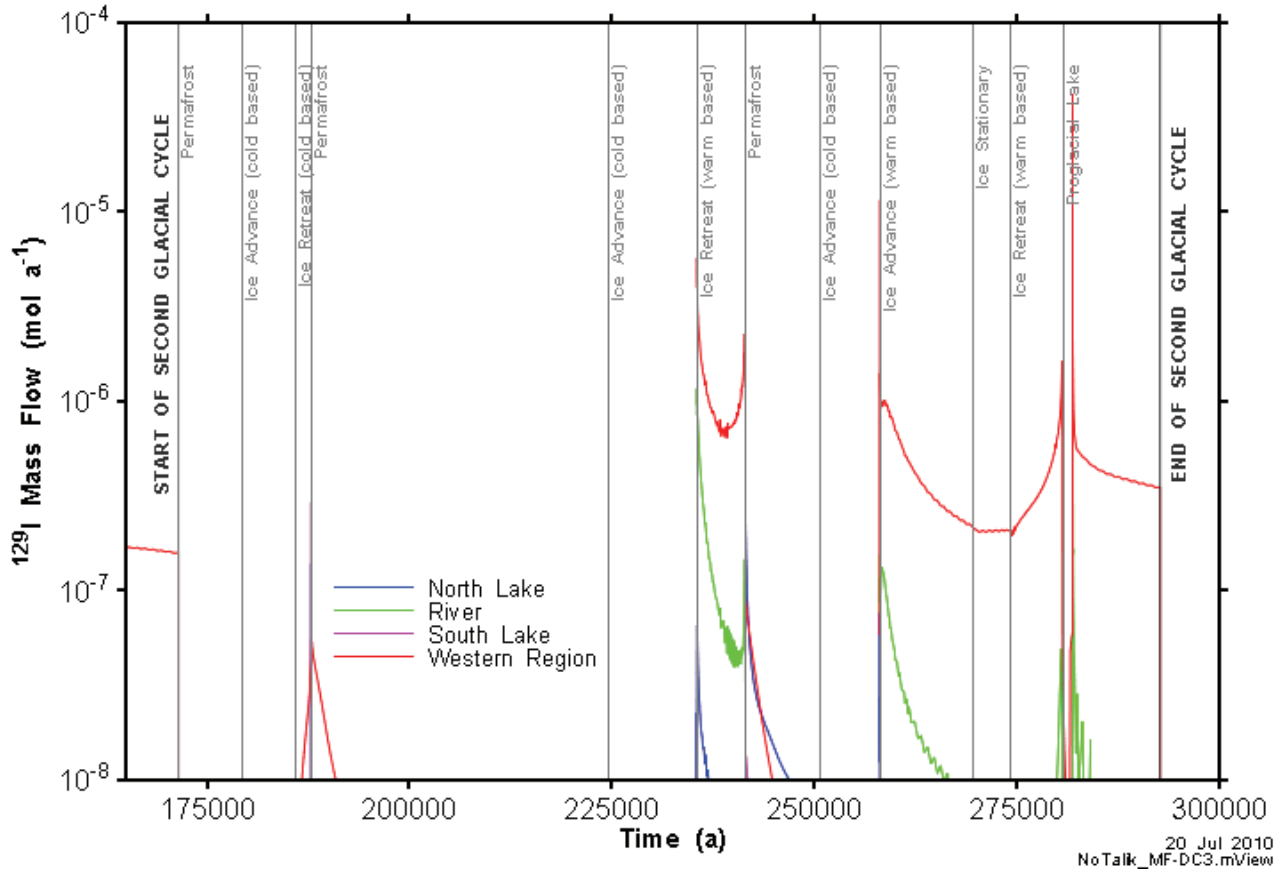
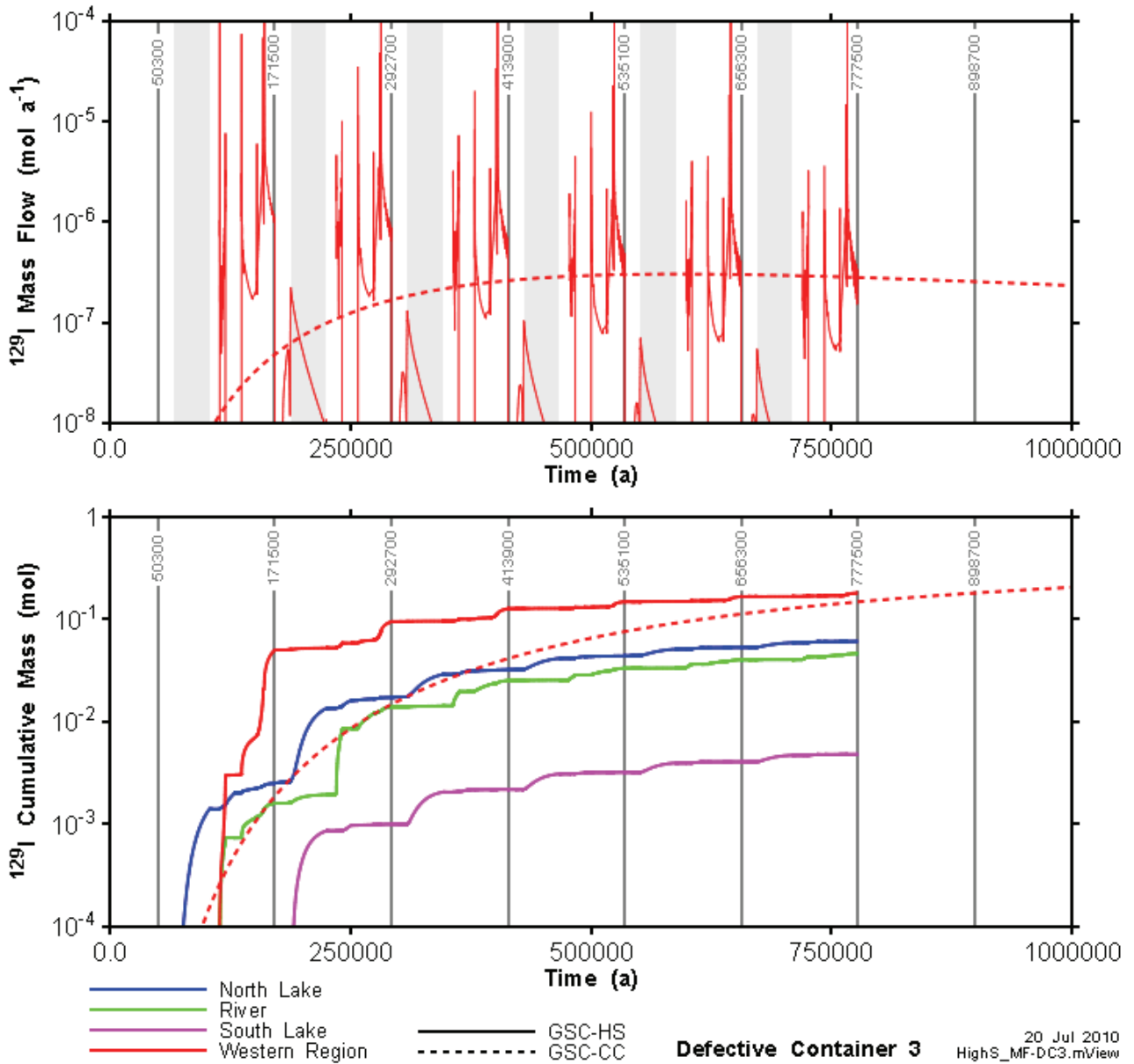


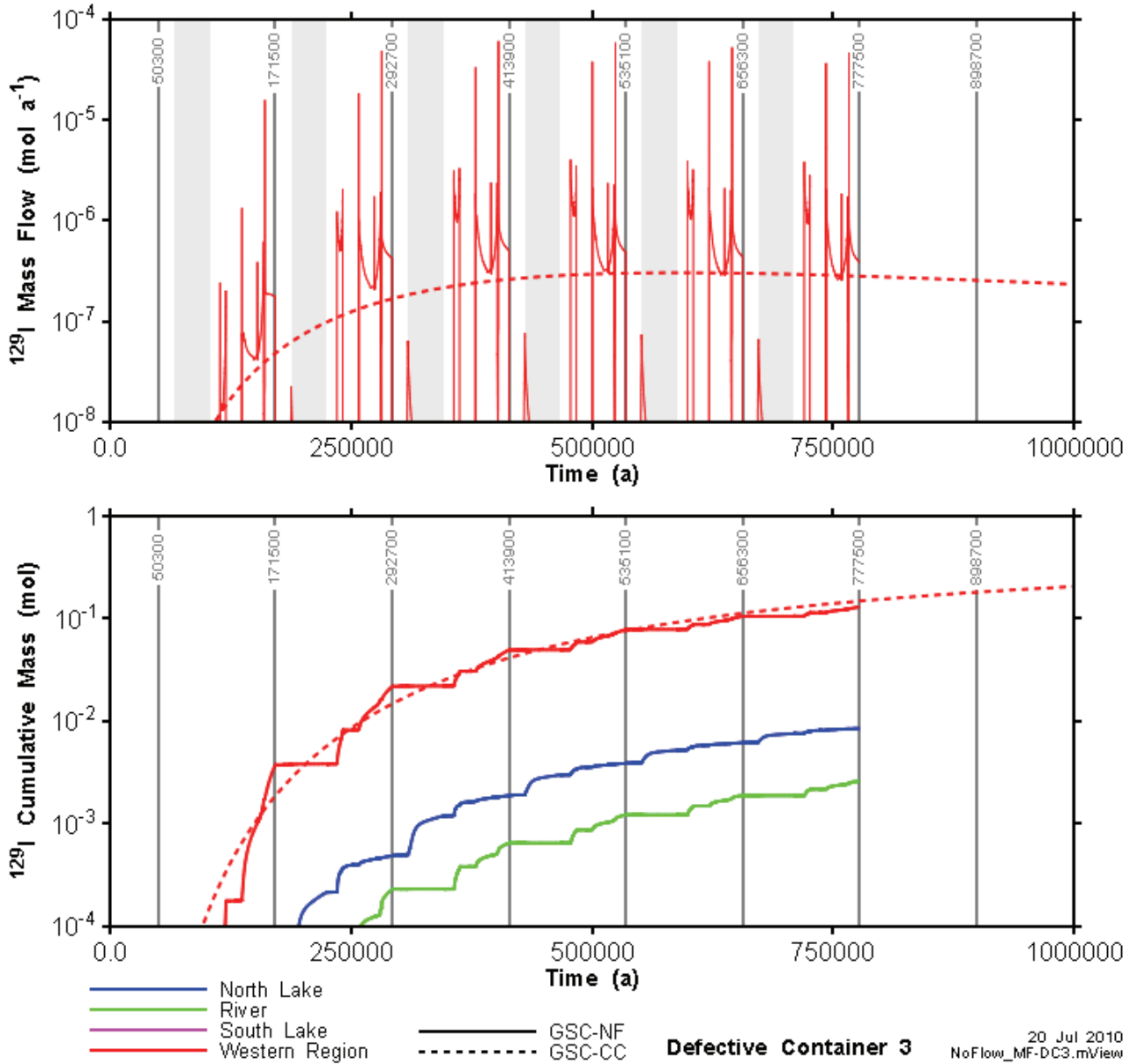
Figure 5.69: GSC-RC DC3 <sup>129</sup>I mass flow rates for second glacial cycle.

Figure 5.70 shows <sup>129</sup>I mass flow results from the GSC-HS model, with the DC3 source location. Unlike the GSC-RC model, among the highest sustained mass flows are seen during the postglacial temperate phases as the high postglacial heads persist well into the temperate stage due to the higher storage coefficient. Otherwise, the highest mass flows occur during warm-based glacial retreats. The higher average velocity in the GSC-HS model leads to much higher mass flows across the Western zone during the first 250,000 years. At later times however, the dilution of the source leads to lower mass flows, such that at the end of the assessment period the cumulative mass flow across the Western zone is similar to that in the GSC-RC model. The greater spreading of the plume in the GSC-HS model causes much higher radionuclide mass flows across the North Lake, South Lake, and River control planes than was seen in the Reference Case model.



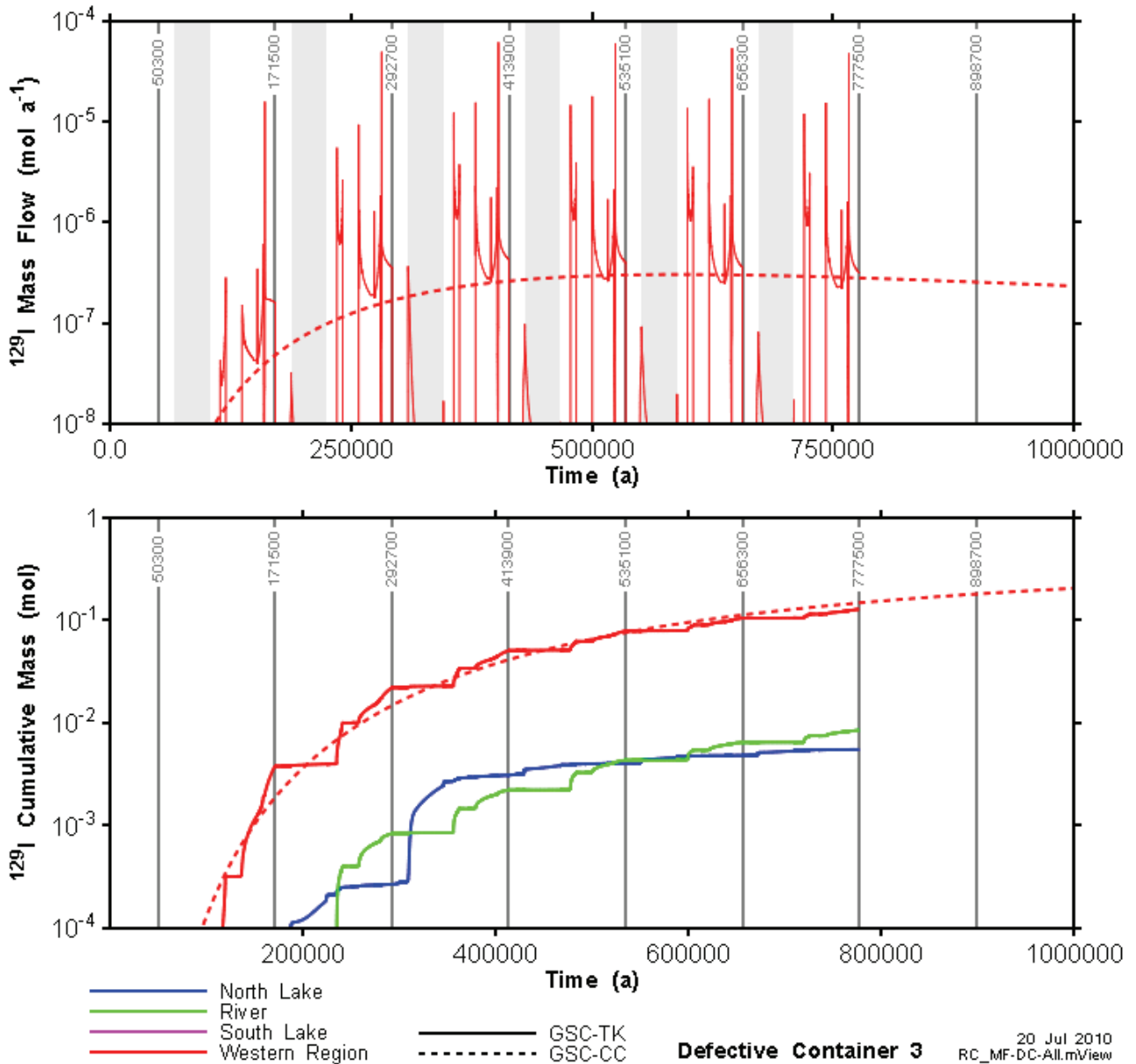
**Figure 5.70: GSC-HS <sup>129</sup>I mass flow rate and cumulative mass from DC3, compared to GSC-CC (no well). Mass flow only plotted for Western region to improve legibility of plot. Mass flow data processed to remove small negative flows. Shaded regions show the second permafrost state in each glacial cycle.**

Figure 5.71 shows the <sup>129</sup>I mass flow curves for the GSC-NF model. Overall, the mass flows are very similar to the Reference Case model. The correspondence between the transient GSC-NF and the steady-state GSC-CC Western region cumulative mass flow curves is also remarkable, when one considers the very different mass flow rate curves for the GSC-NF and GSC-CC cases. The open talik during cold-based glaciation events causes an increase in <sup>129</sup>I transport across the North Lake control surface, and an overall reduction in transport across the River control surface due to reduced transport to the south.



**Figure 5.71: GSC-NF <sup>129</sup>I mass flow rate and cumulative mass from DC3, compared to GSC-CC (no well). Mass flow only plotted for Western region to improve legibility of plot. Mass flow data processed to remove small negative flows. Shaded regions show the second permafrost state in each glacial cycle.**

Figure 5.72 shows the <sup>129</sup>I mass flow curves for the GSC-TK model. In general, the mass flows are very similar to the Reference Case model. The open talik during cold-based glaciation events causes an increase in radionuclide transport across the North Lake control surface and an overall reduction in transport across the River control surface.



**Figure 5.72: GSC-TK <sup>129</sup>I mass flow rate and cumulative mass from DC3, compared to GSC-CC (no well). Mass flow only plotted for Western region to improve legibility of plot. Mass flow data processed to remove small negative flows.**

#### 5.3.3.4 Well Concentration

Concentrations of <sup>129</sup>I in well water are presented in Figure 5.73 for the transient and steady-state temperate calculation cases. Concentration trends in the well for the steady-state and transient cases are generally similar. In some cases the transient model predicted much higher well concentration than the steady state model, while in other cases the predicted well concentration was consistently lower. Of all the calculation cases, the GSC-HS model always predicted the highest well concentrations, but the concentration drops from its peak much more rapidly than the GSC-RC model. For all transient DC1 scenarios, the well concentration peaks at 160,700 years, at the start of the second temperate period. This is much earlier than for the GSC-CC case, for which the well

concentration peaks at 400,000 years. This earlier peak is consistent with what was observed for the mass flow curves in section 5.3.3.2.

The sharp peaks in the  $^{129}\text{I}$  well water concentrations at the beginning of the temperate periods are likely caused by the rapid drainage of the proglacial lake. This peak is particularly pronounced for the GSC-HS case. For this case, the peak does not persist for long and within 200 years the  $^{129}\text{I}$  well water concentration drops by about one order of magnitude. For the other glaciation cases, the well concentration decreases more slowly.

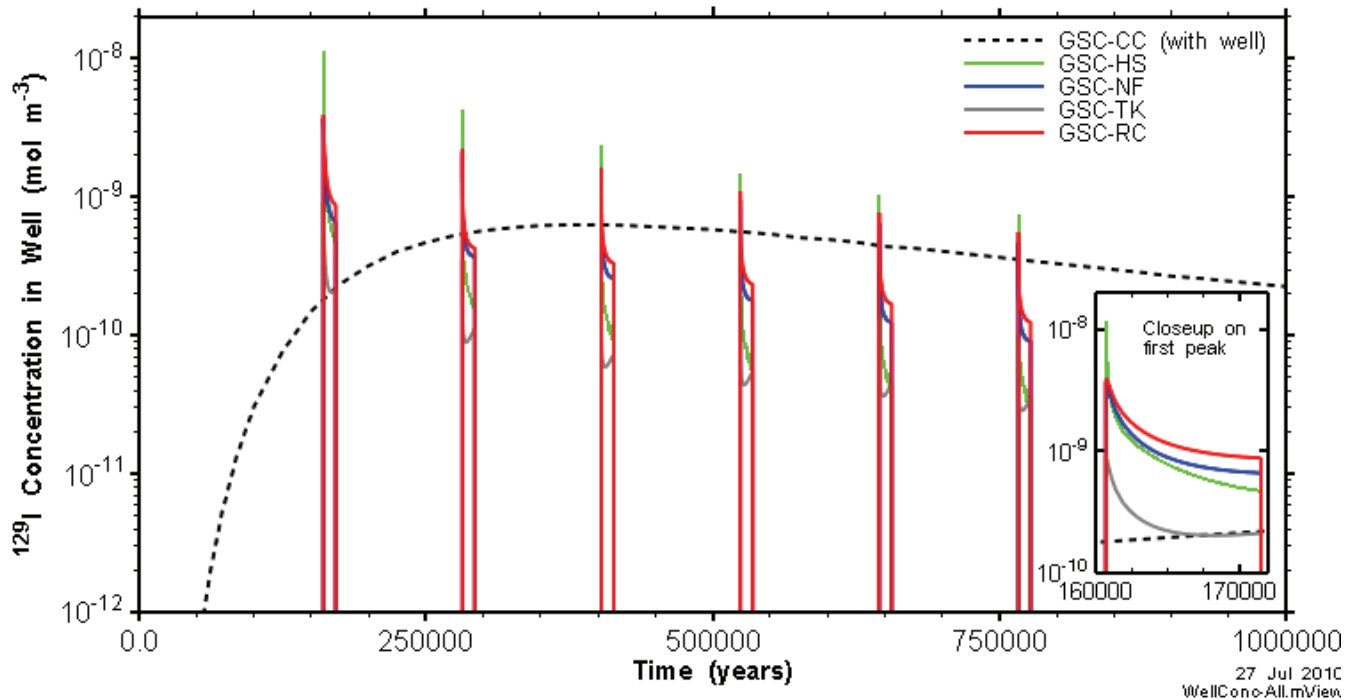


Figure 5.73:  $^{129}\text{I}$  concentrations in water-supply well for all DC1 calculation cases.

#### 5.4 Is Mass Transport Diffusion or Advection Dominated?

The issue of advection versus diffusion dominated transport often arises in contaminant transport modelling. This can be difficult to reliably determine, and often depends on the choice of material parameters and modelling assumptions. One simple way to gain insight into the relative importance of diffusive versus advective transport is to calculate the spatial distribution of the "figure of merit" (FOM) (Little et al., 2009). The FOM variable is given by:

$$FOM = \frac{\alpha V}{D_p} \tag{5.1}$$

where

- $\alpha$  = longitudinal dispersivity (m)
- $V$  = advective velocity magnitude (m/s)
- $D_p$  = pore water diffusion coefficient ( $\text{m}^2/\text{s}$ )

For  $FOM < 0.1$ , diffusion is the dominant transport mechanism. For  $FOM > 10$ , advection dominates. If  $FOM$  lies between these values, diffusive, dispersive, and advective processes all contribute a significant proportion to the total mass flux. Figure 5.74 shows the figure of merit in the Reference

Case model for the cross-section intersecting defective container 1 (DC1). In Figure 5.74 (a) and (c), transport is neither diffusion nor advection dominated. For the short-lived period of high flow rates at the beginning of the permafrost stage (Figure 5.74 (b)), transport is clearly advection dominated. It is important to note that this calculation considers only the magnitude of the velocity (not the direction), and that this calculation is very sensitive to both  $\alpha$  and  $D_p$ . The high value of  $\alpha$  used in this model was selected to ensure numerical stability, given the large grid size, and is not based on field measurements. Given this high  $\alpha$  value, dispersive transport has probably been overestimated.

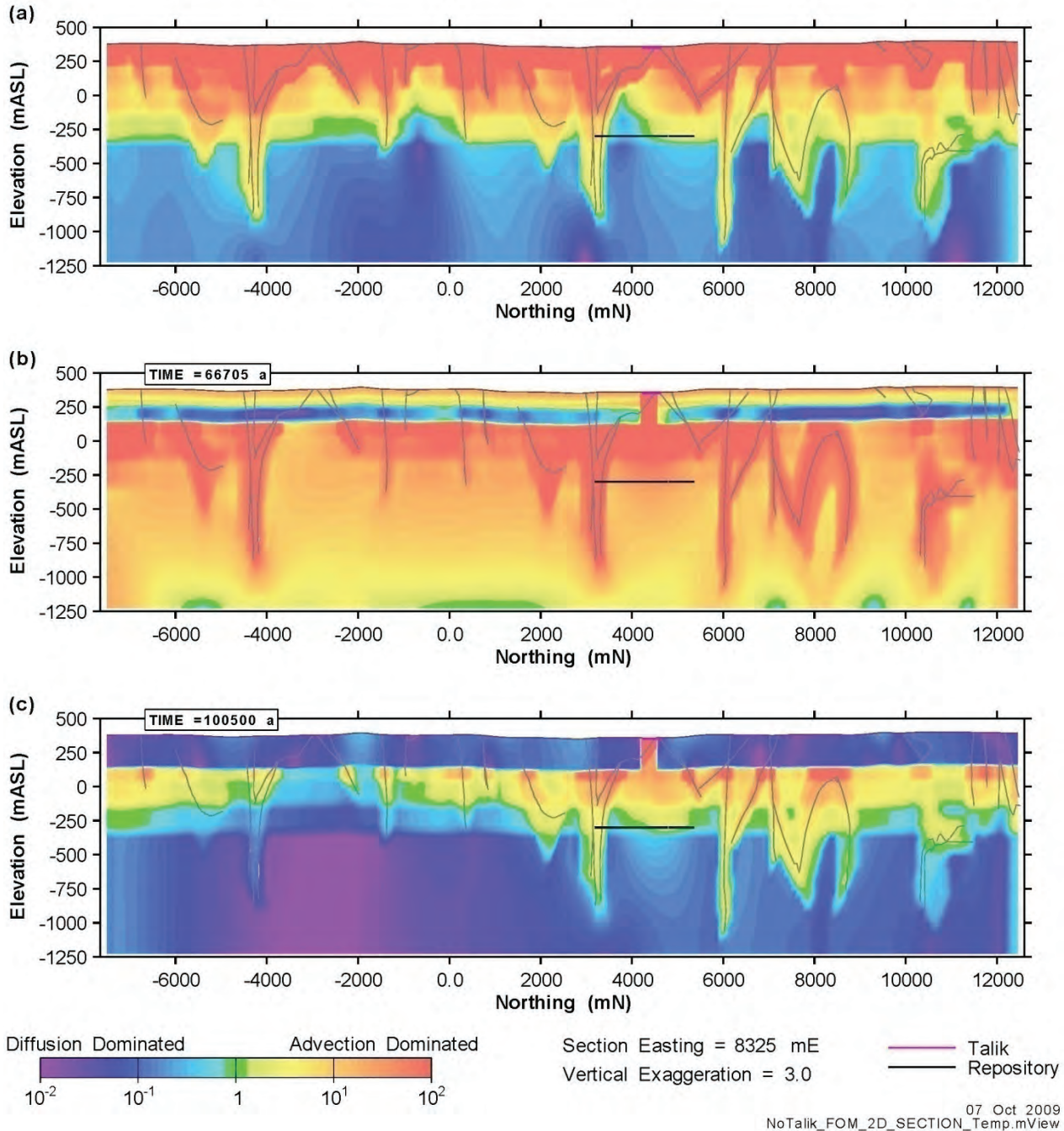


**Figure 5.74: Figure of Merit during at (a) temperate climate, (b) the start of the second permafrost period (following glaciation), and (c) the end of the same period, when glacially induced overpressures have dissipated. Section easting is 8325 mE.**

Away from the local influence of the talik, the FOM looks different. Figure 5.75 shows the FOM at the same times, but on a different cross section at 5425 mE, which intersects the location of defective container location 3 (DC3). Source DC3 is located at the northern end of the repository, and we can see that at this location diffusion is generally a more significant contributor to overall transport, but the transport regime cannot be described unequivocally as diffusion dominated.

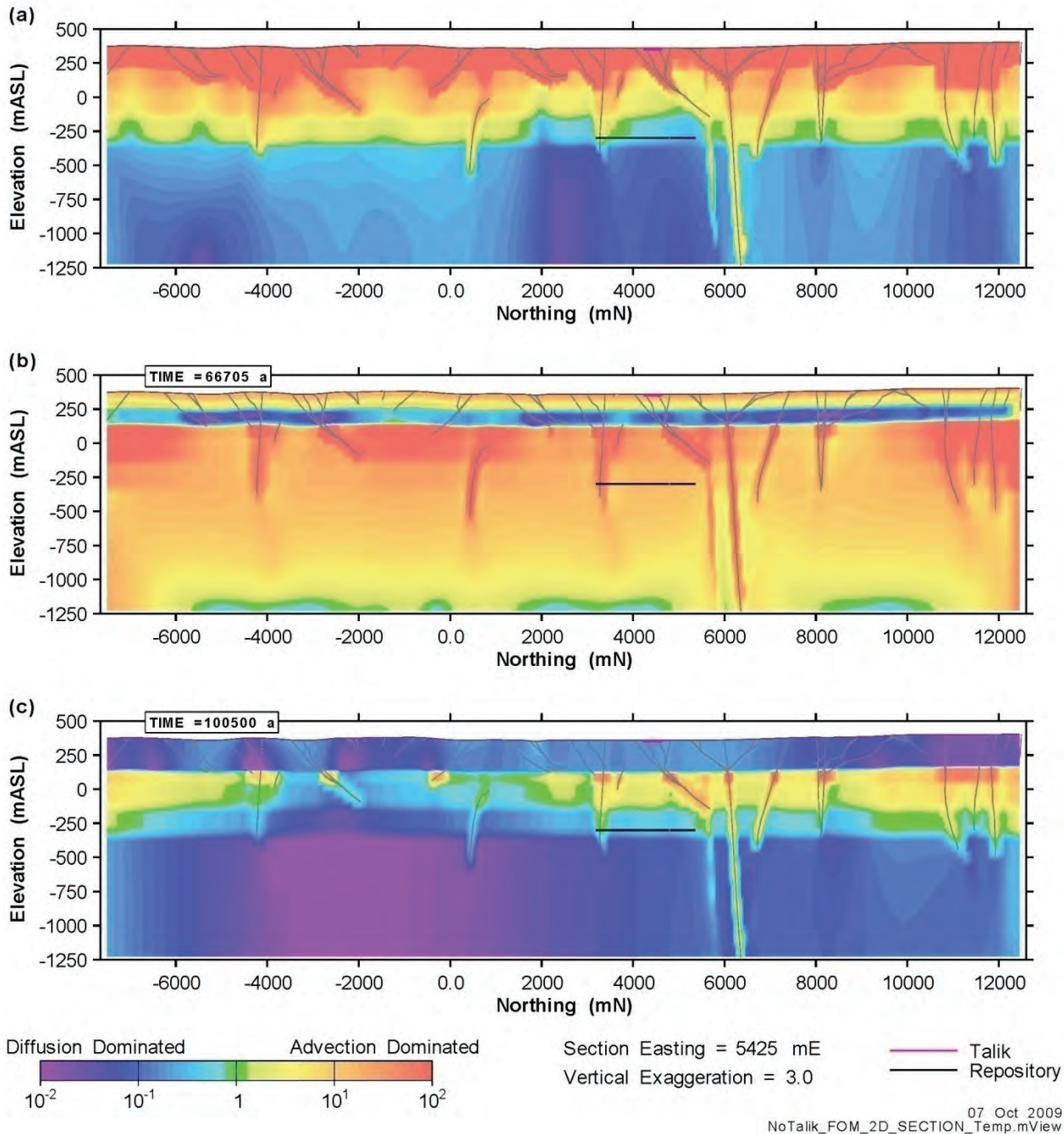


**Figure 5.75: Figure of Merit during at (a) temperate climate, (b) the start of the second permafrost period (following glaciation), and (c) the end of the same period, when glacially induced overpressures have dissipated. Section easting is 5425 mE.**

## 5.5 Numeric Performance

The transient simulations conducted for this report are the most computationally intensive deterministic groundwater flow and transport simulations that the authors of this report are aware of. The GSC study grid discretizations were significantly coarsened relative to the HBC study flow and transport grid to reduce the number of nodes and thus matrix solution effort. However, even with the coarsened grid, the transient models required approximately 120 days of continuous execution on a dedicated state-of-the-art desktop computer to reach 777,000 years. Each glacial cycle required approximately three weeks of execution time. Several tens of terabytes of results were generated, which were reduced in post-processing to slightly more than 3 TB of binary files.

The transient flow solution at each time step was the most significant component of the total execution time. The GSC-CC case, which required a single solution to the flow model, required approximately 10 hours to complete a 1 Ma transport simulation.

The 1D hydromechanical coupling was a significant component of the transient flow system execution time. Simulation of a single glacial advance without hydromechanical coupling took approximately 25 to 50 percent less time than the equivalent model with hydromechanical coupling.

## 6. ADDITIONAL NUMERIC STUDIES

Additional numeric studies were carried out to examine other aspects of the glacial cycle: glacial meltwater intrusion into the geosphere, and the effects of rapid drainage of the proglacial lake.

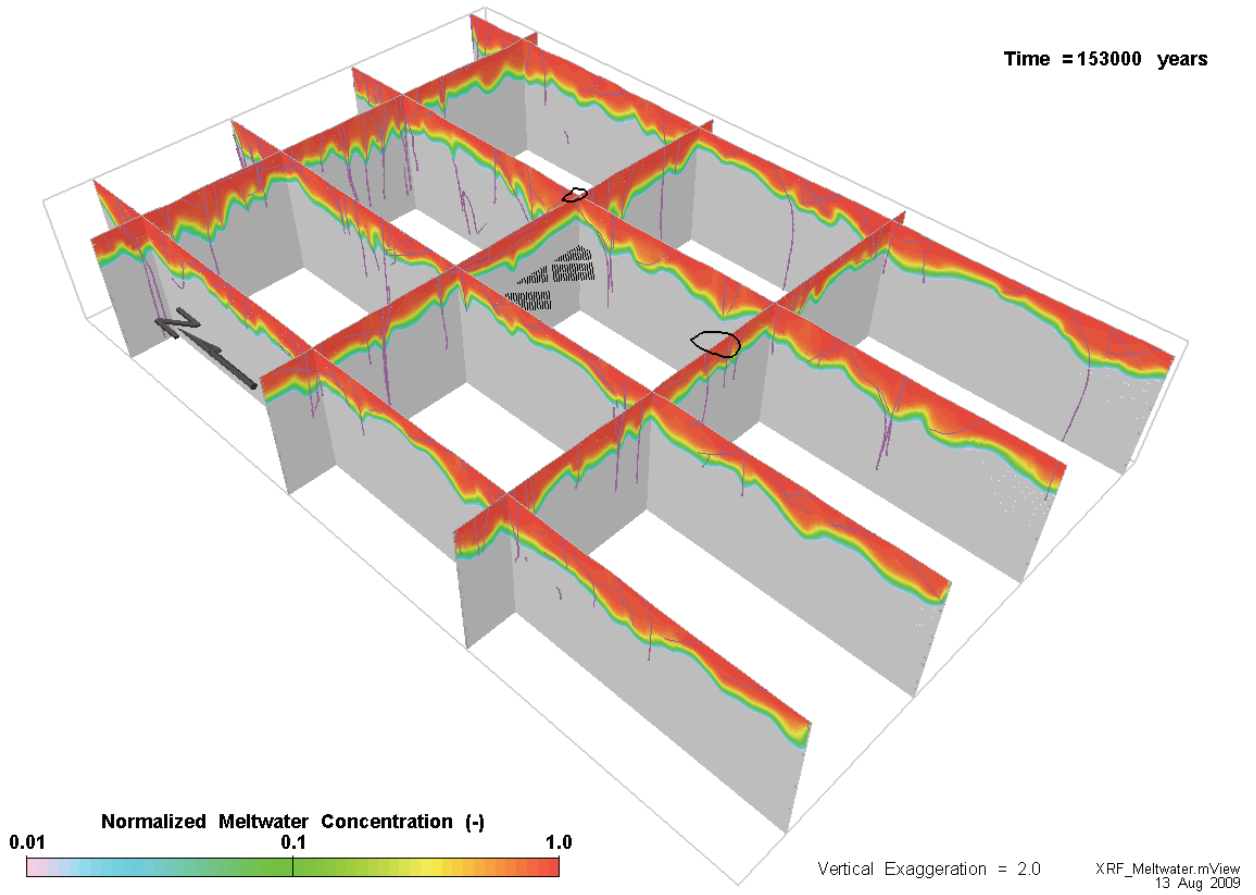
### 6.1 Glacial Meltwater Intrusion

Groundwater chemistry and geochemical processes are affected by the oxygen content of groundwaters. Generally, reducing conditions are observed at depth within the Canadian Shield bedrock. However, the recharge of oxygenated meltwater from underneath the glacier during the ice sheet cover phase may alter these conditions as oxygenated waters mix with resident porewaters. Meltwater intrusion simulations were performed to assess the possible depth and extent of water mixing. The meltwater was simulated as a dissolved species with an arbitrary concentration of 1.0 at surface. This fixed concentration boundary condition was applied to all surface nodes in the model. The third glacial stage (warm-based sequences 10 and 11) was simulated as there is no permafrost under the glacier during these sequences and hence the depth of meltwater intrusion should be greatest for this stage.

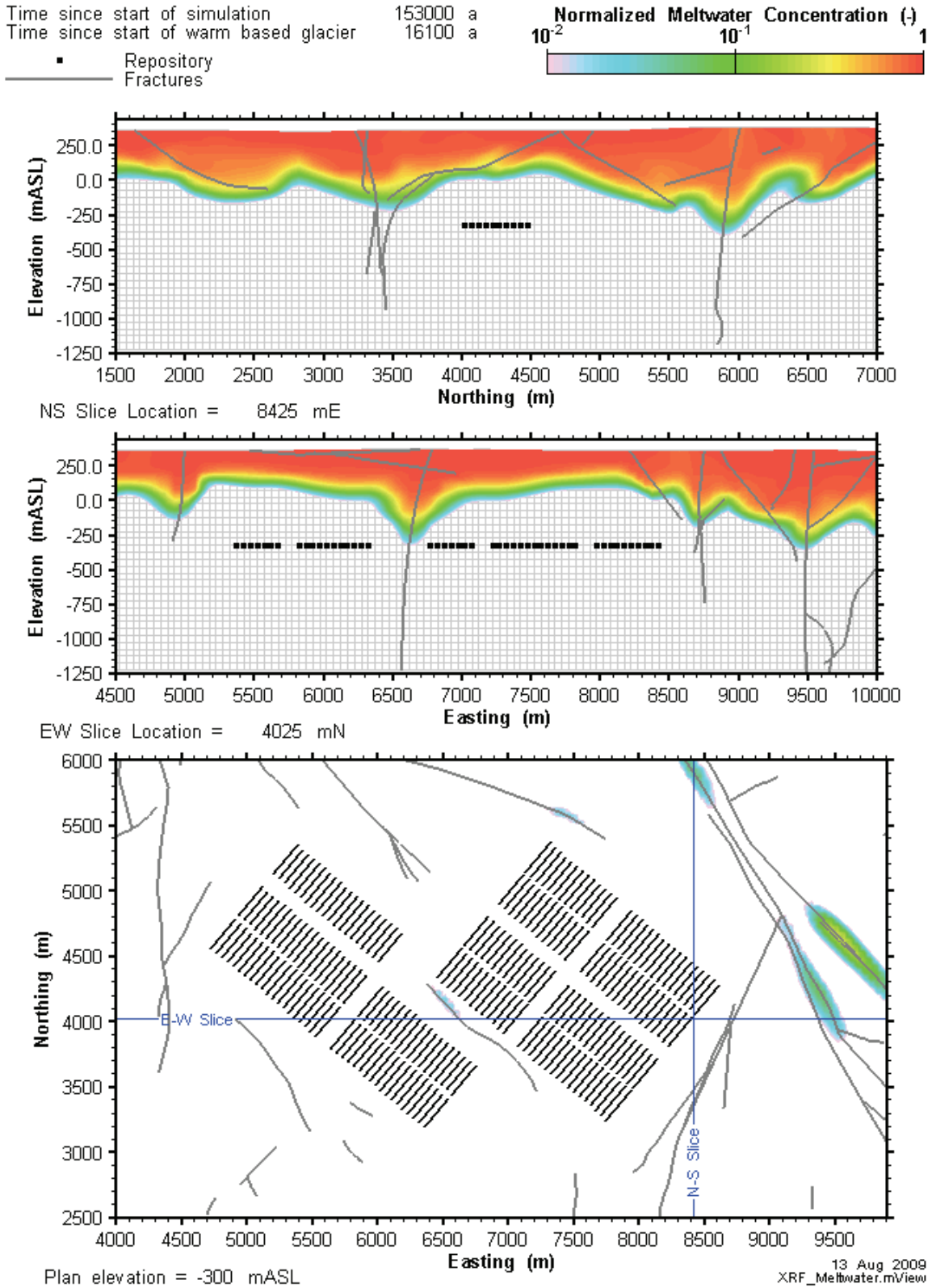
The depth of intrusion of meltwater is not representative of the depth of intrusion of oxygen since minerals within the rock could scavenge the oxygen before it reaches significant depths. For example, studies on fractured rock of the Canadian Shield indicate that oxygen signatures can be found only down to depths of about 50 m whereas cold water signatures can be found in fracture zones down to between 200 m and 400 m (Gascoyne et al. 2004).

Figure 6.1 shows the meltwater concentrations throughout the model domain at 153,000 years, the end of the third glacial advance, for the GSC-RC model. Penetration depths are similar throughout the model domain, and are clearly dependent on the presence or absence of fracture zones.

Figure 6.2 shows the concentration of meltwater at the end of the third glacial advance in the vicinity of the repository, along two vertical transects and a plan section at the repository elevation. This is a snapshot of the penetration depth just before the glacier begins its retreat from the model area. The depth of penetration is approximately a maximum at this time. It is clear from the figure that the penetration of meltwater to the depth of the repository is highly dependent on the presence of permeable fractures.



**Figure 6.1: Normalized meltwater concentrations at 153,000 years, the end of the third glacial advance.**

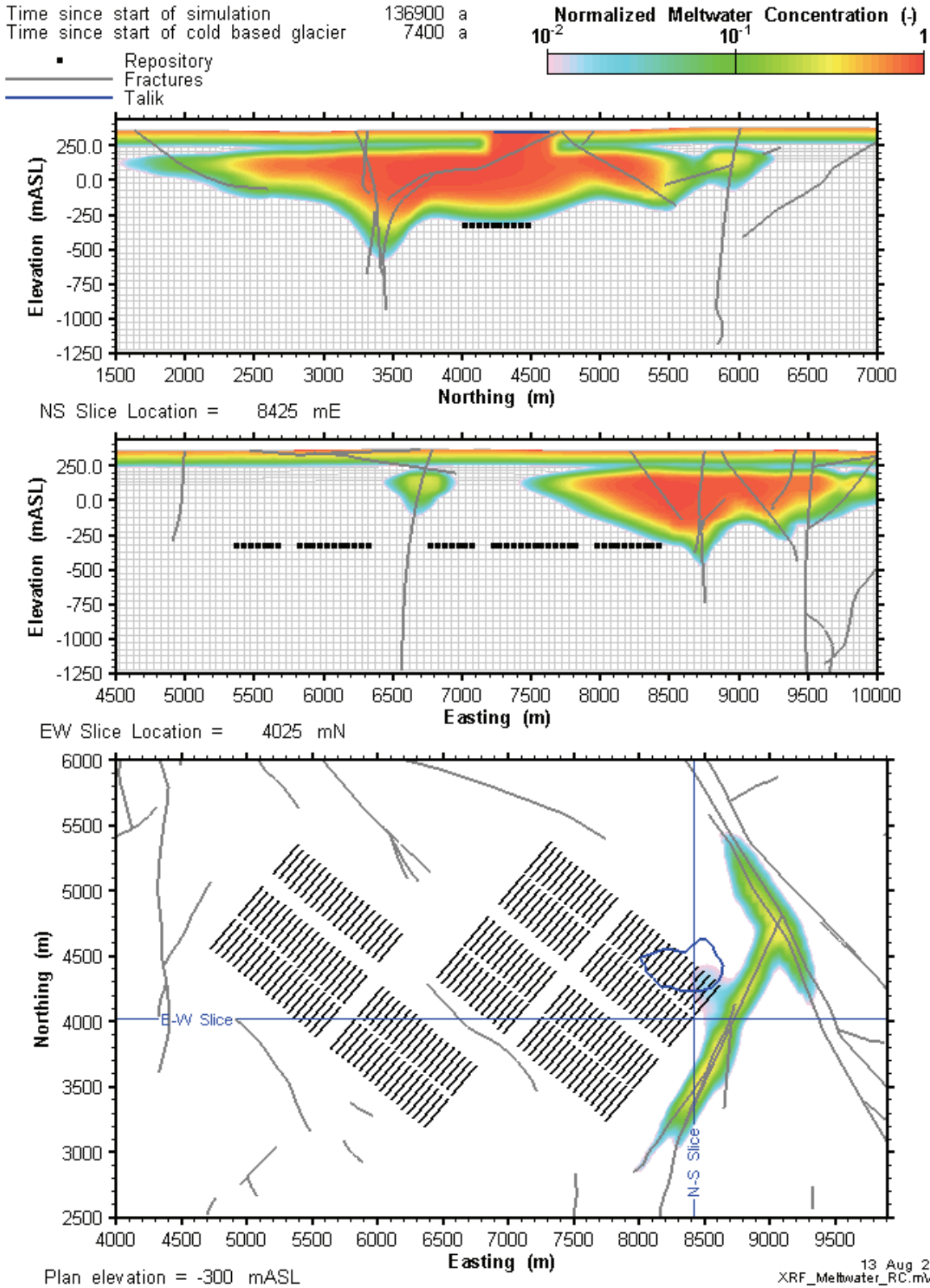


**Figure 6.2: Reference case normalized meltwater concentration in the vicinity of the repository at 153,000 years, the end of the third glacial cycle. The location of the two cross-sections is shown in the plan section.**

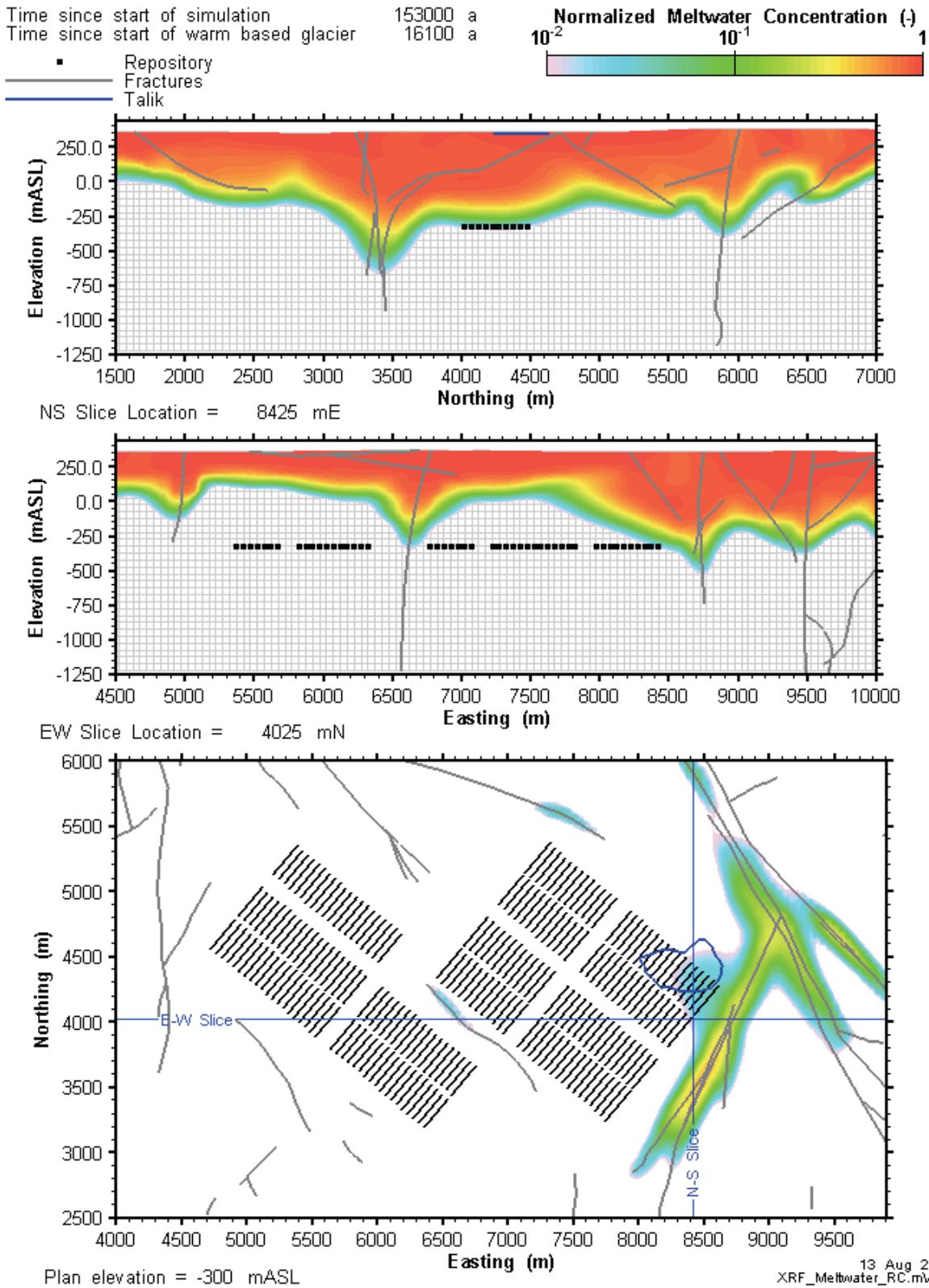
At the end of the glacial advance, 16,100 years after the start of glaciation, the meltwater has traveled throughout the fracture system, down to an average depth of roughly 350 mBGS. The simulation indicates that after 16,100 years of warm based ice cover, significant amounts of meltwater have not penetrated to the depth of the repository. This result is conservative in that it ignores the effect of density gradients on meltwater penetration. However, these findings are highly dependent on the fracture permeability, as well as fracture distribution and the specified head surface boundary condition.

Figure 6.3 shows glacial meltwater penetration under a cold-based glacier with two taliks interrupting the otherwise continuous permafrost (GSC-TK). After 7400 years of cold-based glacial advance, a limited amount of meltwater has travelled down through the fracture system directly below the talik and reached the repository elevation, although meltwater concentrations within the repository footprint do not exceed 0.01 (1% of source concentration). Meltwater from the talik has also traveled laterally under the permafrost. The simulation results indicate that vertical penetration of meltwater through the permafrost has reached a depth of approximately 100m. Permafrost permeability and porosity available for transport are not known, so these results may not be representative. Figure 6.4 shows the meltwater penetration after an additional 16,100 years of warm-based glacial advance. If Figure 6.4 is compared to Figure 6.2, it is evident that the ultimate effect of the talik, at least in terms of meltwater penetration depth, is relatively minor. However, it may affect the duration of the presence of meltwater at repository depths. Figure 6.5 shows a three-dimensional view of the meltwater penetration at the end of the cold-based advance.

Figure 6.6 shows glacial meltwater penetration under a warm-based glacier after 16,100 years of warm-based glacial advance for the GSC-HS model. Penetration depths are somewhat deeper than predicted by the Reference Case, although significant proportions of glacial meltwater (i.e., exceeding ten percent) do not reach the repository itself. As seen in other models, the depth of meltwater penetration is highly dependent on the presence or absence of fracture zones.



**Figure 6.3: GSC-TK normalized meltwater concentration in the vicinity of the repository at 136,900 years, the end of the cold based advance during the third glacial cycle. The location of the two cross-sections is shown in the plan section.**



**Figure 6.4: GSC-TK normalized meltwater concentration in the vicinity of the repository at 153,000 years, the end of the warm based advance during the third glacial cycle. The location of the two cross-sections is shown in the plan section.**

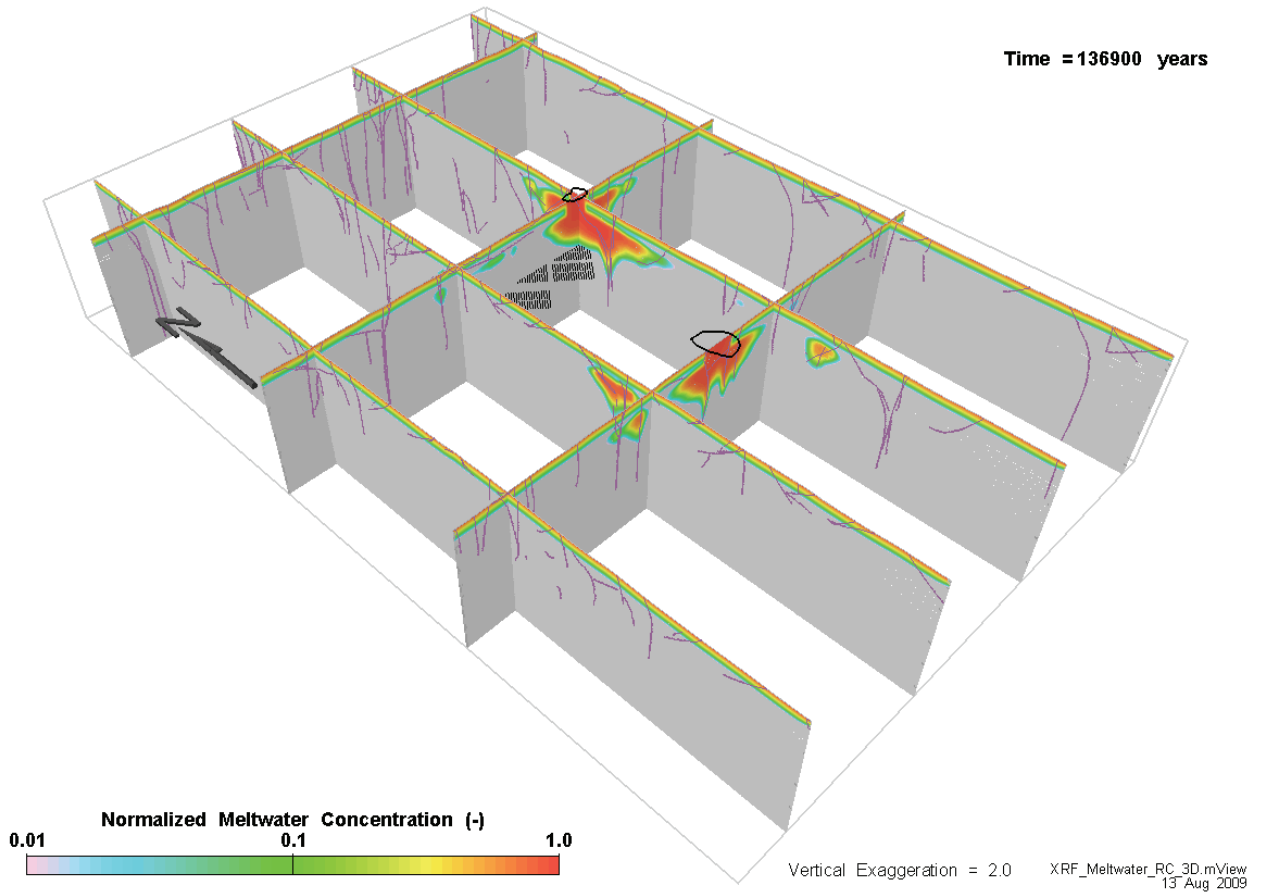


**Figure 6.5: Normalized meltwater concentrations at 136,900 years, the end of the cold-based ice advance during the third glacial cycle.**

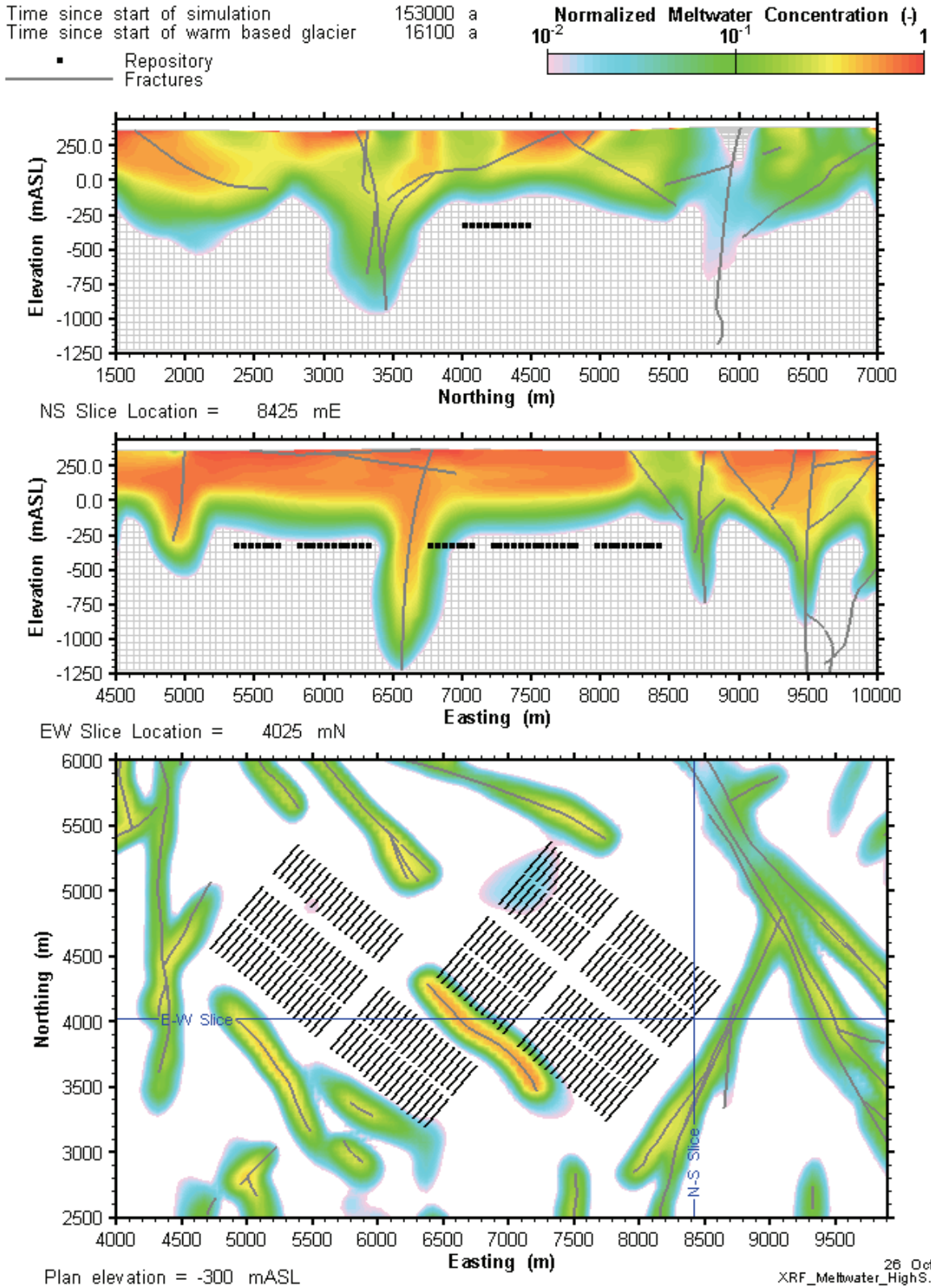


**Figure 6.6: GSC-HS normalized meltwater concentration in the vicinity of the repository at 153,000 years, the end of the warm based advance during the third glacial cycle. The location of the two cross-sections is shown in the plan section.**

## 6.2 Rapid Drainage of Proglacial Lake

The rapid drainage of a proglacial lake may occur, for instance, due to the failure of an ice dam. In preliminary modelling work, the rapid drainage of the proglacial lake caused a large spike in mass flows to the surface, due to the sudden change in the hydraulic head at the surface. To examine this possibility, two additional models were run for the second Proglacial Lake stage, between 280,700 and 281,900 years. This stage was chosen because for the Reference Case the peak mass flow rate across the North Lake during a Proglacial Lake period was observed.

In the Reference Case, and all other calculation cases, the surface hydraulic head was held constant for the first 800 years of the Proglacial Lake stage, and then reduced slowly over the next 400 years until it reached the surface elevation. In Rapid Drainage Case 1, the surface head was once again left constant for the first 800 years. At this point the head was rapidly reduced (with a drainage time of one year), a head drop of roughly 165 m. This did lead to a short lived spike in the  $^{129}\text{I}$  mass flow rates as the hydraulic system moved toward a new equilibrium. However, the maximum  $^{129}\text{I}$  mass flow rate of  $3.57 \times 10^{-7}$  mol per year was much lower than that observed during other stages in the glacial cycle (see Figure 5.62). Another simulation (rapid Drainage Case 2) was performed in which the lake was rapidly drained after only 100 years. The maximum mass flow rate was comparable to Rapid Drainage Case 1. The results of this modelling are presented in Figure 6.7 and Figure 6.8.

The simulations indicate that that spikes in  $^{129}\text{I}$  mass flow may occur following rapid drainage of large proglacial lakes. However, the peak mass flow rates, for both the DC1 and DC3 sources, are considerably lower than during other stages of the glacial cycle. Furthermore, the corresponding  $^{129}\text{I}$  concentration changes will be limited due to the accompanying spikes in the groundwater discharges. For these reasons, rapid drainage of the proglacial lake was neglected in the current study.

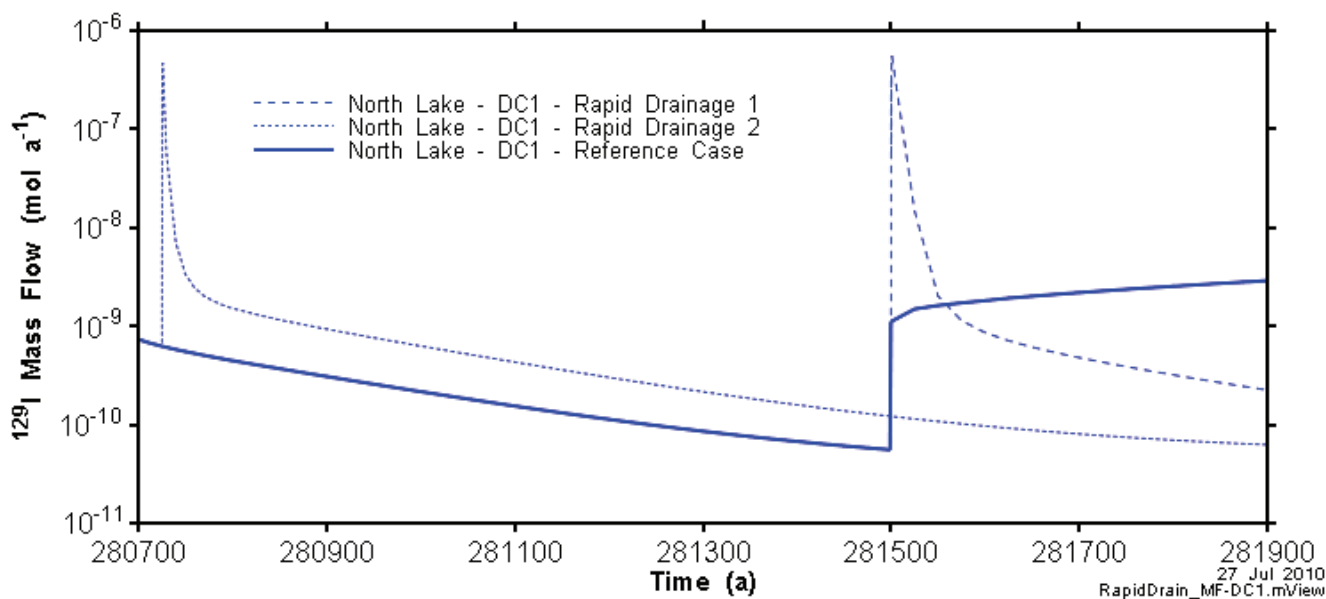
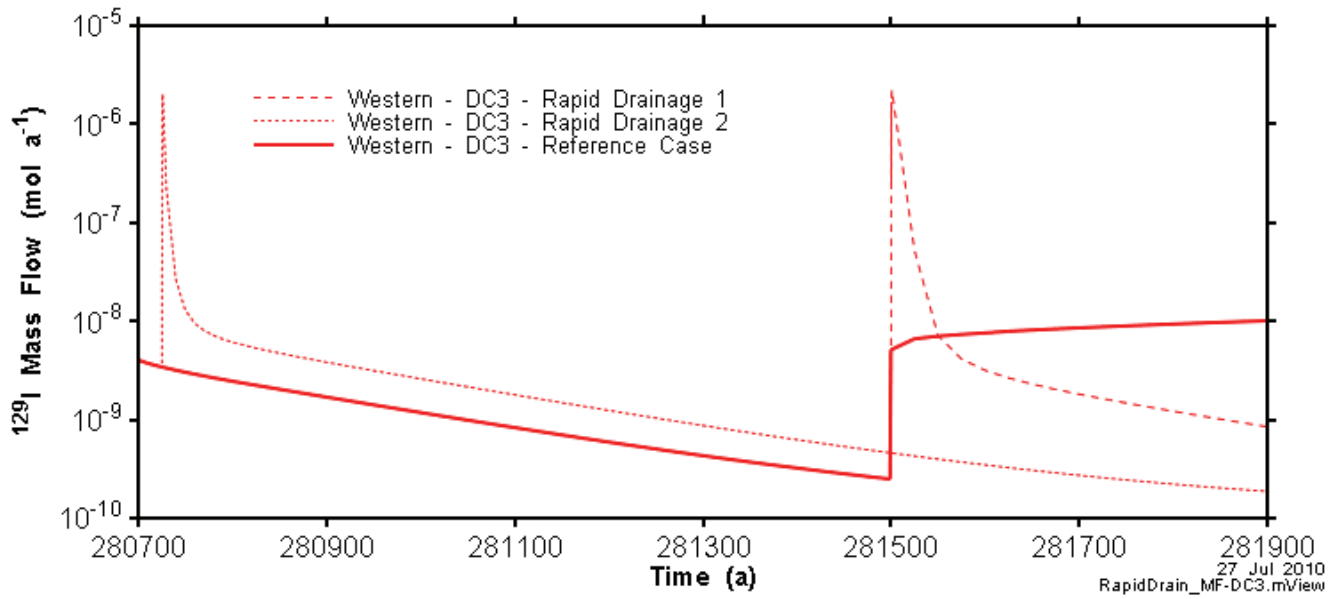


Figure 6.7: Mass flow rate across North Lake control surface for the Rapid Drainage DC1 cases, compared to GCS-RC DC1 result.



**Figure 6.8: Mass flow rate across Western control surface for the Rapid Drainage DC3 cases, compared to GCS-RC DC3 result.**

## 7. CONCLUSIONS

A general approach has been developed which captures the impact of glacial cycles on a complex, fractured flow system. Radionuclide transport has been illustrated over repository assessment time periods of up to 1 Ma years. Results of the simulations are informative, showing the wide range of advective velocities that occur at the repository horizon, and also the profound variation in flow path structure between the different climate periods.

The glaciation Reference Case model (GSC-RC) is generally more conservative than the Constant Climate model (GSC-CC), in that it predicts higher water supply well concentrations (albeit for limited time periods), higher peak  $^{129}\text{I}$  mass flows to the biosphere, and higher average  $^{129}\text{I}$  mass flows to the biosphere (as indicated by the higher cumulative mass flow). The peak  $^{129}\text{I}$  concentrations and mass flows in the glaciation model also occurred earlier than in the steady state model.

The results also show that the advective velocities around the repository are still low, and that there is a tendency for these flows to integrate out to zero over a glacial cycle. Diffusion remains an important transport mechanism near the repository, although dispersion and advection cannot be discounted. Furthermore, while the extensive changes in the shallow groundwater system lead to notable changes in the fringes of any contaminant plume, the core bulk of the contaminant mass remains largely unaffected. That is, the cumulative impact on transport of repeated cycles of advance and retreat tend to effectively "cancel out", leading to a general plume structure that is not substantially different from the steady-state flow and transport model.

As the ice-sheet advances and retreats, flow through the talik disperses  $^{129}\text{I}$  in the upper zones below the permafrost creates a larger, very dilute plume. The higher permeability fracture system is the primary conduit for plume dispersal. Finally, rapid rates of ice-sheet retreat result in overpressures at depth that can persist for thousands of years after the ice-sheet itself has retreated, impacting transport to the surface.

In the transient flow and transport models, the taliks are a dominant factor, focusing flow from a large portion of the model domain at a discrete location. These isolated gaps in the permafrost act as pathways for the dissipation of hydraulic pressure from preceding glacial events. After the stored glacial pressure has been drained and the system reaches equilibrium, the inclusion of two taliks also leads to a dipole flow system from the talik at higher elevation to that at a lower elevation. The presence of additional taliks could significantly reduce the duration of the glacially induced overpressures and perhaps also the volume of flow through individual taliks, decreasing the influence of an individual talik. The presence of taliks during cold-based glacial advances leads to the flushing with uncontaminated water of the upper, more permeable layers adjacent to the talik, leading to the dilution and displacement of the upper part of the radionuclide plume. For the DC1 source in particular, this significantly reduced the concentrations in the drinking water well, many thousands of years later. There are large differences between the transport model predictions with continuous and deep permafrost underlying a glacier, or with gaps (i.e., taliks) in the permafrost underlying cold-based glaciers.

Proximity of the source location to a talik was also an important predictor of peak and cumulative mass flow, both of which were generally higher for source DC1 (conservatively placed directly below the northern talik) than for DC3 (approximately 2 km west of northern talik). This difference was greatest during permafrost periods.

Altering the storage coefficient also had a considerable effect on the flow results, but the impact on radionuclide transport to the surface was less dramatic. When the storage coefficient was increased by a factor of 10, more persistent glacial overpressures during the post-glacial permafrost period

resulted in higher  $^{129}\text{I}$  mass flows to the biosphere. These persistent flows of water also caused increased spreading of the radionuclide plume, making it larger and more dilute. However, it is important to recall that for this simulation the storage coefficient was increased while other parameters relevant to the flow solution (i.e., porosity and Biot's  $\alpha$ ) were held constant. This caveat is described in more detail in section 4.

Changing the northern and southern boundaries from constant head to no-flow boundaries (GSC-NF) had a significant effect on the flow solution. During cold-based glacial advances and retreats the flow velocity was greatly reduced as compared to the Reference Case, leading to a smaller, more concentrated plume. Conversely, a higher and longer-lasting  $^{129}\text{I}$  mass flow was observed during the permafrost period directly after the first glacial advance and retreat (which was cold-based). During this permafrost period, the two taliks provided the only hydraulic outlets in the model domain for the dissipation of hydromechanically induced heads stored during the preceding glaciation, as no water was able to escape across the northern and southern boundaries. Consequently, the glacially induced heads persisted for a much longer time, and all flow and transport in the model was towards the two taliks.

Figure 7.1 shows the total cumulative  $^{129}\text{I}$  mass flow to the surface biosphere from the DC1 and DC3 sources for all sensitivity cases. For source DC1, which was directly below the northern talik, all transient models predicted higher mass transport to the surface than the steady-state model, particularly at earlier times. However, with the exception of the initial breakthrough, the cumulative mass was generally less than an order of magnitude greater than for the steady-state model.

For source DC3, where the influence of the northern talik was greatly reduced, the cumulative mass flow of three of the transient models was very similar to the steady-state model. However, the High Storage coefficient model (GSC-HS) changed the velocity field enough that even in the absence of a nearby talik there was an increase in the cumulative mass flow from source DC3 to the surface. The model results show that away from the hydraulic influence of the talik, the cumulative mass flow is rather insensitive to fairly significant alterations in the flow field.

Simulations showed the depths of meltwater penetration possible under the hydraulic gradient presented by the advancing ice sheet. Talik features enhanced the meltwater penetration depth to some degree when allowed under the cold-based glacier. However, the penetration depth is unsurprisingly much greater during warm based glaciation periods. The highly connected and relatively permeable fracture system was critical in allowing meltwater to penetrate beyond the upper more permeable layers, allowing a small fraction of glacial meltwater to eventually achieve repository depths.

Numeric tractability was a significant factor in this modelling, with the entire glacial sequence simulation taking about five months of computer execution time (for a 0.8Ma simulation) and producing terabytes of data. The model presented here assumed fluids of constant density; variable-density flow simulations in large 3D flow systems would likely be far too time-consuming to be used for more than a small segment of the total glacial cycle scenario.

There are several software enhancements to FRAC3DVS-OPG that would be useful to mitigate these concerns. First, application of domain decomposition approaches to matrix solution would allow effective use of multi-processor systems. Such an approach has proven extremely useful with the TOUGH2 variant TOUGH2\_MP. Secondly, the ability to perform transport simulations on existing flow simulation results would dramatically reduce the time to perform constant-density glacial cycle simulations. Currently, the majority of the execution time is taken up with the transient flow-system solution (as opposed to radionuclide transport). This solution is identical for each of the glacial cycles, but must nonetheless be repeated for transport runs. Modification of FRAC3DVS-OPG to allow radionuclide transport calculations to be performed on previously executed flow simulations could offer

significant speed increases. For example, if head and velocity fields from a single glacial cycle were stored at 1000 year increments, these would likely provide sufficient temporal resolution to accurately calculate transport. This approach would also be of benefit in assessing sensitivity cases for transport parameters and source locations. Finally, using the 1D hydromechanical coupling module dramatically increased execution times for this model, and may be another area for potential improvement to the numerical code.

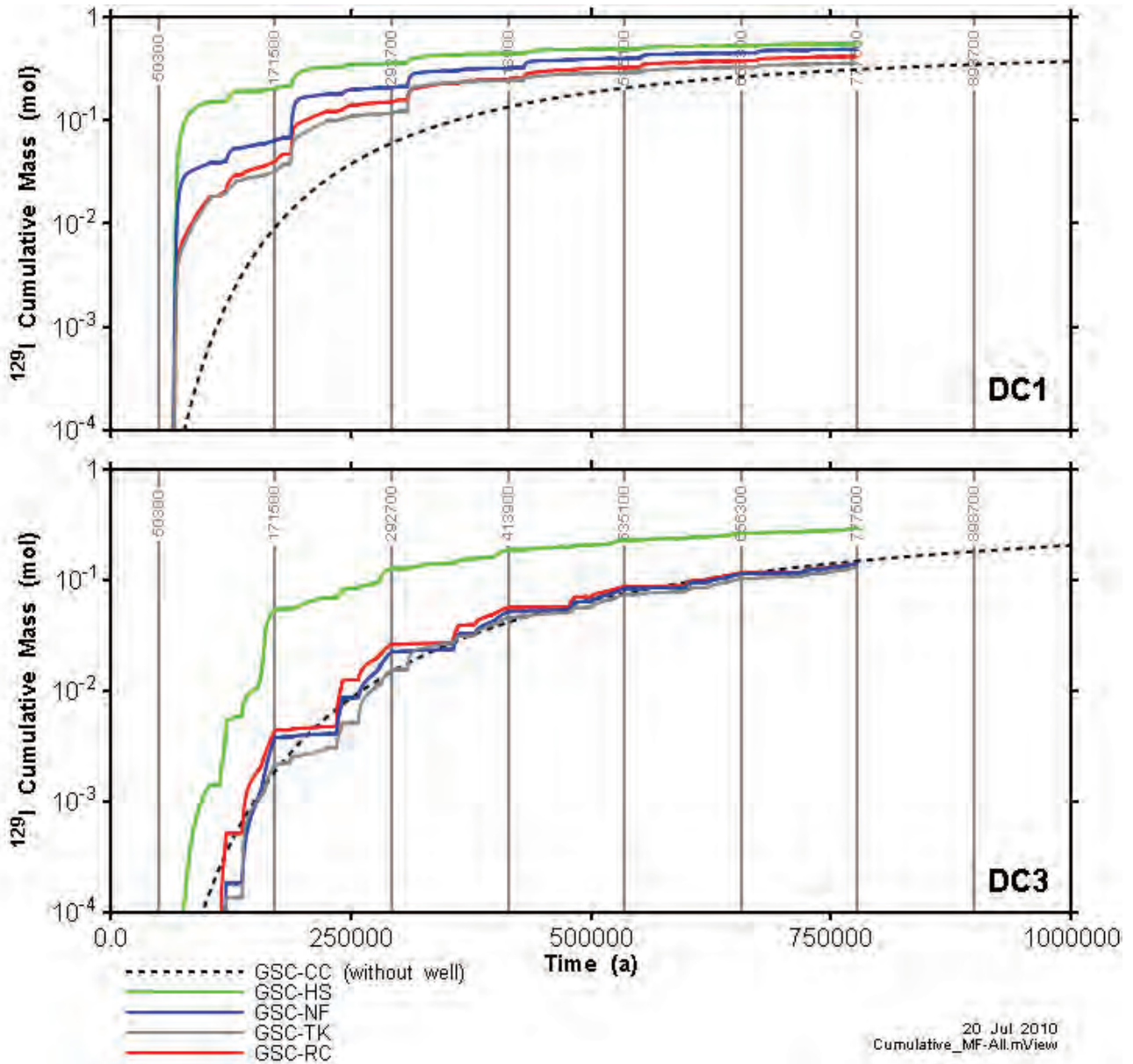


Figure 7.1: Total cumulative mass for all sensitivity cases.  $^{129}\text{I}$  mass is summed over all transport mass flow calculation zones.

The results presented here represent a small set of parameter choices, many of which are uncertain (glacier profile, geosphere storativity, hydrodynamic dispersivity, fracture permeability, loading efficiency, and permafrost properties), distributions of material properties, site features (talik locations) and conceptual models (e.g., simplified hydromechanical coupling and constant-density flow). The instantaneous changes in permeability in the upper layers, used to simulate the application of permafrost, may also be a source of error, and potentially magnify spikes in iodine mass flux. Furthermore, the model does not consider how high surface loading and hydraulic pressure might lead to permanent or transient alterations of the hydraulic conductivity of the rock mass. It has been suggested that uneven surface loading, particularly at the glacial terminus, could lead to widespread opening of vertical joints. Alternatively, the high vertical confining stresses exerted by two to three kilometres of ice would be expected to significantly reduce the permeability of the underlying rock, both vertically and horizontally. A different distribution of material parameters, for instance compressible rock underlying harder rock, could change the water flow rates and flow directions during the various stages of the glaciation scenario.

The groundwater and transport modelling results will clearly vary with other parameters or model choices, but the parameters considered here are plausible (and in some cases bounding – e.g., taliks always present over the repository, and directly over the defective container in the case of DC1). Of course, analysis of more cases will improve our confidence in the conclusions.

## REFERENCES

- Boulton, G., Caban, P., and K. van Gijssel. 1995. Groundwater flow beneath ice sheets: Part I - large scale patterns. *Quaternary Science Reviews*, 14, 545-562.
- Boulton, G., Lunn, R., Vidstrand, P., and S. Zatespin. 2007a. Subglacial drainage by groundwater-channel coupling, and the origin of esker systems: Part 1—glaciological observations. *Quaternary Science Reviews*, 26, 1067-1090.
- Boulton, G., Lunn, R., Vidstrand, P., and S. Zatespin. 2007b. Subglacial drainage by groundwater-channel coupling, and the origin of esker systems: Part II—theory and simulation of a modern system. *Quaternary Science Reviews*, 26, 1091-1105.
- Chan, T. and Stanchell, F. 2008. DECOVALEX THMC TASK E – Implications of glaciation and coupled thermohydromechanical processes on shield flow system evolution and performance assessment. Nuclear Waste Management Organization Report NWMO-TR-2008-03. Toronto, Canada.
- Clarke, G., 2005. Subglacial processes. *Annual Review of Earth and Planetary Sciences* 33, 247-76.
- Douglas, M., I.D. Clark, K. Raven, D. Bottomley 2000. Groundwater mixing dynamics at a Canadian Shield mine. *Journal of Hydrology* 235, 88-103
- Garisto, F., J. Avis, N. Calder, P. Gierszewski, C. Kitson, T. Melnyk, K. Wei and L. Wojciechowski. 2005. Horizontal borehole concept case study. Ontario Power Generation, Nuclear Waste Management Division Report 06819-REP-01200-10139-R00. Toronto, Canada.
- Garisto, F., J. Avis., T. Chshyolkova, P. Gierszewski, M. Gobien, C. Kitson, T. Melnyk, J. Miller, R. Walsh and L. Wojciechowski. 2010. Glaciation scenario: Safety assessment for a used fuel geological repository. Nuclear Waste Management Organization Technical Report NWMO TR-2010-10. Toronto, Canada.
- Gascoyne, M., J. McMurry and R. Ejeckam. 2004. Paleohydrogeologic case study of the Whiteshell Research Area. Ontario Power Generation Report 06819-REP-01200-10121-R00, Toronto, Canada.
- Gierszewski, P., J. Avis, N. Calder, A. D'Andrea, F. Garisto, C. Kitson, T. Melnyk, K. Wei and L. Wojciechowski. 2004a. Third Case Study - Postclosure safety assessment. Ontario Power Generation, Nuclear Waste Management Division Report 06819-REP-01200-10109-R00. Toronto, Canada.
- Gierszewski, P., M. Jensen, P. Maak, and A. Vorauer. 2004b. Third Case Study – Site and design description. Ontario Power Generation, Nuclear Waste Management Division Report 06819-REP-01200-10124-R00. Toronto, Canada.
- Hooke, R., Laumann, T., and J. Kohler. 1990. Subglacial water pressures and the shape of subglacial conduits. *Journal of Glaciology*, 36, 67-71.
- Lemieux, J, E. Sudicky, W. Peltier, and L. Tarasov. 2008. Simulating the impact of glaciations on continental groundwater flow systems: 1. Relevant processes and model formulation. *Journal of Geophysical Research*, 113, F3.

- Little, R., Avis, J., Calder, N., Garisto, N., Humphreys, P., King, F., Limer, L., Metcalf, R., Penfold, J., Rees, J., Savage, D., Suckling, P., Towler, G., Walke, R., and R. Walsh. 2009. Postclosure Safety Assessment (V1) Report. Nuclear Waste Management Organization Report NWMO DGR-TR-2009-01. Toronto, Canada.
- Moeller, C., Mickelson, D., Anderson, M., and C. Winguth. 2007. Groundwater flow beneath the Late Weichselian glacier in Nordfjord, Norway. *Journal of Glaciology*, 53, 84-90.
- Neuzil, C. 2003. Hydromechanical coupling in geological processes, *Hydrogeology Journal*, 11:41-83.
- Normani, S.D. 2009. Paleoevolution of pore fluids in glaciated geologic settings. Ph.D. Thesis, Civil Engineering, University of Waterloo. Waterloo, Canada.
- Normani, S.D., Y.-J. Park, J.F. Sykes and E.A. Sudicky. 2007. Sub-regional case study 2005-2006 status report. Nuclear Waste Management Organization Report NWMO-TR-2007-07. Toronto, Canada.
- Oerlemans, J. 2005. Analytical ice-sheet models. Karthaus 2005 Lecture notes. This article can be found on the web at the address:  
[http://www.phys.uu.nl/~oerlemans/Oerlemans-analytical\\_ice-sheet\\_models.pdf](http://www.phys.uu.nl/~oerlemans/Oerlemans-analytical_ice-sheet_models.pdf)
- Peltier, W.R. 2003. Long-term climate change - glaciation. Ontario Power Generation, Nuclear Waste Management Division, Technical Report 06819-REP-01200-10113-R00. Toronto, Canada.
- Peltier, W.R. 2006. Boundary conditions data sets for spent fuel repository performance assessment. Ontario Power Generation, Nuclear Waste Management Division Report 06819-REP-01200-10154-R00. Toronto, Canada.
- Piotrowski, J. A., and A. Kraus (1997), Response of sediment to ice sheet loading in northwestern Germany: Effective stresses and glacier bedstability, *Journal of Glaciology*, 43, 495–502.
- Srivastava, R.M. 2002. The discrete fracture network model in a local scale flow system for the Third Case Study. Ontario Power Generation, Nuclear Waste Management Division Report 06819-REP-01300-10061-R00. Toronto, Canada.
- Therrien, R. and E.A. Sudicky. 1996. Three-dimensional analysis of variably-saturated flow and solute transport in discretely-fractured porous media. *J. Contaminant Hydrology* 23, 1-44.
- Therrien, R., R. McLaren, E. Sudicky, S. Sanday, and V. Guvanasen, V. 2007. FRAC3DVS-OPG: A three-dimensional numerical model describing subsurface flow and solute transport (DRAFT). Groundwater Simulations Group, University of Waterloo.
- Wang, H. 2000. Theory of linear poroelasticity with application to geomechanics and hydrology, Princeton University Press, Princeton, New Jersey.

## **APPENDIX: REFERENCE CASE CONCENTRATION PLOTS**

During the assessment period, over the course of multiple glacial cycles, the radionuclide plume expands, contracts, and changes shape many times. The plots in this appendix show the evolution of the Reference Case DC1  $^{129}\text{I}$  plume in greater temporal detail than in Section 5. It is intended to show with greater fidelity the evolution of the plume during the entire assessment period, and give the interested reader greater insight into how multiple glacial cycles impact the transport of radionuclides.



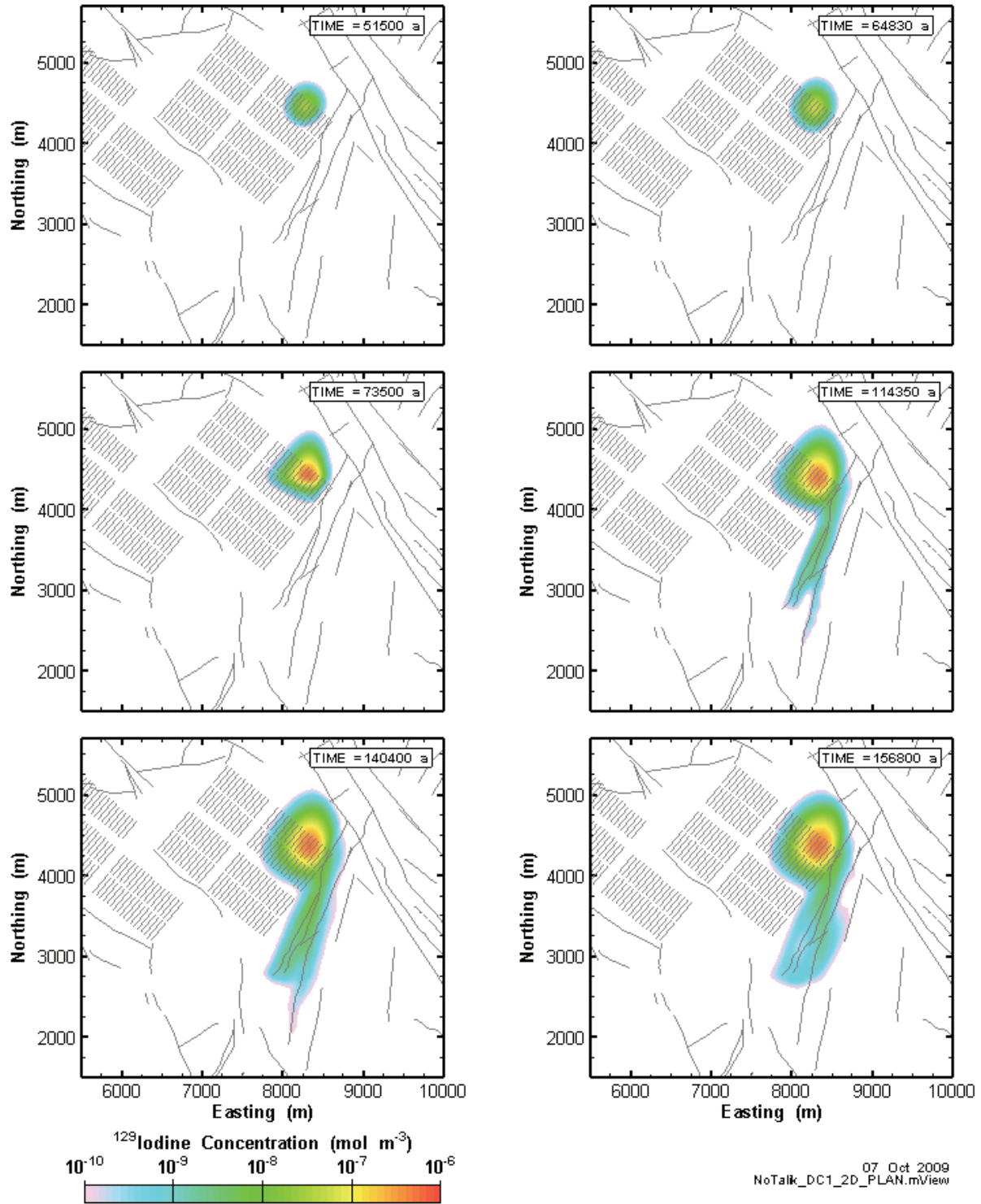


Figure A.1: GSC-RC DC1  $^{129}\text{I}$  transport model results for first glacial cycle (between 0 and 160,700 years) at an elevation of 0.0 mASL (approximately 350 mBGS).

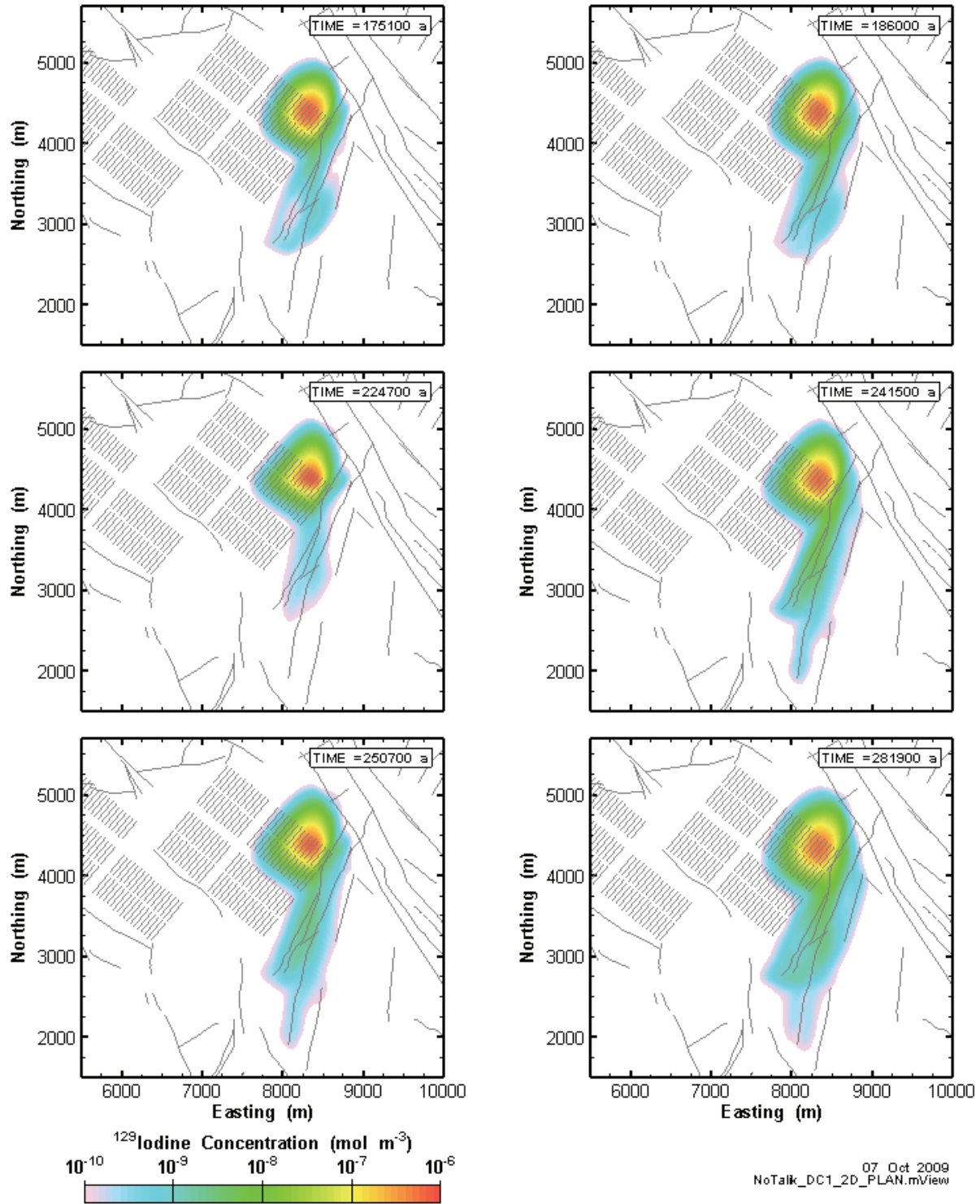


Figure A.2: GSC-RC DC1  $^{129}\text{I}$  transport model results for second glacial cycle (between 160,700 and 281,900 years) at an elevation of 0.0 mASL (approximately 350 mBGS).

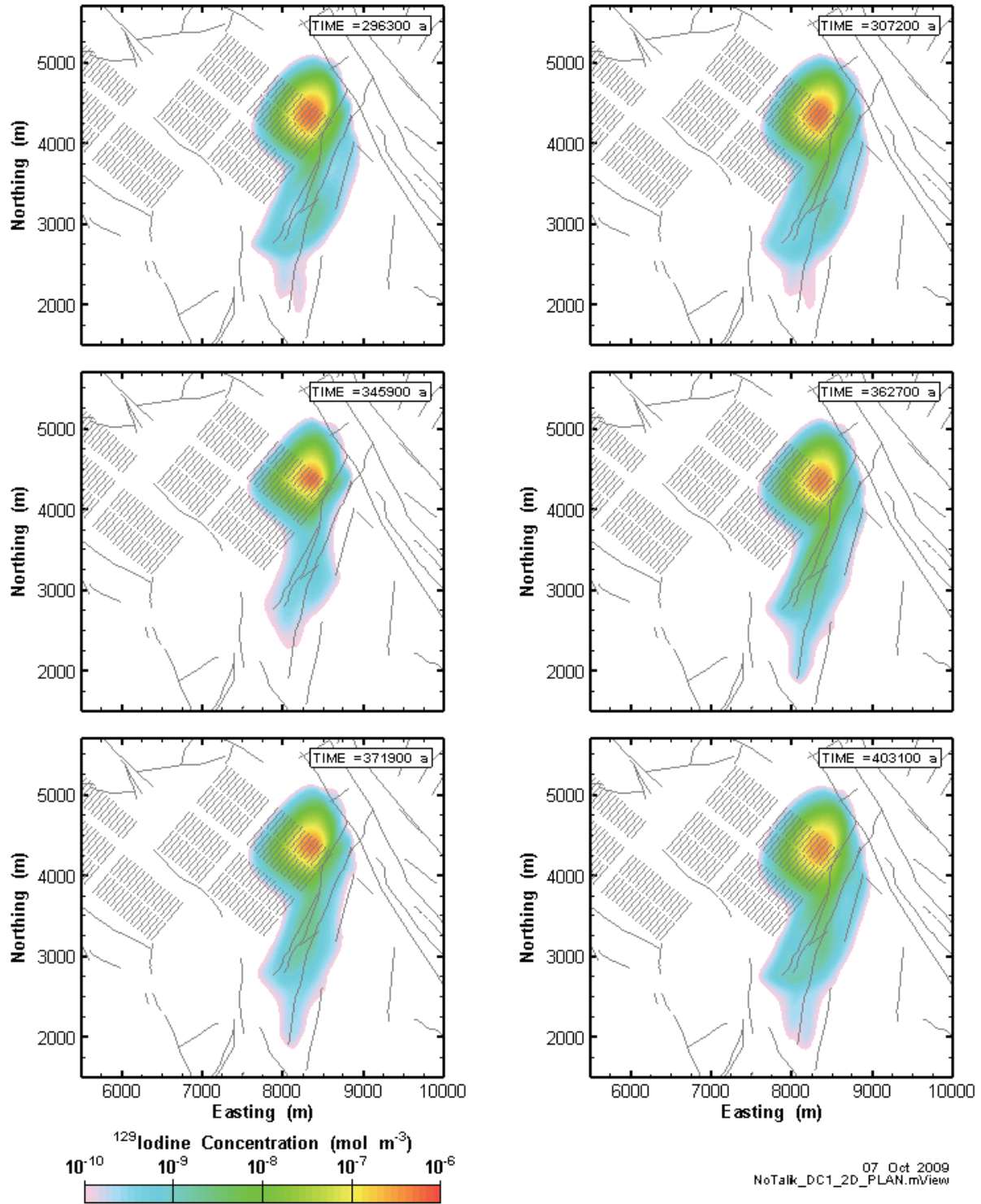


Figure A.3: GSC-RC DC1  $^{129}\text{I}$  transport model results for third glacial cycle (between 281,900 and 403,100 years) at an elevation of 0.0 mASL (approximately 350 mBGS).

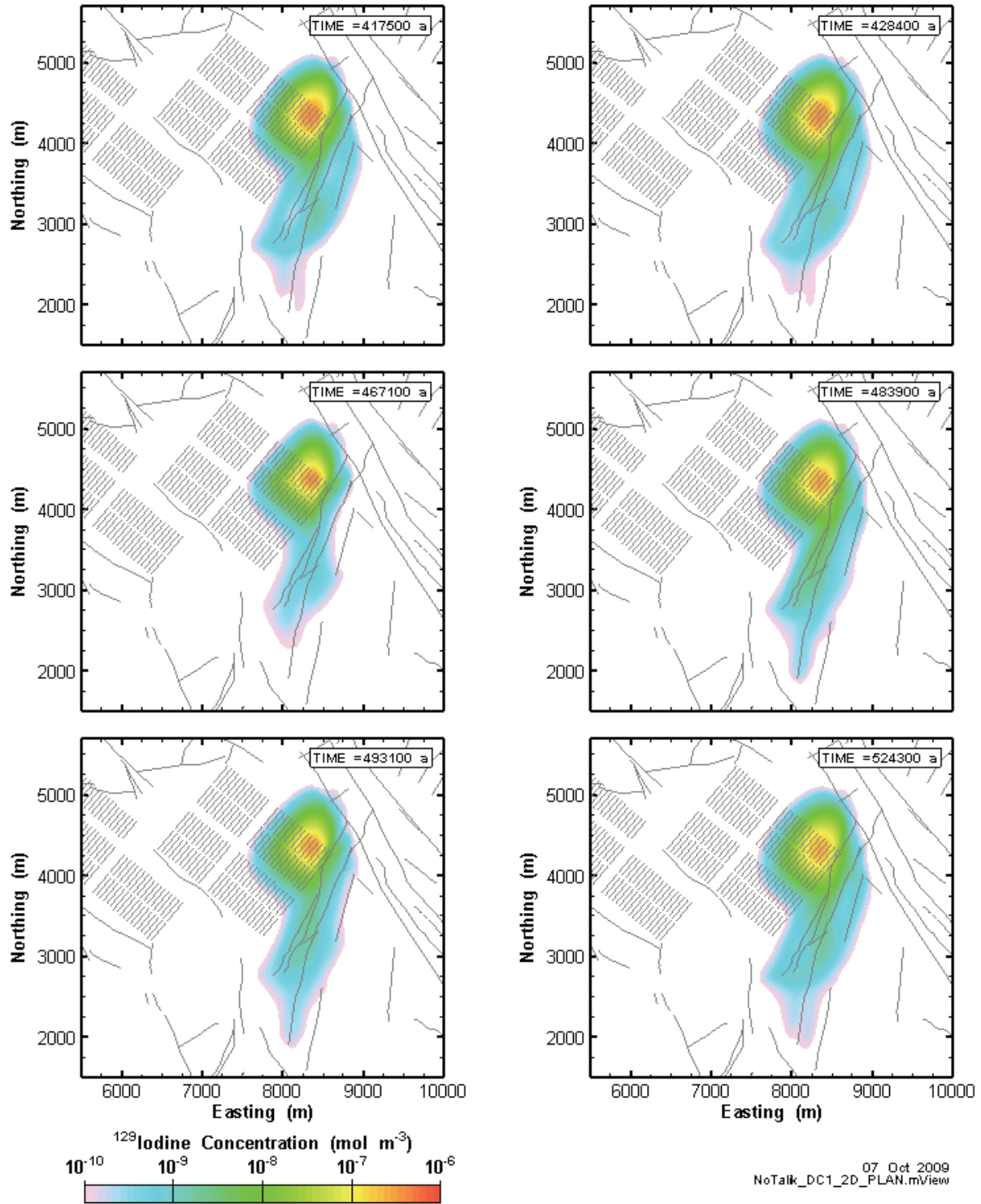


Figure A.4: GSC-RC DC1  $^{129}\text{I}$  transport model results for fourth glacial cycle (between 403,100 and 524,300 years) at an elevation of 0.0 mASL (approximately 350 mBGS).

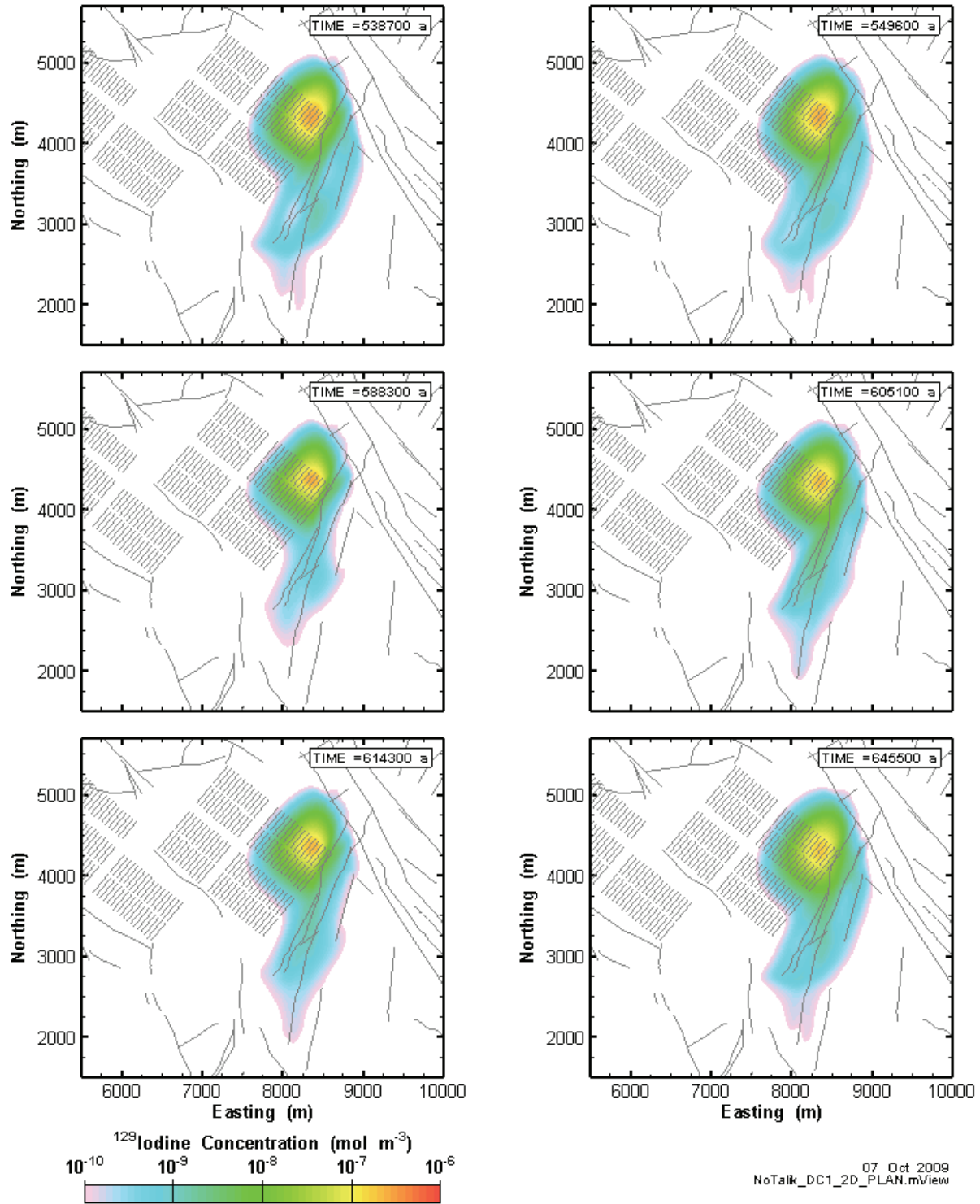


Figure A.5: GSC-RC DC1  $^{129}\text{I}$  transport model results for fifth glacial cycle (between 524,300 and 645,500 years) at an elevation of 0.0 mASL (approximately 350 mBGS).

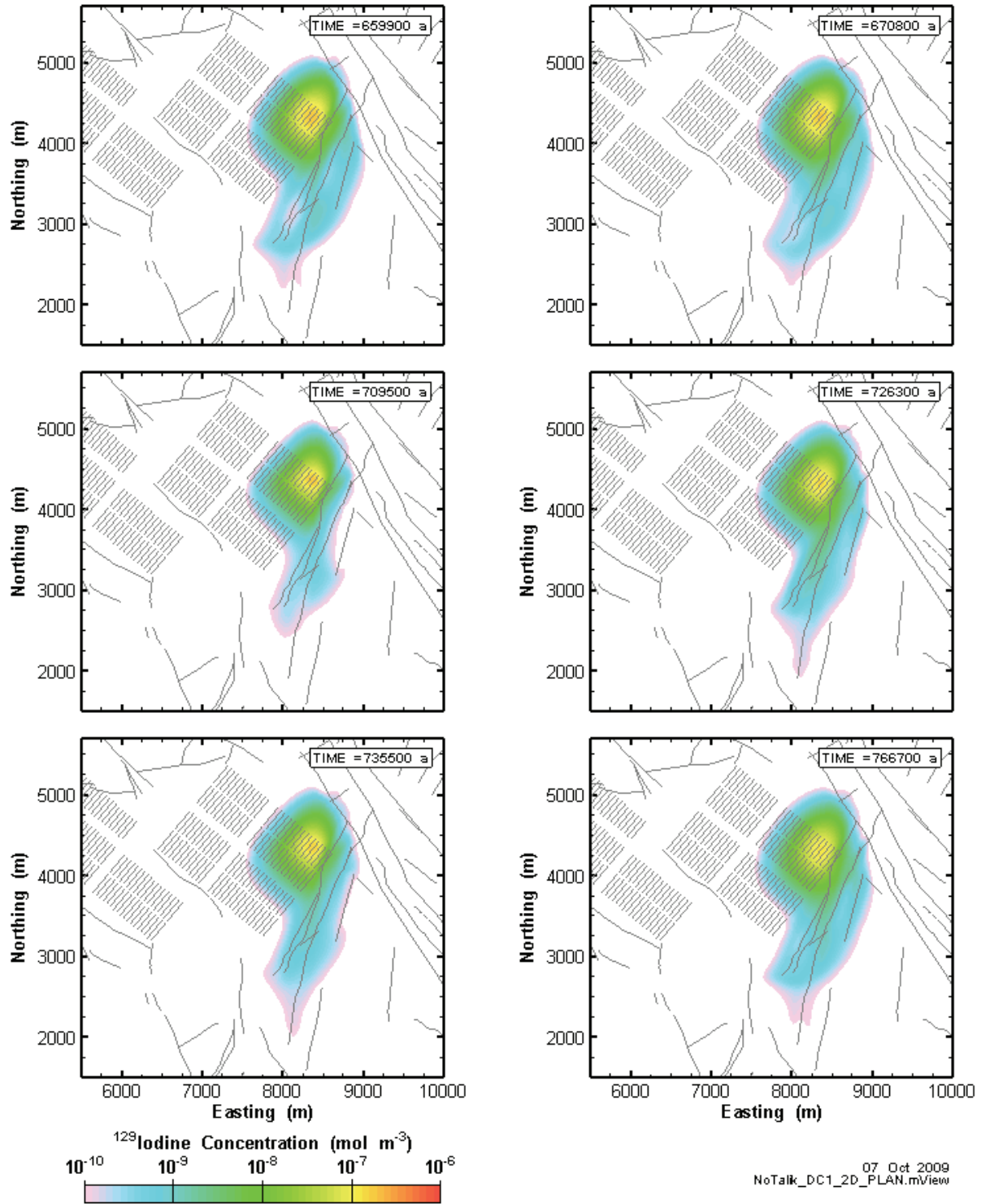


Figure A.6: GSC-RC DC1  $^{129}\text{I}$  transport model results for sixth glacial cycle (between 645,500 and 766,700 years) at an elevation of 0.0 mASL (approximately 350 mBGS).